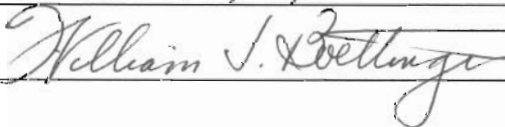
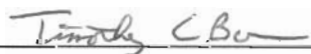


INTERFACE THERMODYNAMICS
WITH APPLICATIONS TO ATOMISTIC SIMULATIONS

by

Timofey Frolov
A Dissertation
Submitted to the
Graduate Faculty
of
George Mason University
in Partial Fulfillment of
The Requirements for the Degree
of
Doctor of Philosophy
Physics

Committee:

 _____	Dr. Yuri Mishin, Dissertation Director
 _____	Dr. William J. Boettinger, Committee Member
 _____	Dr. Michael E. Summers, Committee Member
 _____	Dr. Karen L. Sauer, Committee Member
 _____	Dr. Michael E. Summers, Department Chairperson
 _____	Dr. Timothy L. Born, Associate Dean for Student and Academic Affairs, College of Science
 _____	Dr. Vikas Chandhoke, Dean, College of Science

Date: December 2, 2011

Fall Semester 2011
George Mason University
Fairfax, VA

Interface Thermodynamics
with Applications to Atomistic Simulations

A dissertation submitted in partial fulfillment of the requirements for the degree of
Doctor of Philosophy at George Mason University

By

Timofey Frolov
Bachelor of Science
South Ural State University, 2004

Director: Dr. Yuri Mishin, Professor
Department of Physics and Astronomy

Fall Semester 2011
George Mason University
Fairfax, VA

Copyright © 2011 by Timofey Frolov
All Rights Reserved

Dedication

To C. Montgomery Burns

Acknowledgments

I would like to thank my advisor Dr. Yuri Mishin for his constant motivation, support, advice and direction. I also would like to thank my dissertation committee members for their valuable feedback. I am especially grateful to my friend and collaborator Dr. William J. Boettinger for his support, advice and valuable comments on my dissertation. I also would like to thank professors of South Ural State University for providing me with a solid foundation in physics and math. Finally, I would like to acknowledge support of my family: parents Vladimir and Natalia Frolov, sister Yulia Kudasheva, grandfather Vasiliy Kozhevnikov and my wife Rebekah M. Evans Frolov.

Table of Contents

	Page
List of Tables	x
List of Figures	xii
Abstract	xxiii
1 Introduction	1
1.1 Interfaces	1
1.2 Thermodynamics of interfaces	3
2 Coherent phase boundaries	8
2.1 Thermodynamics of a solid phase	8
2.1.1 Kinematics of deformation of a solid phase	8
2.1.2 Thermodynamic description of a homogeneous solid phase	10
2.1.3 Relevant thermodynamic potentials	13
2.1.4 The Gibbs-Duhem equation	16
2.2 Equilibrium between two solid phases separated by a coherent interface	17
2.2.1 Phase equilibrium conditions	17
2.2.2 Derivation of the phase change equilibrium condition	20
2.2.3 Equation of coherent phase coexistence in the parameter space	22
2.3 Interface thermodynamics	24
2.3.1 The interface free energy γ	24
2.3.2 The adsorption equation	31
2.3.3 Lagrangian and physical forms of the adsorption equation	37
2.3.4 Thermodynamic integration	38
2.3.5 Maxwell relations	39
2.4 Application of the treatment to other types of interfaces	43
2.4.1 Interfaces in two-phase systems	43
2.4.2 Interfaces in a single-phase systems	45
2.5 Discussion and conclusions	49
2.6 Examples of thermodynamic equations for particular systems	52
2.6.1 Single component system	52

2.6.2	Binary substitutional alloy	54
2.6.3	Binary interstitial alloy	55
2.6.4	Interface stress	56
3	Methodology of Atomistic Simulations	58
3.1	Simulation Methods	58
3.1.1	Molecular dynamics (MD)	58
3.1.2	Monte Carlo (MC)	58
3.2	Modeling of interatomic interactions	59
3.2.1	Embedded atom method	59
3.2.2	Employed interatomic potentials	60
4	Temperature dependence of the surface free energy and surface stress: An atom- istic calculation for Cu (110).	61
4.1	Introduction	61
4.2	Thermodynamic relations	64
4.2.1	Solid surface	64
4.2.2	Solid-liquid interface	67
4.3	Methodology of atomistic simulations	69
4.3.1	Simulated models	69
4.3.2	Monte Carlo simulations	70
4.3.3	Structural order analysis	71
4.3.4	Surface and interface stress calculations	72
4.3.5	Thermodynamic integration	73
4.4	Results	74
4.5	Discussion and conclusions	80
4.6	Thermodynamic equations	84
5	Orientation dependence of the solid-liquid interface stress: atomistic calculations for copper.	88
5.1	Introduction	88
5.2	The interface stress as an excess quantity	89
5.3	Methodology of atomistic simulations	90
5.3.1	Simulated models	90
5.3.2	MD simulations	91
5.3.3	Interface positions and profiles	92
5.3.4	Interface excesses calculations	93
5.4	Results and discussion	95
5.5	Discussion	99

6	Solid-liquid interface free energy in binary systems: theory and atomistic calculations for the (110) Cu-Ag interface	101
6.1	Introduction	101
6.2	Thermodynamic relations for a binary solid-liquid interface	103
6.2.1	Interface free energy as an excess quantity	103
6.2.2	Adsorption equation	109
6.2.3	Thermodynamic integration schemes	112
6.2.4	The case of an interstitial solid solution	115
6.3	Methodology of atomistic simulations	117
6.3.1	Model system and methodology of Monte Carlo simulations	117
6.3.2	Interface excess quantities and thermodynamic integration	119
6.4	Simulation results	122
6.5	Discussion and conclusions	126
7	Effect of non-hydrostatic stresses on solid-fluid equilibrium. I. Bulk thermodynamics	129
7.1	Introduction	129
7.2	Thermodynamics of non-hydrostatic solid-fluid equilibrium	131
7.2.1	Thermodynamic relations	131
7.2.2	Deformation of a solid in equilibrium with the same fluid	142
7.3	Methodology of atomistic simulations	143
7.3.1	Simulated models	143
7.3.2	Simulations at constant zero pressure in the liquid	144
7.3.3	Simulations at constant temperature	145
7.3.4	Calculation of elastic constants and elastic compliances	146
7.4	Results	146
7.4.1	The phase coexistence surface	146
7.4.2	Instability of non-hydrostatic systems	151
7.5	Discussion and conclusions	154
7.6	Maxwell relations for an elastic solid	157
7.7	Non-hydrostatic stress-strain transformation	159
7.8	Iso-fluid equations in terms of strains	165
7.9	Stability of the fluid with respect to crystallization to a hydrostatic solid . .	167
8	Effect of non-hydrostatic stresses on solid-fluid equilibrium. II. Interface thermodynamics.	170
8.1	Introduction	170
8.2	Thermodynamics of solid-fluid interfaces	172

8.2.1	Interface free energy γ and the adsorption equation.	172
8.2.2	The interface stress	176
8.2.3	Relation to the Shuttleworth equation	185
8.2.4	Thermodynamic integration methods	186
8.3	Methodology of atomistic simulations	188
8.3.1	Simulation block and molecular dynamics methodology	188
8.3.2	Calculation of profiles and excess quantities	189
8.4	Results	190
8.5	Summary and conclusions	196
9	Grain boundaries under stress	199
9.1	Introduction	199
9.2	Thermodynamics of grain boundaries	200
9.2.1	Grain boundaries versus phase boundaries	200
9.2.2	Thermodynamic description of the system	203
9.2.3	Excess GB free energy	205
9.2.4	The adsorption equation.	207
9.2.5	Lagrangian and physical forms of the adsorption equation	209
9.2.6	Thermodynamic integration	210
9.2.7	Maxwell relations	211
9.3	Methodology of atomistic simulations	214
9.3.1	Description of the studied GB	214
9.3.2	Simulation block	216
9.3.3	Single component copper system and copper-silver binary alloy . . .	216
9.3.4	0K calculations. Single component Cu system.	216
9.3.5	Single component Cu system at finite temperatures	218
9.3.6	Binary CuAg System	219
9.3.7	Test of Maxwell relations in case of binary system at finite temperature	220
9.4	Results	220
9.4.1	0K calculations	221
9.4.2	Single component Cu system at finite temperature	228
9.4.3	Binary CuAg system at finite temperature	230
9.4.4	Effects of mechanical deformation and temperature on segregation .	236
9.5	Discussion and conclusions	239
9.6	Work of lateral deformation	241
10	Liquid nucleation at superheated grain boundaries	243

10.1	Introduction	243
10.2	GB premelting	244
10.3	Nucleation	250
10.3.1	2D	251
10.3.2	3D	254
10.4	MD simulations of nucleation	256
10.4.1	Results and Discussion	258
11	Summary	262
11.1	Thermodynamics of phase boundaries	262
11.2	Symmary of atomistic simulation	264
	Bibliography	270

List of Tables

Table	Page	
5.1	Dimensions of the simulation block (in Å) and the total number of atoms N used in this work for different orientations of the solid-liquid interface. The interface plane is normal to the z direction.	91
5.2	Interface stress components (τ_{11} and τ_{22}) and their average (τ) in J/m ² for different orientations of the solid-liquid interface in copper.	97
7.1	Elastic constants and elastic compliances of Cu at $T_H = 1327$ K with $[\bar{1}10]$, $[001]$ and $[110]$ crystallographic directions aligned with x , y and z axes. Due to crystal symmetry, there are only four distinct elastic constants (compliances), only three of which are independent. The two-index elastic constants in the cubic system at T_H are $c_{11} = 106.6$ GPa, $c_{12} = 86.4$ GPa and $c_{44} = 41.1$ GPa, which are smaller than the 0 K values $c_{11} = 169.9$ GPa, $c_{12} = 122.6$ GPa and $c_{44} = 76.2$ GPa.	147
7.2	Lateral strains and stresses in the solid and the corresponding solid-liquid equilibrium temperatures predicted by Eq. (7.36) (T_{Theor}) and computed directly from MD simulations (T_{MD}) for variations at constant zero pressure in the liquid.	147
7.3	Biaxial lateral strains, stresses in the solid, and the equilibrium pressures in the liquid predicted by Eq. (7.37) (p_{Theor}) and computed directly from MD simulations (p_{MD}) for isothermal variation at T_H	148
9.1	Derivatives involved in the Lagrangian form of Maxwell relations Eqs. (9.14) - (9.17) computed at 0 K. The expressions in the first row represent the denominator of the partial derivative, while the first column contains the numerators. The derivatives were evaluated at a stress free state of the bulk. The table is symmetrical (within accuracy of our calculations) in accord with predictions of the Maxwell relations.	228

9.2 Derivatives involved in the physical form of Maxwell relations Eqs. (9.14) - (9.17) computed at 0 K. The expressions in the first row represent the denominator of the partial derivative, while the first column contains the numerators. The derivatives were evaluated at a stress free state of the bulk. The table is symmetrical (within accuracy of our calculations) in accord with predictions of the Maxwell relations. 229

List of Figures

Figure	Page
1.1 Construction of the Gibbs dividing surface.	4
2.1 Two-dimensional schematic of a volume element undergoing a finite deformation. In the reference state (dashed lines), the volume element is a unit square. The components of the deformation gradient \mathbf{F} represent the new lengths or projections of the cube edges in the deformed state (solid lines.)	11
2.2 (a) Two-dimensional schematic of a reference volume element (shaded unit square) transforming to coherent phases α (dashed lines) and β (solid lines). The differences between the deformation-gradient components F_{13} , F_{23} and F_{33} of the phases form the transformation vector \mathbf{t} . (b,c) Two-dimensional schematic of two phases, α and β , separated by a coherent interface. When the interface moves down, the striped region of phase α shown in (b) transforms the striped region of phase β shown in (c). During the transformation, the deformation-gradient components F_{11} , F_{12} and F_{22} remain the same in both phases.	17
2.3 Two solid phases separated by coherent interface. Interface region shown by solid red line includes homogeneous parts of phases α and β . Regions inside homogenous parts of the phases are shown in green.	28
2.4 Coherent transformation of the region initially located inside phase α (a) into a layer containing both phases and an interface (b). (c) is a zoomed view of the reference region with the dotted line showing an approximate interface position in reference coordinates. (d) is a zoomed view of the deformed region of phase α (dashed lines) and the two-phase region (solid lines). The dash-dotted line outlines a shape defining the average deformation gradient $\bar{\mathbf{F}}$. The open circles mark imaginary markers embedded in the reference and deformed states of the bulk phases.	32

3.1	Schematic representation of a simulation box with particles in MD simulations. The arrows indicate the velocity vectors.	59
3.2	Schematic representation of a simulation box with particles in MC simulations. The figure illustrates accepted random displacement.	60
4.1	Simulation blocks and positions of the interface and bulk regions employed in the calculations of thermodynamic properties of (a) solid surfaces and (b) solid-liquid interfaces. The quantities computed in different regions are indicated. The bracketed quantities refer to the surface/interface layer, whose bounds can be chosen arbitrary as long as they lie within the homogeneous bulk phases. The bulk regions can lie beyond the surface/interface layer, as in this figure, or inside it (not shown).	63
4.2	Typical MC snapshot of (a) (110) solid film at 1320 K and (b) (110) solid-liquid coexistence system at 1327 K. The open circles mark instantaneous atomic positions projected on the $(1\bar{1}0)$ plane parallel to the page. The top and bottom surfaces of both systems are exposed to vacuum. The distances h , d and d' are discussed in the text.	69
4.3	Typical MC snapshot of the solid film at three temperatures. The open circles mark instantaneous atomic positions projected on the $(1\bar{1}0)$ plane parallel to the page. Note the perfectly ordered surface structure at low temperatures and premelting at high temperatures.	73
4.4	Thickness of the (110) surface layer as a function of temperature. The vertical dashed line indicates the bulk melting point.	75
4.5	Average stress τ and the surface structure factor $ S(\mathbf{k}) _{top}$ of the (110) surface as a function of temperature. The vertical dashed line indicates the bulk melting point.	75
4.6	Temperature dependence of the average surface stress computed by MC simulations of systems with 1024, 2240 and 9856 atoms, and by molecular dynamics simulations of a 896-atom system. Note that the shape of the curve does not depend on the model size or the simulation method.	76
4.7	Temperature dependence of the surface-stress anisotropy $\tau_{22} - \tau_{11}$. The vertical dashed line indicates the bulk melting point.	77

4.8	Temperature dependence of the excess free energy and stress of the (110) surface. Three values of the free energy, γ^l , of the liquid-vacuum interface are shown for comparison. The vertical dashed line indicates the bulk melting point.	78
4.9	Temperature and bulk-strain dependencies of the surface stress obtained by MC simulations and by 0 K static calculations. In the latter case, the data are plotted against the temperature at which thermal expansion would give the corresponding strain. The close agreement below 800 K indicates the dominant role of the bond-stretching effect in the temperature dependence of surface stress of atomically ordered surfaces.	79
4.10	Temperature dependence of the excess entropy of the (110) Cu surface. The vertical dashed line indicates the bulk melting point.	80
5.1	a) A typical snapshot of the simulation block containing two solid-liquid interfaces with the (110) orientation. The liquid regions are exposed to vacuum. b) Schematic presentation of the simulation block showing the regions used for the interface stress calculations.	94
5.2	Typical snapshots of the simulated solid-liquid interfaces with different orientations. For clarity, only a part of the simulation block is shown in each case. Note the (111) facets formed by the (110) interface.	95
5.3	The number density of atoms (n , in \AA^{-3}) as a function of distance from the solid-liquid interface with the (110) orientation.	96
5.4	Computed profiles of the lateral stresses across solid-liquid interfaces with different orientations. For the (100) and (111) orientations, only the average of the two stress components is shown.	98
6.1	Schematic presentation of a binary solid-liquid system. The left part of the block is the solid phase, the right part is the liquid phase. The vertical dashed line indicates the approximate position of the interface. Atoms in circles belong to a conceptually selected layer bounded by imaginary planes aa' and bb'. Three positions of the layer are shown: (a) the layer is inside the solid, (b) the layer is just touching the interface, and (c) the interface is approximately in the middle of the later. The total number of atoms inside the layer is constant while its volume and average chemical composition can vary.	104

6.2	The Cu-Ag phase diagram predicted by the embedded-atom potential used in this work. The red lines mark the equilibrium solid and liquid compositions implemented in this work.	118
6.3	(a) Snapshot of the simulation block at 1000 K. The solid phase is sandwiched between two liquid layers, each exposed to vacuum to ensure zero pressure in the z -direction. The yellow and gray colors designate Cu and Ag atoms, respectively. (b) Schematic presentation of different regions involved in the calculations of excess quantities. L is the total thickness of the layer used for interface excess calculations. The solid-liquid interfaces are indicated by vertical red lines. The curly braces mark homogeneous solid and liquid regions. Distances d and d' are discussed in the text.	119
6.4	Profiles of (a) Ag concentration and (b) lateral components of stress in the $[1\bar{1}0]$ and $[001]$ directions of the solid at 1000 K.	120
6.5	Principal components of the solid-liquid interface stress as functions of temperature. The vertical dashed line indicates the melting point of pure Cu.	123
6.6	Excess values of internal energy U at the solid-liquid interface for two different choices of the conserved properties X and Y . This plot demonstrates that the excess of U depends on the choice of the conserved variables.	123
6.7	Ag segregation $[N_2]_{NV}$ at the solid-liquid interface as a function of temperature. Note the agreement between the direct and indirect calculations (see text for detail). The vertical dashed line indicates the melting point of pure Cu.	125
6.8	Temperature dependence of the solid-liquid interface free energy computed with different choices of the conserved properties X and Y . As expected, the computed values are identical within the accuracy of calculations. The vertical dashed line indicates the melting point of pure Cu.	126

7.1	Schematic illustration of solid-fluid coexistence surfaces at constant pressure p in the fluid and $q_{12} = 0$ in the solid. The equilibrium temperature T is plotted as a function of two remaining non-hydrostatic components of the stress in the solid. (a) Path of biaxial tension and compression on the coexistence surface. (b) Iso-fluid path obtained by intersection of the paraboloid with an isothermal plane. (c) Phase coexistence surface when the initial hydrostatic state is a special point. If $q_{12} \neq 0$, the coexistence surfaces shown here become 3D and are difficult to visualize, but they remain paraboloids in (a) and (b) and an ellipsoidal double-cone in (c).	140
7.2	Equilibrium temperature T as a function of lateral stresses σ_{11} ($[\bar{1}10]$ direction) and σ_{22} ($[001]$ direction) in the solid computed for copper with the (110) solid-liquid interface. Pressure in the liquid remains zero. The blue surface is the theoretical prediction from Eq. (7.36), the red points are results of direct MD simulations.	149
7.3	Equilibrium temperature as a function of the non-hydrostatic stress component q_{11} in the solid subject to biaxial tension or compression. Pressure in the liquid remains zero. The points are results of direct MD simulations, the line was computed from Eq. (7.36).	149
7.4	Equilibrium pressure in the liquid as a function of the non-hydrostatic stress component q_{11} in the solid subject to biaxial tension or compression at a constant temperature T_H . The points are results of direct MD simulations, the line was computed from Eq. (7.37).	150
7.5	(a) Snapshot of the simulation block during crystallization at $T = 1271$ K. (b) Profiles of the lateral components of stress σ_{11} and σ_{22} across the simulation block. Before the crystallization, the stresses in the solid were $\sigma_{11} = 3.4$ GPa and $\sigma_{22} = 2.3$ GPa.	152
7.6	(a) Simulation block with edge dislocations visualized using central symmetry analysis. Atoms with large values of the symmetry parameter are invisible. (b) Different views of $\frac{1}{2}[110]$ edge dislocations showing its dissociation into partials.	153
8.1	Schematic of a solid-fluid system with a plane interface. The interface layer and the homogeneous solid and fluid regions are outlined.	173

8.2	Equilibrium temperature T as a function of non-hydrostatic components of strain E_{ij} at a constant pressure p in the fluid and a constant E_{12} . (a) The line of biaxial tension/compression. (b) An iso-fluid path. The triangle shows the slope of the iso-fluid path at a particular point marked by a cross. . . .	183
8.3	(a) Typical snapshot of the simulation block with the solid and liquid phases. (b) Schematic illustration of regions selected for calculations of excess quantities.	188
8.4	Profiles of (a) atomic density, (b) energy density, and stress components (c) σ_{11} and (d) σ_{22} when the solid is under compression ($T = 1325.2$ K), tension ($T = 1325.5$ K) and nearly hydrostatic ($T = 1326.4$ K). The vertical dashed line indicates the position of the Gibbsian dividing surface.	192
8.5	Excess energy per unit area, $[U]_{NV}/A$, as a function of biaxial strain. The vertical dashed line indicates the stress-free state of the solid phase.	193
8.6	Components of the interface stress $\hat{\tau}^{NV}$ as functions of biaxial strain. The vertical dashed line indicates the stress-free state of the solid phase.	193
8.7	Iso-fluid interface stresses as functions of biaxial strain. The vertical dashed line indicates the stress-free state of the solid phase.	194
8.8	The slope of the iso-fluid path as a function of biaxial strain. The value -1.62 computed from Eq. (8.27) is shown by the horizontal dashed line. The open circle is a reminder that the slope is undefined for the hydrostatic state.	195
8.9	Interface free energy γ as a function of equilibrium temperature T for biaxial compression and tension. The red and blue lines were computed from Eq. (8.32), while the black line was computed using Eq. (8.34). The results of the two calculations coincide within the error of integration. The vertical dashed line indicates the stress-free state of the solid phase.	196
9.1	Schematics of a bicrystal forming a symmetrical tilt boundary. The grain boundary plane is normal to the z direction.	201
9.2	Schematic representation of the system with the GB. Grains 1 and 2 are in neutral equilibrium. The figure shows a spontaneous migration of the GB. .	204
9.3	Structure of the symmetrical tilt $\Sigma 5(310)$ GB. The figure shows projections of the perfect atomic positions on the (001) plane. The tilt axis is normal to the plane of the figure.	215

9.4	Simulation block with the GB. The position of the GB is indicated by red coloration. Atoms colored in grey belong to boundary regions 1 and 2. Boundary conditions in the GB plane are periodic.	215
9.5	Single component Cu system, 0 K. γ as a function of lateral strain at constant zero σ_{31} and σ_{33} a) the simulation block was elastic ally deformed by the same amount along x and y directions (biaxially $e = e_{11} = e_{22}$) b) uniaxial strain e_{11} was applied along the x direction c) uniaxial strain e_{22} was applied along the y direction	222
9.6	Single component Cu system, 0 K. Excess GB volume per unit area $[V]_N/A$ as a function of σ_{33} computed at fixed lateral dimensions.	224
9.7	Single component Cu system, 0 K. γ as a function of normal stress σ_{33} at fixed lateral dimensions. The discrete point on the plot correspond to direct calculation of γ using Eq. (9.29), while the continuous line was obtained from thermodynamic integration using Eq. (9.30).	224
9.8	(a) Displacement of atoms in the direction of shear parallel to the GB plane with shear stress $\sigma_{31} = 1.5$ GPa computed relative to the stress free state. In the bulk grains the displacement is proportional to the z coordinate. There is an excess displacement in the GB region. (b) Excess GB shear as function of shear stress σ_{31}	226
9.9	Single component Cu system, 0 K. γ shear as a function of shear stress σ_{31} parallel to the tilt axes. The discrete points on the plot correspond to direct calculations from Eq. (9.31), while the continuous line was obtained from thermodynamic integration using Eq. (9.32).	226
9.10	Single component Cu system at 0 K. Test of Maxwell relation (9.14) in the physical form.	227
9.11	Single component Cu system at 0 K. Test of Maxwell relation (9.15) in the Lagrangian form.	228
9.12	Single component Cu system. Excess GB energy per unit area $[U]_N/A$ as a function of temperature. The discrete points were obtained from MD simulations. The continuous line was plotted to guide an eye.	230
9.13	Single component Cu system. Components τ_{11} and τ_{22} of excess GB stress as functions of temperature. The discrete points were obtained from MD simulations. The continuous line was plotted to guide an eye.	231

9.14	Single component Cu system. GB free energy γ as a function of temperature computed by thermodynamic integration (9.34). The reference value of γ at $T = 300$ K indicated by a solid circle was computed from harmonic approximation. The value of γ at $T = 0$ K is indicated by a solid circle. . .	232
9.15	Binary CuAg system. Snapshots of the simulation block with the bulk concentration of silver c_{Ag} (a) 0.036%, (b) 0.24%, and (c) 0.58% at $T = 800$ K.	233
9.16	Binary CuAg system. Excess GB volume per area $[V]_N/A$ as a function of silver concentration c_{Ag} in the bulk at $T = 800$ K.	234
9.17	Binary CuAg system. Components τ_{11} and τ_{22} of GB stress as a function of silver concentration c_{Ag} in the bulk at $T = 800$ K.	234
9.18	Binary CuAg system. GB segregation $[N_2]_N/A$ as a function of silver concentration c_{Ag} in the bulk at $T = 800$ K.	235
9.19	Binary CuAg system. GB free energy γ as a function of silver concentration c_{Ag} in the bulk at $T = 800$ K.	235
9.20	Test of the Lagrangian form of Maxwell relation in Eq. (9.18) in binary CuAg system. The discrete points on the figures correspond to MC simulations data, while the dashed lines are linear fits. (a) GB segregation $[N_2]_N$ as a function of biaxial strain parallel to the boundary. (b) Sum of the principal components τ_{11} and τ_{22} of the GB stress as a function of the diffusion potential $M_{21} \equiv M_{Ag}$. The derivative was evaluated for a stress free state in the bulk at $T = 800$ K and $c_{Ag} = 0.036\%$. On the plots this state is indicated by vertical dashed lines. The computed derivatives $\frac{\partial [N_2]_N/A_{ref}}{\partial e} = 0.46 \pm 0.01$ $^{-2}$ and $\frac{\partial (\tau_{11} + \tau_{22})/A_{ref}}{\partial M_{Ag}} = -0.46 \pm 0.08$ $^{-2}$ confirms the correctness of the relation within accuracy of our calculations.	236

- 9.21 Test of the Maxwell relation in Eq. (9.20) in binary CuAg system. The discrete points on the figures correspond to MC simulations data, while the dashed lines are linear fits. (a) GB segregation $[N_2]_N$ as a function of stress σ_{33} normal to the plane of the GB. (b) Excess GB volume per area (GB thickness) as a function of the diffusion potential $M_{21} \equiv M_{Ag}$. The derivative was evaluated for a stress free state in the bulk at $T = 800\text{ K}$ and $c_{Ag} = 0.036\%$. On the plots this state is indicated by vertical dashed lines. The computed derivatives $\frac{\partial [N_2]_N / A_{ref}}{\partial \sigma_{33}} = 0.030 \pm 0.0006\text{ }^{-2}\text{GPa}^{-1}$ and $\frac{\partial [V]_N / A_{ref}}{\partial M_{Ag}} = 0.027 \pm 0.004\text{ }^{-2}\text{GPa}^{-1}$ confirms the correctness of the relation within accuracy of our calculations. 238
- 9.22 Test of the Lagrangian form of Maxwell relation in Eq. (9.24) in binary CuAg system. The discrete points on the figures correspond to MC simulations data, while the dashed lines are linear fits. (a) GB segregation $[N_2]_N$ divided by temperature as a function of temperature. (b) Potential $[\Psi]_N / T^2 = [U - N_2 M_{21}]_N / T^2$ as a function of the diffusion potential $M_{21} \equiv M_{Ag}$. The derivative was evaluated for a stress free state in the bulk at $T = 800\text{ K}$ and $c_{Ag} = 0.036\%$. On the plots this state is indicated by vertical dashed lines. The computed derivatives $\frac{\partial ([N_2]_N / T) / A_{ref}}{\partial T} = -(2.7 \pm 0.1) \times 10^{-8}\text{ }^{-2}\text{K}^{-2}$ and $\frac{\partial ([\Psi]_N / T^2) / A_{ref}}{\partial M_{Ag}} = -(3.0 \pm 0.9) \times 10^{-8}\text{ }^{-2}\text{K}^{-2}$ confirms the correctness of the relation within accuracy of our calculations. 239
- 9.23 Excess shear and excess volume of GB. (a) The dashed line indicates initial homogeneous bulk region. As the GB enters this region at constant σ_{31} and σ_{33} excess shear and excess volume are produced. These excesses are indicated by red arrows. (b) \mathbf{n} is the normal vector direction of which depends on vector \mathbf{b} . \mathbf{t} is the traction vector. 242
- 10.1 Schematics presentation of the GB model with a disjoining potential. (a) Equilibrium GB; (b) Liquid nucleation on the boundary. 244

- 10.2 Schematic representation of the functions $\varphi'(w)$ and $\Gamma(w)$ involved in the calculation of equilibrium states of a plane grain boundary. (a) Typical shape of $\varphi'(w)$ for a disjoining potential with a single minimum and a single inflection point. Solutions of Eq. (10.27) correspond to intersections of the plot with horizontal lines $g = \text{const}$ for different values of the superheating parameter g . The equation has one solution when $g \leq 0$ (no superheating), two solutions when $0 < g < g_c$ and no solutions when $g > g_c$. (b) The GB free energy Γ as a function of boundary width w for selected values of g . When $g = 0$, this plot gives the disjoining potential $\varphi(w)$ (shifted by $1 + \beta$) with a minimum at $w = 1$. For a superheated boundary, $\Gamma(w)$ has a minimum at w_e and a maximum at w_e^- . The plot also shows the construction to determine the critical thickness w^* of 2D nucleus. The three widths w_e , w_e^- and w^* converge to a common value w_e^c at the critical point shown by a filled circle. 249
- 10.3 Shapes of a critical nucleus in the 2D and 3D cases. (a) 2D case: w is a function of x . The nucleus extends infinitely in the direction y normal to the figure. (b) 3D case: w is a function of the radial distance ρ . The shape of the nucleus in cylindrical coordinates ρ and z is obtained by rotation of $w(\rho)$ around the z axis. w_e indicates the equilibrium thickness of the premelted GB. 251
- 10.4 Shapes of the critical nuclei computed from the model at $T = 1349$ K for the 2D (blue) and 3D (red) geometries. The finite thickness away from the nuclei represents the premelted boundary and equals 0.5 nm at T_m 256
- 10.5 Premelted grain boundary (GB) with a three-dimensional critical nucleus at 1357 K stabilized by adiabatic trapping and visualized by centrosymmetry coloring. Atoms with fcc coordination are not shown for clarity. (a) Top view; the dislocation lines are vertical. (b) Dislocation lines are normal to the page. (c) Dislocation lines are horizontal. Although not apparent due to fluctuations, the average shape of the nucleus does not possess a twofold symmetry around the GB normal due to the lack of such symmetry in the GB structure and anisotropy of γ_{SL} . The dots in the grains mark vacancies. See supplementary materials for animations. 259

10.6	The grain boundary (GB) thickness W_e (Δ) and the nucleus thickness W^* (\square, \circ) as functions of temperature. The points are results of molecular dynamics (MD) simulations. The GB thickness increases from 0.5 nm at T_m to 0.75 nm at T_c . In (a) the lines are fits of the classical nucleation theory (CNT) to the MD data; in (b) the lines are fits of the proposed model. Note the qualitative difference at high temperatures.	260
10.7	Nucleation barriers computed from the proposed model and classical nucleation theory (CNT). The model predicts a critical temperature of superheating at which the barrier vanishes and the boundary becomes unstable against melting. Note that CNT gives a finite barrier at all temperatures and is not capable of predicting a critical temperature.	261

Abstract

INTERFACE THERMODYNAMICS WITH APPLICATIONS TO ATOMISTIC SIMULATIONS

Timofey Frolov, PhD

George Mason University, 2011

Dissertation Director: Dr. Yuri Mishin

Interfaces are ubiquitous in natural phenomena. While the description of interfaces in fluid systems is well developed, solid-fluid and solid-solid interfaces are not well understood. This deficiency is especially true for solid-solid interfaces, which play critical roles in materials engineering, solid-state physics and solid-state chemistry. In this thesis, the Gibbs theory of interfaces is generalized to describe phase boundaries under non-hydrostatic stress in multicomponent systems. We obtain equations that describe coherent solid-solid interfaces with shear stresses parallel to the boundary plane, incoherent solid-solid interfaces for certain constraint variations, solid-fluid interfaces, grain boundaries and surfaces.

In the second part of the thesis, the developed theory is applied to study particular types of interfaces using atomistic simulations. We modeled solid surface, solid-liquid interface and grain boundaries. The simulations allowed to calculate values of key thermodynamic properties, clarify behavior of these properties with temperature, composition and stress and test the predictions of the theory.

Surface surface free energy and surface stress in a single component system were computed as functions of temperature. The values of these two excess properties do not converge near the melting point despite the extensive surface premelting.

Solid-liquid interface free energy was computed using the developed thermodynamic integration technique as a function of composition in CuAg binary alloy and as a function of biaxial strain in a single component Cu system. In the later case the equilibrium states between the non-hydrostatically stressed solid and liquid were accurately predicted using the derived Clausius–Clapeyron type equation. We show that for non-hydrostatic equilibrium interfaces stress is not unique and compute different interface stresses using our simulation data.

We also studied effects of elastic deformation, temperature and chemical composition on properties of a symmetrical tilt grain boundary in Cu and CuAg alloy. Excess grain boundary free energy was computed as a function of lateral strain, normal stress and shear stress parallel to the boundary plane. We also employed the derived thermodynamic integration method to compute grain boundary free energy as a function of temperature and composition. Maxwell type relations predicted by the adsorption equation were tested and verified.

We proposed a thermodynamic model of liquid nucleation on superheated grain boundaries based on the sharp-interface approximation with a disjoining potential. The model predicts the shape and size of the critical nucleus by using a variational approach. Contrary to the classical nucleation theory, the model predicts the existence of a critical temperature of superheating and offers a simple formula for its calculation. The model is tested against molecular dynamic simulations in which liquid nuclei at a superheated boundary were obtained by an adiabatic trapping procedure.

Chapter 1: Introduction

1.1 Interfaces

Interface is generally defined as a boundary region between two distinct phases. In some cases an interface can be formed between two grains of the same phase, if they have different crystallographic orientation. Such interfaces are called grain boundaries (GBs). Surface is another type of interface when one of the phases is vacuum. In the interfacial region thermodynamic properties of one phase transition into the other phase, making this region inherently inhomogeneous. In equilibrium this inhomogeneous structure is unique. Interfacial properties both mechanical and electronic are generally different from the bulk properties.

In multicomponent systems chemical composition of the interface region is generally distinct from the bulk. Some components tend to have higher concentration in the interface region. This phenomenon is called interface segregation and it is governed by the “desire” of the system to minimize its interface free energy. Different chemical composition of interfaces results in different mechanical properties, which can be either beneficial or catastrophic for the properties of materials. In some cases, intrinsically ductile materials become brittle after being exposed to certain chemical environment. Bi segregates to GBs in Cu and Ni and at high concentration form a uniform layer in the GB region. Due to weaker bonding between Bi atoms, the GB becomes brittle [1].

Interfaces play a crucial role in material science [2]. They directly affect materials manufacturing process as well as the subsequent service. Materials are generally not single crystals but made of grains separated by interfaces. These grains usually appear when solid is formed from a melt by nucleation process. In this process nuclei of solid phase appear in the melt and grow until liquid phase disappear. Different nuclei have different

crystallographic orientation, so when they collide as a result of growth, solid-solid interfaces are formed. The barrier of nucleation and nucleation rate are directly affected by interface free energy. The rate of nucleation as well as subsequent thermal treatment will determine the average grain size of material. As solid nucleus grows solidification happens faster along some directions resulting in dendritic growth. Snowflakes are familiar example of dendrites (nucleation and growth of ice in vapor). The process of dendritic growth is affected by anisotropy of interface free energy [3].

Nucleus of unstable phase can nucleate if solid-liquid interface free energy of this phase is lower than the interface free energy between melt and stable phase [4]. For example, nucleation of metastable bcc phase instead of stable fcc occurs in Fe and Ni based alloys when melt is rapidly quenched [4-7]. From these examples we conclude that both magnitude and anisotropy of γ determine microstructure of materials, which in turn determines the properties of materials [3].

The sizes of grains range from nanoscale to microscale. Orientation, shape and size of grains and interfaces represent a microstructure of a material. Microstructure (grain size, interfaces) determines mechanical, thermal and electronic properties of materials. For example, yield strength of material is inversely proportional to grain size. This phenomenon is called Hall-Petch strengthening. Plastic deformation in materials occurs due to dislocation motion. GBs impede dislocation motion, as a result higher stresses are required for plastic deformation of a polycrystalline material. Thus, presence of interfaces inside a material is often desirable.

Microstructure evolution does not end after material is produced. Larger grains grow at the expense of smaller ones in a process called Ostwald ripening [8]. In many technological applications, materials are exposed to extreme conditions such as high temperatures variations, aggressive chemical environment and severe mechanical loadings. Under changing external conditions microstructure of materials evolve: interfaces migrate and change their structure, new phases may nucleate inside existing grains or at interfaces. These processes

may result in a failure of a material with catastrophic consequences. To develop new materials that can serve in extreme environments, it is necessary to study how temperature, composition and stress affect interfaces.

Interfaces and GBs are preferable routes for electromigration in microelectronic devices [9]. While momentum transfer from the electric current to atoms is negligible in the bulk material, atoms in the boundaries are able to diffuse in the direction of the current. This process shortens the lifetime of microelectronic devices.

The magnitude of γ determines contact angles in wetting process. By manipulating thermodynamic variables, one can modify interface free energies and in turn change contact angles. This phenomenon is employed in electrowetting [10], where one can manipulate with interface free energies in the system containing droplet on the substrate by varying external electric field. The ability to achieve desired contact angles found applications in digital microfluidics (lab-on chip technology) [11]. Using electrowetting large droplet can be split into smaller droplets of the desired size. These discrete droplets are then used to store and transport chemical substances and to cause chemical reactions by merging the individual droplets together. This ability to perform complex operations step by step (by adding droplets in a discrete way) is useful in applications such as chemical synthesis and biological assay. Electrowetting have been used to develop liquid lenses with focal lengths tunable by voltage, change color of pixels in electronic screens and even convert mechanical energy into electrical energy [12].

The several examples mentioned above demonstrate that interface phenomena plays a crucial role in many physical processes. In the next section briefly describe current thermodynamic theory of interfaces and point out to unsolved problems that will be addressed in this work.

1.2 Thermodynamics of interfaces

As we mentioned earlier interface is inherently inhomogeneous. Therefore, thermodynamic description of homogeneous bulk phases cannot be applied immediately. Thermodynamics

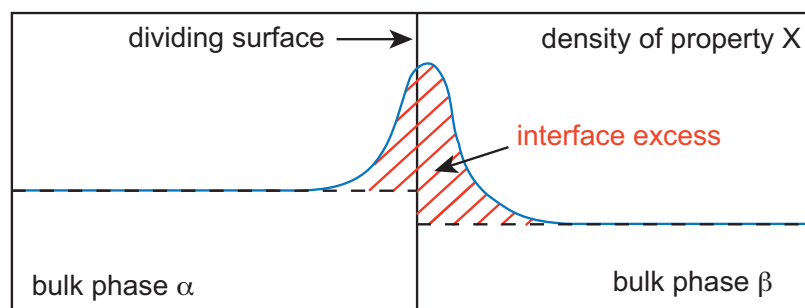


Figure 1.1: Construction of the Gibbs dividing surface.

of interfaces was developed by Gibbs [13]. He considered two phases α and β in equilibrium with each other. Thermodynamic properties like density, composition, entropy and energy are uniform within each phase. Gibbs, argued, that since interface is in thermodynamic equilibrium with the phases, its properties can be described using the intensive variables that describe the bulk phases. To treat an inhomogeneous system, Gibbs introduced a concept of a dividing surface, which is schematically illustrated in Fig. 1.1. On the figure an imaginary plane is placed between the two homogeneous phases and the properties of each phase are extrapolated to the dividing surface. The difference between the amounts of an extensive thermodynamic property X in the system with interface and the two bulk phases extrapolated to the dividing surface constitutes an excess of this thermodynamic property. Gibbs introduced excesses of number of components, known as segregation, excess entropy and energy. These excesses depend on the particular choice of the dividing surface and can be positive, negative or zero. Gibbs also defined interface free energy γ as a reversible work required to create a unit of interface. He showed that γ is unique for plane interfaces and thus a meaningful and measurable quantity. He derived an adsorption equation that provides a differential of γ in terms of differentials of intensive parameters that describe phase equilibrium. Gibbs treatment of the interfaces is very general. Interface region is treated as a black box: particular behavior of thermodynamic properties in the interface region is irrelevant.

Gibbs treatment was focused on interfaces in fluid systems. Discussing solid-fluid interfaces he pointed out that interface area can change in two ways. One is when a new interface is created between two phases at a fixed thermodynamic state and the second is when solid phase is elastically stretched. In these two cases the final interface areas may be the same, but the thermodynamic states of the phases and the interface are actually different. Gibbs limited his analysis of solid-fluid interfaces to variations at constant interface area.

Gibbs showed that a non-hydrostatically stressed single-component solid can be equilibrated with three multicomponent fluids each having a different chemical potential of the solid component [13]. This implies that the chemical potential of the solid component cannot be defined uniquely. To avoid the notion of chemical potential of the substance of the solid, Gibbs placed the dividing surface, so that the excess of this component would vanish. This eliminates the term in the adsorption equation that would otherwise require knowledge of the chemical potential. Gibbs did not consider continuous variations of the chemical composition of the solid, although the solid in his treatment was generally multicomponent. This assumption of constancy of the chemical composition allowed Gibbs to introduce a substance of the solid and subsequently treat the solid as if it was composed of a single component. In a two phase system with the solid phase composed of a single component, it is possible to place the dividing surface so that the excess of this substance vanish.

Using the Gibbsian definition of γ , Cahn [14] derived a more general form of the adsorption equation for hydrostatic systems by solving a system of Gibbs-Duhem equations for the bulk phases and a layer containing the interface. Cahn's method is a mathematical reformulation of Gibbs theory of interfaces. It affords a greater freedom of choice of the intensive variables used in the adsorption equation. It rigorously introduces the interface excess volume, a quantity which is zero by definition in the Gibbsian treatment. The freedom of choice of variables and the conjugate interface excess quantities offers significant advantages for experimental and computational applications. Another advantage of Cahn's method [14] is that the Gibbs phase rule is directly embedded in the formalism, making all variations in the adsorption equation automatically consistent with phase coexistence.

Although Gibbs analyzed solid-fluid interfaces and pointed out to the key differences from interfaces in fluid systems, his analysis was limited to variations of state at a fixed interface area. Shuttleworth analyzed elastic variations of the interface. He introduced new quantity interface stress τ and derived relation between γ and τ [15–17]. Shuttleworth analysis was limited to single component solid surface and did not address effects of temperature and composition. In Gibbs treatment all the interface properties were rigorously introduced as excesses over the bulk properties for a given placement of the dividing surface. Shuttleworth did not provide an expression for interface stress as an excess quantity and did not give a rigorous recipe how to compute it. As a result, it is not clear how to compute τ for solid-liquid and solid-solid interfaces. Another open question is whether interface stress is unique like interface free energy or does it depend on the placement of the dividing surface (just as all other excess properties).

The second limitation of Gibbs treatment of a constant chemical composition was due to the thermodynamic model of a solid. This assumption was made by Gibbs because solid state diffusion was unknown at that time. Thermodynamics of multicomponent solid under stress with varying chemical composition of both substitutional and interstitial components was analyzed by Larche and Cahn [18,19]. They employed the variational approach of Gibbs to derive equilibrium conditions for a single solid phase and two phases separated by coherent and incoherent interfaces. To describe the continuous compositional changes on the substitutional lattice Larche and Cahn introduced diffusion potentials and showed that they are uniform throughout the system in equilibrium. They also showed that individual chemical potentials of interstitial atoms are well defined and uniform throughout the system. Excess interfacial properties were not considered by Larche and Cahn [18].

Although some limitations of Gibbs theory of interfaces and bulk solids were addressed by Shuttleworth and Larche and Cahn, description of coherent plane solid-solid interfaces under general state of stress faces several difficulties. The first difficulty arises from the necessity of defining the individual chemical potentials of the substitutional atoms [20,21]. If the solid is treated as multicomponent to account for continuous changes in composition,

it is impossible to place the dividing surface so that excesses of all substitutional atoms in the solid would vanish. The same problem arises even in a truly single component system, when the interface separates two grains of the same material (grain boundaries). In this case the atomic density is the same in both grains, and no placement of the dividing surface would make the interfacial excess of this component vanish (unless the density in the interfacial region is identical to the bulk which is generally not the case).

The second issue arises from the fundamental difference between coherent and incoherent (or solid-fluid) boundaries. Coherent boundaries support shear stresses parallel to the boundary plane. In case of solid-fluid interfaces analyzed by Gibbs, these shear stresses were identically zero. The effects of the shear stresses are not included in the current thermodynamic treatments.

In this work we address the issues discussed above. We develop a thermodynamic treatment of coherent plane solid-solid interfaces in a multicomponent system with both substitutional and interstitial components. The phases in equilibrium are under general non-hydrostatic state of stress, which includes shear stresses parallel to the interface. Once the thermodynamic theory is developed, we will study excess thermodynamic properties using atomistic simulations. In particular we compute interface free energy of surfaces, solid-liquid interfaces and grain boundaries as a functions of temperature, composition and non-hydrostatic stresses. Atomistic simulations also allow to test the proposed thermodynamic theory.

Chapter 2: Coherent phase boundaries

2.1 Thermodynamics of a solid phase

Before presenting thermodynamics of coherent interfaces it is necessary to discuss thermodynamics multicomponent solid phases subject to mechanical stresses and formulate conditions of coherent equilibrium between such phases. In this Section we first describe finite deformations of a solid and then introduce thermodynamic variables describing equilibrium with respect to exchange of heat and variations in chemical composition and deformation.

2.1.1 Kinematics of deformation of a solid phase

We will consider the most general case of finite deformations employing the concept of a reference state [22]. To be able to define deformations, we have to assume that the solid contains a penetrating network permitting identification of the same physical point in the reference and deformed states [18,23,24]. This network is also capable of carrying mechanical loads and allows the solid to reach mechanical equilibrium under non-hydrostatic conditions (a property which distinguishes a true solid from a viscous fluid) [18, 23, 24]. We do not associate the network with a particular lattice or sublattice of the crystal structure. We only assume that the network (i) exists and is not destroyed by any deformations, (ii) supports non-hydrostatic loads, and (iii) provides markers to identify the same location before and after deformation.

The choice of the reference state is arbitrary. We assume that both the reference and the deformed coordinate frames are Cartesian. A physical point is defined by its coordinates x'_i ($i = 1, 2, 3$) in the reference state [22]. The coordinates x_i in the deformed state are functions of the reference coordinates,

$$\mathbf{x} = \mathbf{x}(\mathbf{x}'). \quad (2.1)$$

Any infinitesimal vector dx_i in the deformed state is related to an infinitesimal vector dx'_j in the reference state by a linear transformation

$$dx_i = \sum_{j=1,2,3} F_{ij} dx'_j, \quad (2.2)$$

where F_{ij} is the deformation gradient with components

$$F_{ij} = \frac{\partial x_i}{\partial x'_j}. \quad (2.3)$$

The components of \mathbf{F} are generally functions of reference coordinates unless the solid is homogeneous. It is assumed that $J \equiv \det \mathbf{F} \neq 0$ and thus the reference coordinates can be expressed as functions of deformed coordinates:

$$\mathbf{x}' = \mathbf{x}'(\mathbf{x}). \quad (2.4)$$

The corresponding infinitesimal vectors are related by the inverse of the deformation gradient \mathbf{F}^{-1} ,

$$dx'_i = \sum_{j=1,2,3} F_{ij}^{-1} dx_j. \quad (2.5)$$

Only six components of \mathbf{F} are needed to completely describe all deformations (strains) of a solid. Without loss of generality we will set all sub-diagonal components of \mathbf{F} to zero:

$$\mathbf{F} = \begin{pmatrix} F_{11} & F_{12} & F_{13} \\ 0 & F_{22} & F_{23} \\ 0 & 0 & F_{33} \end{pmatrix}. \quad (2.6)$$

Fig. 2.1 illustrates deformations of a small volume element when \mathbf{F} is given by Eq. (2.6). The bottom and top faces of the volume element remain normal to the x'_3 axis during the deformation. Furthermore, the edge parallel to the x'_1 axis remains parallel to it during the deformation. The Jacobian of \mathbf{F} equals

$$J = F_{11}F_{22}F_{33}. \quad (2.7)$$

\mathbf{F}^{-1} also has a right triangular form similar to \mathbf{F} with diagonal elements

$$F_{ii}^{-1} = 1/F_{ii}, \quad i = 1, 2, 3. \quad (2.8)$$

These relations will be used below to simplify some of the equations.

2.1.2 Thermodynamic description of a homogeneous solid phase

We start with a thermodynamic description of a homogeneous solid phase in a state of equilibrium. An extension to inhomogeneous phases will be presented later.

We consider a homogeneous multicomponent solid containing K substitutional and L interstitial chemical components. The substitutional atoms occupy lattice sites and are subject to the lattice constraint: the total number N of substitutional atoms equals the number of lattice sites. The interstitial atoms can freely migrate from one place to another and are not subject to constraints. It is assumed that each chemical component is either substitutional or interstitial.

Consider a block of such a solid containing a total of N substitutional and n interstitial atoms and obtained by deformation of a reference region of a volume V' . Suppose N and

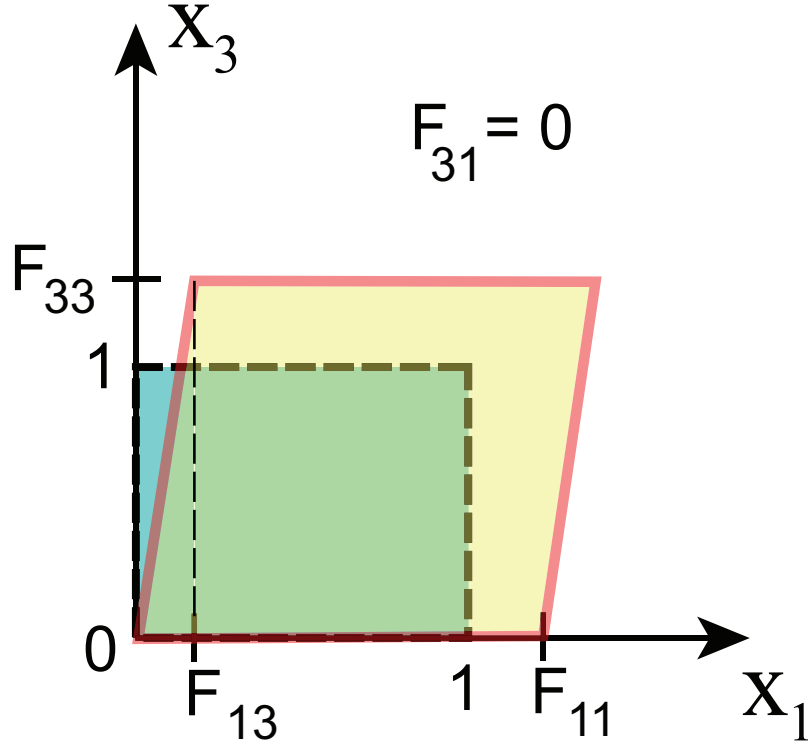


Figure 2.1: Two-dimensional schematic of a volume element undergoing a finite deformation. In the reference state (dashed lines), the volume element is a unit square. The components of the deformation gradient \mathbf{F} represent the new lengths or projections of the cube edges in the deformed state (solid lines.)

V' are fixed. Then the internal energy U of the solid is a function of its entropy S , the amounts of individual chemical components N_k and n_l , and the deformation gradient \mathbf{F} :

$$U = U(S, N_1, \dots, N_K, n_1, \dots, n_L, \mathbf{F}). \quad (2.9)$$

Due to the imposed constraint $\sum_k N_k = N$, only $K - 1$ independent variations of N_k are possible. To implement this constraint, we can arbitrarily choose one of the substitutional components as the reference component and assume that each time we add an atom of a different component k , we simultaneously remove an atom of the reference component [18, 23, 24]. We choose component 1 as the reference and treat all other substitutional

components as independent. The amounts of interstitial components can be varied without restrictions.

Consider a reversible variation in the state of the solid when it exchanges heat with the environment, changes its chemical composition and performs mechanical work. Continuing to keep N , the differential of energy is given by [18, 23]

$$dU = TdS + \sum_{k=2}^K M_{k1} dN_k + \sum_{l=1}^L \mu_l dn_l + \sum_{i,j=1,2,3} V' P_{ij} dF_{ji}, \quad (2.10)$$

where T is temperature, μ_l are chemical potentials of the interstitial atoms and M_{k1} are $K-1$ diffusion potentials of the substitutional atoms. According to Eq. (2.10), the diffusion potential M_{k1} is the energy change when an atom of component k is substituted for an atom of component 1 while keeping all other variables fixed:

$$M_{k1} = \frac{\partial U}{\partial N_k} - \frac{\partial U}{\partial N_1}, \quad k = 2, \dots, K. \quad (2.11)$$

In the last term of Eq. (2.10), \mathbf{P} is the first Piola-Kirchhoff tensor, which is generally not symmetrical and is related to the symmetrical Cauchy stress tensor $\boldsymbol{\sigma}$ by [22]

$$\mathbf{P} = J\mathbf{F}^{-1} \cdot \boldsymbol{\sigma} \quad (2.12)$$

(the dot denotes inner product of tensors). Because \mathbf{F}^{-1} is a right triangular matrix, the components P_{31} , P_{32} and P_{33} are proportional to the corresponding components of $\boldsymbol{\sigma}$:

$$P_{3i} = F_{11}F_{22}\sigma_{3i} = (J/F_{33})\sigma_{3i}, \quad i = 1, 2, 3, \quad (2.13)$$

where we used Eqs. (2.6), (2.7) and (2.8).

To prepare for the analysis of an interface between phases with boundary normal to 3 axis in Section 2.3, it will be convenient to rewrite the mechanical work term in Eq. (2.10)

by separating the differentials dF_{11} , dF_{12} and dF_{22} from dF_{13} , dF_{23} and dF_{33} :

$$\begin{aligned}
dU &= TdS + \sum_{k=2}^K M_{k1} dN_k + \sum_{l=1}^L \mu_l dn_l \\
&+ \sum_{i=1,2,3} V' F_{11} F_{22} \sigma_{3i} dF_{i3} + \sum_{i,j=1,2} V' P_{ij} dF_{ji}.
\end{aligned} \tag{2.14}$$

The $(K + L + 6)$ differentials in the right-hand side of Eq. (2.14) are independent and their number gives the total number of degrees of freedom of a homogeneous solid phase.

2.1.3 Relevant thermodynamic potentials

Various thermodynamic potentials can be derived from Eq. (2.14) by Legendre transformations. As will become apparent later, the potential which is relevant to the coherent interface problem is

$$\Phi_1 = \Phi_1(T, M_{21}, \dots, M_{K1}, \mu_1, \dots, \mu_L, \sigma_{31}, \sigma_{32}, \sigma_{33}, F_{11}, F_{12}, F_{22}), \tag{2.15}$$

where subscript 1 indicates the reference chemical component. For a homogeneous solid, this potential is defined by

$$\Phi_1 \equiv U - TS - \sum_{k=2}^K M_{k1} N_k - \sum_{l=1}^L \mu_l n_l - \sum_{i=1,2,3} (VF_{i3}/F_{33}) \sigma_{3i}, \tag{2.16}$$

where $V = JV'$ is the actual (deformed) volume of the block. Using Eq. (2.14), we obtain

$$\begin{aligned}
d\Phi_1 &= -SdT - \sum_{k=2}^K N_k dM_{k1} - \sum_{l=1}^L n_l d\mu_l \\
&- \sum_{i=1,2,3} (VF_{i3}/F_{33}) d\sigma_{3i} + \sum_{i,j=1,2} V' Q_{ij} dF_{ji},
\end{aligned} \tag{2.17}$$

where

$$\mathbf{Q} \equiv J\mathbf{F}^{-1} \cdot \left(\boldsymbol{\sigma} - \sum_{m=1,2,3} \frac{F_{m3}}{F_{33}} \sigma_{3m} \mathbf{I} \right) \quad (2.18)$$

($\mathbf{I} \equiv \delta_{ij}$ is the identity tensor). Although \mathbf{Q} is a 3×3 tensor, only its components Q_{11} , Q_{21} and Q_{22} appear in Eq. (2.17).

The potential Φ_1 depends on the choice of coordinate axes through the variable σ_{31} , σ_{32} , σ_{33} , F_{11} , F_{12} and F_{22} . In addition, Φ_1 depends on the choice of the reference state of strain through \mathbf{F} .

Eq. (2.16) defines Φ_1 for a homogeneous block containing a fixed number N of substitutional atoms. We can also define an intensive potential ϕ_1 as Φ_1 per substitutional atom:

$$\begin{aligned} \phi_1 &\equiv \Phi_1/N = U/N - TS/N - \sum_{k=2}^K M_{k1} C_k \\ &- \sum_{l=1}^L \mu_l c_l - \sum_{i=1,2,3} (\Omega F_{i3}/F_{33}) \sigma_{3i}. \end{aligned} \quad (2.19)$$

Here $C_k = N_k/N$ and $c_l = n_l/N$ are concentrations of substitutional and interstitial atoms per substitutional atom. Likewise, U/N , S/N and Ω are the energy, entropy and volume per substitutional atom, respectively.

Furthermore, we can introduce K different potentials Φ_m , and accordingly ϕ_m , by choosing different substitutional components m as the reference species:

$$\begin{aligned}
\phi_m &\equiv \Phi_m/N = U/N - TS/N - \sum_{k=1}^K M_{km} C_k \\
&- \sum_{l=1}^L \mu_l c_l - \sum_{i=1,2,3} (\Omega F_{i3}/F_{33}) \sigma_{3i}.
\end{aligned} \tag{2.20}$$

Note that we have extended the summation with respect to k from 1 to K using the property $M_{kk} \equiv 0$. Combining Eq. (2.20) with other properties of diffusion potentials [18, 23, 24], $M_{ik} = -M_{ki}$ and $M_{ij} = M_{kj} + M_{ik}$, the following relationship between different ϕ -potentials can be derived:

$$\phi_m - \phi_n = M_{mn}, \quad m, n = 1, \dots, K. \tag{2.21}$$

It follows that

$$\sum_{k=1}^K M_{km} C_k = \sum_{k=1}^K (\phi_k - \phi_m) C_k = \sum_{k=1}^K \phi_k C_k - \phi_m. \tag{2.22}$$

Using Eqs. (2.20) and (2.21) we obtain the following relation for a homogeneous non-hydrostatic solid:

$$U - TS - \sum_{i=1,2,3} (V F_{i3}/F_{33}) \sigma_{3i} = \sum_{m=1}^K N_m \phi_m + \sum_{l=1}^L n_l \mu_l. \tag{2.23}$$

This equation closely resembles Gibbs' equation for hydrostatic systems [13], with ϕ_k playing a role of chemical potentials. Indeed, in the hydrostatic case the left-hand side of Eq. (2.23) reduces to the Gibbs free energy $U - TS + pV$, where p is external pressure.

2.1.4 The Gibbs-Duhem equation

We can now derive a Gibbs-Duhem type equation for a stressed solid. To this end, we again consider a variation of state in which the solid exchanges heat with the environment, performs mechanical work and changes its chemical composition by switching chemical sorts of substitutional atoms at a fixed N and changing the amounts of interstitial atoms. Differentiating Eq. (2.16) and using the relation $d\Phi_1 = Nd\phi_1$ and dU from Eq. (2.14), we obtain the following Gibbs-Duhem equation for a multicomponent solid under a non-hydrostatic stress:

$$\begin{aligned}
0 &= -SdT - \sum_{k=2}^K N_k dM_{k1} - Nd\phi_1 - \sum_{l=1}^L n_l d\mu_l \\
&\quad - \sum_{i=1,2,3} (VF_{i3}/F_{33}) d\sigma_{3i} + \sum_{i,j=1,2} V'Q_{ij} dF_{ji}.
\end{aligned} \tag{2.24}$$

Applying Eq. (2.21), this equation can also be written as

$$\begin{aligned}
0 &= -SdT - \sum_{k=1}^K N_k d\phi_k - \sum_{l=1}^L n_l d\mu_l \\
&\quad - \sum_{i=1,2,3} (VF_{i3}/F_{33}) d\sigma_{3i} + \sum_{i,j=1,2} VQ_{ij} dF_{ji}.
\end{aligned} \tag{2.25}$$

For hydrostatic processes $Q_{ij} \equiv 0$ while $\sum_{i=1,2,3} (VF_{i3}/F_{33}) d\sigma_{3i} = -Vdp$. Furthermore, ϕ_k become real chemical potentials as evident from Eq. (2.23). As a result, Eq. (2.25) reduces to the classical Gibbs-Duhem equation for fluids [13].

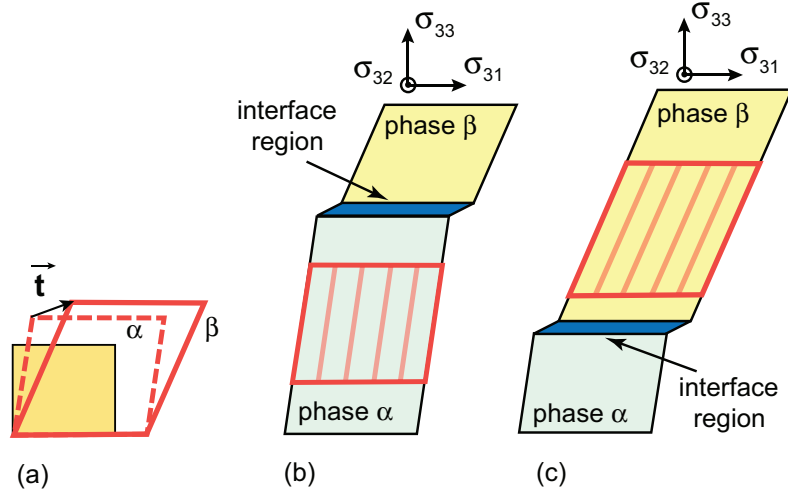


Figure 2.2: (a) Two-dimensional schematic of a reference volume element (shaded unit square) transforming to coherent phases α (dashed lines) and β (solid lines). The differences between the deformation-gradient components F_{13} , F_{23} and F_{33} of the phases form the transformation vector \mathbf{t} . (b,c) Two-dimensional schematic of two phases, α and β , separated by a coherent interface. When the interface moves down, the striped region of phase α shown in (b) transforms the striped region of phase β shown in (c). During the transformation, the deformation-gradient components F_{11} , F_{12} and F_{22} remain the same in both phases.

2.2 Equilibrium between two solid phases separated by a coherent interface

2.2.1 Phase equilibrium conditions

We next discuss coherent equilibrium between two homogeneous solid phases whose thermodynamic properties were introduced in Section 2.1. We assume that the phases, which will be referred to as α and β , contain the same K substitutional and L interstitial components and are separated by a plane coherent interface normal to the x_3 direction (Fig. 2.2). The definition of coherency used in this work is essentially the same as given by Robin [25]. When a region of phase α transforms coherently into a region in phase β by migration of the interface, the two regions are one-to-one maps of each other. As in the kinematics of deformation discussed in Section 2.1.1, the one-to-one mapping is established between network sites and not individual atoms. Atoms are allowed to diffuse during the phase

transformation as long as their diffusion preserves the network. There is a single network penetrating through both phases and deformed during the transformation. The one-to-one mapping implies that there is no slip between the phases along the interface. The interface structure may contain localized disordered regions such as misfit dislocation cores. As long as their motion during the interface migration preserves the network, the interface is considered coherent. Due to the no-slip condition, a coherent two-phase system can support shear stresses applied parallel to the interface.

The following kinematic description of coherent phases is introduced in this work. The deformation gradients of the phases, \mathbf{F}^α and \mathbf{F}^β , are taken relative to the *same* reference state and have the right triangular forms

$$\mathbf{F}^\alpha = \begin{pmatrix} F_{11} & F_{12} & F_{13}^\alpha \\ 0 & F_{22} & F_{23}^\alpha \\ 0 & 0 & F_{33}^\alpha \end{pmatrix}, \quad (2.26)$$

$$\mathbf{F}^\beta = \begin{pmatrix} F_{11} & F_{12} & F_{13}^\beta \\ 0 & F_{22} & F_{23}^\beta \\ 0 & 0 & F_{33}^\beta \end{pmatrix}. \quad (2.27)$$

These forms ensure that the x_3 direction in both phases remains normal to the interface during all deformations. In addition, the lateral components F_{11} , F_{12} and F_{22} are common to both phases, preserving the interface coherency during all deformations. Thus, the phase deformations differ only in the components F_{i3} . The differences between these components in the phases form a vector,

$$\mathbf{t} = \left(F_{13}^\beta - F_{13}^\alpha, F_{23}^\beta - F_{23}^\alpha, F_{33}^\beta - F_{33}^\alpha \right), \quad (2.28)$$

which we call the transformation vector. Its geometric meaning is illustrated by a two-dimensional schematic in Fig. 2.2(a).

The conditions of the coherent phase equilibrium were derived by Robin[25] for a single component system. Larch and Cahn [18, 23] generalized Robin's analysis to (i) multicomponent systems with both substitutional and interstitial components and (ii) non-planar interfaces between inhomogeneous phases. Their equilibrium conditions can be summarized as follows:

- (i) Temperature is uniform throughout the system.
- (ii) Diffusion potentials M_{k1} of all substitutional components and chemical potentials μ_l of all interstitial components are uniform throughout the system.
- (iii) The internal mechanical equilibrium condition, $\nabla' \cdot \mathbf{P} = 0$, is satisfied inside each phase (the divergence is taken with respect to the reference coordinates).
- (iv) The traction vector at the interface is continuous,

$$\mathbf{n}'^\alpha \cdot \mathbf{P}^\alpha = -\mathbf{n}'^\beta \cdot \mathbf{P}^\beta, \quad (2.29)$$

where the superscripts indicate the phases and vectors \mathbf{n}'^α and $\mathbf{n}'^\beta = -\mathbf{n}'^\alpha$ are their unit normals in the reference state.¹ Using Eqs. (2.29) and (2.13) it follows that the stress components σ_{31} , σ_{32} and σ_{33} are also continuous across the interface.

- (v) Finally, the so-called phase change equilibrium condition [18, 23] must be satisfied:

$$\begin{aligned} U^\alpha - TS^\alpha - \sum_{k=2}^K M_{k1} N_k^\alpha - \sum_{l=1}^L \mu_l n_l^\alpha - \sum_{i=1,2,3} (V F_{i3}/F_{33})^\alpha \sigma_{3i} \\ = U^\beta - TS^\beta - \sum_{k=2}^K M_{k1} N_k^\beta - \sum_{l=1}^L \mu_l n_l^\beta - \sum_{i=1,2,3} (V F_{i3}/F_{33})^\beta \sigma_{3i}. \end{aligned} \quad (2.30)$$

Here U , S , V are the energy, entropy and volume of the phases obtained by deformation of the same reference region. The total number of substitutional atoms is the same in both

¹Larche and Cahn used the first Piola-Kirchoff tensor which is a transpose of the one used in this work.

phases ($N^\alpha = N^\beta$), whereas the total number of interstitial components can be different ($n^\alpha \neq n^\beta$).

The equilibrium conditions (i)-(iii) are common to all types of interfaces. The differences between the coherent, incoherent and other types of interfaces are reflected only in conditions (iv) and (v).

2.2.2 Derivation of the phase change equilibrium condition

The phase change equilibrium condition (2.30) can be obtained from equation (41) of Larch and Cahn [18] by substituting our right triangular deformation gradients (2.26) and (2.27) and the interface normal $\mathbf{n} = (0, 0, 1)$. Note that Eq. (2.30) contains the terms $\left(V^\beta F_{13}^\beta / F_{33}^\beta - V^\alpha F_{13}^\alpha / F_{33}^\alpha\right) \sigma_{31}$ and $\left(V^\beta F_{23}^\beta / F_{23}^\beta - V^\alpha F_{23}^\alpha / F_{23}^\alpha\right) \sigma_{32}$ proportional to the shear stresses σ_{31} and σ_{32} . These terms are specific to coherent phases and vanish for incoherent, solid-fluid and fluid-fluid systems. To elucidate the meaning of these terms and prepare the discussion of interface thermodynamics (Section 2.3), we will present an alternate derivation of Eq. (2.30) assuming that the phase equilibrium conditions (i) through (iv) are already satisfied.

At fixed values of the intensive variables $T, M_{21}, \dots, M_{K1}, \mu_1, \dots, \mu_L, \sigma_{31}, \sigma_{32}, \sigma_{33}, F_{11}, F_{12}$ and F_{22} the equilibrium between the phases is neutral, i.e., the interface can migrate reversibly up or down without altering the thermodynamic states of the bulk phases. The phase change equilibrium condition expresses the neutrality of the two-phase equilibrium with respect to such spontaneous displacements of the interface. To formulate this condition in terms of thermodynamic properties, consider a region of phase α containing the total of N substitutional atoms. Suppose the interface traverses this region and transforms it to a regions phase β containing the same total number of substitutional atoms (the total number of interstitial atoms may change). The initial and transformed states of the region are shown schematically in Fig. 2.2(b,c).

What is the change in internal energy of this region? Because the transformation is

reversible, this change depends only on the initial and final states (homogeneous phases α and β) and not on the transformation path. As the interface traverses the region, it creates intermediate states that are not homogeneous. However, instead of this transformation path we will consider another, imaginary path on which the transformation occurs by homogeneous deformation of the region with a simultaneous change in its chemical composition and entropy. Since the system remains homogeneous during this process, its energy change can be obtained by integrating Eq. (2.14) derived for homogeneous variations. Remembering that the intensive parameters are fixed, the integration gives

$$\begin{aligned}
U^\beta - U^\alpha = & T (S^\beta - S^\alpha) + \sum_{k=2}^K M_{k1} (N_k^\beta - N_k^\alpha) + \sum_{l=1}^L \mu_l (n_l^\beta - n_l^\alpha) \\
& + \sum_{i=1,2,3} \sigma_{3i} \left(V^\beta F_{i3}^\beta / F_{33}^\beta - V^\alpha F_{i3}^\alpha / F_{33}^\alpha \right).
\end{aligned} \tag{2.31}$$

The last term in Eq. (2.14) does not contribute to this result because F_{11} , F_{12} and F_{22} are not varied to keep the phases coherent. Eq. (2.31) recovers the phase change equilibrium condition (2.30).

This derivation shows that the last term in Eq. (2.31) represents the mechanical work, W_m , done by the stress components σ_{3i} during the phase transformation. This work can be rewritten as

$$W_m = \sum_{i=1,2,3} \sigma_{3i} F_{11} F_{22} V' \left(F_{i3}^\beta - F_{i3}^\alpha \right) = F_{11} F_{22} V' \boldsymbol{\sigma} \cdot \mathbf{t}, \tag{2.32}$$

where \mathbf{t} is the transformation vector defined by Eq. (2.28) and illustrated in Fig. 2.2(a).² It is important to note that, while $V^\alpha F_{i3}^\alpha / F_{33}^\alpha$ and $V^\beta F_{i3}^\beta / F_{33}^\beta$ depend on the choice of the reference state of strain, \mathbf{t} is an invariant and in principle measurable quantity characterizing the crystallography of the transformation.³ For incoherent and other interfaces not capable of supporting shear stresses, the work term reduces to $F_{11} F_{22} V' \sigma_{33} t_3 = \sigma_{33} (V^\beta - V^\alpha)$. For

²Robin[25] was the first to express the mechanical work term in the phase change equilibrium condition through a transformation vector (which he denoted \mathbf{v}) instead of \mathbf{F} .

³See Section 2.5 for a discussion of possible uniqueness of \mathbf{t} .

coherent interfaces, additional work is done by the shear stresses along the component of \mathbf{t} parallel to the interface plane.

Using the thermodynamic potential ϕ_1 defined by Eq. (2.19), the phase change equilibrium condition can be expressed as $\phi_1^\alpha = \phi_1^\beta$. Moreover, by choosing other substitutional components for the reference species, the following K relations can be obtained:

$$\phi_m^\alpha = \phi_m^\beta \equiv \phi_m, \quad m = 1, \dots, K. \quad (2.33)$$

Thus, there are K potentials that have the same value in two phases equilibrated with each other. Condition in Eq. (2.33) replicates equilibrium conditions (ii) and (v). This resembles the Gibbsian condition of hydrostatic equilibrium [13] with ϕ_m playing the role of chemical potentials.

2.2.3 Equation of coherent phase coexistence in the parameter space

The Gibbs-Duhem equation (2.24) establishes a relation between differentials of intensive parameters which characterize the thermodynamic state of a single-phase solid under stress. When two solid phases coexist, their equilibrium imposes additional constraints on possible variations of state of the phases. These constraints can be expressed by requiring that the Gibbs-Duhem equations of the phases be expressed through the same set of intensive parameters and that these equations hold simultaneously:

$$\begin{aligned} 0 = & -S^\alpha dT - \sum_{k=2}^K N_k^\alpha dM_{k1} - N^\alpha d\phi_1 \\ & - \sum_{l=1}^L n_l^\alpha d\mu_l - \sum_{i=1,2,3} (V^\alpha F_{i3}^\alpha / F_{33}^\alpha) d\sigma_{3i} + \sum_{i,j=1,2} V'^{\alpha} Q_{ij}^\alpha dF_{ji}, \end{aligned} \quad (2.34)$$

$$\begin{aligned}
0 &= -S^\beta dT - \sum_{k=2}^K N_k^\beta dM_{k1} - N^\beta d\phi_1 \\
&\quad - \sum_{l=1}^L n_l^\beta d\mu_l - \sum_{i=1,2,3} \left(V^\beta F_{i3}^\beta / F_{33}^\beta \right) d\sigma_{3i} + \sum_{i,j=1,2} V'^\beta Q_{ij}^\beta dF_{ji}.
\end{aligned} \tag{2.35}$$

Solving this system of equations using Cramer's rule of linear algebra, we obtain

$$\begin{aligned}
0 &= -\{S\}_X dT - \sum_{k=2}^K \{N_k\}_X dM_{k1} - \{N\}_X d\phi_1 \\
&\quad - \sum_{l=1}^L \{n_l\}_X d\mu_l - \sum_{i=1,2,3} \{V F_{i3} / F_{33}\}_X d\sigma_{3i} \\
&\quad + \sum_{i,j=1,2} \{V' Q_{ij}\}_X dF_{ji},
\end{aligned} \tag{2.36}$$

where X is one of the extensive properties S , N_k , N , n_l , $V F_{i3} / F_{33}$ or $V' Q_{ij}$. The curly braces are defined by

$$\{Z\}_X \equiv \frac{\begin{vmatrix} Z^\alpha & X^\alpha \\ Z^\beta & X^\beta \end{vmatrix}}{X^\beta} = Z^\alpha - Z^\beta X^\alpha / X^\beta \tag{2.37}$$

for any extensive properties X and Z . By specifying X , one of the differentials in Eq. (2.36) is eliminated because $\{X\}_X = 0$. The remaining differentials are independent and form a differential equation describing a coherent phase coexistence surface in the configuration space of intensive parameters. Thus, the system of two coherent phases is capable of $(K + L + 5)$ independent variations, which is one degree of freedom less than for each phase separately. Knowing one equilibrium state of the system, all other states can be found by integration of Eq. (2.36) along coexistence paths.

Eq. (2.36) relies on the assumption of coherency of the interface. The phase coexistence equation for incoherent interfaces cannot be obtained as a particular case of Eq. (2.36)

when σ_{31} and σ_{32} are zero. In the absence of coherency, the lateral deformation-gradient components $F_{11}^\alpha, F_{12}^\alpha, F_{22}^\alpha$ and $F_{11}^\beta, F_{12}^\beta, F_{22}^\beta$ are no longer restricted to be the same, because the phases can be deformed independently parallel to the interface. The phase coexistence equation can be re-derived from the beginning in a straightforward manner; however this derivation is beyond the scope of this paper.

2.3 Interface thermodynamics

2.3.1 The interface free energy γ

We are now ready to discuss thermodynamic properties of coherent interfaces. In this section we will derive expressions for the interface free energy γ , which is defined as reversible work of creation of a unit interface area.

As above, we imagine two coexisting phases α and β separated by a coherent plane interface (Fig. 2.4) but now considering the interface as part of the system. The presence of the interface makes the thermodynamic treatment more complicated for at least two reasons. Firstly, recall that the separation of the chemical species into substitutional and interstitial was introduced in Section 2.1.2 for homogeneous phases. In the inhomogeneous interface region, this separation can be ambiguous. For example, if the interface structure contains locally disordered regions such as dislocation cores, the concepts of a lattice, substitutional and interstitial atoms may lose their significance. Nevertheless, we will continue to refer to the chemical components present in the system as substitutional or interstitial, according to their behavior inside the bulk phases. This is only a matter of terminology which does not imply any additional assumptions. Secondly, the deformation gradients \mathbf{F}^α and \mathbf{F}^β were defined for the bulk phases are not a well-defined within the interface region with an atomic-level thickness. We therefore need to devise a method of introducing γ and other interface excess quantities without defining a local deformation gradient.

As discussed earlier, the two-phase equilibrium is neutral when the intensive parameters $T, M_{21}, \dots, M_{K1}, \mu_1, \dots, \mu_L, \sigma_{31}, \sigma_{32}, \sigma_{33}, F_{11}, F_{12}, F_{22}$ are fixed. Consider a homogeneous

region of phase α with the shape of a parallelepiped two faces of which are parallel to the interface and one edge is parallel to the x'_1 axis, as shown by the striped pattern in Fig. 2.4(a). Suppose the interface spontaneously migrates and enters this region, turning it into a two-phase system (Fig. 2.4(b)). The interface position within this region is arbitrary as long as its upper and lower boundaries are located in homogeneous parts of the phases. Suppose the lower boundary is fixed while the placement of the upper boundary is adjusted so that to keep the total number N of substitutional atoms in the region fixed. The cross-section of the region parallel to the interface remains constant and the same at every height due to the coherency condition. We assume that the shape change of this system with N substitutional atoms and varying number of interstitial atoms can be traced by monitoring the shape of an imaginary envelope. In particular systems this shape change can be identified by looking at lattice planes. Example of such an envelope for solid-liquid interface is given on Fig. 6.1, in which case the shape remains rectangular but the volume changes.

As a result of this transformation, the upper boundary of the region translates by a vector \mathbf{B} . We *formally* define a *homogeneous* deformation gradient, $\bar{\mathbf{F}}$, mapping the reference region onto this parallelepiped:

$$\bar{\mathbf{F}} = \begin{pmatrix} F_{11} & F_{12} & (F_{13}^\alpha + B_1 A'/V') \\ 0 & F_{22} & (F_{23}^\alpha + B_2 A'/V') \\ 0 & 0 & (F_{33}^\alpha + B_3 A'/V') \end{pmatrix}, \quad (2.38)$$

where V' is the volume of the reference region and A' is the cross-sectional area of the interface in the reference state. We will refer to $\bar{\mathbf{F}}$ as the average deformation gradient of the region. Note that both \mathbf{B} and $\bar{\mathbf{F}}$ characterize the entire two-phase region and depend on its reference thickness V'/A' and the position of the interface in it. During such a transformation substitutional atoms rearrange (from bulk structure into interface) and may become a part of disordered interface dislocation cores; however calculation of the vector \mathbf{B} should be still possible because the upper boundary of the region with N substitutional

atoms is located inside crystalline phase where lattice is well defined.

We now wish to calculate the change in internal energy of the region when it transforms from the single-phase state to the two-phase state. Instead of tracking the actual motion of the interface into the region, we will take its initial and final states and consider a different reversible process between them. Specifically, consider a process of homogeneous phase transformation $\alpha \rightarrow \beta$ in the upper part of the region at fixed values of the intensive parameters and N . The transformation occurs in an open system whose energy changes due to the processes: (i) heat exchange with the environment, (ii) diffusion of atoms in and out of the system (keeping constant N), (iii) mechanical work W_m performed by stresses applied to boundaries of the region, and (iv) non-mechanical work W_{nm} associated with local atomic rearrangements leading to the formation of the interface.

Since the cross-section of the region remains fixed, the mechanical work is performed only by the stress components σ_{3i} to displace the upper boundary of the region by the vector \mathbf{B} . Thus, $W_m = A \mathbf{n}^\alpha \cdot \boldsymbol{\sigma} \cdot \mathbf{B}$, where \mathbf{n}^α is the unit normal to the interface pointing into phase β and A is the cross-sectional area. To keep a similarity with the work terms derived previously for the homogeneous phases, see e.g. Eq. (2.31), we will express W_m through $\bar{\mathbf{F}}$ by inserting B_i from Eq. (2.38):

$$W_m = A \sum_{i=1,2,3} \sigma_{3i} B_i = \sum_{i=1,2,3} \sigma_{3i} (V \bar{F}_{i3} / \bar{F}_{33} - V^\alpha F_{i3}^\alpha / F_{33}^\alpha),$$

where we denoted

$$\bar{F}_{i3} \equiv (F_{i3}^\alpha + B_i A' / V'). \quad (2.39)$$

Using this expression for W_m , the energy change is

$$\begin{aligned} U - U^\alpha &= T(S - S^\alpha) + \sum_{k=2}^K M_{k1} (N_k - N_k^\alpha) + \sum_{l=1}^L \mu_l (n_l - n_l^\alpha) + \\ &+ \sum_{i=1,2,3} \sigma_{3i} (V \bar{F}_{i3} / \bar{F}_{33} - V^\alpha F_{i3}^\alpha / F_{33}^\alpha) + W_{nm}, \end{aligned} \quad (2.40)$$

where the extensive quantities without the superscript α refer to the final state of the system.

We define the interface free energy γ as the non-mechanical work per unit interface area, i.e., $\gamma A = W_{nm}$. Using Eq. (2.19) for ϕ_1 , this finally obtain

$$\gamma A = U - TS - \sum_{k=2}^K M_{k1} N_k - \phi_1 N - \sum_{l=1}^L \mu_l n_l - \sum_{i=1,2,3} \sigma_{3i} V \bar{F}_{i3} / \bar{F}_{33}, \quad (2.41)$$

or using Eq. (2.21),

$$\gamma A = U - TS - \sum_{k=1}^K \phi_k N_k - \sum_{l=1}^L \mu_l n_l - \sum_{i=1,2,3} \sigma_{3i} V \bar{F}_{i3} / \bar{F}_{33}. \quad (2.42)$$

These expressions for γA can be written in a shorter form by defining the Φ_1 potential of the region by analogy with Eq. (2.16):

$$\Phi_1 \equiv U - TS - \sum_{k=2}^K M_{k1} N_k - \sum_{l=1}^L \mu_l n_l - \sum_{i=1,2,3} (V \bar{F}_{i3} / \bar{F}_{33}) \sigma_{3i}. \quad (2.43)$$

Then

$$\gamma A = \Phi_1 - N \phi_1, \quad (2.44)$$

showing that γ is the excess of the Φ_1 potential per unit interface area.

Eqs. (2.41) and (2.42) express the total interface free energy γA through properties of an arbitrary region containing the interface. While γA is well-defined, the individual terms appearing in the right-hand side depend on the location of the boundaries of the region. To express those terms through interface excesses independent of the choice of the region, we should subtract contributions of the homogeneous phases. To this end, we select two arbitrary regions inside the homogeneous parts of the phases. Such regions can be chosen

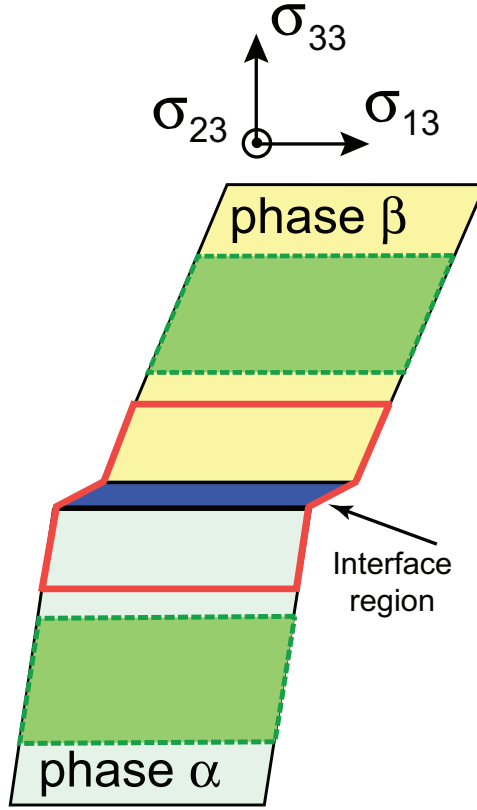


Figure 2.3: Two solid phases separated by coherent interface. Interface region shown by solid red line includes homogeneous parts of phases α and β . Regions inside homogeneous parts of the phases are shown in green.

within the region containing the interface or outside this region. The latter case is illustrated in Fig. 2.3. Let the total numbers of substitutional species in the homogeneous regions be N^α and N^β , respectively. Eq. (2.19) applied to each of these regions gives

$$0 = U^\alpha - TS^\alpha - \sum_{k=2}^K M_{k1} N_k^\alpha - \phi_1 N^\alpha - \sum_{l=1}^L \mu_l n_l^\alpha - \sum_{i=1,2,3} \sigma_{3i} V^\alpha F_{i3}^\alpha / F_{33}^\alpha \quad (2.45)$$

and

$$0 = U^\beta - TS^\beta - \sum_{k=2}^K M_{k1} N_k^\beta - \phi_1 N^\beta - \sum_{l=1}^L \mu_l n_l^\beta - \sum_{i=1,2,3} \sigma_{3i} V^\beta F_{i3}^\beta / F_{33}^\beta. \quad (2.46)$$

Eqs. (2.41), (2.45) and (2.46) form a system of linear equations with respect to differentials of the intensive variables. We proceed by solving this system using Cramer's rule of linear algebra to obtain [26]

$$\begin{aligned} \gamma A &= [U]_{XY} - T[S]_{XY} - \sum_{k=2}^K M_{k1} [N_k]_{XY} - \phi_1 [N]_{XY} \\ &\quad - \sum_{l=1}^L \mu_l [n_l]_{XY} - \sum_{i=1,2,3} \sigma_{3i} [V \bar{F}_{i3} / \bar{F}_{33}]_{XY}, \end{aligned} \quad (2.47)$$

or using Eq. (2.21),

$$\begin{aligned} \gamma A &= [U]_{XY} - T[S]_{XY} - \sum_{k=1}^K \phi_k [N_k]_{XY} \\ &\quad - \sum_{l=1}^L \mu_l [n_l]_{XY} - \sum_{i=1,2,3} \sigma_{3i} [V \bar{F}_{i3} / \bar{F}_{33}]_{XY}. \end{aligned} \quad (2.48)$$

Here X and Y are any two of the extensive quantities U , S , $V \bar{F}_{i3} / \bar{F}_{33}$, N_k and n_l . The coefficients $[Z]_{XY}$ are computed as a ratio of two determinants [14]

$$[Z]_{XY} \equiv \frac{\begin{vmatrix} Z & X & Y \\ Z^\alpha & X^\alpha & Y^\alpha \\ Z^\beta & X^\beta & Y^\beta \end{vmatrix}}{\begin{vmatrix} X^\alpha & Y^\alpha \\ X^\beta & Y^\beta \end{vmatrix}}. \quad (2.49)$$

The quantities in the first row of the numerator are computed for a region containing the interface, whereas the quantities in other rows are computed for homogeneous regions of phases α and β .

The quantity $[Z]_{XY}$ has the meaning of the interfacial excess of property Z when a region containing the interface contains the same amounts of X and Y as the bulk phases combined (i.e., when the excesses of X and Y are both zero). The excess of Z is generally not unique and depend on the choice of X and Y . Due to properties of determinants,

$$[X]_{XY} = [Y]_{XY} = 0. \quad (2.50)$$

Thus, two terms in Eqs. (2.47) and (2.48) are zero. The excesses $[N_k]_{XY}$ and $[n_l]_{XY}$ have the meaning of interfacial segregation of substitutional and interstitial components, respectively. The terms $[V]_{XY}$, $[V\bar{F}_{13}/\bar{F}_{33}]_{XY}$ and $[V\bar{F}_{23}/\bar{F}_{33}]_{XY}$ represent the excess volume and excess shears of the interface, respectively. The excess shears are properties specific to coherent interfaces. They have no significance for incoherent and other interfaces can cannot be equilibrated under shear stresses parallel to their plane. By contrast, the excess volume $[V]_{XY}$ is common to all interfaces [14].

As already noted, γA represents an excess of the Φ_1 potential. Using the square bracket notations,

$$\gamma A = [U - TS - \sum_{k=2}^K M_{k1} N_k - \sum_{l=1}^L \mu_l n_l - \sum_{i=1,2} \sigma_{3i} V \bar{F}_{i3} / \bar{F}_{33}]_{NV} \equiv [\Phi_1]_{NV}, \quad (2.51)$$

i.e., the excess of Φ_1 should be computed under a fixed total number of substitutional atoms and a fixed volume. In fact, γA can be expressed through excesses of different thermodynamic potentials corresponding to different choices of X and Y . For example,

$$\gamma A = [U - \sum_{k=2}^K M_{k1} N_k - \sum_{l=1}^L \mu_l n_l - \sum_{i=1,2,3} \sigma_{3i} V \bar{F}_{i3} / \bar{F}_{33}]_{NS}, \quad (2.52)$$

where the excesses of the total number of substitutional atoms and entropy are zero. The flexibility in expressing the same γA through excesses of different thermodynamic potentials can be useful in applications.

2.3.2 The adsorption equation

Having introduced the interface free energy, we are now in a position to derive the adsorption equation. As a first step, we will compute the energy differential dU the two-phase region containing the interface (Fig. 2.4(b,d)). The corners of this region define an imaginary parallelepiped shown in Fig. 2.4(e). Due to the coherency condition, the region has the same cross-section at every height x_3 , as does the parallelepiped. Therefore, the parallelepiped can be thought of as obtained by mental slicing of the region into infinitely thin layers and their translation parallel to the interface. Since all properties of the system as assumed to be uniform in the directions parallel to the interface, the parallelepiped has exactly the same energy as the region. This remains true at every point of any equilibrium process that the region may undergo by deformation and or changes.

Thus, instead of computing dU for the initial region we can compute dU for the parallelepiped, which in fact is also a two-phase region containing the interface but having a

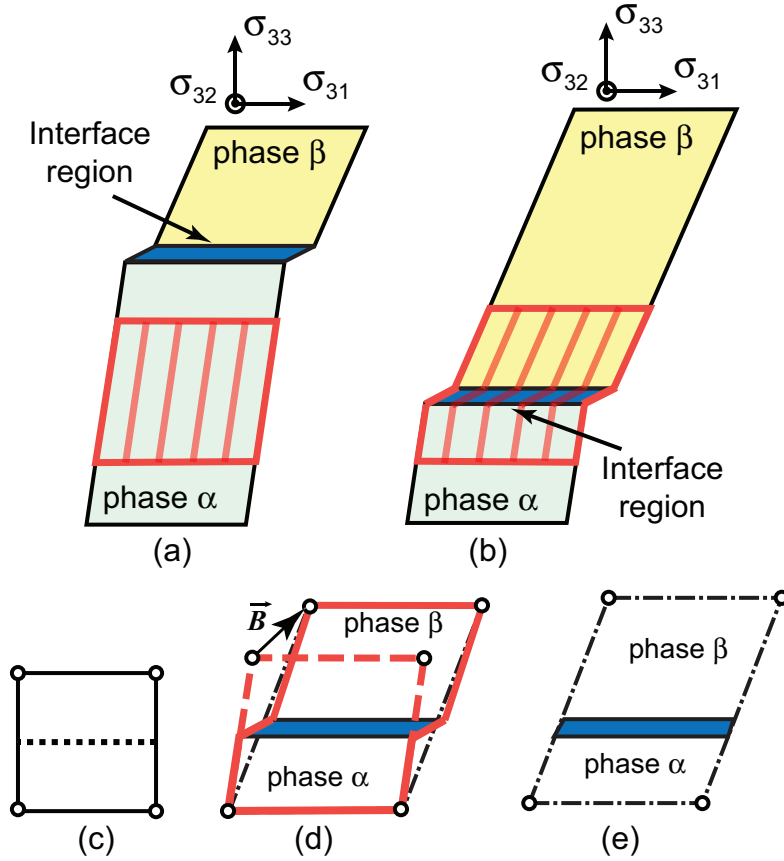


Figure 2.4: Coherent transformation of the region initially located inside phase α (a) into a layer containing both phases and an interface (b). (c) is a zoomed view of the reference region with the dotted line showing an approximate interface position in reference coordinates. (d) is a zoomed view of the deformed region of phase α (dashed lines) and the two-phase region (solid lines). The dash-dotted line outlines a shape defining the average deformation gradient $\bar{\mathbf{F}}$. The open circles mark imaginary markers embedded in the reference and deformed states of the bulk phases.

different shape. The advantage is that the mechanical work term can now be expressed through the average deformation gradient $\bar{\mathbf{F}}$ employed in the definition of γA . If the parallelepiped changes its shape (while still keeping its bottom face fixed, the top face parallel to the interface and one of the edges parallel to the x'_1 axis), the mechanical work dW_m done by the stresses applied to its facets is the sum of the relevant forces times the facet displacements. The calculation of this work is simplified by formally considering $\bar{\mathbf{F}}$ as a

homogeneous deformation gradient relative the same reference space as used for the homogeneous phases and mapping the reference region of phase α to the parallelepiped (Fig. 2.4).

This gives

$$dW_m = \sum_{i=1,2,3} V' F_{11} F_{22} \sigma_{3i} d\bar{F}_{i3} + \sum_{i,j=1,2} V' \bar{P}_{ij} dF_{ji}, \quad (2.53)$$

where $\bar{\mathbf{P}} \equiv J\bar{\mathbf{F}}^{-1} \cdot \bar{\boldsymbol{\sigma}}$ is a formal analog of the first Piola-Kirchhoff stress tensor and $\bar{\boldsymbol{\sigma}}$ is the true stress tensor averaged over the parallelepiped. Because σ_{3i} are coordinate-independent, it is only the lateral stress components σ_{3i} , $i, j = 1, 2$, that should be averaged over the coordinate x_3 to obtain $\bar{\boldsymbol{\sigma}}$.

In a more general variation of state, the region also exchanges heat and matter with its environment. Keeping, as usual, the total number of substitutional atoms fixed, we obtain

$$\begin{aligned} dU &= TdS + \sum_{k=2}^K M_{k1} dN_k + \sum_{l=1}^L \mu_l dn_l + \\ &+ \sum_{i=1,2,3} V' F_{11} F_{22} \sigma_{3i} d\bar{F}_{i3} + \sum_{i,j=1,2} V' \bar{P}_{ij} dF_{ji}. \end{aligned} \quad (2.54)$$

This equation looks similar to Eq. (2.14) and represents a generalization of the latter to an inhomogeneous system containing an interface.

As the next step towards the adsorption equation, Differentiating Eq. (2.41) and using expression for dU from Eq. (2.54) we obtain

$$\begin{aligned}
d(\gamma A) &= -SdT - \sum_{i=1,2,3} (VF_{i3}/F_{33}) d\sigma_{3i} - \\
&- \sum_{k=2}^K N_k dM_{k1} - Nd\phi_1 - \sum_{l=1}^L n_l d\mu_l \\
&+ \sum_{i,j=1,2} \int_{V'} J \sum_{r=1,2,3} F_{ir}^{-1} \left(\sigma_{rj} - \sum_{m=1,2,3} \frac{F_{m3}}{F_{33}} \sigma_{3m} \delta_{rj} \right) dF_{ij} dV' \\
&= d\Phi_1 - Nd\phi_1.
\end{aligned} \tag{2.55}$$

Eq. (2.55) provides an expression for tensor \mathbf{Q} of a inhomogeneous region

$$\mathbf{Q} = \frac{1}{V'} \int_{V'} J \mathbf{F}^{-1} \left(\boldsymbol{\sigma} - \sum_{m=1,2,3} \frac{F_{m3}}{F_{33}} \sigma_{3m} \mathbf{I} \right) dV' \tag{2.56}$$

For a homogeneous system Eq. (2.56) reduces to earlier introduced \mathbf{Q} in Eq. (2.18).

The differentials in the RHS in Eq. (2.55) are not independent. There are two additional equations of constraint imposed by the Gibbs-Duhem type equations (2.34) and (2.35) of the phases α and β . Solving the system of equations (2.55), (2.34) and (2.35) using Cramer's rule, we obtain the adsorption equation

$$\begin{aligned}
d(\gamma A) &= -[S]_{XY} dT - \sum_{i=1,2,3} [VF_{i3}/F_{33}]_{XY} d\sigma_{3i} - \\
&- \sum_{k=2}^K [N_k]_{XY} dM_{k1} - [N]_{XY} d\phi_1 \\
&- \sum_{l=1}^L [n_l]_{XY} d\mu_l + \sum_{i,j=1,2} [V'Q_{ij}]_{XY} dF_{ji}.
\end{aligned} \tag{2.57}$$

where X and Y are two of the extensive properties S , VF_{i3}/F_{33} , N_k , n_l or $V'Q_{ij}$.

Note the significant difference between Eqs. (2.55) and (2.57) for the same differential $d(\gamma A)$. In Eq. (2.55), the differential coefficients are the properties of the region containing the interface. These properties depend on the choice of the region boundaries and thus, have no physical significance. In the adsorption equation (2.57), on the other hand, the differential coefficients are the excesses $[Z]_{XY}$ introduced earlier by Eq. (2.49). For a given choice of X and Y , these excesses are independent of the choice of the interface region or the bulk regions.

The second major difference is the number of differentials on the RHS. In Eq. (2.55), it exceeds the number of degrees of freedom available to the system of two coexisting phases. Eq. (2.55) is not a perfect differential and symbol δ instead of d is perhaps more suitable.

On the other hand, due to the property of determinants two terms in Eq. (2.50), are eliminated in Eq. (2.57) by specifying X and Y . This leaves only independent differentials in the adsorption equation. Thus, the number of degrees of freedom is $K + L + 5$ which is consistent with the phase rule in Eq. (2.36) and the adsorption equation (2.57) is a perfect differential. As a result, each excess $[Z]_{XY}$ can be expressed as a partial derivative of γA , and is a measurable quantity.

The adsorption equation corresponding to the Gibbs dividing surface can be obtained by choosing $X = V$, so that the volume of the layer containing the interface is equal to the sum of the volumes of the phases α and β . Although the excess volume $[V]_{VY}$ is zero in this case, the terms $[VF_{13}/F_{33}]_{VY}$ and $[VF_{23}/F_{33}]_{VY}$ are generally not zero and present in the adsorption equation for coherent interfaces.

Interface stress

The last term in the adsorption equation describes contribution to γA from elastic deformation of the interface [16, 17]. This deformation is fully described by the lateral components F_{11} , F_{12} and F_{22} of the deformation gradient. The coefficients $[V'Q_{ij}]_{XY}$ are the excess quantities which form a (2×2) tensor and which we identify with components of the interface stress tensor. As other excess quantities, $[V'Q_{ij}]_{XY}$ generally depends on the choice

of the extensive variables X and Y and therefore is not unique. It does become unique, however, when both phases are hydrostatic. Under certain conditions (for example, a free standing film), different $[V'Q_{ij}]_{XY}$ are expected to be very close to each other.

If we divide the adsorption equation (2.57) by the interface area in the reference state, we can introduce Lagrangian excess quantities. The reference area is not affected by elastic deformation, so each term in the adsorption equation can be divided by the reference area even the terms under the differential like $d(\gamma A)$. The Lagrangian interface stress, for example, gives the excess of stress over the bulk stresses computed per unit of the reference area.

If the current state of one of the phases is taken as the reference state, $F_{11} = F_{22} = 1$, $F_{12} = 0$ and Eq. (2.57) becomes

$$\begin{aligned}
d(\gamma A) = & -[S]_{XY}dT - \sum_{i=1,2,3} [VF_{i3}/F_{33}]_{XY}d\sigma_{3i} - \\
& - \sum_{k=2}^K [N_k]_{XY}dM_{k1} - [N]_{XY}d\phi_1 - \sum_{l=1}^L [n_l]_{XY}d\mu_l + \sum_{i,j=1,2} \tau_{ij}^{XY} Ade_{ji}
\end{aligned} \tag{2.58}$$

where

$$\tau_{11}^{XY} \equiv \frac{1}{A}[VQ_{11}]_{XY} \quad \tau_{22}^{XY} \equiv \frac{1}{A}[VQ_{22}]_{XY} \quad \tau_{12}^{XY} = \tau_{21}^{XY} \equiv \frac{1}{A}[VQ_{12}]_{XY} \tag{2.59}$$

In Eq. (2.58) \mathbf{e} is the small strain tensor with $de_{11} = dF_{11}$, $de_{22} = dF_{22}$ and $de_{12} = de_{21} = \frac{1}{2}dF_{12}$. The components e_{12} and e_{21} are identical and should not be treated as independent variables. $\boldsymbol{\tau}$ defined by Eq. (2.59) is the interface stress tensor. It describes the change in interface free energy due to elastic deformation of the interface. The four components of $\boldsymbol{\tau}$ given in Eq. (2.59) form a (2×2) symmetrical tensor.

In the remainder of this paper, we will use the small strain \mathbf{e} instead of the deformation

gradient \mathbf{F} to describe elastic variations parallel to the interface . However, all relations derived below can be obtained in a straightforward manner from Eq. (2.57) and rewritten in a more general form containing \mathbf{F} .

2.3.3 Lagrangian and physical forms of the adsorption equation

In the adsorption equation (2.58), the differential of the total interface free energy γA is expressed through differentials of the intensive parameters. We call this form of the adsorption equation Lagrangian. One can also derive the physical form of the adsorption equation by differentiating γA in Eq. (2.58). Using $dA = A \sum_{i,j=1,2} \delta_{ij} de_{ij}$ and dividing both

sides of the equation by the physical area A , we obtain

$$\begin{aligned}
d\gamma &= -\frac{[S]_{XY}}{A} dT - \sum_{i=1,2,3} \frac{[VF_{i3}/F_{33}]_{XY}}{A} d\sigma_{3i} - \\
&- \sum_{k=2}^K \frac{[N_k]_{XY}}{A} dM_{k1} - \frac{[N]_{XY}}{A} d\phi_1 \\
&- \sum_{l=1}^L \frac{[n_l]}{A} d\mu_l + \sum_{i,j=1,2} \left(\tau_{ij}^{XY} - \delta_{ij}\gamma \right) de_{ji}
\end{aligned} \tag{2.60}$$

In Eq. (2.60), the excess quantities are computed per unit of the current physical area. From Eq. (2.60) we immediately obtain the generalized Shuttleworth equation [15]

$$\left(\frac{\partial \gamma}{\partial e_{ij}} \right)^{XY} = \tau_{ij}^{XY} - \delta_{ij}\gamma. \tag{2.61}$$

In Eq. (2.61), the partial derivative with respect to strain is taken while all other independent variables are held constant. Eq. (2.61) actually represents several equations, because the set of independent variables in the adsorption equation depends on the choice of X and Y .

Eqs. (2.58) and (2.60) represent the perfect differentials of the total and specific interfacial free energy, respectively, and generate two sets of Maxwell relations which will be discussed in Sec. 2.3.5.

2.3.4 Thermodynamic integration

In this section we derive another version of the adsorption equation which can be useful in applications. Interface free energy γ can be computed by integration of the adsorption equation along a coexistence path knowing an initial value. However, in applications the excess entropy $[S]_{XY}$ is rarely accessible. To avoid calculation of $[S]_{XY}$, we combine Eqs. (2.47) and (2.58) to eliminate the entropy term and derive the interface version of the well known Gibbs-Helmholtz equation:

$$\begin{aligned}
d\left(\frac{\gamma A}{T}\right) &= -\frac{[\Psi]_{XY}}{T^2}dT + \sum_{i=1,2,3} \frac{[VF_{i3}/F_{33}]_{XY}}{T}d\sigma_{3i} - \\
&- \sum_{k=2}^K \frac{[N_k]_{XY}}{T}dM_{k1} - \frac{[N]_{XY}}{T}d\phi_1 \\
&- \sum_{l=1}^L \frac{[n_l]_{XY}}{T}d\mu_l + \frac{1}{T} \sum_{i,j=1,2} \tau_{ij}^{XY} de_{ji},
\end{aligned} \tag{2.62}$$

where the thermodynamic potential Ψ is defined by

$$\Psi \equiv U - \sum_{i=1,2,3} \sigma_{3i}VF_{i3}/F_{33} - \sum_{k=2}^K N_k M_{k1} - N\phi_1 - \sum_{l=1}^L n_l d\mu_l \tag{2.63}$$

Eq. (2.62) can be integrated to compute γ as a function of the intensive variables and does not require knowledge of $[S]_{XY}$. This equation has the same number of independent variables as the adsorption equation (2.58). It is strait forward to derive the physical form of the equation, which will contain the differential $d(\gamma/T)$. Since Eq. (2.62) becomes a

perfect differential after the extensive quantities X and Y are specified, it produces new Maxwell relations that do not involve the excess entropy. Such relations will be analyzed in the next section.

2.3.5 Maxwell relations

As we mentioned earlier, the adsorption equation generates a number of Maxwell relations between derivatives of the excess quantities. We will focus on relations that involve the effects of mechanical stresses on interface properties. For hydrostatic processes, such relations were discussed by Cahn [14]. New variables in the adsorption equation introduced in this work, such as the shear stresses σ_{31} and σ_{32} and the diffusion potentials M_{k1} of substitutional components, lead to new Maxwell type relations. The Lagrangian and physical forms of the adsorption equation produce different Maxwell relations, which will be analyzed simultaneously. In the equations appearing below, the variables held constant are dictated by a particular choice of the extensive variables X and Y . Thus, each Maxwell relation in fact represents a set of relations corresponding different choices of X and Y .

Mechanical-mechanical relations

The first set of Maxwell relations examines how the lateral deformations e_{ij} and the stresses σ_{3k} affect interface excess volume, excess shear and interface stress. From the Lagrangian form of the adsorption equation (2.58) and the physical form (2.60), we obtain

$$\frac{\partial \left(\tau_{ij}^{XY} A \right)}{\partial e_{kl}} = \frac{\partial \left(\tau_{kl}^{XY} A \right)}{\partial e_{ij}}, \quad \frac{\partial \left(\tau_{ij}^{XY} - \delta_{ij} \gamma \right)}{\partial e_{kl}} = \frac{\partial \left(\tau_{kl}^{XY} - \delta_{kl} \gamma \right)}{\partial e_{ij}}, \quad (2.64)$$

$$i, j, k, l = 1, 2,$$

$$\frac{\partial \left(\tau_{ij}^{XY} A \right)}{\partial \sigma_{33}} = - \frac{\partial [V]_{XY}}{\partial e_{ij}}, \quad \frac{\partial \left(\tau_{ij}^{XY} - \delta_{ij} \gamma \right)}{\partial \sigma_{33}} = - \frac{\partial ([V]_{XY}/A)}{\partial e_{ij}}, \quad (2.65)$$

$$i, j = 1, 2,$$

$$\frac{\partial \left(\tau_{ij}^{XY} A \right)}{\partial \sigma_{3k}} = - \frac{\partial ([VF_{k3}/F_{33}]_{XY})}{\partial e_{ij}},$$

$$\frac{\partial \left(\tau_{ij}^{XY} - \delta_{ij} \gamma \right)}{\partial \sigma_{3k}} = - \frac{\partial ([VF_{k3}/F_{33}]_{XY}/A)}{\partial e_{ij}}, \quad (2.66)$$

$$i, j, k = 1, 2,$$

$$\frac{\partial ([VF_{k3}/F_{33}]_{XY})}{\partial \sigma_{33}} = \frac{\partial [V]_{XY}}{\partial \sigma_{3k}}, \quad k = 1, 2. \quad (2.67)$$

Eq. (2.65) describes the interfacial Poisson effect, in which lateral deformation of the interface produces change in the “interface thickness” (excess volume per unit area). Because Eqs. (2.64) - (2.66) involve changes in interface area, Lagrangian and physical forms of these relations are different. By contrast, the Lagrangian and physical forms of Eq. (2.67) are identical, because the derivatives are taken at constant area.

Mechanical-chemical relations

Elastic deformation parallel and normal to the interface plane affect segregation. These changes in segregation, in turn, are related to changes in interface stress and the excess volume and shear. Here we show the Maxwell relations for substitutional components when the diffusion potential M_{k1} is varied. For interstitial components, the relations have a similar form with the diffusion potentials replaced by chemical potentials μ_l . The effect of

deformation parallel to the interface on segregation is described by the relations

$$\frac{\partial \left(\tau_{ij}^{XY} A \right)}{\partial M_{k1}} = - \frac{\partial [N_k]_{XY}}{\partial e_{ij}}, \quad \frac{\partial \left(\tau_{ij}^{XY} - \delta_{ij} \gamma \right)}{\partial M_{k1}} = - \frac{\partial ([N_k]_{XY} / A)}{\partial e_{ij}}, \quad (2.68)$$

$$i, j = 1, 2, \quad k = 2, \dots, K.$$

Because interface area changes, there are two forms of this relation. The effect of the σ_{31} , σ_{32} and σ_{33} stresses on segregation is represented by the relations

$$\frac{\partial [V]_{XY}}{\partial M_{k1}} = \frac{\partial [N_k]_{XY}}{\partial \sigma_{33}}, \quad k = 2, \dots, K, \quad (2.69)$$

$$\frac{\partial ([V F_{i3} / F_{33}]_{XY})}{\partial M_{k1}} = \frac{\partial [N_k]_{XY}}{\partial \sigma_{3i}}, \quad (2.70)$$

$$i, j = 1, 2, \quad k = 2, \dots, K.$$

Since the derivatives are taken at constant area, the Lagrangian and physical forms of Maxwell relations are identical.

Mechanical-thermal relations

Such relations involve effects of temperature on interface stress, excess volume and excess shear. The corresponding Maxwell relations generated by Eq. (2.58) would contain a derivative of $[S]_{XY}$ with respect to strains and stresses. Alternatively, the Gibbs-Helmholtz version of the adsorption equation does not require knowledge of $[S]_{XY}$ and gives the Maxwell relations that involve the temperature derivative. These relations are

$$\begin{aligned}\frac{\partial \left(\tau_{ij}^{XY} A/T \right)}{\partial T} &= - \frac{\partial \left([\Psi]_{XY}/T^2 \right)}{\partial e_{ij}}, \\ \frac{\partial \left\{ \left(\tau_{ij}^{XY} - \delta_{ij} \gamma \right) / T \right\}}{\partial T} &= - \frac{\partial \left([\Psi]_{XY}/A \right)}{\partial e_{ij}},\end{aligned}\tag{2.71}$$

$i, j = 1, 2,$

$$\frac{\partial \left([V]_{XY}/T \right)}{\partial T} = \frac{\partial \left([\Psi]_{XY}/T^2 \right)}{\partial \sigma_{33}},\tag{2.72}$$

$$\frac{\partial \left([VF_{k3}/F_{33}]_{XY}/T \right)}{\partial T} = \frac{\partial \left([\Psi]_{XY}/T^2 \right)}{\partial \sigma_{3k}}, \quad k = 1, 2.\tag{2.73}$$

In Eq. (2.71), the Lagrangian and physical forms of the relation are different. The potential Ψ is given by Eq. (2.63).

Chemical-thermal relations

Using the interface version of the Gibbs-Helmholtz equation, Eq. (2.62), we can evaluate the effect of temperature on segregation of substitutional and interstitial components. The corresponding derivatives involve $[\Psi]_{XY}$ instead of $[S]_{XY}$:

$$\frac{\partial \left([N_k]_{XY}/T \right)}{\partial T} = \frac{\partial \left([\Psi]_{XY}/T^2 \right)}{\partial M_{k1}}, \quad k = 2, \dots, K,\tag{2.74}$$

$$\frac{\partial \left([n_l]_{XY}/T \right)}{\partial T} = \frac{\partial \left([\Psi]_{XY}/T^2 \right)}{\partial \mu_l} \quad l = 1, \dots, L.\tag{2.75}$$

For substitutional components, the derivatives are taken with respect to the diffusion potentials, while for interstitial components with respect to the chemical potentials are involved.

2.4 Application of the treatment to other types of interfaces

Thermodynamic equations derived for coherent solid-solid interfaces can be formally applied to describe incoherent, solid-fluid and fluid-fluid interfaces by setting terms containing shear stresses σ_{31} and σ_{32} to zero. For incoherent solid-solid interfaces these equations are valid for variations when $F_{11}^\alpha = F_{11}^\beta$, $F_{12}^\alpha = F_{12}^\beta$ and $F_{22}^\alpha = F_{22}^\beta$. Incoherent solid-solid interfaces are capable of additional variations when each phase is deformed independently [16, 27, 28]. These variations are not considered here. In this section we analyze equations for incoherent solid-solid, solid-fluid and fluid-fluid interfaces as well as equations for surfaces and grain boundaries.

2.4.1 Interfaces in two-phase systems

Incoherent solid-solid interfaces

Incoherent solid-solid interfaces do not support shear stresses parallel to the interface plane. Because sliding can occur, excess interface shears have no meaning. However, the excess volume is still well defined. In the definition of the interface free energy in Eq. (2.47), we set shear stresses σ_{31} and σ_{32} to zero. For the same reason, in the adsorption equation in Eq. (2.58) the differentials of σ_{31} and σ_{32} are identically zero. Keeping in mind the constraint $F_{11}^\alpha = F_{11}^\beta$, $F_{12}^\alpha = F_{12}^\beta$ and $F_{22}^\alpha = F_{22}^\beta$, the number of degrees of freedom in this case is $K + L + 3$. The potentials ϕ_m are defined for the non-hydrostatically stressed phases through Eq. (2.20). When shear stresses are zero these potentials are independent of the reference state.

Solid-fluid interfaces

Just as incoherent solid-solid interfaces, solid-fluid interfaces do not support shear stresses parallel to the interface. Therefore, vanishing of the shear terms discussed in the preceding paragraph applies here as well. In addition, the fluid is hydrostatic and potentials ϕ_m become the real chemical potentials in the fluid.

Fluid-fluid interfaces

Finally, we discuss fluid-fluid interfaces. In the treatment of coherent solid-solid interfaces we considered elastic deformations of the phases to derive the adsorption equation which includes a work term with the interface stress $\boldsymbol{\tau}$. For a fluid system, we can imagine that this elastic work is done by the walls of the rigid envelope which incloses the fluids. The bulk parts of the phases exert the hydrostatic stress $-p$ on the walls. However, along the perimeter where the phases meet, the stresses exerted on the walls are different from $-p$ due to the interface tension. Thus, the average stress exerted on the walls is non-hydrostatic even though the phases and the interface are fluid. The expression for interface free energy and the adsorption equation become

$$\gamma A = [U]_{XY} - T[S]_{XY} + p[V]_{XY} - \sum_{k=1}^{K+L} \mu_k [N_k]_{XY}, \quad (2.76)$$

$$d(\gamma A) = -[S]_{XY} dT + [V] dp - \sum_{k=1}^{K+L} [N_k]_{XY} d\mu_k + \tau dA, \quad (2.77)$$

where μ_k are chemical potentials of the components of the fluids. In fluids there is no need to separate substitutional and interstitial components and they are grouped together.

The interface stress computed using Eq. (2.59) is

$$\tau_{ij} = (\sigma_{ij} + \delta_{ij} p) V/A, \quad i, j = 1, 2. \quad (2.78)$$

Here σ_{ij} are the average lateral components of the stress computed for some region of volume V that contains interface as well as homogeneous parts of the phases α and β . The terms $(\sigma_{ij}^\alpha + \delta_{ij} p)$ and $(\sigma_{ij}^\beta + \delta_{ij} p)$ in Eq. (2.59) are identically zero due to the hydrostaticity of the phases. Thus, as we mentioned earlier, when phases are hydrostatic (not necessarily fluid), the interface stress is unique (independent of the choices of X and Y) and is given

by Eq. (2.78). It is safe to assume that the interface properties are isotropic within a plane parallel to the interface, which means that $\tau_{11} = \tau_{22}$ and $\tau_{12} = 0$. This allows us to define interface tension $\tau = \tau_{11} = \tau_{22}$, which has a meaning of the excess force per unit area acting on the interface. Since τ is a scalar, we wrote $\tau_{ij}Ade_{ij}$ in Eq. (2.77) as simply τdA

At this point the interface free energy γ is defined as an excess of the thermodynamic potential in Eq. (2.76), whereas interface tension τ is introduced through the work term in the adsorption equation (2.77). Equality of these quantities has not been assumed so far. To prove this equality, we now consider the following thought experiment at constant T and μ_k (open system), when the walls of the envelope slowly (reversibly) move in lateral dimensions and simultaneously in the direction normal to the interface in a such a way that p remains constant. As a result of this process, the interfacial area is increased at constant T , p and μ_k . Eq. (2.77) for this process becomes

$$d(\gamma A) = \tau dA.$$

In this process we change A at a fixed coexistence point and thus a constant γ . Thus, $d(\gamma A)$ becomes

$$\gamma dA = \tau dA. \tag{2.79}$$

Eq. (2.79) demonstrates that, for fluid-fluid interfaces, γ and τ are identical, although they were introduced as two different physical quantities. If one of the phases was solid, this imaginary process could not be implemented and the relation $\tau = \gamma$ would not have to be valid.

2.4.2 Interfaces in a single-phase systems

Grain boundaries

Grain boundary is a particular type of phase boundary when the coexisting phases are thermodynamically identical. Generally, two grains of an elastically anisotropic material

under stress have different thermodynamic states. If they are brought together, one grain will begin to grow at the expense of the other. Therefore, such grains should be treated as two separate phases. The equilibrium can be achieved if the conditions (i) through (v) are satisfied. Possible variations of state preserving equilibrium are described by Eq. (2.36). An example of such system is an asymmetrical GB. When non-hydrostatic stresses are present, energy, entropy and volume per atom will be different in the two grains. Such GBs should be treated as a heterophase interface.

The equilibrium between two grains can be considered as a single-phase equilibrium, if the conditions (i) - (iv) hold and the phase change condition (2.31) is satisfied because all individual terms are zero. In this case all the thermodynamic properties of individual grains are identical. Possible variations of state also have to be consistent with a single-phase description. This requires that Eq. (2.36) is also satisfied trivially with all the terms equal to zero individually. Below we give an example showing that these requirements may impose constraints on possible variations of state of the system with a GB.

Just as phase boundaries GBs can be coherent and incoherent. Coherent GBs represent the most complex case of interfaces in a single phase system, because they can support shear stresses parallel to the GB plane, along with other stresses parallel and normal to the GB plane. Coherency here should be understood in the same context as for the phase boundaries. When temperature [29] or chemical composition [30] changes, some GBs change their structure and grains begin to slide under applied shear stress. We refer to these GBs as incoherent.

When two grains are thermodynamically identical, certain equilibrium states cannot be realized. Consider for example two grains of the same phase forming a symmetrical tilt GB. The transformation of one grain into another is accompanied by a relative displacement of the grains normal to the tilt axis and parallel to the GB plane. Such transformation is described by a deformation gradient with one non-zero difference $F_{13}^{\beta} - F_{13}^{\alpha}$, where the superscripts indicate the two grains. Because the grains are thermodynamically identical, all terms in Eqs.(2.31) and (2.36) vanish except for the non-zero work due to shear displacement

in the x_1 direction. To satisfy equilibrium, shear stress σ_{31} must be zero in Eq. (2.31) and constant in Eq. (2.36). Otherwise, the system is not in equilibrium and the GB moves by coupled motion [31,32]. This example shows that while both grains can be deformed (under applied shear σ_{31}) producing identical solids, when they are joined together, the equilibrium is broken. Notice, that the potentials ϕ^α and ϕ^β can still be defined for the two grains. Their difference $\phi^\beta - \phi^\alpha = (F_{13}^\alpha - F_{13}^\beta)\sigma_{31}\Omega$ gives the driving force per atom for coupled motion, which is linear in shear stress. Here, Ω is a volume per atom, which is the same in both grains.

From the phase change equilibrium condition (2.31) and Eq. (2.36) we conclude that, for a coherent transformation described by a deformation gradient with non-zero differences $F_{13}^\beta - F_{13}^\alpha$ or $F_{23}^\beta - F_{23}^\alpha$, the corresponding shear stresses must be zero. At the same time, if $F_{13}^\beta - F_{13}^\alpha$ or $F_{23}^\beta - F_{23}^\alpha$ is identically zero, the corresponding shear stresses may be finite. When these conditions are satisfied, then two identical grains under stress will be in equilibrium.

Assuming that the system with a GB can be described as a single-phase, Eqs. (2.45) and (2.46) are the same and γA is obtained by solving the system of only two equations:

$$\begin{aligned} \gamma A &= [U]_X - T[S]_X - \sum_{i=1,2,3} \sigma_{3i}[VF_{i3}/F_{33}]_X - \\ &- \sum_{k=2}^K M_{k1}[N_k]_X - [N]_X d\phi_1 - \sum_{l=1}^L \mu_l[n_l]_X, \end{aligned} \quad (2.80)$$

where

$$[Z]_X \equiv \frac{\begin{vmatrix} Z & X \\ Z^\alpha & X^\alpha \end{vmatrix}}{X^\alpha} = Z - Z^\alpha X/X^\alpha. \quad (2.81)$$

By specifying X , only one variable can be eliminated. Similarly, Eqs. (2.34) and (2.35) are identical and the adsorption equation is obtained by solving a system of only two

equations:

$$\begin{aligned}
d(\gamma A) = & -[S]_X dT - \sum_{i=1,2,3} [VF_{i3}/F_{33}]_X d\sigma_{3i} - \sum_{k=2}^K [N_k]_X dM_{k1} - \\
& - [N]_X d\phi_1 - \sum_{l=1}^L [n_l]_X d\mu_l + \sum_{i,j=1,2} \tau_{ij}^X A d\epsilon_{ji}.
\end{aligned} \tag{2.82}$$

Again, one variable in Eq. (2.82) is eliminated by specifying the extensive property X . Notice, that since there is no constraint on phase equilibrium between the two grains, the number of independent differentials in Eq. (2.82) is one more than in Eq. (2.58) for two phase equilibrium. In reality in single phase systems not all variations can be realized because of the equilibrium constraints discussed above.

In the direction with finite shear stress the expression for the excess shear takes a particularly simple form. Let this finite shear be σ_{31} , then $F_{13}^\alpha = F_{13}^\beta = 0$ (current state of one of the grains taken as a reference) and $[VF_{13}/F_{33}]_N/A = b_1$, where we chose $X = N$. b_1 has a simple physical meaning. It is the excess displacement in the direction of shear of the system with a GB relative to the bulk system containing the same number of atoms.

The case of incoherent GBs is treated by simply setting shear stresses and their differentials to zero in Eqs. (2.80) and (2.82).

Interfaces with static walls and surfaces

Finally, we discuss static walls and surfaces. In these cases the expression for γA and the adsorption equation is also obtained by solving a system of only two equations. The terms containing shear stresses σ_{31} and σ_{32} and their differentials disappear. The important difference between static walls and surfaces is that the former support normal stress σ_{33} and have a definite excess volume $[V]_X$. For surfaces it is impossible to define $[V]_X$ and unnecessary because σ_{33} is identically zero. Thus, the expression for γA and the adsorption equation for static walls are

$$\gamma A = [U]_X - T[S]_X + p[V]_X - \sum_{k=1}^K \phi_k [N_k]_X - \sum_{l=1}^L \mu_l [n_l]_X, \quad (2.83)$$

$$\begin{aligned} d(\gamma A) &= -[S]_X dT + [V]_X dp - \sum_{k=2}^K [N_k]_X dM_{k1} - \\ &- [N]_X d\phi_1 - \sum_{l=1}^L [n_l]_X d\mu_l + \sum_{i,j=1,2} \tau_{ij}^X A d\epsilon_{ji}, \end{aligned} \quad (2.84)$$

with $p = 0$ and $dp = 0$ for surfaces.

For fluid surfaces the equality of τ and γ can be shown by applying the adsorption equation to a thought experiment similar to the one discussed in Sec. 2.4.1

2.5 Discussion and conclusions

In this work we developed a thermodynamic treatment of solid-solid interfaces in a multi-component system under a general non-hydrostatic state of stress that includes shear stresses parallel to the interface. Shear stresses parallel to the interface affect two-phase equilibrium conditions. The phase change equilibrium condition derived by Robin [25] contains term which describes mechanical work of shape change during a coherent transformation under shear stress.

The later stresses also contribute to work γ required to create a unit of the interface area between the phases in equilibrium. The expression for γ was derived by considering a process in which an interface was created reversibly between two solid phases. The total interface free energy γA was then expressed through excess of an appropriate thermodynamic potential which included the shear stresses σ_{31} and σ_{32} and corresponding excesses of interface shear. In our analysis we did not use the concept of the dividing surface [13], which allowed to track the shape change of the system with interface in a straightforward manner and avoid defining individual chemical potentials of the substitutional atoms. When one of

the extensive parameters X or Y is equal to V and shear stresses σ_{31} and σ_{32} are zero, the excess quantities are identical to those introduced by Gibbs.

We also derived the adsorption equation which describes change in γ due to thermal, chemical and mechanical variations of state. In the adsorption equation the diffusion potentials for substitutional components appear instead of the chemical potentials. The expression for γA and the adsorption equation introduces a new excess quantity: excess of shear at a coherent interface. The adsorption equation derived in this work describes processes which include deformation of the interface area and contains the work term of this elastic deformation parallel to the interface plane. The later work is done by interface stress τ . The adsorption equation gives a recipe how to compute τ as an excess quantity.

The thermodynamic treatment of interfaces developed in this work assumes that equilibrium conditions (i)-(v) are satisfied. These conditions, in turn, assume that the path of coherent transformation is unique. However, crystal symmetry can lead to multiplicity of paths of coherent transformation [31]. In case of coherent migration of grain boundaries these paths are called coupling modes. A two-phase equilibrium state is defined among other intensive parameters by the stresses σ_{31} , σ_{32} and σ_{33} . It is not clear why multiple equilibrium states should not exist as a result of multiplicity of paths of the coherent transformation. If at a fixed values of σ_{31} , σ_{32} and σ_{33} , which correspond to one equilibrium transformation, other coupling modes can be activated, then the very existence of an equilibrium state becomes questionable and the analysis of interface thermodynamics does not apply. At the same time, if the crystallography permits multiple paths, but only one mode is actually realized (because of energetics or boundary conditions) vector \mathbf{t} is unique and the presented analysis holds. Different modes of boundary motion can be dominant in different regions of the configuration space. For example, different transformation paths can be realized at different temperatures. The switch in the coupling mode, may cause discontinuous change in the excess shear of the interface, because it is computed as an excess of \mathbf{F} for two different transformations. Therefore, this change can be viewed as an interfacial phase transition [33].

As we pointed out that one of the major challenges in thermodynamics of solid-solid interfaces is a necessity to define chemical potentials of substitutional atoms. Chemical potentials are defined as work required to add an atom to the system. For a non-hydrostatically stressed solid chemical potentials are not uniquely defined. Analyzing equilibrium of non-hydrostatic solids Larche and Cahn [18] avoided definition of chemical potentials of substitutional atoms. In this work we only considered variations in chemical composition of substitutional atoms (with no restriction on composition and total number of interstitial atoms) at constant N , so it was unnecessary to define individual chemical potentials of substitutional atoms.

Performing Legendre transformation of Eq. (2.14) we introduced thermodynamic potentials ϕ_m of a homogeneous solid under stress. When two phases, separated by a coherent interface, are in equilibrium, these potentials have the same value in the phases. The ϕ_m potentials allow to conveniently write thermodynamic equations in a form identical to that of hydrostatic systems. Moreover, when a phase is hydrostatic, ϕ_m become real chemical potentials. It is important to notice, that in this work, the potentials ϕ_m were defined for a homogeneous solid containing constant number of atoms. Based on this definition alone, ϕ_m cannot be identified with chemical potentials of a substitutional atoms. On the other hand, there is no ambiguity in their definition.

As we mentioned before, the values of ϕ_m depend on the choice of the reference state and defined up to a term $\sum_{i=1,2} (VF_{i3}/F_{33}) \sigma_{3i}$. Also, for the same homogeneous solid three different potentials ϕ_m can be constructed performing Legendre transformation for three planes perpendicular to the coordinate axis. These three potentials will, in turn, depend on the orientation of the coordinate axis. At the same time, the diffusion potentials are invariant with respect to orientation of the coordinate axis and choice of the planes (out of three) and choice of the reference state. In case of the two-phase coherent equilibrium the choice of the plane is dictated by the orientation of the interface.

Analysis of interface phenomena requires understanding of the bulk phase equilibrium.

In this work we derived a Gibbs-Duhem type equation for solid under general state of stress. Solving a system of two Gibbs-Duhem equations for two solid phases in coherent equilibrium, we obtained the equation which describes the equilibrium surface of the two-phase coexistence in configuration space. This equation is analog of the Clausius–Clapeyron relation [34] generalized for non-hydrostatic multicomponent solid system. If one equilibrium state is known, other nearby states can be predicted using this equation. The phase equilibrium conditions (i)-(v) are embedded in (2.36). Therefore, testing the relations predicted by this equation one tests the correctness of the equilibrium conditions. Test of Eq. (2.36) in experiment or atomistic simulations is subject to future work.

2.6 Examples of thermodynamic equations for particular systems

In this section we provide explicit thermodynamic expressions for three simple and most common cases of coherent solid-solid coexistence: a single component system, a binary substitutional alloy and a binary interstitial alloy. These relations are easily transformed to describe grain boundaries by changing $[Z]_{XY}$ to $[Z]_X$.

2.6.1 Single component system

Common examples of the coherent interface in a single component systems are Ferrite(BCC)-Austenite(FCC) interface in iron or HCP-FCC interface in cobalt. Equation of the two-phase coexistence in this case is given by

$$\begin{aligned}
0 = & -\{S\}_X dT - \sum_{i=1,2,3} \{VF_{i3}/F_{33}\}_X d\sigma_{3i} - \\
& - \{N\}_X d\phi + \sum_{i,j=1,2} \{V'Q_{ij}\}_X dF_{ji}.
\end{aligned} \tag{2.85}$$

The potential ϕ does not have a subscript because there is only one component in the

system. The expression for the interface free energy given in Eq. (2.47) becomes

$$\gamma A = [U]_{XY} - T[S]_{XY} - \sum_{i=1,2,3} \sigma_{3i} [VF_{i3}/F_{33}]_{XY} - \phi[N]_{XY}. \quad (2.86)$$

The adsorption equation in Eq. (2.58) becomes

$$\begin{aligned} d(\gamma A) &= -[S]_{XY} dT - \sum_{i=1,2,3} [VF_{i3}/F_{33}]_{XY} d\sigma_{3i} - \\ &- [N]_{XY} d\phi + \sum_{i,j=1,2} \tau_{ij}^{XY} A de_{ji}. \end{aligned} \quad (2.87)$$

The Gibbs-Helmholtz type equation in this case is given by

$$\begin{aligned} d\left(\frac{\gamma A}{T}\right) &= -\frac{[\Psi]_{XY}}{T^2} dT + \sum_{i=1,2,3} \frac{[VF_{i3}/F_{33}]_{XY}}{T} d\sigma_{3i} - \\ &- \frac{[N]_{XY}}{T} d\phi + \frac{1}{T} \sum_{i,j=1,2} \tau_{ij}^{XY} de_{ji}, \end{aligned} \quad (2.88)$$

where

$$\Psi \equiv U - \sum_{i=1,2,3} \sigma_{3i} VF_{i3}/F_{33} - N\phi. \quad (2.89)$$

The most convenient in the equations above is $X = N$, which makes the calculation or constancy of the potential ϕ unnecessary.

A particular example of the two phase single component system is coexistence of two non-hydrostatically stressed grains of the same material (and same crystalline structure). If two grains are deformed (one under compression another under tension), properties of the grains such volume per atom will generally be different.

2.6.2 Binary substitutional alloy

In the second example, the coherent interface separates two binary solid phases both formed by substitutional mechanism. The equations will now contain the diffusion potential M_{21} to describe the compositional changes and segregation $[N_2]_{XY}$ of the second component. The equation describing the phase coexistence becomes

$$\begin{aligned}
 0 = & -\{S\}_X dT - \sum_{i=1,2,3} \{VF_{i3}/F_{33}\}_X d\sigma_{3i} - \{N_2\}_X dM_{21} - \\
 & - \{N\}_X d\phi + \sum_{i,j=1,2} \{V'Q_{ij}\}_X dF_{ji}.
 \end{aligned} \tag{2.90}$$

It contains additional variation dM_{21} in comparison to the single component case. The expression for interface free energy in Eq. (2.47) is given by

$$\begin{aligned}
 \gamma A = & [U]_{XY} - T[S]_{XY} - \sum_{i=1,2,3} \sigma_{3i}[VF_{i3}/F_{33}]_{XY} - \\
 & - \phi_1[N]_{XY} - M_{21}[N_2]_{XY}.
 \end{aligned} \tag{2.91}$$

The adsorption equation in Eq. (2.58) takes form

$$\begin{aligned}
 d(\gamma A) = & -[S]_{XY} dT - \sum_{i=1,2,3} [VF_{i3}/F_{33}]_{XY} d\sigma_{3i} - \\
 & - [N_2]_{XY} dM_{21} - [N]_{XY} d\phi_1 + \sum_{i,j=1,2} \tau_{ij}^{XY} A de_{ji}.
 \end{aligned} \tag{2.92}$$

The Gibbs-Helmholtz type equation for thermodynamic integration

$$\begin{aligned}
 d\left(\frac{\gamma A}{T}\right) = & -\frac{[\Psi]_{XY}}{T^2} dT + \sum_{i=1,2,3} \frac{[VF_{i3}/F_{33}]_{XY}}{T} d\sigma_{3i} - \\
 & - \frac{[N_2]_{XY}}{T} dM_{21} - \frac{[N]_{XY}}{T} d\phi_1 + \frac{1}{T} \sum_{i,j=1,2} \tau_{ij}^{XY} de_{ji},
 \end{aligned} \tag{2.93}$$

where

$$\Psi \equiv U - \sum_{i=1,2,3} \sigma_{3i} V F_{i3} / F_{33} - N_2 M_{21} - N \phi_1. \quad (2.94)$$

2.6.3 Binary interstitial alloy

Finally we consider binary interstitial alloy. In this case the substitutional lattice of the two phases are different, while the interstitial component freely migrates inside the coexisting phases. The common example is already mentioned Ferrite(BCC)-Austenite(FCC) interface in iron with a finite concentration of interstitial carbon. The equation of the phase coexistence is given by

$$\begin{aligned} 0 = & -\{S\}_X dT - \sum_{i=1,2,3} \{V F_{i3} / F_{33}\}_X d\sigma_{3i} - \\ & - \{N\}_X d\phi - \{n\}_X d\mu + \sum_{i,j=1,2} \{V' Q_{ij}\}_X dF_{ji}. \end{aligned} \quad (2.95)$$

The expression for interface free energy in Eq. (2.47) becomes

$$\begin{aligned} \gamma A = & [U]_{XY} - T[S]_{XY} - \sum_{i=1,2,3} \sigma_{3i} [V F_{i3} / F_{33}]_{XY} - \\ & - \phi [N]_{XY} - \mu [n]_{XY}. \end{aligned} \quad (2.96)$$

The adsorption equation

$$\begin{aligned} d(\gamma A) = & -[S]_{XY} dT - \sum_{i=1,2,3} [V F_{i3} / F_{33}]_{XY} d\sigma_{3i} - \\ & - [N]_{XY} d\phi - [n]_{XY} d\mu + \sum_{i,j=1,2} \tau_{ij}^{XY} A d\epsilon_{ji}. \end{aligned} \quad (2.97)$$

The Gibbs-Helmholtz type equation for thermodynamic integration

$$\begin{aligned}
d\left(\frac{\gamma A}{T}\right) &= -\frac{[\Psi]_{XY}}{T^2}dT + \sum_{i=1,2,3} \frac{[VF_{i3}/F_{33}]_{XY}}{T}d\sigma_{3i} - \\
&- \frac{[N]_{XY}}{T}d\phi_1 - \frac{[n]_{XY}}{T}d\mu + \frac{1}{T} \sum_{i,j=1,2} \tau_{ij}^{XY} de_{ji},
\end{aligned} \tag{2.98}$$

where

$$\Psi \equiv U - \sum_{i=1,2,3} \sigma_{3i}VF_{i3}/F_{33} - N\phi - nd\mu. \tag{2.99}$$

2.6.4 Interface stress

Interface stress is computed using Eq. (2.59) as an excess of stresses in the system. As a result, the expression for $\boldsymbol{\tau}$ is identical for all of the three systems described above. When the current state of one of the phases is taken as the reference, then for both phases $F_{11} = F_{22} = 1$ and $F_{12} = 0$. The components F_{13} , F_{23} and F_{33} of the other phase and the layer containing the interface remain finite and have to be known from the coherent transformation. Then the explicit expressions to compute the components of $\boldsymbol{\tau}$ become

$$\tau_{11} = \frac{1}{A} \left[\int_{V'} (F_{33}\sigma_{11} - 2F_{13}\sigma_{31} - F_{23}\sigma_{23} - F_{33}\sigma_{33}) dV' \right]_{XY}, \tag{2.100}$$

$$\tau_{12} = \frac{1}{A} \left[\int_{V'} F_{33}\sigma_{21} + F_{23}^{-1}F_{33}\sigma_{31} dV' \right]_{XY}, \tag{2.101}$$

$$\tau_{22} = \frac{1}{A} \left[\int_{V'} (F_{33}\sigma_{22} - 2F_{23}\sigma_{32} - F_{13}\sigma_{13} - F_{33}\sigma_{33}) dV' \right]_{XY}. \tag{2.102}$$

In the homogeneous parts of the phases α and β the integration over the reference

volume is equivalent to multiplication of the terms under the integral sign by V'^α and V'^β respectively. For the layer containing interface integration gives average stress and average components of the deformation gradient that are related to vector \mathbf{B} . This shows that precise knowledge of the deformation and atomic rearrangement in the interface region is not required. After the integration over the reference volume we obtain:

$$\tau_{11} = \frac{1}{A} [\bar{\sigma}_{11}V - 2AB_{13}\sigma_{31} - B_{23}A\sigma_{32} - \sigma_{33}V]_{XY}, \quad (2.103)$$

$$\tau_{12} = [\bar{\sigma}_{21}V - AB_{23}\sigma_{31}]_{XY}, \quad (2.104)$$

$$\tau_{22} = \frac{1}{A} [\bar{\sigma}_{22}V - 2AB_{23}\sigma_{32} - B_{13}A\sigma_{31} - \sigma_{33}V]_{XY}. \quad (2.105)$$

Eqs. (2.100)-(2.105) give a recipe how to compute the components of $\boldsymbol{\tau}$ for a given state, when the current state is taken as the reference.

Chapter 3: Methodology of Atomistic Simulations

3.1 Simulation Methods

The two methods employed in this work were Molecular Dynamics (MD) and Monte Carlo (MC). Simulations were performed in canonical (NVT), micro-canonical (NVE) and semi-grand canonical ensembles. Simulation block shown in Figs. 3.1 and 3.2 contains N particles which interact according to a known interatomic potential. Various types of boundary conditions from all periodic to open surfaces can be applied depending on a goal of simulations. Both methods allow to model equilibrium states. Details of each method are described below.

3.1.1 Molecular dynamics (MD)

In MD simulation motion of atoms is realized by solving a system of Newton's equations of motion. In canonical ensemble the temperature was controlled with Noose-Hoover thermostat. In addition to motion of individual particles, the size of the simulation box can fluctuate to impose a desired external pressure (NPT ensemble). MD method was implemented in ITAP Molecular Dynamics (IMD) program [35].

3.1.2 Monte Carlo (MC)

In the MC simulations, the temperature is fixed while the atoms are movable. At each MC step, a randomly chosen atom is displaced by a random amount in a random direction and this move is accepted or rejected by the Metropolis algorithm [36,37] as shown in Fig. 3.2.

In this work we performed simulations in semi-grand canonical ensemble to model a binary system. In this ensemble, the temperature, total number of atoms N and the chemical

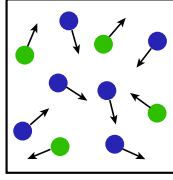


Figure 3.1: Schematic representation of a simulation box with particles in MD simulations. The arrows indicate the velocity vectors.

potential difference M_{21} are held fixed, whereas positions and chemical sorts of atoms can vary. Each step of the MC process includes a random selection of an atom and its random displacement with a simultaneous random change of its chemical species. This trial move is accepted or rejected according to the Metropolis algorithm. Using this method, the equilibrium state of a binary system can be reached much faster than by molecular dynamics simulations, since the redistribution of chemical species in the MC method does not involve their actual diffusion (a very slow process in solids). In alloys, the formation of an equilibrium surface/interface segregation requires a redistribution of the chemical species over the system by diffusion mechanisms, which makes molecular dynamics simulations highly impractical. MC method was implemented in SOLD software package.

3.2 Modeling of interatomic interactions

3.2.1 Embedded atom method

The energy of atomic interaction is described by Embedded Atom Method (EAM). The energy of an atom is given by

$$E_i = \Phi_\alpha \left(\sum_{i \neq j} \rho_\beta(r_{ij}) \right) + \frac{1}{2} \sum_{i \neq j} \Psi_{\alpha\beta}(r_{ij}), \quad (3.1)$$

where the symbols α and β enumerate atoms, i and j are Cartesian components of the vectors and tensors, $r_{\alpha\beta}^i$ is the vector connecting atoms α and β separated by a distance

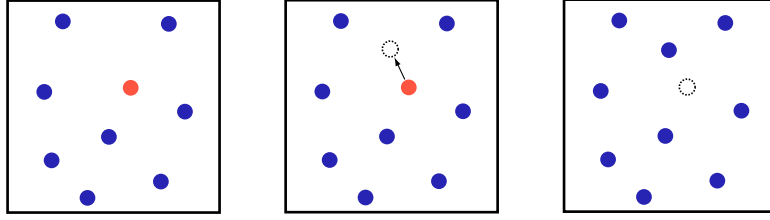


Figure 3.2: Schematic representation of a simulation box with particles in MC simulations. The figure illustrates accepted random displacement.

r_{ij} , $\Phi(r_{\alpha\beta})$ is the pair interaction function, $\rho(r_{ij})$ is the electron density function assigned to atoms, Ψ is the embedding energy of atom α . EAM permits direct calculations of the average stress tensor σ_{ij} of a system using the virial expression [38].

3.2.2 Employed interatomic potentials

We chose copper as a model material, with atomic interactions described with an embedded-atom method potential fit to experimental and first-principles data [39]. This potential accurately reproduces the lattice parameter, cohesive energy, elastic constants, phonon frequencies, thermal expansion, lattice-defect energies and other properties of Cu. The melting temperature of Cu predicted by this potential is $T_m = 1327$ K (1356 K in experiment).

We chose the copper-silver system as a model binary system, with atomic interactions described by the embedded-atom potential developed in Ref. [40]. This potential utilizes existing Cu [39] and Ag [40] potentials, with the cross-interaction function fit to first-principles formation energies of several imaginary compounds of the Cu-Ag system. This potential reproduces the Cu-Ag phase diagram in semi-quantitative agreement with experiment [41]. The phase diagram contains three phases: liquid, Cu-rich and Ag-rich terminal solid solutions formed by the substitutional mechanism. The melting point of Cu and the eutectic temperature predicted by this potential are 1327 K and 935 K, the experimental values being 1356 K and 1053 K, respectively [41].

Chapter 4: Temperature dependence of the surface free energy and surface stress: An atomistic calculation for Cu (110).

4.1 Introduction

Gibbs [13] defined the surface free energy as reversible work per unit area needed to create a new surface, and the surface stress as reversible work of elastically stretching the surface. These two quantities are related by [15]

$$\tau_{ij} = \delta_{ij}\gamma + \frac{\partial\gamma}{\partial e_{ij}}, \quad i, j = 1, 2, \quad (4.1)$$

where the derivative is taken at a constant temperature, e_{ij} is a strain tensor of the surface and δ_{ij} is the Kronecker symbol. Two of the Cartesian axes are assumed to be parallel to the surface and the third one is normal to it. While γ is a scalar, the surface stress $\boldsymbol{\tau}$ is a symmetrical second rank tensor. These quantities are usually of the same order of magnitude. Due to the second term in Eq. (4.1), components of $\boldsymbol{\tau}$ can be larger than γ , smaller, or even negative, which γ can never be for a plane interface[13]. Defining the average surface stress as $\tau = (\tau_{11} + \tau_{22})/2$, Eq. (4.1) can be rewritten as

$$\tau = \gamma + A \frac{\partial\gamma}{\partial A}, \quad (4.2)$$

where A is surface area.

The fundamental differences between γ and $\boldsymbol{\tau}$ have been recently discussed by Kramer and Weissmuller [42]. In contrast to solids, γ and τ of liquids are numerically equal because

liquids respond to strains by exposing more or less atoms to the surface without changing γ , resulting in $\partial\gamma/\partial e_{ij} = 0$ [14, 16, 42]. At high temperatures, γ of a solid can exceed the sum of the liquid-vacuum and solid-liquid free energies. To minimize the free energy, the solid surface can premelt, creating a thin liquid-like layer [43]. Gurney [44] argued that because at high temperatures surface atoms can migrate like in a liquid, the surface free energy should become equal to the surface stress. This assumption was later used in the experimental work of Bailey and Watkins [45]. Herring [46] disagreed with Gurney's conclusion, questioning the way Gurney related the chemical potentials of the surface atoms to the surface stress.

Unfortunately, most of the data for surface stresses reported in the literature refer to either 0 K or to a certain fixed temperature, making it difficult to determine whether τ and γ converge with temperature. The temperature dependence of γ was studied experimentally [47] and by atomistic simulations [48, 49], and it was found that γ decreases with temperature. The experiments of Vermaak and Wilsdorf [47] indicated that the second term in Eq. (4.1) linearly increased with temperature.

Eq. (4.1) can also be applied to solid-liquid interfaces, provided the derivative is taken along a constant-temperature direction on the solid-liquid coexistence surface in the parameter space. It can be expected that τ and γ would be again different, but this has not been tested experimentally. Recent atomistic simulations indicate that τ of solid-liquid interfaces can be positive or negative, depending on the material [50].

The goal of this work is to clarify the behavior of the surface stress and surface free energy with temperature, particularly near the bulk melting point. We employ atomistic computer simulations using a (110) copper surface as a model. For the interpretation of the surface premelting behavior, we have also studied isolated solid-liquid and liquid-vacuum interfaces. Our calculations of the surface and interface properties are based on thermodynamics relations that we derive here in a mathematical form suitable for atomistic calculations.

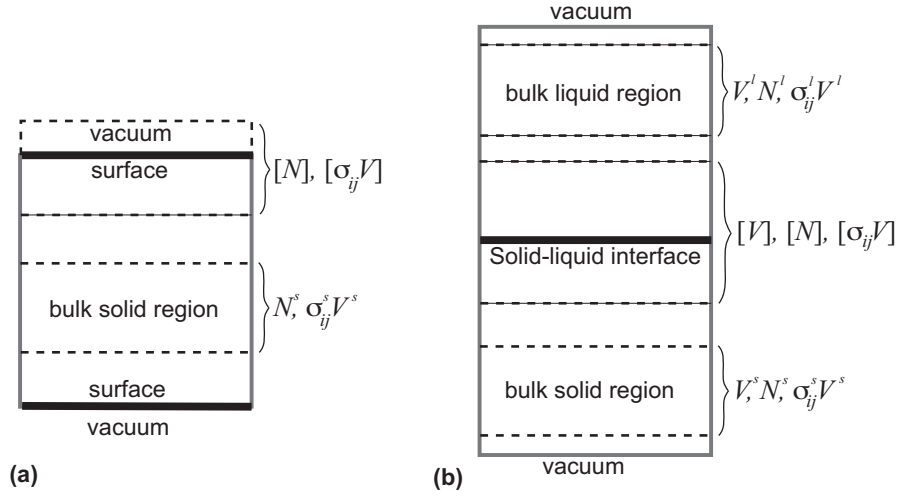


Figure 4.1: Simulation blocks and positions of the interface and bulk regions employed in the calculations of thermodynamic properties of (a) solid surfaces and (b) solid-liquid interfaces. The quantities computed in different regions are indicated. The bracketed quantities refer to the surface/interface layer, whose bounds can be chosen arbitrary as long as they lie within the homogeneous bulk phases. The bulk regions can lie beyond the surface/interface layer, as in this figure, or inside it (not shown).

Such derivations are needed for the following reasons. Taking surface stress as an example, Eq. (4.1) can be rewritten as

$$\tau_{ij} = \frac{\partial(\gamma A)}{A \partial e_{ij}}, \quad i, j = 1, 2, \quad (4.3)$$

where γA is the total excess free energy of a surface whose area A can vary only by elastic straining.

After introducing our methodology (Section 4.3), we perform atomistic simulations of thermodynamics of the (110) Cu surface at temperatures from 0 K to the bulk melting point (Section 4.4). In the same section we compute the stresses of the solid-liquid and liquid-vacuum interfaces. In Section 4.5 we analyze our results and draw conclusions.

4.2 Thermodynamic relations

In this Section we review the relations of surface thermodynamics that will be used in this work. Although we are interested in the surface/interface free energy γ , it is convenient to formulate all equations in terms of the *total* excess free energy of the simulation block, γA , and defer a separation of γ until the end of the calculation. In all thermodynamic processes considered here, A changes by elastic deformation only. Although in the atomistic simulations the solid is almost stress-free, it still contains some residual stresses which are not hydrostatic. To enable corrections for such residual stresses, all equations will be derived for the general case of a non-hydrostatically stressed solid. The cases of a solid surface and a solid-liquid interface will be discussed separately.

4.2.1 Solid surface

Consider an elemental solid in a non-hydrostatic state of strain whose plane surface is exposed to vacuum. A reversible variations of the total excess free energy are given by

$$d(\gamma A) = -[S]_N dT - [N]_N df^s + \sum_{i,j=1,2} [\sigma_{ij}V]_N de_{ij}, \quad (4.4)$$

where the state variables are temperature T , the Helmholtz free energy per atom of the bulk solid f^s , and the elastic strain tensor \hat{e} . Conjugate to these variables are the surface excesses of the entropy S , of the number of atoms N , and of the volume-averaged lateral components of the stress tensor $\boldsymbol{\sigma}$ multiplied by the total volume V . As γA , these excess quantities refer to the *entire* simulation block, not per unit surface area. To satisfy mechanical equilibrium, one of the principal axes of $\boldsymbol{\sigma}$ must be normal to the surface, with $\sigma_{33} = 0$. Following Cahn's method [14], we have expressed the surface excesses through the determinants in

which, for example,

$$[S]_N \equiv \frac{\begin{vmatrix} [S] & [X] \\ S^s & X^s \end{vmatrix}}{X^s} = [S] - S^s[X]/X^s$$

with similar expressions for the excesses of N and $\sigma_{ij}V$. Here X is one of the extensive quantities S , N or $\sigma_{ij}V$, which can be chosen arbitrarily. The square brackets, such as $[S]$ or $[X]$, indicate the amount of the extensive quantity in a thick enough layer containing the surface (Fig. 4.1(a)). One of the bounds of the layer is placed in vacuum and the other in the bulk of the solid, both far enough from the surface to neglect its effect. The superscript s refers to properties of a homogeneous solid region chosen as a comparison system. Since $[X/X] = 0$, one of the terms in Eq. (4.4) is necessarily zero, reflecting the constraint imposed by the bulk equation of state. The remaining terms express $d(\gamma A)$ as a perfect differential and that the surface excesses do not depend on the thickness of the surface layer as long as its bounds are beyond the influence of the surface [14].

Choosing $X = N$, Eq. (4.4) becomes

$$d(\gamma A) = -[S]_N dT + \sum_{i,j=1,2} \tau_{ij} A de_{ij} \quad (4.5)$$

where τ_{ij} the surface stress tensor given by

$$\tau_{ij} = \frac{1}{A} \left(\frac{\partial(\gamma A)}{\partial e_{ij}} \right)_T = \frac{[\sigma_{ij}V]_N}{A} = \frac{\begin{vmatrix} [\sigma_{ij}V] & [N] \\ \sigma_{ij}^s V^s & N^s \end{vmatrix}}{AN^s} = \frac{[\sigma_{ij}V] - \sigma_{ij}^s V^s [N]/N^s}{A} \quad (4.6)$$

Furthermore, with this choice of X , γA itself becomes the excess of the Helmholtz free energy: $\gamma A = [F]_N$. Therefore,

$$\gamma A = [U - TS]_N, \quad (4.7)$$

where

$$[U]_N = [U] - U^s[N]/N^s \quad (4.8)$$

is the total excess of internal energy. Combining Eqs. (4.5) and (4.7), we obtain

$$d\left(\frac{\gamma A}{T}\right) = -\frac{[U]_N}{T^2} dT + \frac{1}{T} \sum_{i,j=1,2} \tau_{ij} A d e_{ij}. \quad (4.9)$$

This equation can be used for computations of γA by thermodynamic integration. For example, consider a process in which temperature is increased while the solid is stretched biaxially to maintain zero bulk stress, $\sigma_{ij}^s = 0$ ($i, j = 1, 2, 3$), at every temperature. In this process, the biaxial strain e increases with temperature to accommodate the thermal expansion of the solid. As a result, T and e are no longer independent variables and Eq. (4.9) becomes

$$d\left(\frac{\gamma A}{T}\right) = -\frac{[U]_N}{T^2} dT + \frac{2\tau A}{T} \left(\frac{\partial e}{\partial T}\right)_{\sigma_{ij}^s=0} dT. \quad (4.10)$$

The second term in the right-hand side includes the linear thermal expansion factor,

$$\alpha = \frac{1}{a} \left(\frac{\partial a}{\partial T}\right)_{\sigma_{ij}^s=0} = \left(\frac{\partial e}{\partial T}\right)_{\sigma_{ij}^s=0}, \quad (4.11)$$

where a is the bulk lattice parameter of the solid at temperature T . Note that α is a function of temperature only, as are $[U]_N$, A and τ . Knowing $(\gamma A)_0$ at some reference temperature T_0 , Eq. (4.10) can be integrated to obtain γA at another temperature T :

$$\gamma A(T) = (\gamma A)_0 \frac{T}{T_0} + T \int_{T_0}^T \left[-\frac{[U]_N}{T'^2} + \frac{2\alpha\tau A}{T'} \right] dT'. \quad (4.12)$$

In atomistic simulations, U^{ex} , τ and α can be computed for a set of temperatures and used to obtain $\gamma A(T)$ by numerical integration of Eq. (4.12). The physical value of γ is then

recovered by dividing γA by the physical area of the surface at the respective temperature. This procedure was implemented in this work as will be discussed later.

4.2.2 Solid-liquid interface

Consider the same non-hydrostatically stressed solid but now in contact and equilibrium with its melt at a pressure p . The mechanical equilibrium condition between the two phases requires that one of the principal axes of the stress tensor in the solid be normal to the interface, with $\sigma_{33} = -p$. The differential of total excess free energy of the solid-liquid interface is given by

$$d(\gamma A) = -[S]_{XY} dT + [V]_{XY} dp - [N]_{XY} d\mu + \sum_{i,j=1,2} [(\sigma_{ij} + \delta_{ij}p)V]_{XY} de_{ij}, \quad (4.13)$$

where μ is the chemical potential in the liquid. Any two of the intensive variables S , V , N or $(\sigma_{ij} + \delta_{ij}p)V$ (denoted by X and Y) can be eliminated, because each phase imposes a constraint expressed by a Gibbs-Duhem equation [14]. The determinant $[Z]_{XY}$ is defined by

$$[Z]_{XY} = \frac{\begin{vmatrix} [Z] & [X] & [Y] \\ Z^s & X^s & Y^s \\ Z^l & X^l & Y^l \end{vmatrix}}{\begin{vmatrix} X^s & Y^s \\ X^l & Y^l \end{vmatrix}}. \quad (4.14)$$

As before, the square brackets designate the extensive property Z of a thick enough layer containing the interface (Fig. 4.1(b)), whereas the superscripts s and l refer to arbitrarily chosen regions of the homogeneous solid and liquid phases.

Choosing N and V for X and Y , Eq. (4.13) reduces to

$$d(\gamma A) = -[S]_N dT + \sum_{ij=1,2} \tau_{ij} A de_{ij} \quad (4.15)$$

with the interface stress tensor given by

$$\tau_{ij} = \frac{[(\sigma_{ij} + \delta_{ij}p)V]_{NV}}{A} = \frac{\begin{vmatrix} [(\sigma_{ij} + \delta_{ij}p)V] & [N] & [V] \\ (\sigma_{ij}^s + \delta_{ij}p)V^s & N^s & V^s \\ 0 & N^l & V^l \end{vmatrix}}{A \begin{vmatrix} N^s & V^s \\ N^l & V^l \end{vmatrix}}. \quad (4.16)$$

Equations (4.6) and (4.16) express the surface and interface stresses τ_{ij} as excesses of the stress tensor $\hat{\sigma}$ in forms convenient for computations. They involve only extensive properties and do not require calculations of interface profiles. For the particular case of a hydrostatic solid or a liquid system, these equations reduce to

$$\tau_{ij} = [\sigma_{ij}V]/A, \quad (\text{plane solid or liquid surface}) \quad (4.17)$$

$$\tau_{ij} = [(\sigma_{ij} + \delta_{ij}p)V]/A \quad (\text{plane solid-liquid interface}) \quad (4.18)$$

Eqs. (4.6) and (4.16) will be used in the atomistic simulations.

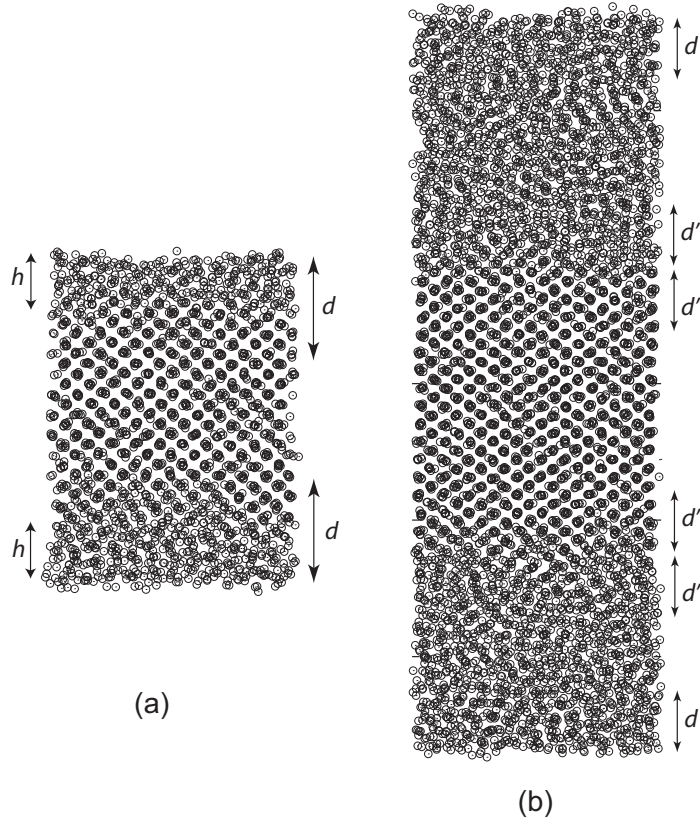


Figure 4.2: Typical MC snapshot of (a) (110) solid film at 1320 K and (b) (110) solid-liquid coexistence system at 1327 K. The open circles mark instantaneous atomic positions projected on the $(\bar{1}\bar{1}0)$ plane parallel to the page. The top and bottom surfaces of both systems are exposed to vacuum. The distances h , d and d' are discussed in the text.

4.3 Methodology of atomistic simulations

4.3.1 Simulated models

We chose copper as a model material. The (110) surface was modeled in a $26 \times 25 \times 41 \text{ \AA}$ (2240 atoms) simulation block with periodic boundaries in the x and y directions and free surfaces in the z -direction, a geometry which mimics an infinitely large thin film (Fig. 4.2(a)). The coordinate axes were aligned parallel to $[\bar{1}\bar{1}0]$, $[001]$ and $[110]$, respectively. To study a liquid surface, the film was completely melted by increasing the temperature above T_m and cooled down to temperatures of interest around T_m .

The (110) solid-liquid interface was modeled in a $26 \times 25 \times 110 \text{ \AA}$ (5600 atoms) block containing a $\sim 40 \text{ \AA}$ thick solid layer sandwiched between two $\sim 35 \text{ \AA}$ thick liquid layers exposed to vacuum (Fig. 4.2(b)). The solid part had the same crystallographic orientation as the previously described solid film, with periodic boundary conditions in x and y . The exposure to vacuum guaranteed zero pressure in the liquid.

Prior to the Monte Carlo (MC) simulations, each block was uniformly expanded by the linear thermal expansion factor at the simulated temperature using the expansion factors computed previously [39]. Although this pre-expansion eliminated most of the thermal stresses in the solid, there were always some non-hydrostatic residual stresses due to statistical errors in the thermal expansion factors.

4.3.2 Monte Carlo simulations

Off-lattice MC simulations [51, 52] were employed to study the surface and interface properties at finite temperatures. At each temperature, the initial configuration was brought to equilibrium by 10^4 - 10^5 MC steps per atom (depending on the system size), followed by a production run of $(2-6) \times 10^5$ additional MC steps. Snapshot files containing instantaneous atomic positions were saved every 20-30 MC steps and used in subsequent calculations of stresses, energies and other properties.

The solid surface calculations were performed at temperatures from 0 to 1320 K, the liquid surface calculations at 1300, 1327 and 1350 K, and the solid-liquid interface calculation at 1327 K only. In the latter case, despite spontaneous random displacements of the interfaces during the simulations, the solid layer thickness remained at least 35 \AA and the thickness of each liquid layers at least 25 \AA . These thicknesses were considered large enough to neglect interactions between the interfaces.

4.3.3 Structural order analysis

To analyze the structural changes in the surface region and to identify the interface positions, we employed the structure factor $S(\mathbf{k})$ whose modulus is given by

$$|S(\mathbf{k})| = \frac{1}{N} \sqrt{\left(\sum_i \cos(\mathbf{k}\mathbf{r}_i)\right)^2 + \left(\sum_i \sin(\mathbf{k}\mathbf{r}_i)\right)^2}, \quad (4.19)$$

where $\mathbf{k} = 2\pi[2\sqrt{2}/a, 0, 0]$ is a chosen reciprocal lattice vector parallel to the x -direction, \mathbf{r}_i is the radius vector of atom i , and the summation goes over the N atoms contained in a region of interest. $|S(\mathbf{k})|$ equals to 1 for perfectly ordered FCC structure at 0 K and 0 for a disordered structure such as liquid. The structure factor was computed for a set of layers parallel to the surface/interface and plotted as a function of distance z normal to the layers.

For the solid surface, positions of (220) atomic planes in the bulk were identified and extrapolated towards the surface, keeping the total number of real and extrapolated planes constant at all temperatures. Each atom was assigned to the nearest plane and $|S(\mathbf{k})|$ was computed by summation over the atoms assigned to each plane. At low temperatures, the $|S(\mathbf{k})|$ values thus obtained refer to actual atomic planes. When the surface becomes disordered at high temperatures, the $|S(\mathbf{k})|$ values in the surface region are formally assigned to imaginary planes, whereas the values in the bulk still refer to the actual atomic planes. The average structure factor, $|S(\mathbf{k})|_{top}$, of the top two surface layers was used as a metric of surface disorder. The thickness h of the surface region was estimated as the distance between the top surface plane and the point at which $|S(\mathbf{k})|(z) \approx (|S(\mathbf{k})|_{top} + |S(\mathbf{k})|_s)/2$, where $|S(\mathbf{k})|_s$ is the value of the structure factor in the bulk solid.

For the block containing two solid-liquid interfaces, $|S(\mathbf{k})|$ was computed for atoms located within 6 \AA thick windows parallel to the interfaces. The profile $|S(\mathbf{k})|(z)$ was calculated by moving the center of the window by small increments in the z direction. The

interface positions were estimated from the relation $|S(\mathbf{k})|(z) \approx |S(\mathbf{k})|_s/2$. The liquid surface positions were identified with the maximum and minimum values of the z -coordinates of all atoms.

The interface positions defined through the structure factor slightly depend on the choice of the \mathbf{k} -vector. There is also some arbitrariness in the positions of the liquid surfaces. We emphasize, however, that we do not assign these definitions of the surface/interface positions any thermodynamic meaning. We use them only as a guide for selecting reasonable bounds of the homogeneous bulk regions as discussed below.

4.3.4 Surface and interface stress calculations

The surface and interface stresses were computed from Eqs. (4.6), (4.17) and (4.16) for each individual snapshot and the results were averaged over all snapshots. Note that those equations contain only products of the stresses times the respective volumes. Thus, the calculation does not require partitioning of the volume between atoms. For the solid and liquid surfaces, the quantities $[\sigma_{ij}V]$ and $[N]$ were computed for the entire simulation block. For the solid surface, the bulk values of $\sigma_{ij}^s V^s$ and N^s were calculated for an inner region of the film, whose bounds were a distance d away from the upper and lower surfaces.

For the solid-liquid interface, $[\sigma_{ij}V]$, $[V]$ and $[N]$ were determined for a layer whose bounds were a distance d away from the upper and lower liquid surfaces and which contained two solid-liquid interfaces. A region inside the solid layer that was separated by a distance d' from each of the solid-liquid interfaces was selected to compute $\sigma_{ij}^s V^s$, V^s and N^s . Similarly, V^l , and N^l were computed for bulk liquid regions chosen a distance d' always from the solid-liquid interfaces and a distance d away from the liquid surfaces.

The distances d and d' were chosen to be large enough to exclude the influence of the surfaces and interfaces on bulk quantities, which was verified by increasing these distances until the computed surface/interface stresses reached constant values within statistical errors of the calculations. Typical values of d and d' were around 9 \AA . Note that these distances

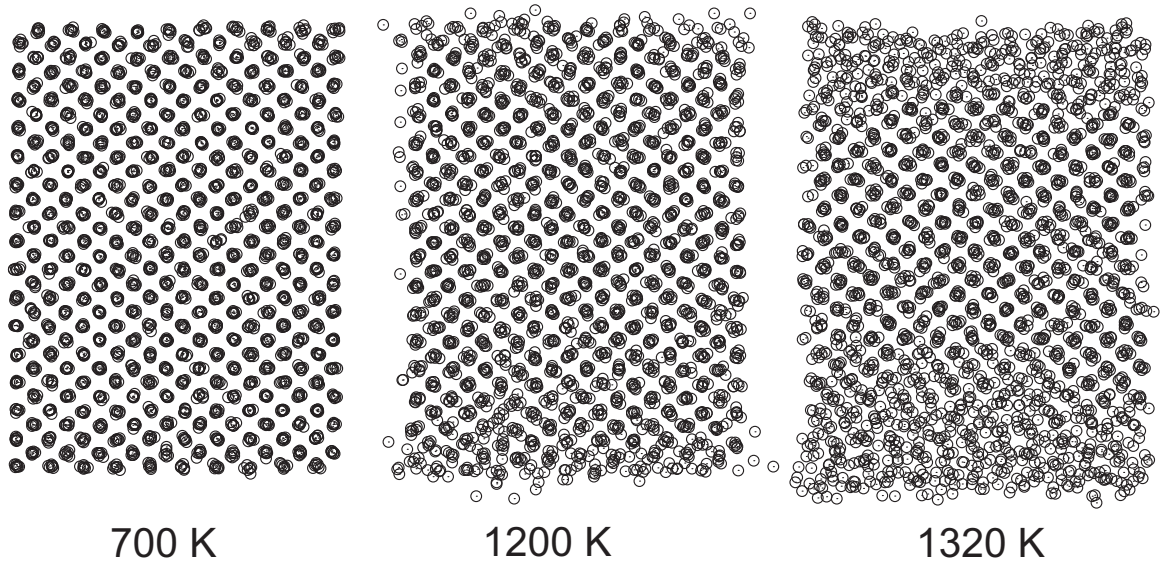


Figure 4.3: Typical MC snapshot of the solid film at three temperatures. The open circles mark instantaneous atomic positions projected on the $(\bar{1}10)$ plane parallel to the page. Note the perfectly ordered surface structure at low temperatures and premelting at high temperatures.

were taken relative to the *instantaneous* positions of the interfaces in each snapshot. Since the interfaces constantly deviated slightly away from their average positions due to thermal fluctuations, the bulk regions selected for the stress calculations varied from one snapshot to another, implementing additional statistical averaging of the bulk properties.

In addition to averaging over the snapshots, the final values of the surface/interface stresses were obtained by averaging over several different choices of d and d' . The error bars of the calculations were estimated by dividing the entire set of 3×10^4 snapshots into 10 subsets and computing the standard deviation of the subset averages from the global average. Clearly, this error bar depends on the number of subsets.

4.3.5 Thermodynamic integration

The free energy γ of the solid surface was computed as a function of temperature by thermodynamic integration based on Eq.(4.12). $[U]_N$ was determined from the MC simulations at

several temperatures using Eq. (4.8). The values of U and N were computed for the entire simulation block and U^s and N^s for the bulk solid region selected as discussed above. The integrand of Eq. (4.12) computed at several temperatures was approximated by a fourth order polynomial and integrated analytically. Increasing the power of the polynomial did not affect the results significantly.

The reference temperature was chosen to be $T_0 = 300$ K. The reference value γ_0 was obtained in the classical quasi-harmonic approximation to atomic vibrations [48]. It was checked that other choices of T_0 within ± 50 K produced only minor changes in the results.

4.4 Results

Examination of the MC snapshots shows that the atomically ordered solid surface becomes increasingly disordered at high temperatures, developing a relatively thick liquid-like layer near T_m (Fig. 4.3). This trend is quantified in Fig. 4.4, showing that the surface thickness h is on the order of the interatomic distance at low temperatures but rapidly increases with temperature at $T > 1100$ K. The thickness appears to diverge to infinity near T_m , but this remains to be verified by future detailed calculations in a very close vicinity of T_m . The surface structure factor $|S(\mathbf{k})|_{top}$ decreases with temperature approximately linearly until about 800 K (Fig. 4.5), which can be attributed to increased amplitudes of atomic vibrations in the otherwise atomically perfect surface structure. At temperatures around 800 K, the atoms of the top surface layer begin to abandon their regular positions and jump on top of the layer, forming adatoms and leaving surface vacancies behind. The amount of this structural disorder rapidly increases with temperature. Accordingly, $|S(\mathbf{k})|_{top}$ decreases more rapidly than below 800 K, producing a breaking point on the curve. As expected, $|S(\mathbf{k})|_{top}$ is small near T_m , reflecting the formation of a liquid-like layer on the surface.

Because the coordinate axes are chosen to be parallel to crystallographic directions with twofold symmetry, the surface stress tensor is diagonal. Its components calculated at 0 K using Eq. (4.6) with $\sigma_{ij}^s = 0$ are $\tau_{11} = 1.19$ J/m² and $\tau_{22} = 1.33$ J/m², showing moderate

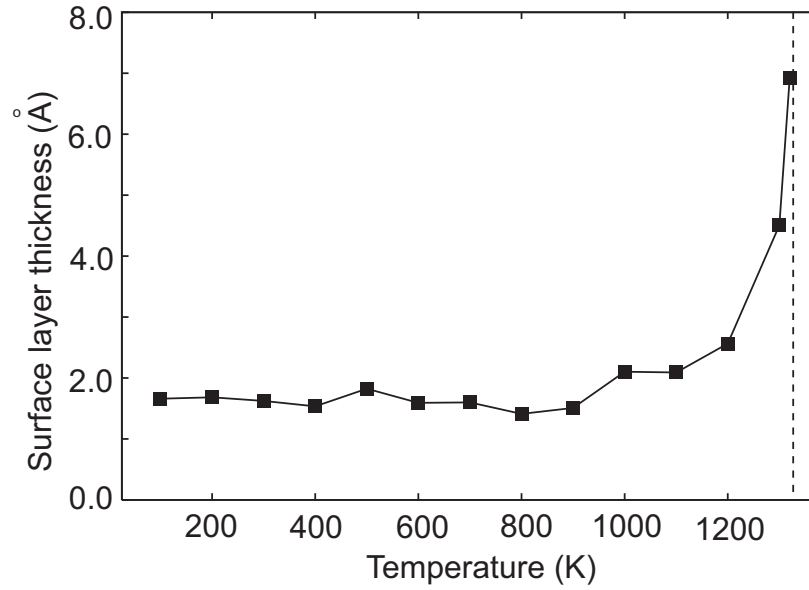


Figure 4.4: Thickness of the (110) surface layer as a function of temperature. The vertical dashed line indicates the bulk melting point.

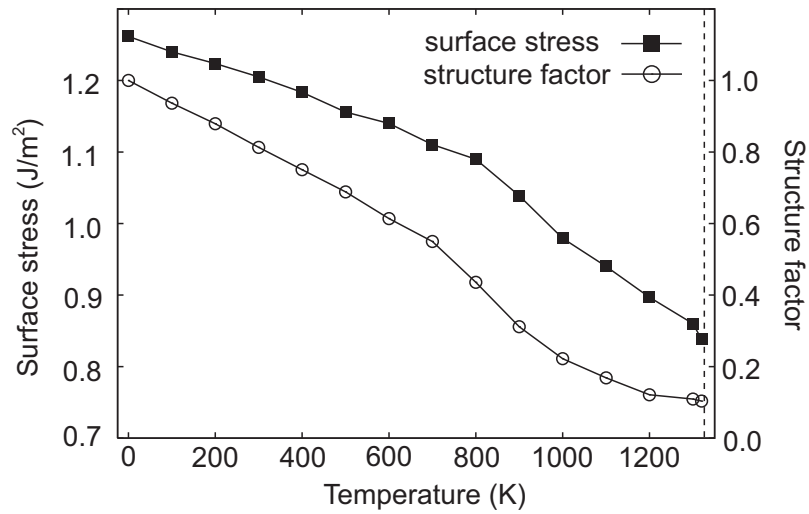


Figure 4.5: Average stress τ and the surface structure factor $|S(\mathbf{k})|_{top}$ of the (110) surface as a function of temperature. The vertical dashed line indicates the bulk melting point.

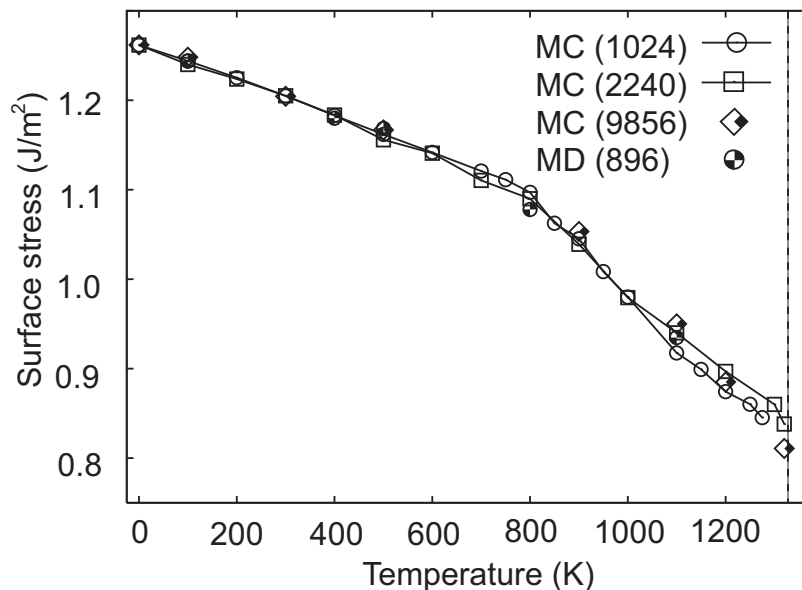


Figure 4.6: Temperature dependence of the average surface stress computed by MC simulations of systems with 1024, 2240 and 9856 atoms, and by molecular dynamics simulations of a 896-atom system. Note that the shape of the curve does not depend on the model size or the simulation method.

anisotropy. Both components are positive and smaller than the 0 K surface energy, $\gamma = 1.472$ J/m². The average surface stress decreases with temperature from $\tau = 1.26$ J/m² at 0 K to 0.83 J/m² at 1320 K (Fig. 4.5). This decrease is almost linear between 0 and about 800 K but accelerates and becomes noticeably nonlinear above 800 K. This behavior is remarkably similar to the temperature dependence of the surface structure factor, demonstrating that τ is a sensitive parameter to the surface disordering at high temperatures.

To verify that this similarity is not a numerical artifact arising from the size effect or the simulation method, additional MC calculations of τ were conducted for two different block sizes. Furthermore, additional calculations were performed for yet another block size using molecular dynamics instead of MC. The results are summarized in Fig. 4.6, showing that all the points lie on a common curve whose shape is very similar to Fig. 4.5.

The anisotropy of the surface stress, $\tau_{22} - \tau_{11}$, increases with temperature as long as the surface remains perfectly ordered (Fig. 4.7), reaches a maximum around 800 K where

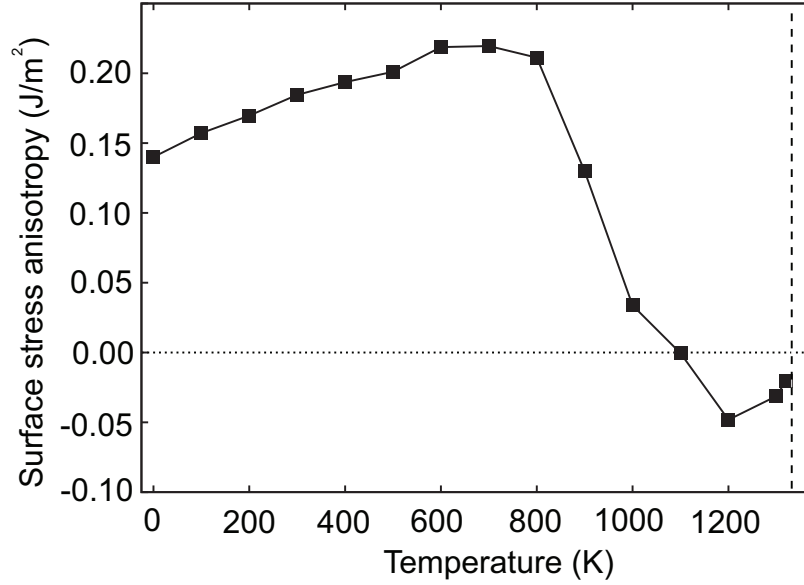


Figure 4.7: Temperature dependence of the surface-stress anisotropy $\tau_{22} - \tau_{11}$. The vertical dashed line indicates the bulk melting point.

the surface disordering starts, and then drops and reaches a slightly negative value near the melting point. This behavior confirms the sensitivity of the surface stress to the structural order at the surface, which is consistent with Fig. 4.5 and 4.6.

The surface free energy decreases with temperature from $\gamma = 1.472 \text{ J/m}^2$ at 0 K to 1.130 J/m^2 at 1320 K (Fig. 4.8), remaining always larger than τ . The onset of surface disordering at 800 K is accompanied by a noticeable change in the slope of $\gamma(T)$, but the curve is much smoother than $\tau(T)$. Note that γ and τ do not have the same value at the melting point. The liquid-vacuum interface stress at T_m is $\tau^l = 0.925 \text{ J/m}^2$, which can be identified with the free energy γ^l of this interface. This value lies between γ and τ for the solid surface.

The solid-liquid interface stress obtained from the solid-liquid coexistence simulations is $\tau^{sl} = -0.131 \text{ J/m}^2$. To give an idea of the error bar, the individual components of the stress are $\tau_{11}^{sl} = -0.129 \pm 0.035 \text{ J/m}^2$ and $\tau_{22}^{sl} = -0.132 \pm 0.033 \text{ J/m}^2$. The negative value of the stress indicates that this interface is in a state of compression. This interface stress would produce a biaxial expansion in a free-standing (110) Cu film immersed in its melt at

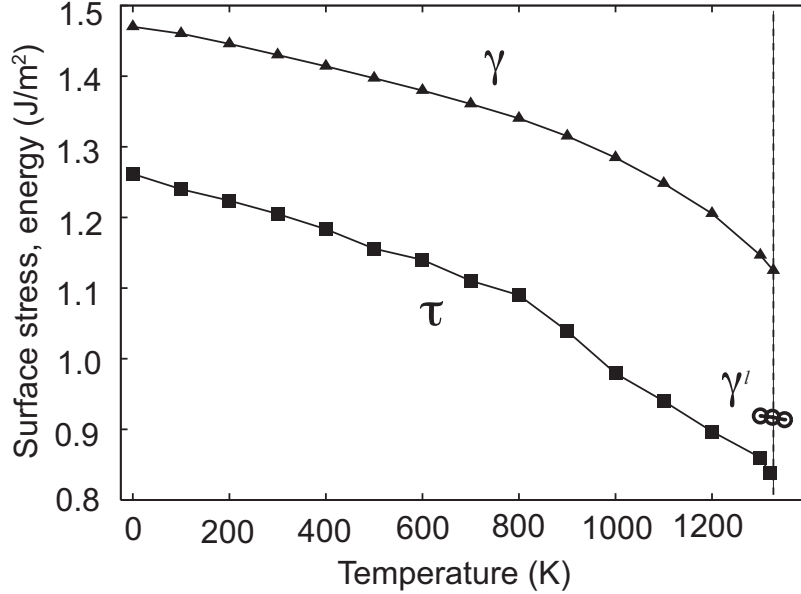


Figure 4.8: Temperature dependence of the excess free energy and stress of the (110) surface. Three values of the free energy, γ^l , of the liquid-vacuum interface are shown for comparison. The vertical dashed line indicates the bulk melting point.

the solid-liquid equilibrium temperature.

Recall that the calculation of τ^{sl} included corrections for the residual stresses within the solid. When such corrections were ignored, the interface stress variations during the MC simulations became much larger, resulting in $\tau_{11}^{sl} = -0.081 \pm 0.177$ J/m² and $\tau_{22}^{sl} = -0.151 \pm 0.175$ J/m². Although the residual stresses were relatively small (on the level of 10 MPa), we see clear indications that taking them into account produces a stabilizing effect and yields more accurate values of the interface stress. The same was found in the surface stress calculations for the solid and liquid films.

Finally, for the interpretation of the results in the next section, we computed the surface stress in the solid film as a function of imposed biaxial strain at 0 K. The strain was increased by small increments from 0 to 0.0252, a range which corresponds to linear thermal expansion factors at temperatures between 0 and 1320 K. The atomic positions were relaxed after each increment of strain. The surface stress was found to decrease as a linear function of strain

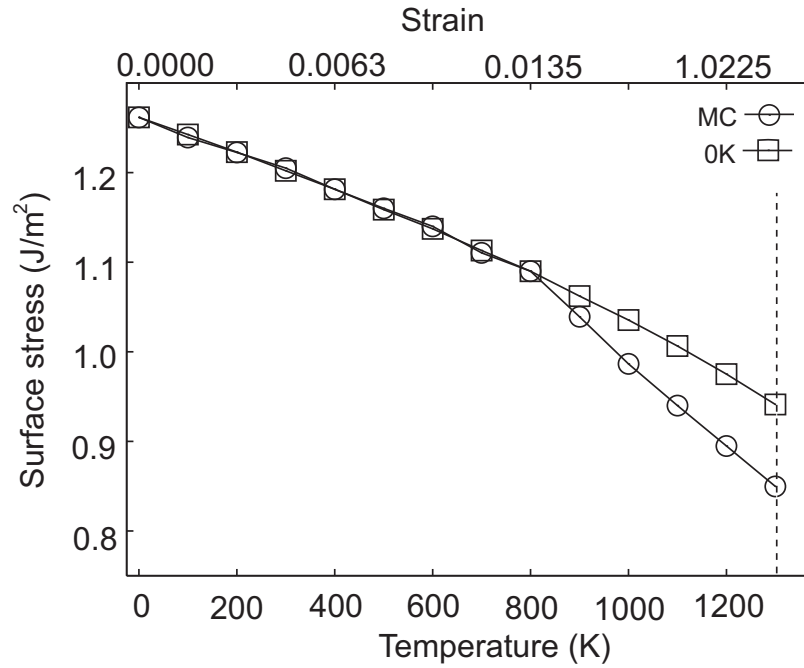


Figure 4.9: Temperature and bulk-strain dependencies of the surface stress obtained by MC simulations and by 0 K static calculations. In the latter case, the data are plotted against the temperature at which thermal expansion would give the corresponding strain. The close agreement below 800 K indicates the dominant role of the bond-stretching effect in the temperature dependence of surface stress of atomically ordered surfaces.

from 1.26 J/m^2 at zero strain to 0.941 J/m^2 at the maximum strain.

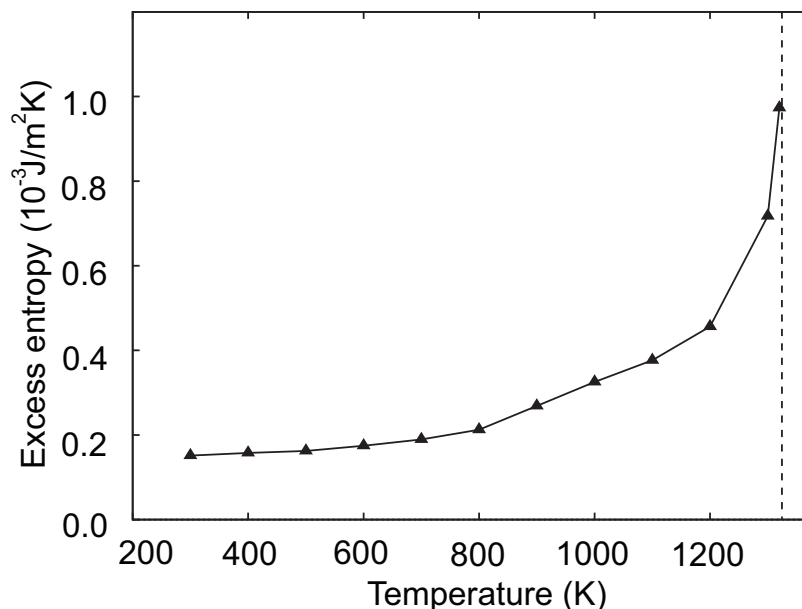


Figure 4.10: Temperature dependence of the excess entropy of the (110) Cu surface. The vertical dashed line indicates the bulk melting point.

4.5 Discussion and conclusions

We have shown how surface and interface stresses and free energies in elemental systems can be computed as appropriate excesses when the solid phase is in a non-hydrostatic state. Instead of constructing profiles of intensive properties and choosing dividing surfaces [13], we applied Cahn’s method [14] to express the excess quantities through determinants containing only extensive properties such as the number of atoms, volume and the total virial stress. All such quantities are immediately accessible by atomistic simulations employing either MC or molecular dynamics methods. Our approach is general enough to permit extensions to multi-component systems, solid-solid interfaces and other complex systems in the future. We applied this method to examine the temperature dependence of the surface free energy and surface stress of (110) copper modeled by an embedded-atom potential. Although thermal expansion was applied to minimize the bulk stress, some residual stress remained and was taken into account in the calculations.

The (110) Cu surface stress was found to decrease with temperature, reaching about 66% of its 0 K value near the bulk melting point. The plot of τ versus temperature (Fig. 4.5) exhibits two distinct parts, which will be discussed separately.

At temperatures from 0 to about 800 K, τ decreases with temperature almost linearly. The surface structure remains perfectly ordered (Fig. 4.3) and the concomitant decrease of the surface structure factor $|S(\mathbf{k})|_{top}$ is due to increasing amplitudes of atomic vibrations. The decrease in τ could be caused by two physical factors: (i) the vibration factor (the amplitudes at the surface and in the bulk both increase with temperature but at different rates, leading to a change in the excess entropy of the surface), and (ii) the expansion factor (the thermal expansion stretches interatomic bonds, altering the state of tension on the surface). To evaluate the role of the second factor, τ computed as a function of biaxial strain at 0 K is plotted against the temperatures at which the respective strains would be produced by thermal expansion (Fig. 4.9). The curve is compared with the actual surface stress as a function of temperature. In effect, the two curves represent the surfaces stresses for the same state of lateral strain in the bulk but at different temperatures. Note that the normal strains in the bulk are different: the thermal expansion in the normal direction is not captured by the 0 K calculations. The curves are in very close agreement up to 800 K but diverge at higher temperatures. This agreement indicates that, as long as the surface structure is perfectly ordered, the decrease of τ with temperature is strongly dominated by the bond-stretching effect produced by thermal expansion. This conclusion emphasizes the importance of including thermal expansion factors in surface-stress calculations at finite temperatures.

At $T > 800$ K, the surface stress decreases with temperature more rapidly than below 800 K due to rapid accumulation of surface disorder. It is due to this structural disordering that the plots of τ and $|S(\mathbf{k})|_{top}$ versus temperature have a distinct breaking point at about 800 K.

The surface free energy decreases with temperature (Fig. 4.8) and is less sensitive to the onset of surface disordering at 800 K. If the strain was kept constant, the slope of γ versus

T would give us the negative of the excess surface entropy. In our simulations, however, the strain was varied with temperature to accommodate the thermal expansion. As a result, our slope includes not only S^{ex} but also the work done against the surface stress, which is expressed by the additional term in Eqs. (4.5) and (4.10). An omission of this term would be thermodynamically incorrect and, for the particular surface studied here, would underestimate its free energy by about 0.1 J/m^2 near the melting point. The excess surface entropy $[S]_N$ can be readily determined from Eq. (4.7) using the obtained values of γA and $[U]_N$. This quantity per unit physical area is plotted as a function of temperature in Fig. 4.10, showing a slow initial growth followed by a rapid acceleration above the surface disordering temperature.

Although the solid surface is covered with a relatively thick (e.g., about 7 \AA at 1320 K) liquid-like film at temperatures approaching T_m , the free energy of the premelted surface remains quite different from the free energy of the liquid-vacuum interface or from the surface stress. This difference can be attributed to the excess quantities associated with the interface between the premelted layer and the bulk solid. As a simple model, the premelted surface can be considered as a layer of real liquid bounded by the solid-liquid and liquid-vacuum interfaces. Neglecting interactions (“disjoining potential”) between these interfaces, the following relations should hold near T_m :

$$\gamma = \gamma^{sl} + \gamma^l, \quad (4.20)$$

$$\tau = \tau^{sl} + \gamma^l. \quad (4.21)$$

In these relations, $\gamma = 1.130 \text{ J/m}^2$, $\gamma^l = 0.925 \pm 0.018 \text{ J/m}^2$ and $\tau = 0.83 \pm 0.012 \text{ J/m}^2$ have been determined by the MC simulations. Solving these equations for γ^{sl} and τ^{sl} , we obtain $\gamma^{sl} = 0.199 \pm 0.018 \text{ J/m}^2$ and $\tau^{sl} = -0.088 \pm 0.018 \text{ J/m}^2$. The solid-liquid interface free energy compares well with the experimental value $\gamma^{sl} = 0.177 \text{ J/m}^2$ from indirect

measurements for an average orientation [53]. Likewise, the solid-liquid interface stress deduced from (4.21) is in adequate agreement with $\tau^{sl} = -0.131 \pm 0.034 \text{ J/m}^2$ obtained by the MC simulations.

This consistency indicates that our interpretation of the premelted surface structure as two interfaces is reasonable. We emphasize, however, that this conclusion was reached for the highly energetic (110) surface orientation, which premelts more readily than low-energy orientations such as (111). In a separate study, we were able to overheat the (111) Cu surface well above T_m without the formation of a liquid layer or even significant disordering. The effect of the surface orientation on premelting behavior will be the subject of a separate publication. It is interesting to note that, in our simulations of the (110) solid-liquid coexistence, we clearly observed spontaneous formation and destruction of small facets with the (111) orientation. Since this faceting increases the actual interface area, we conclude that the (111) orientation has a lower interface free energy than (110).

Finally, the negative sign of τ^{sl} suggests that the (110) solid-liquid interface is in a state of compression, a finding which can have implications for crystal nucleation models. Because this stress is an order of magnitude smaller than typical surface stresses, it is very difficult to measure or compute. Negative values of solid-liquid interface stresses were previously reported for Lennard-Jones [49, 54] and hard sphere [55] systems. It is interesting to note that the hard-sphere simulations gave a larger absolute value of τ^{sl} for the (111) orientation than for (100) [55]. In a more recent simulation [50], negative τ^{sl} values were obtained for a binary Lennard-Jones system but positive for Ni and Si modeled by embedded-atom and Stillinger-Weber potentials, respectively. Further research into anisotropy of interface stresses is needed to determine whether the negative sign of τ^{sl} is a feature of this particular orientation or a general property of copper modeled with this potential.

4.6 Thermodynamic equations

In this section we present derivations of Eqs. (4.4) and (4.13). Consider a rectangular simulation block containing an interface normal to one of its edges z . The block contains a fixed number of atoms N , all of which are of the same chemical species, and is subject to periodic boundary conditions in the x and y directions parallel to the interface. The x - y cross-section of the solid part of the block contains a fixed number of unit cells. We assume that the solid is in a non-hydrostatic state of stress. It is either exposed to vacuum or is in contact and equilibrium with a liquid phase at a pressure p . The temperature T is assumed to be homogeneous throughout.

This system can only receive/release heat and do mechanical work by deformation. In such processes, the differential of the total Helmholtz free energy is

$$dF = -SdT + \sum_{i,j=1,2} \sigma_{ij}Vde_{ij} + \sigma_{33}AdL, \quad (4.22)$$

where L is the system size in z and σ_{ij} are the volume-averaged stress components on the lateral faces of the block. The following mechanical equilibrium conditions are assumed to be satisfied everywhere inside the solid: (1) $\sigma_{33} = -p$ for the solid-liquid interface and $\sigma_{33} = 0$ for the solid surface, and (2) $\sigma_{3i} = 0$, $i = 1, 2$. According to Gibbs' definition of γ as a work term [13], this quantity can be expressed as the free energy cost of creating a unit area of new surface/interface in a closed system at a constant T without doing any other work.

For a solid surface, γA can be found as the free energy excess over a bulk solid at a constant number of atoms:

$$\gamma A = F - f^s N \equiv [F]_X, \quad (4.23)$$

where f^s is the free energy per atom of the homogeneous solid phase. Taking a differential

of Eq. (4.23) at constant N and combining it with dF from Eq. (4.22),

$$d(\gamma A) = -SdT - Ndf^s + \sum_{i,j=1,2} \sigma_{ij} V de_{ij}. \quad (4.24)$$

Applying the same procedure to Eq. (4.23) with $\gamma A = 0$, we obtain the Gibbs-Duhem equation for the bulk solid:

$$0 = -S^s dT - N^s df^s + \sum_{i,j=1,2} \sigma_{ij}^s V^s de_{ij}. \quad (4.25)$$

The system of two equations, (4.24) and (4.25), can be solved for $d(\gamma A)$ using Cramer's rule [14],

$$d(\gamma A) = -[S]_X dT - [N]_X df^s + \sum_{i,j=1,2} [\sigma_{ij} V]_X de_{ij}, \quad (4.26)$$

which is identical to Eq. (4.4) of the main text. Depending on the choice of X , one of the terms in Eq. (4.26) vanishes and the corresponding variable becomes a function of the remaining independent variables.

For the solid-liquid interface, since the interface creation can be accompanied by a volume effect, the corresponding mechanical work (if $p \neq 0$) must be eliminated by identifying γA with the excess of F at constant N and V :

$$\gamma A = [F]_{XY} = \frac{\begin{vmatrix} F & N & V \\ F^s & N^s & V^s \\ F^l & N^l & V^l \end{vmatrix}}{\begin{vmatrix} N^s & V^s \\ N^l & V^l \end{vmatrix}}. \quad (4.27)$$

The free energies of the bulk phases are given by

$$F^l = -pV^l + N^l\mu, \quad (4.28)$$

$$F^s = -pV^s + N^s\mu, \quad (4.29)$$

where μ is the chemical potential in the liquid. (Note that these equations include only the liquid chemical potential, see Gibbs' discussion of the non-uniqueness of chemical potential of non-hydrostatic solids.) Eq. (4.29) expresses the solid-liquid equilibrium condition derived by Gibbs. Substituting Eqs. (4.28) and (4.29) in Eq. (4.27), it is straightforward to obtain

$$\gamma A = F - \mu N + pV. \quad (4.30)$$

Taking a differential of (4.30) at constant N and using Eq. (4.22) in conjunction with $dV = V \sum_{i,j=1,2} \delta_{ij} de_{ij} + AdL$, we arrive at

$$d(\gamma A) = -SdT + Vdp - Nd\mu + \sum_{i,j=1,2} (\sigma_{ij} + \delta_{ij}p)V de_{ij}. \quad (4.31)$$

This equation should be considered simultaneously with the Gibbs-Duhem equations for the bulk phases, which are easily obtained from (4.31) by setting $\gamma A \equiv 0$:

$$0 = -S^s dT + V^s dp - N^s d\mu + \sum_{i,j=1,2} (\sigma_{ij}^s + \delta_{ij}p)V^s de_{ij}, \quad (4.32)$$

$$0 = -S^l dT + V^l dp - N^l d\mu. \quad (4.33)$$

Using these bulk equations, any two terms in Eq. (4.31) can be eliminated by applying

Cramer's rule [14]:

$$d(\gamma A) = -[S]_{XY} dT + [V]_{XY} dp - [N]_{XY} d\mu + \sum_{i,j=1,2} [(\sigma_{ij} + \delta_{ij}p)V]_{XY} de_{ij}, \quad (4.34)$$

where the notation $[Z/XY]$ is explained by Eq. (4.14).

The above equations include the extensive quantities S , V , N and $\sigma_{ij}V$ related to the entire simulation block. However, their excesses do not change if, instead of the entire block, we use a more narrow layer containing the surface/interface. As long as the bounds of the layer are beyond the influence of the surface/interface, the addition of new bulk regions results only in adding multiples of the second and/or third rows of the determinants to the first one, which does not change the value of the determinant [14]. Designating the layer properties by square brackets, Eqs. (4.26) and (4.34) become completely equivalent to Eqs. (4.4) and (4.13) appearing in the main text.

Chapter 5: Orientation dependence of the solid-liquid interface stress: atomistic calculations for copper.

5.1 Introduction

Solid-liquid interfaces have been extensively studied by computer simulations, see e.g. [56] for a recent review. If the solid is perfectly hydrostatic, the average interface stress τ can be computed by [57]

$$\tau \equiv \frac{1}{2}Tr(\hat{\tau}) = \int_0^{L_z} [P_{\perp}(z) - P_{\parallel}(z)]dz, \quad (5.1)$$

where P_{\perp} and P_{\parallel} are the negatives of the stress components normal and parallel to the interface, z is the distance normal to the interface, and L_z is the system size in the z -direction. Using this hydrostatic approximation, τ was computed for several model systems. Negative values of τ were reported for Lennard-Jones (LJ) [49, 54, 57, 58] and hard-sphere [55] solid-liquid systems for several interface orientations. On the other hand, τ was found positive for systems described by the Stillinger-Weber and embedded-atom method (EAM) potentials [57]. It was suggested [57] that the different signs of the interface stress could be explained by the atomic density differences between the solid and liquid phases in the simulated systems.

After the equilibration of an initially hydrostatic simulation block, its solid part is often found in a non-hydrostatic state of stress [57, 59]. Although the deviations from hydrostaticity can be small, Eq. (5.1) is strictly speaking not valid for such cases. Because the values of P_{\parallel} in the two bulk phases are different, the interface stress computed from Eq. (5.1) may depend on the sizes of the solid and liquid portions of the block. Using the full

non-hydrostatic formulation of the interface stress proposed in in previous chapters, more accurate and stable values of $\boldsymbol{\tau}$ can be obtained. This approach was tested by computing the principal components of $\boldsymbol{\tau}$ for the (110) Cu solid-liquid interface with atomic interactions described by an EAM potential. Both principal components of $\boldsymbol{\tau}$ were found to be negative, suggesting that this particular interface is in a state of compression.

In this chapter we investigate the orientation dependence of the interface stress by systematic calculations of $\boldsymbol{\tau}$ for the (100), (110), (111) and (310) orientations of the solid-liquid interface in Cu. Our goal is to evaluate the possible range of the orientation dependence of $\boldsymbol{\tau}$ in real metals using an accurate model of atomic interactions, and to determine if its sign can be changed by varying the interface orientation for the same material. Using our methodology described in Sec. 5.2 and 5.3, we compute the interface stress tensor for these orientations and present our results in Sec. 5.4.

5.2 The interface stress as an excess quantity

The interface stress tensor $\boldsymbol{\tau}$ is defined through a partial derivative of the total interface free energy γA with respect to lateral components of the strain tensor e_{ij} [60,61]:

$$\tau_{ij} = \frac{1}{A} \frac{\partial(\gamma A)}{\partial e_{ij}} = \frac{\begin{vmatrix} (\sigma_{ij} + \delta_{ij}P)V & N & V \\ (\sigma_{ij}^s + \delta_{ij}P)V^s & N^s & V^s \\ 0 & N^l & V^l \end{vmatrix}}{A \begin{vmatrix} N^s & V^s \\ N^l & V^l \end{vmatrix}}. \quad (5.2)$$

Here, indices $i, j = 1, 2$ are Cartesian coordinates parallel to the interface, δ_{ij} is the Kronecker symbol, A is the interface area, σ_{ij} is the stress averaged over a layer containing the solid-liquid interface, σ_{ij}^s is the bulk stress tensor in the solid, P is pressure in the liquid, N and V are the numbers of atoms and volumes of the layer and of homogeneous solid

(superscript s) and liquid (superscript l) regions, respectively. The thickness of the layer is chosen so that its boundaries are inside the bulk phases and are not affected by the interface. Likewise, the homogeneous solid and liquid regions are chosen inside the bulk phases and are assumed to be homogeneous and unperturbed by the interface. Such region may be chosen either inside or outside the layer containing the interface.

In the particular case when the solid phase is hydrostatic, $\sigma_{ij}^s + \delta_{ij}P = 0$ and Eq. (5.2) gives

$$\tau_{ij} = (\sigma_{ij} + \delta_{ij}P) / A. \quad (5.3)$$

This equation shows that, although the bulk phases are hydrostatic, the interface stress is generally anisotropic. This equation is more general than Eq. (5.1) as it permits calculations of individual components τ_{ij} . Taking a half of the trace of Eq. (5.3), the average interface stress τ reduces to Eq. (5.1) with $P_{\perp} \equiv P$ and $P_{\parallel} \equiv -(\sigma_{11} + \sigma_{22}) / 2$. In this work, however, the interface stress tensor was computed from the most general equation (5.2).

5.3 Methodology of atomistic simulations

5.3.1 Simulated models

Four simulation blocks with the (100), (110), (111) and (310) oriented plane copper solid-liquid interfaces were created, each containing a ~ 100 Å thick layer of the solid phase sandwiched between two ~ 100 Å thick layers of liquid. The dimensions and the total numbers of atoms in the simulation blocks are listed in Table 5.1. Periodic boundary conditions were imposed in the x and y directions parallel to the interface, with open surfaces in the z direction. The open surfaces of the liquid portions of the block ensured zero pressure in the liquid phase.

Prior to the molecular dynamics (MD) simulations, the block was pre-expanded by the thermal expansion factor at the simulated temperature in order to minimize the bulk stresses

Table 5.1: Dimensions of the simulation block (in Å) and the total number of atoms N used in this work for different orientations of the solid-liquid interface. The interface plane is normal to the z direction.

Interface orientation	L_x	L_y	L_z	N
(100)	59.3	59.3	290	76800
(110)	62.9	59.3	325	92160
(111)	62.9	54.5	300	77760
(310)	51.9	70.4	340	94080

in the solid. In spite of this pre-expansion, the solid was still under some residual non-hydrostatic stresses arising from the statistical errors of the thermal expansion coefficient and other factors.

5.3.2 MD simulations

The prepared blocks were used as initial configurations for the MD simulations, which were performed in the NVE (microcanonical) ensemble. The solid-liquid coexistence could also be modeled in the NVT (canonical) ensemble. However, NVT simulations require the knowledge of the *exact* melting temperature T_m in order to prevent a drift of the interface towards one of the phases. Even in this ideal case, the thermodynamic equilibrium is *neutral* and the interface can freely wander inside the simulation block by a random walk caused by thermal fluctuations. Over a long simulation time, this walk can result in a significant displacement of the interface in a randomly chosen direction. In some cases, the system can even completely melt or completely crystallize.

By contrast, in NVE simulations the total energy of the system is conserved and the solid-liquid coexistence is *stable*, preventing the interface from large displacements [62]. To understand why, consider a fluctuation away from the NVE equilibrium accompanied by melting of a small portion of the solid phase. The latent heat required for the melting will come from the kinetic energy of the atoms since the system is adiabatic. This will cause a decrease of temperature, which will stabilize the solid phase relative to the liquid and prevent the solid from further melting. Similarly, a spontaneous crystallization releases some

amount of heat and increases the temperature, stabilizing the liquid against the solid. As a result, once the system has reached equilibrium, the interface can only implement limited displacements around its average position, accompanied by small temperature fluctuations around the melting point. This stability permits very long simulation runs without changing the average amounts of the phases.

In our simulations, the initial configuration was equilibrated by a 2 ns *NVE* run. To verify that the system has been equilibrated, the probability distribution of potential energy was computed and found to be Gaussian. The equilibration was followed by a 30 ns long production run. During this run, snapshots containing atomic positions and stresses on individual atoms were saved every 2 ps and used during post-processing. This interval is on the time scale of noticeable structural changes in the system. The stresses were computed using the standard virial expression. In addition, we monitored the interface position to verify that there was no significant change of the thickness of the solid portion of the block during the production run. The equilibrium temperature was found to be very close to 1327 K.

5.3.3 Interface positions and profiles

For each interface orientation, profiles of the number density of atoms and the stress components across the interface were computed at the post-processing stage. Although such profiles were not used directly for the interface stress calculations, it was instructive to examine their shapes and compare them for different interface orientations.

To create a profile, the simulation block was divided into a set of bins of equal width. To obtain profiles independent of the binning process [55], each atom was represented by a Gaussian instead of a single point. Accordingly, all properties such as density and stress were distributed over an interval of finite length (perpendicular to the interface) and weighted according to the Gaussian distribution. The property of interest was then averaged within each bin and plotted as a function of z . The Gaussian width of the atoms was adjusted to produce smooth profiles while preserving their detailed shapes in the interface region. The

size of the bins reported in this work was 0.3 Å.

Although the average amounts of the solid and liquid phases were preserved during the MD simulations, the interface could slightly migrate around its average position by simultaneous crystallization of material on one side and melting on the other. The interface movements led to an additional smearing of the profiles. To eliminate this extra smearing, the profiles computed for individual snapshots were centered relative to the instantaneous interface position and then averaged. The interface positions in individual snapshots were identified using the profile of the structure factor $|S(\mathbf{k})|$, where \mathbf{k} is a reciprocal lattice vector chosen differently for each interface orientation. Its magnitude is inversely proportional to the crystal periodicity in the respective direction. Although the interface positions defined through the structure factor may slightly depend on the choice of the \mathbf{k} -vector, the final profile shape is not affected significantly. To compare the profiles computed for different interface orientations, their positions were centered at the Gibbsian dividing surface, which was found from the density profiles.

5.3.4 Interface excesses calculations

The interface stress was calculated directly from Eq. (5.2). The quantities appearing in the determinants in Eq. (5.2) were computed for individual snapshots using homogeneous bulk regions and layers containing the interfaces. The obtained quantities were then averaged over all snapshots before inserting them in the determinants.

To select the appropriate regions in a given snapshot, we first computed approximate positions of the solid-liquid interfaces and of the liquid surfaces. The positions of the solid-liquid interfaces were determined using the profile of $|S(\mathbf{k})|(z)$ [60,61]. The positions of the liquid surfaces were identified with the maximum and minimum values of the z -coordinates of all atoms. Fig. 5.1 illustrates how the regions were selected. The solid part of the block separated from the solid-liquid interfaces by a distance d was chosen as a bulk solid region. Two liquid regions separated from the solid-liquid interfaces and from the liquid surfaces by a distance d were identified as bulk liquid. The interface layer included two solid-liquid

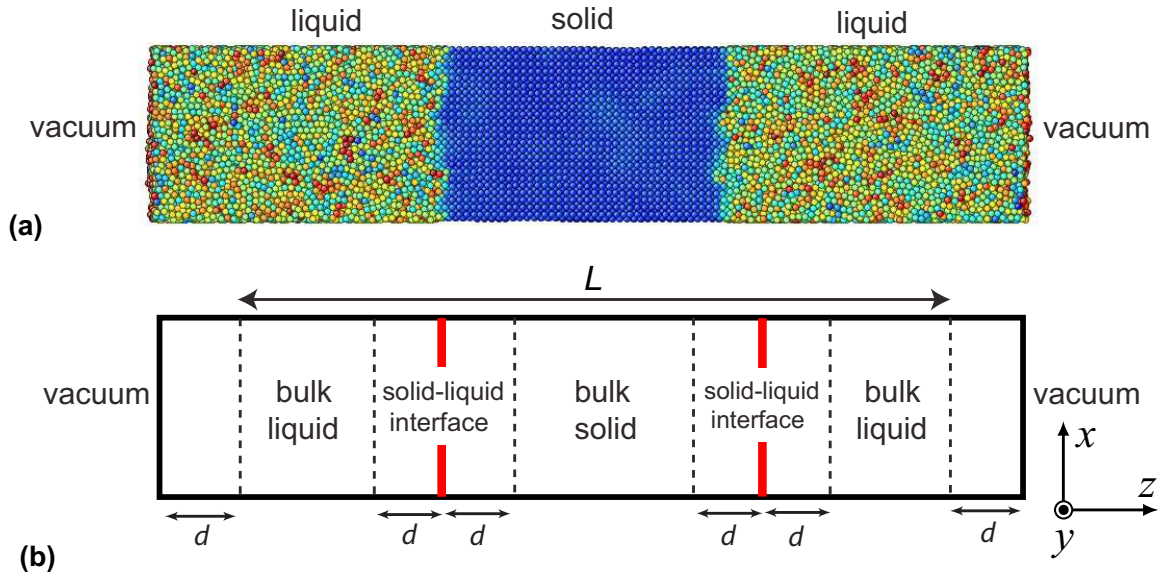


Figure 5.1: a) A typical snapshot of the simulation block containing two solid-liquid interfaces with the (110) orientation. The liquid regions are exposed to vacuum. b) Schematic presentation of the simulation block showing the regions used for the interface stress calculations.

interfaces and its boundaries were located a distance d away from the liquid surfaces. This layer is designated by L in Fig. 5.1. The distance d is chosen to be large enough to exclude any effect of the surfaces and interfaces on bulk properties while keeping the bulk regions as large as possible for better statistics. In this work we used $d = 20 \text{ \AA}$. When computing the quantities appearing in the determinants, the atoms of the chosen regions were represented by the same Gaussian as in profiles calculations (Sec. 5.3.3). The error bars were estimated by dividing the snapshots into several groups and computing the standard deviation of the group-averaged values from the global average.

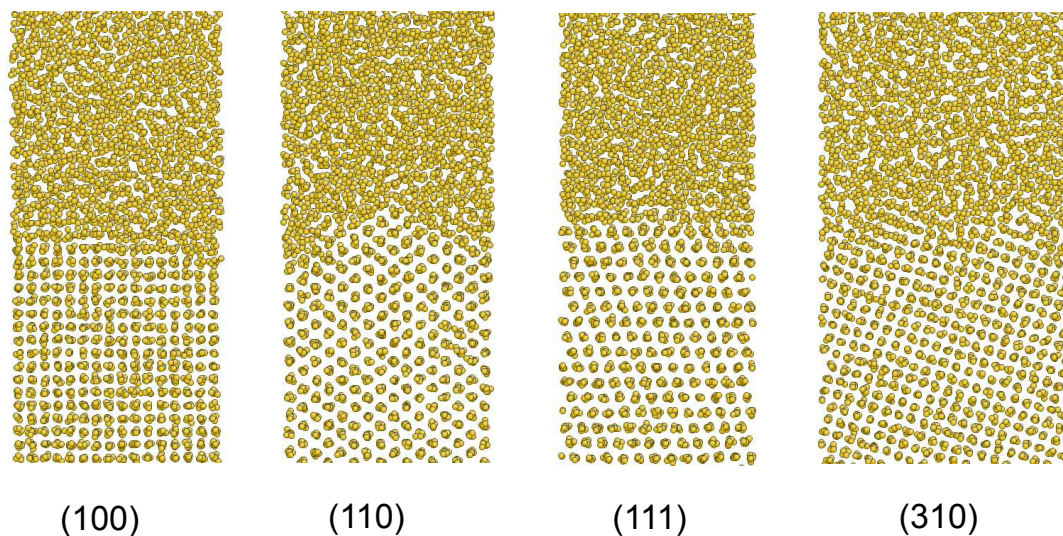


Figure 5.2: Typical snapshots of the simulated solid-liquid interfaces with different orientations. For clarity, only a part of the simulation block is shown in each case. Note the (111) facets formed by the (110) interface.

5.4 Results and discussion

Figure 5.2 illustrates the atomic structure of the interfaces with different orientations studied in this work. The crystallographic direction normal to the page is $[001]$ for the (100) and (310) interfaces and $[\bar{1}10]$ for the (110) and (111) interfaces. Note that the (110) interface tends to form facets with the (111) orientation. Such facets are dynamic, in that they constantly form and disappear in the course of the simulations. It is also apparent that the (100) and (111) interfaces are sharper than the (110) and (310) interfaces.

Figure 5.3 shows the density profile computed for the (110) interface. The interface thickness estimated from this profile is a few angstroms, which is consistent with its atomic structure. The density profiles computed for other interface orientations look very similar and are not shown here.

The profiles of the lateral components of the stress tensor across the interfaces are presented in Fig. 5.4. By crystal symmetry, the principal directions of the stress tensor are parallel to the coordinate axes. Thus, σ_{11} and σ_{22} shown in these plots are two principal

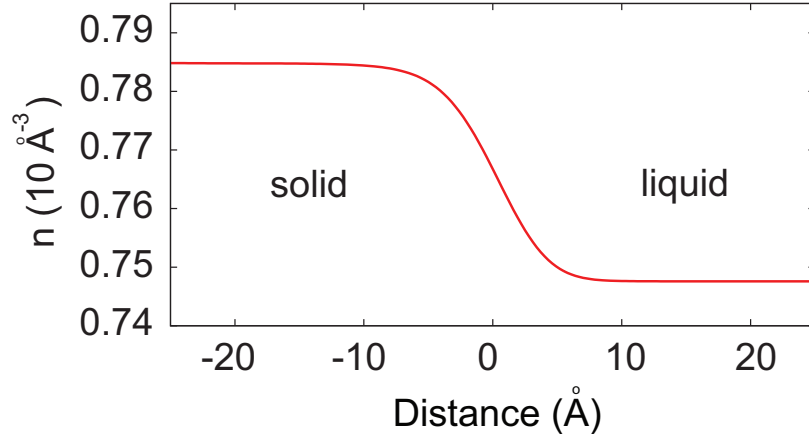


Figure 5.3: The number density of atoms (n , in \AA^{-3}) as a function of distance from the solid-liquid interface with the (110) orientation.

values of σ_{ij} (the third principal value being $\sigma_{33} = -P = 0$). Furthermore, due to the fourfold and threefold symmetries of the (100) and (111) interfaces, the stress tensor must be isotropic in these cases. Our calculations confirm that the profiles of σ_{11} and σ_{22} for these interfaces are indeed identical within statistical errors; accordingly, we plot only the average of σ_{11} and σ_{22} . For the (110) and (310) interfaces, both stress components are shown and are seen to be different as expected.

Fig. 5.4 reveals that for the (100) and (310) interfaces, a narrow solid region adjacent to the interface is under lateral compression (negative stress) whereas the opposing liquid region is under lateral tension (positive stress). The same is true for σ_{11} (parallel to [100]) in the (110) interface, but in this case σ_{22} (parallel to $[1\bar{1}0]$) remains compressive in the entire interface region. For the (111) orientation, most of the interface region is under lateral compression in all directions. For all orientations, the stress becomes very small away from the interface region, but it is different from zero; it is too small to be seen clearly on the scale of Fig. 5.4.

For the (100), (110) and (111) interfaces, the shapes of the computed stress profiles are similar to those observed in the previous hard-sphere [55] and LJ [58] calculations. This may reflect structural similarities between the interfaces modeled with different atomic

Table 5.2: Interface stress components (τ_{11} and τ_{22}) and their average (τ) in J/m² for different orientations of the solid-liquid interface in copper.

Interface orientation	τ_{11}	τ_{22}	τ
(100)	0.081 ± 0.003	0.081 ± 0.003	0.081 ± 0.003
(110)	-0.105 ± 0.004	-0.110 ± 0.002	-0.107 ± 0.004
(111)	-0.103 ± 0.004	-0.103 ± 0.004	-0.103 ± 0.004
(310)	0.038 ± 0.003	0.062 ± 0.002	0.050 ± 0.003

interaction models.

Table 5.2 summarizes the computed interface stresses for each orientation. The interface stresses of the (100) and (310) orientations are positive, i.e. these interfaces are under tension. The stress profiles of these interfaces (Fig. 5.4) suggest that the positive sign of their τ_{11} and τ_{22} originates primarily from the tensile state of the narrow liquid layer adjacent to the interface. Likewise, for the (110) and (111) orientations the negative sign of the interface stresses can be associated with the compressive state of the narrow solid layer next to the interface (Fig. 5.4). In other words, it appears that the sign of the interface stress is decided by competition between two trends in the stress behavior within the interface region: the liquid layer “wants” to shrink while the solid layer “wants” to expand. If the first trend is stronger than the second, the interface stress is positive; otherwise it is negative.

For the (100) and (111) orientations, the computed τ_{11} and τ_{22} are identical as expected from crystal symmetry. The (110) interface shows only a slight anisotropy in agreement with our previous calculations [60]. (In [60], this interface was modeled using a Monte Carlo method and a much smaller simulation block.) The (310) interface has the smallest magnitude of the interface stress and the largest anisotropy.

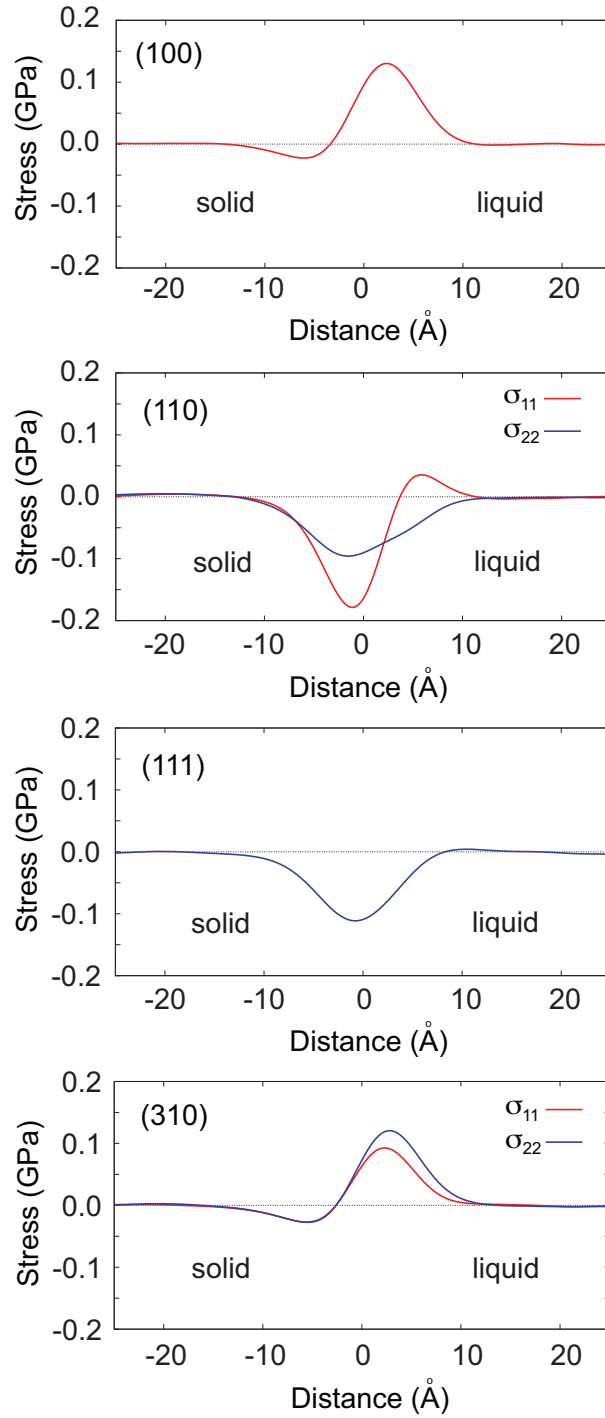


Figure 5.4: Computed profiles of the lateral stresses across solid-liquid interfaces with different orientations. For the (100) and (111) orientations, only the average of the two stress components is shown.

5.5 Discussion

We computed the interface stress tensor for four different orientations of the solid-liquid interface in EAM Cu. Our methodology of stress calculations is applicable to solids in a non-hydrostatic state of stress and does not require the construction of accurate profiles of stresses or any other properties across the interface region. All calculations are made in terms of *extensive* properties, such as the number of atoms, volume and integrated stress for selected regions. These extensive properties serve as input to the determinants defined by Eq. (5.2). We find, however, that accurate profiles can be very useful as a guide during the selection of the homogeneous phase regions and at other steps of the data processing. Furthermore, they can be very helpful for understanding the interface structure and the origin of the interface stress. Although the bulk stresses implemented in this work were small, making appropriate corrections for such stresses was important as it leads to more accurate and stable values of the interface stresses [60, 61].

We have shown that the average interface stress τ can be positive or negative for the same material, depending on the interface orientation (Table 5.2). A change of sign with orientation was also observed in previous studies. For example, τ was computed for the (100), (110) and (111) interfaces in a LJ system [58]. For the (110) and (111) orientations, the stress was found to be negative in agreement with our calculations. For these two orientations, negative interface stresses were also reported in hard-sphere simulations [55]. For the (100) interface, however, the situation is more complex. In [58], the interface stress was found to be negative at the critical point but increased with temperature and became positive at higher temperatures. The positive sign of τ for this interface is consistent with our calculations performed at a temperature which is much higher than the critical point. A positive τ for the (100) interface was also found in recent EAM Ni simulations [57]. But the same paper reported a negative value of τ for the same interface in a LJ system [57]. Thus, while the negative signs of the (110) and (111) interface stresses were reproduced in several studies using different atomic interaction models, the results for the (100) orientation are

less robust. The reason is not apparent and requires further investigations.

Our calculations also demonstrate that the solid-liquid interface stress can be anisotropic, unless its isotropy is prescribed by crystal symmetry. In fact, we find that the (310) interface displays a very significant anisotropy, even though the magnitude of the stress is relatively small.

The fact that the interface orientation can reverse the sign of τ for the same material suggests that the explanations of the sign of τ based on just the solid and liquid densities and/or the type of interatomic bonding (e.g., pairwise versus many-body, with or without angular forces) [57] may need further refinement. An interesting trend revealed by the stress profiles (Fig. 5.4) is that the interface region contains adjacent liquid and solid layers that are under lateral tension and compression, respectively. The sign of τ is ultimately decided by balance between the tensile and compressive contributions, whose magnitudes vary with the interface orientation. For example, the relatively small magnitude of the (310) interface stress is the result of near cancellation of the tensile and compressive stresses in the interface region, although the magnitudes of these stresses are as large as for all other interface orientations (Fig. 5.4). A predictive model should include a link between the lateral stresses developed in the solid and liquid layers and the crystallography of the solid surface abutting the liquid.

Chapter 6: Solid-liquid interface free energy in binary systems: theory and atomistic calculations for the (110) Cu-Ag interface

6.1 Introduction

Discussing solid-liquid interfaces, Gibbs treated the solid as a single-component substance and placed the dividing surface so that the interface excess of this component would vanish. This resulted in an adsorption equation that did not contain a term with the chemical potential of the solid component. As was recently pointed out [20], this procedure cannot be easily extended to binary or multicomponent solids. Indeed, no choice of the dividing surface can guarantee that the excesses of all solid components would vanish simultaneously.

The complication with a proper definition of γ for multicomponent systems arises from two sources. One is that the state of stress of a solid can be non-hydrostatic. As was shown by Gibbs, a non-hydrostatically stressed solid can be equilibrated with three liquids having different chemical potentials of the components forming the solid. This means that chemical potentials of such components inside the solid are *undefined*. This was exactly the reason why Gibbs chose to eliminate the interface excess of the solid component. Secondly, the Gibbsian construction of the dividing surface is just one possible way of introducing excess quantities. Cahn [14] proposed a more general formulation of the adsorption equation, in which the differential coefficients are defined without using the concept of a dividing surface. Instead, they are expressed via certain determinants composed of extensive properties of the system as will be discussed below. Taking volume as one of such properties is equivalent to introducing a dividing surface, but this is only one particular case in Cahn's formulation [14].

Cahn’s [14] adsorption equation was derived for interfaces between fluids and hydrostatically stressed solids. In a subsequent paper [63], Cahn analyzed the effect of the interface free energy and interface stress on equilibrium between a spherical solid particle and a fluid, but again for a hydrostatic solid. On the other hand, solid-liquid coexistence in multicomponent non-hydrostatic systems was extensively analyzed by Larche and Cahn [18,23]. They showed that under equilibrium conditions, the chemical potentials of all interstitial components in the solid exist and are equal to their chemical potentials in the liquid. For substitutional components, Larche and Cahn [18, 23] introduced another quantity $M_{\alpha\beta}$, which they called a “diffusion potential” and whose definition will be given below (Section 6.2). They showed that at equilibrium, $M_{\alpha\beta}$ is constant everywhere in the system and is equal to the difference between the chemical potentials of components α and β in the liquid. Note, however, Larche and Cahn [18,23] analyzed only equilibrium between bulk phases and did not address interface thermodynamics.

We use the Larche-Cahn [18, 23] equilibrium conditions as the starting point in order to express the interface free energy γ and interface stress as excesses of appropriate thermodynamic potentials. We also derive a generalized adsorption equation and a Gibbs-Helmholtz-type differential equation that can be conveniently applied for thermodynamic integration in atomistic computer simulations.

As a demonstration of utility of our analysis, we apply it to atomistic simulations of a binary solid-liquid coexistence system. In recent years, thermodynamic properties of interfaces have been studied by different simulation methods [50, 59, 64–66]. The interface free energy was computed by the cleavage technique [67, 68], the capillary fluctuation method (CFM) [69], and thermodynamic integration [48, 49, 60]. Unfortunately, the cleavage technique can be only applied to single-component systems or to binary systems where the solute component is insoluble in one of the phases. The CFM method was employed for calculations of γ in hard-sphere [70] and Lennard-Jones systems [50, 71, 72]. Thermodynamic integration was successfully applied to surfaces [48, 49, 60] but not to interfaces in binary two-phase systems. This work appears to be the first one where γ was computed by

thermodynamic integration along a solid-liquid coexistence path.

In Section 6.2 we derive equations for interface thermodynamics of binary solid-liquid systems with a non-hydrostatic solid. These equations and the associated thermodynamic integration schemes are then applied to simulations of a (110) solid-liquid interface in the Cu-Ag system. After introducing our simulation methodology (Section 6.3.1), we present our results (Section 6.4) and draw conclusions of this work (Section 6.5).

6.2 Thermodynamic relations for a binary solid-liquid interface

In this section we derive relations of interface thermodynamics that will be used in our atomistic simulations. As in the previous work [60], all equations are formulated in terms of the total interface excess γA . The interface free energy γ can be recovered by dividing this total excess by the interface area A at the end of the calculation.

6.2.1 Interface free energy as an excess quantity

Consider a rectangular block of material containing two coexisting binary phases, solid and liquid, separated by a planar interface. We assume that the solid phase is formed by the substitutional mechanism and is in a non-hydrostatic state of stress. The case of the interstitial solubility mechanism will be discussed later (Section 6.2.4). The Cartesian direction z is perpendicular to interface, with periodic boundary conditions applied in the x and y directions. The total number of atoms in the system is fixed.

The conditions of phase equilibrium in this system can be formulated as follows [18,23]:

- *Thermal equilibrium*: temperature T is uniform over the system.
- *Mechanical equilibrium*: the direction perpendicular to the interface is one of the principal axes of the stress tensor in the solid and $\sigma_{33} = -p$, where p is pressure in the liquid.

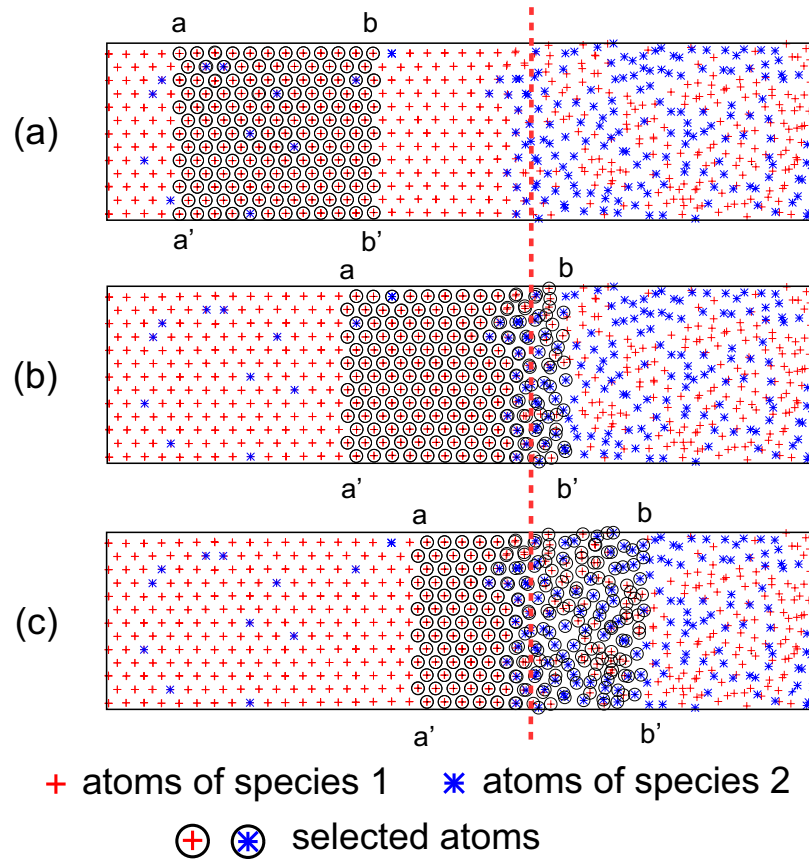


Figure 6.1: Schematic presentation of a binary solid-liquid system. The left part of the block is the solid phase, the right part is the liquid phase. The vertical dashed line indicates the approximate position of the interface. Atoms in circles belong to a conceptually selected layer bounded by imaginary planes aa' and bb' . Three positions of the layer are shown: (a) the layer is inside the solid, (b) the layer is just touching the interface, and (c) the interface is approximately in the middle of the later. The total number of atoms inside the layer is constant while its volume and average chemical composition can vary.

- *Chemical equilibrium:*

- The quantity

$$M_{21} \equiv \left(\frac{\partial U}{\partial N_2} \right)_{N,S,V,e_{ij}} \quad (6.1)$$

is constant everywhere in the system. Here, U , S , and V are the internal energy, entropy and volume of a region containing $N = N_1 + N_2$ atoms, where N_1 and

N_2 are the numbers of atoms of species 1 and 2. The derivative is taken at constant N , S and V . For solid regions, the elastic strain tensor e_{ij} (i, j refer to Cartesian coordinates) is also fixed.¹ Applying Eq. (6.1) to the liquid phase gives the relation

$$M_{21} = \mu_2 - \mu_1, \quad (6.2)$$

where μ_1 and μ_2 are chemical potentials of the components in the liquid.

– For all homogeneous regions inside the phases,

$$0 = U^s - TS^s + pV - \mu_1 N_1^s - \mu_2 N_2^s, \quad (6.3)$$

$$0 = U^l - TS^l + pV - \mu_1 N_1^l - \mu_2 N_2^l, \quad (6.4)$$

where superscripts s and l refer to the solid and liquid, respectively.

To introduce the interface free energy γ , first consider a homogeneous region inside one of the phases. Let this phase be the solid, although it could as well be the liquid. Let the region have the form of a layer bounded by two imaginary geometric planes aa' and bb' with the same area as the cross-section of our system (Fig. 6.1). We assume that the thickness of this layer (i.e., distance between aa' and bb') is much larger than the thickness of the region perturbed by the interface. Consider a thought process in which the bounding plane aa' is moved to the right, whereas bb' is simultaneously displaced in the same direction in a such a way that the total number N of atoms contained between the planes aa' and bb' is conserved (the encircled atoms in Fig. 6.1). Since the solid and liquid phases have different densities and chemical compositions, the volume enclosed between aa' and bb' and its average chemical composition will vary. Now take the view of an observer who moves with the plane aa' and can see only the atoms contained within the layer $abb'a'$. The

¹The equilibrium condition $M_{21} = \text{const}$ with M_{21} defined by Eq. (6.1) applies not only to solid-liquid but also to solid-solid equilibria. Solid-solid interfaces will be discussed in a separate publication.

observer will see a reversible process going on in an open system, in which the temperature, the normal stress $\sigma_{33} = -P$ and M_{21} remain uniform throughout, whereas the volume and chemical composition vary. New atoms enter this system through its boundary bb' , while the same number of atoms leaves the system through aa' .

Let the process stop when the interface is inside the moving layer and the planes aa' and bb' are in homogeneous solid and liquid regions, respectively. Comparing the initial and final states of the layer, we can write the combined first and second laws of thermodynamics as follows:

$$U - U^s = T(S - S^s) - p(V - V^s) + M_{21}(N_2 - N_2^s) + W_{nm}, \quad (6.5)$$

where the quantities with and without the superscript s refer to the initial (solid) and final (two-phase system) states, respectively. The last term in Eq. (6.5) represents the non-mechanical work done *on* the system during this process. Since the creation of the interface is the only outcome that required non-mechanical work, we follow Gibbs' definition and equate W_{nm} to γA , where A is the cross-sectional area of the system. Thus, we arrive at the following expression for γA :

$$\gamma A = U - U^s - T(S - S^s) + p(V - V^s) - M_{21}(N_2 - N_2^s). \quad (6.6)$$

Now recall that the initial state of the layer $abb'a'$ satisfies the solid-liquid equilibrium condition (6.3) with $N_1^s + N_2^s = N$. Subtracting Eq. (6.3) from (6.6) and using (6.2), we finally obtain

$$\gamma A = U - TS + pV - \mu_1 N_1 - \mu_2 N_2. \quad (6.7)$$

Although this equation looks similar to the Gibbsian equation for γA in fluid systems [13], we have derived it for a solid-liquid interface with a non-hydrostatic solid. Although only the normal stress component in the solid ($-P$) appears in this equation explicitly, γA actually depends also on the non-hydrostatic stress components. This dependence will become apparent later when we derive the adsorption equation in Section 6.2.2. Note also

that Eq. (6.7) expresses γA through chemical potentials in the *liquid* phase.

Eq. (6.7) is written for an arbitrarily chosen layer containing the interface. It is obvious, however, that homogeneous regions inside this layer that are not influenced by the interface do not contribute to γA . Indeed, for such regions the right-hand side of Eq. (6.7) is zero by Eqs. (6.3) and (6.4). It should be possible, therefore, to formulate γA as an excess over such homogeneous regions.

To this end, consider Eq. (6.7) together with Eqs. (6.3) and (6.4) applied to some arbitrarily chosen homogeneous solid and liquid regions. These equations together constitute a system of three linear equations with respect to γA and the intensive variables T , p , μ_1 and μ_2 . Two of these variables can be eliminated to express γA as a linear function of two remaining variables. Technically, this is accomplished by solving this system of equations for γA using Cramer's rule of linear algebra [14]:

$$\gamma A = [U]_{XY} - T[S]_{XY} + p[V]_{XY} - \mu_1[N_1]_{XY} - \mu_2[N_2]_{XY}, \quad (6.8)$$

where X and Y are any two of the extensive properties S , V , N_1 and N_2 . The coefficients $[Z]_{XY}$ are defined through the following determinants:

$$[Z]_{XY} \equiv \frac{\begin{vmatrix} Z & X & Y \\ Z^s & X^s & Y^s \\ Z^l & X^l & Y^l \end{vmatrix}}{\begin{vmatrix} X^s & Y^s \\ X^l & Y^l \end{vmatrix}}. \quad (6.9)$$

Here, the first row of the 3×3 determinant is composed on the amounts of Z , X and Y in a layer containing the interface together with adjacent homogeneous regions, whereas all other rows of the determinants represent properties of homogeneous solid and liquid regions.

It can be shown [14] that $[Z]_{XY}$ is independent of the volumes of the homogeneous

regions and of the thickness of the layer as long as the latter is large enough to include all regions perturbed by the interface. Representative homogeneous regions can be chosen either inside or outside the layer. It has also been shown [14] that $[Z]_{XY}$ has the meaning of the excess of property Z when the interface is formed out of two homogeneous regions in such a way that the amounts of X and Y remain the same before and after the interface formation. In other words, the interface excesses of X and Y are zero. We will be, therefore, referring to X and Y as conserved properties. Finally, two terms in Eq. (8.4) are zero because $[X]_{XY} = [Y]_{XY} = 0$.

Eq. (8.4) expresses γA through excesses of U and any two properties out of the set S , V , N_1 and N_2 . This can be written as

$$\gamma A = [\Phi]_{XY}, \quad (6.10)$$

where

$$\Phi \equiv U - TS + pV - \mu_1 N_1 - \mu_2 N_2 \quad (6.11)$$

is the right-hand side of Eq. (6.7). Since two terms in Φ have zero excesses and can be omitted, the final form of Φ depends on the choice of X and Y . For example, $\Phi = U - TS - \mu_2 N_2$ if we choose $X = N_1$ and $Y = V$. Since V is one of the conserved variables, γA can be interpreted as excess of Φ with respect to a dividing surface placed so that the excess of N_1 is zero. Alternatively, $\Phi = U - TS + pV$ if we choose $X = N_1$ and $Y = N_2$. In this case, the excess of Φ cannot be expressed in terms of a dividing surface because volume itself now has a non-zero excess.

We emphasize that these or any other choices of X and Y do not affect the final value of γA . Thus,

$$\gamma A = [U - TS - \mu_2 N_2]_{N_1 V} = [U - TS + pV]_{N_1 N_2} = \dots \quad (6.12)$$

Furthermore, transformations of variables can produce other expressions of γA in the form

of $[\Phi]_{XY}$. For example, introducing the variable $N = N_1 + N_2$ instead of N_1 we have

$$\gamma A = [U]_{XY} - T[S]_{XY} + p[V]_{XY} - \mu_1[N]_{XY} - M_{21}[N_2]_{XY} \quad (6.13)$$

and thus

$$\Phi \equiv U - TS + pV - \mu_1 N - M_{21} N_2, \quad (6.14)$$

with conserved properties X and Y selected out of the set S, V, N and N_2 . Choosing N as one of the conserved properties, we eliminate μ_1 and obtain $\Phi = U - TS - M_{21} N_2$. The advantage of this form is that M_{21} is readily accessible by atomistic simulations.

6.2.2 Adsorption equation

In this Section we derive an adsorption equation for a solid-liquid interface. We consider the same binary solid-liquid system as above. The total number of atoms is fixed while the chemical composition is allowed to vary by exchanging atoms with surrounding bulk regions. We will additionally assume that in all processes considered here, the cross-section of the solid contains a fixed number of lattice sites of its crystal structure. In other words, the Largangian area of the interface is constant, whereas the physical area A can vary by elastic deformation of the solid. Our system can receive or release heat, do mechanical work, and exchange atoms with the environment. Thus, the reversible variation of its internal energy is

$$dU = TdS + \sum_{i,j=1,2} \sigma_{ij} V de_{ij} + \sigma_{33} AdL + M_{21} dN_2, \quad (6.15)$$

where σ_{ij} the stress tensor averaged over the entire volume of our system and L is the dimension of the system normal to the interface.

Taking a full differential of Eq. (6.7) and combining it with Eq. (6.15), we obtain

$$d(\gamma A) = -SdT + Vdp - N_1d\mu_1 - N_2d\mu_2 + \sum_{i,j=1,2} (\sigma_{ij} + \delta_{ij}p) Vde_{ij}, \quad (6.16)$$

where we used $dV = \sum_{i,j=1,2} \delta_{ij}de_{ij} + AdL$ and Eq. (6.2). The seven differentials appearing in the right-hand side are not independent because this equation must satisfy the phase coexistence conditions. Equations expressing such conditions can be readily obtained by applying Eq. (6.16) to homogeneous solid and liquid regions with $\gamma A \equiv 0$. (Alternatively, the above derivation of Eq. (6.16) can be repeated with Eqs. (6.3) and (6.4) instead of (6.7)). This immediately gives us the Gibbs-Duhem equations for the solid and liquid phases:

$$0 = -S^s dT + V^s dp - N_1^s d\mu_1 - N_2^s d\mu_2 + \sum_{i,j=1,2} (\sigma_{ij}^s + \delta_{ij}p) V^s de_{ij}, \quad (6.17)$$

$$0 = -S^l dT + V^l dp - N_1^l d\mu_1 - N_2^l d\mu_2. \quad (6.18)$$

Since the liquid is in a hydrostatic state, the term $\sigma_{ij}^l + \delta_{ij}p$ has vanished. This system of two equations describes the 5-dimensional phase coexistence surface in the parameter space.

To impose the phase coexistence conditions on variations in equation (6.16), we use Eqs. (6.17) and (6.18) to eliminate two differentials from this equation. This can be done by applying Cramer's rule to solve the system of equations (6.16)-(6.18) for $d(\gamma A)$:

$$\begin{aligned} d(\gamma A) &= -[S]_{XY} dT + [V]_{XY} dp - [N_1]_{XY} d\mu_1 - [N_2]_{XY} d\mu_2 \\ &+ \sum_{i,j=1,2} [(\sigma_{ij} + \delta_{ij}p)V]_{XY} de_{ij}. \end{aligned} \quad (6.19)$$

Here, X and Y are any two of the seven extensive properties S , V , N_1 , N_2 and $(\sigma_{ij} + \delta_{ij}p)V$. Each differential coefficient $[Z]_{XY}$ is defined through determinants according

to Eq. (8.5). Recall that $[Z]_{XY}$ has the meaning of interface excess of property Z , the excesses of X and Y being zero. Because two of the seven differential coefficients in Eq. (6.19) are zero, this equation expresses $d(\gamma A)$ as a function of five *independent* differentials. This equation gives a variation of γA along a particular direction on the 5-dimensional phase coexistence surface. The independent variables describing this surface depend on the selection of the conserved properties X and Y .

The last term in Eq. (6.19) describes variations of γA due to elastic straining of the interface and is identified with interface stress tensor τ_{ij} :

$$\begin{aligned} \tau_{ij} &= \frac{1}{A} \left(\frac{\partial(\gamma A)}{\partial e_{ij}} \right) = \frac{1}{A} [(\sigma_{ij} + \delta_{ij}p)V]_{XY} \\ &= \frac{1}{A} \frac{\begin{vmatrix} (\sigma_{ij} + \delta_{ij}p)V & X & Y \\ (\sigma_{ij}^s + \delta_{ij}p)V^s & X^s & Y^s \\ 0 & X^l & Y^l \end{vmatrix}}{\begin{vmatrix} X^s & Y^s \\ X^l & Y^l \end{vmatrix}}. \end{aligned} \quad (6.20)$$

The derivative of γA is taken along the coexistence surface by varying a particular strain component e_{ij} while keeping the other strain components and two of the intensive variables T , p , μ_1 and μ_2 fixed. This equation represents the interface stress as an excess over bulk stresses and gives a recipe for its calculation for non-hydrostatic solids. Because τ_{ij} depends on the choice of the conserved variables, it is generally *not* unique.

In the particular case when the solid is in a hydrostatic state of stress, we have $(\sigma_{ij}^s + \delta_{ij}p)V^s = 0$ and the number of degrees of freedom of the coexistence system reduces to two. The solid and liquid are under the same pressure p . The conserved properties can now be chosen only

out of the set S , V , N_1 and N_2 . It is evident from Eq. (6.20) that the interface stress becomes unique and equal to $\tau_{ij} = (\sigma_{ij} + \delta_{ij}p)V/A$ regardless of the choices of X and Y . We emphasize, however, that all other excess quantities (the differential coefficients in (6.19)) are still non-unique even in the hydrostatic case.

The adsorption equation (6.19) constitutes the main result of this Section. As before, transformations of variables can produce different parameterizations of γA on the phase coexistence surface. For example, using the variable $N = N_1 + N_2$ instead of N_1 we can rewrite the adsorption equation in the form

$$\begin{aligned} d(\gamma A) &= -[S]_{XY} dT + [V]_{XY} dp - [N]_{XY} d\mu_1 - [N_2]_{XY} dM_{21} \\ &+ \sum_{i,j=1,2} [(\sigma_{ij} + \delta_{ij}p)V]_{XY} de_{ij}. \end{aligned} \quad (6.21)$$

As will be seen below, this form has certain advantages for atomistic simulations.

6.2.3 Thermodynamic integration schemes

We are now in a position to derive equations that can be applied for thermodynamic integration of the interface free energy. To this end, we eliminate $[S]_{XY}$ from Eq. (6.21) by inserting $[S]_{XY}$ from Eq. (6.13). After some transformations, we obtain the following Gibbs-Helmholtz type equation

$$\begin{aligned} d\left(\frac{\gamma A}{T}\right) &= -\frac{[\Psi]_{XY}}{T^2} dT + \frac{[V]_{XY}}{T} dP - \frac{[N]_{XY}}{T} d\mu_1 - \frac{[N_2]_{XY}}{T} dM_{12} \\ &+ \frac{1}{T} \sum_{i,j=1,2} [(\sigma_{ij} + \delta_{ij}p)V]_{XY} de_{ij}. \end{aligned} \quad (6.22)$$

where we denoted

$$\Psi \equiv U + pV - \mu_1 N - M_{12} N_2. \quad (6.23)$$

If N is selected as one of the conserved properties, then the term with $d\mu_1$ in Eq. (6.22) and $-\mu_1 N$ in Eq. (6.23) vanish, leaving only properties that are readily accessible by atomistic methods. After elimination of another term, only five independent differentials will remain in the right-hand side of Eq. (6.22). This equation can be then integrated along any path on the phase coexistence surface to find γ at all points of the path knowing its value at the initial point.

For example, if we choose N and V for X and Y , then Eq. (6.22) becomes

$$\begin{aligned} d\left(\frac{\gamma A}{T}\right) &= -\frac{[U - N_2 M_{21}]_{NV}}{T^2} dT - \frac{[N_2]_{NV}}{T} dM_{12} \\ &+ \frac{1}{T} \sum_{i,j=1,2} [(\sigma_{ij} + \delta_{ij} p)V]_{NV} de_{ij}. \end{aligned} \quad (6.24)$$

We can also take N and N_2 for X and Y , which gives

$$\begin{aligned} d\left(\frac{\gamma A}{T}\right) &= -\frac{[U + pV]_{NN_2}}{T^2} dT + \frac{1}{T} [V]_{NN_2} dp \\ &+ \frac{1}{T} \sum_{i,j=1,2} [(\sigma_{ij} + \delta_{ij} p)V]_{NN_2} de_{ij}. \end{aligned} \quad (6.25)$$

To demonstrate an application of these equations, consider a process in which pressure in the liquid is constant while temperature and the strain components e_{ij} in the solid vary maintaining the two-phase equilibrium. This process can be mapped on a path on the phase coexistence surface on which $dp = 0$. This path can be parameterized by any of the

intensive variables. Let this variable be temperature, i.e., $M_{21} = M_{21}(T)$ and $e_{ij} = e_{ij}(T)$.

Then

$$dM_{21} = \left(\frac{dM_{21}}{dT} \right)_{P,coex.} dT,$$

$$de_{ij} = \left(\frac{de_{ij}}{dT} \right)_{P,coex.} dT,$$

where the subscript $p, coex.$ is a reminder that the derivatives are taken on the phase coexistence surface at a constant pressure. Eqs. (6.24) and (6.25) can now be integrated along this path to give

$$\begin{aligned} \gamma A &= \frac{(\gamma A)_0 T}{T_0} - T \int_{T_0}^T \left(\frac{[U - N_2 M_{21}]_{NV}}{T'^2} \right. \\ &\quad - \sum_{i,j=1,2} \frac{[(\sigma_{ij} + \delta_{ij} p)V]_{NV}}{T'} \left(\frac{de_{ij}}{dT} \right)_{P,coex.} \\ &\quad \left. + \frac{[N_2]_{NV}}{T'} \left(\frac{dM_{21}}{dT} \right)_{P,coex.} \right) dT', \end{aligned} \quad (6.26)$$

$$\begin{aligned} \gamma A &= \frac{(\gamma A)_0 T}{T_0} - T \int_{T_0}^T \left(\frac{[U + pV]_{NN_2}}{T'^2} \right. \\ &\quad \left. - \sum_{i,j=1,2} \frac{[(\sigma_{ij} + \delta_{ij} p)V]_{NN_2}}{T'} \left(\frac{de_{ij}}{dT} \right)_{P,coex.} \right) dT', \end{aligned} \quad (6.27)$$

where superscript 0 refers to the initial state of the path.

It should be emphasized that the integrals (6.26) and (6.27) are performed along the *same* path and only differ in the choice of the conserved properties X and Y selected for computing the excess quantities. Since the value of γA at any point of the path is independent of the choice of X and Y , we can equate the two integrands to obtain

$$\begin{aligned}
& \frac{[U - N_2 M_{21}]_{NV}}{T^2} - \sum_{i,j=1,2} \frac{[(\sigma_{ij} + \delta_{ij} p)V]_{NV}}{T} \left(\frac{de_{ij}}{dT} \right)_{P,coex.} \\
& \quad + \frac{[N_2]_{NV}}{T} \left(\frac{dM_{21}}{dT} \right)_{p,coex.} \\
& = \frac{[U + pV]_{NN_2}}{T^2} - \sum_{i,j=1,2} \frac{[(\sigma_{ij} + \delta_{ij} p)V]_{NN_2}}{T} \left(\frac{de_{ij}}{dT} \right)_{p,coex.}. \tag{6.28}
\end{aligned}$$

This relation can be used to express the segregation $[N_2]_{NV}$ through excesses of other properties and derivatives of M_{21} and e_{ij} along the path:

$$\begin{aligned}
[N_2]_{NV} & = \left\{ [U + pV]_{NN_2} - [U]_{NV} \right. \\
& \quad \left. - T \sum_{i,j=1,2} \left\{ [(\sigma_{ij} + \delta_{ij} p)V]_{NN_2} - [(\sigma_{ij} + \delta_{ij} p)V]_{NV} \right\} \left(\frac{de_{ij}}{dT} \right)_{P,coex.} \right\} \\
& \quad / \left(T \left(\frac{dM_{21}}{dT} \right)_{P,coex.} - M_{21} \right). \tag{6.29}
\end{aligned}$$

This relation will be used in Section 6.4 for cross-checking our simulation methodology.

6.2.4 The case of an interstitial solid solution

All previous equations were derived assuming that the solid phase is a substitutional solution. Now suppose that the chemical component 2 dissolves in the solid by the interstitial

mechanism. Assume for simplicity that this component does not change its atomic or molecular state during the dissolution. In this case, the solid-liquid equilibrium conditions formulated in Section 6.2.1 remain valid with one modification: the constancy of M_{12} should be replaced by the condition that the chemical potential μ_2 of the interstitial species (which is now well-defined in the solid [13, 18, 23]) be uniform throughout the system, $\mu_2 = \text{const.}$

To derive γA , we again consider a thought process in which we conceptually select a solid layer bounded by two planes aa' and bb' (Fig. 6.1) and move these planes towards the interface until the latter is approximately in the middle of the layer. This time, however, we keep a fixed number of atoms N_1 of component 1 inside the layer. Comparing the initial (superscript s) and final states of the layer, we write the combined first and second laws of thermodynamics for an open system in the form

$$U - U^s = T(S - S^s) - p(V - V^s) + \mu_2(N_2 - N_2^s) + W_{nm}. \quad (6.30)$$

Recognizing that the non-mechanical work W_{nm} is spent to create the interface, we obtain

$$\gamma A = U - U^s - T(S - S^s) + p(V - V^s) - \mu_2(N_2 - N_2^s). \quad (6.31)$$

Finally, combining this equation with the phase equilibrium condition (6.3) with $N_1^s = N_1$, we exactly recover Eq. (6.7) derived previously for a substitutional solid. It is convenient to rewrite this equation in the form

$$\gamma A = U - TS + pV - \mu_1 N - (\mu_2 - \mu_1) N_2, \quad (6.32)$$

or in the excess form $[\Phi]_{XY}$ with Φ equal to the right-hand side of Eq. (6.32). The latter equation, as well as the corresponding adsorption equation and all thermodynamic integration schemes derived previously, remain the same except that M_{12} must be replaced by $\mu_2 - \mu_1$.

6.3 Methodology of atomistic simulations

6.3.1 Model system and methodology of Monte Carlo simulations

We chose the copper-silver system as a model binary system, with atomic interactions described by the embedded-atom potential developed in Ref. [40]. Our goal is to study an interface between the Cu-rich solid solution and the liquid solution. The chemical compositions of the coexisting solid and liquid phases at different temperatures are defined by the solidus and liquidus lines shown in Fig. 6.2 in red. As temperature decreases starting from pure Cu, the concentration (atomic fraction) of Ag atoms in the liquid phase increases from 0 to 0.46 (eutectic composition), while the concentration in the solid phase never exceeds a few percent. This leads to very large composition differences across the interface at low temperatures.

The (110) orientation of the solid-liquid interface was chosen for this study because the same orientation was used in our previous work on pure Cu [60]. This interface was modeled in a rectangular $26 \times 25 \times 190$ Å (8,960 atoms) simulation block containing a 80 Å thick solid layer and two 55 Å thick liquid layers exposed to vacuum (Fig. 6.3). The $[1\bar{1}0]$ and $[001]$ crystallographic directions of the solid part were aligned parallel to the x and y coordinate axes, respectively. Periodic boundary conditions were applied in the x and y directions, with free surfaces in the z direction. The exposure to vacuum guaranteed zero pressure in the liquid phase.

Prior to the Monte Carlo (MC) simulations (see next paragraph), the block was uniformly expanded by the thermal expansion factor corresponding to the simulated temperature and equilibrium chemical composition of the solid. The expansion factors were computed in separate MC simulations using a single-phase solid block. This pre-expansion procedure eliminated most of the thermal stresses that would otherwise be created in the solid phase. Nevertheless, some non-hydrostatic residual stresses remained due to statistical errors in the expansion factor. We, therefore, applied the full non-hydrostatic treatment of the problem (Section 6.2) to introduce corrections for the residual stresses.

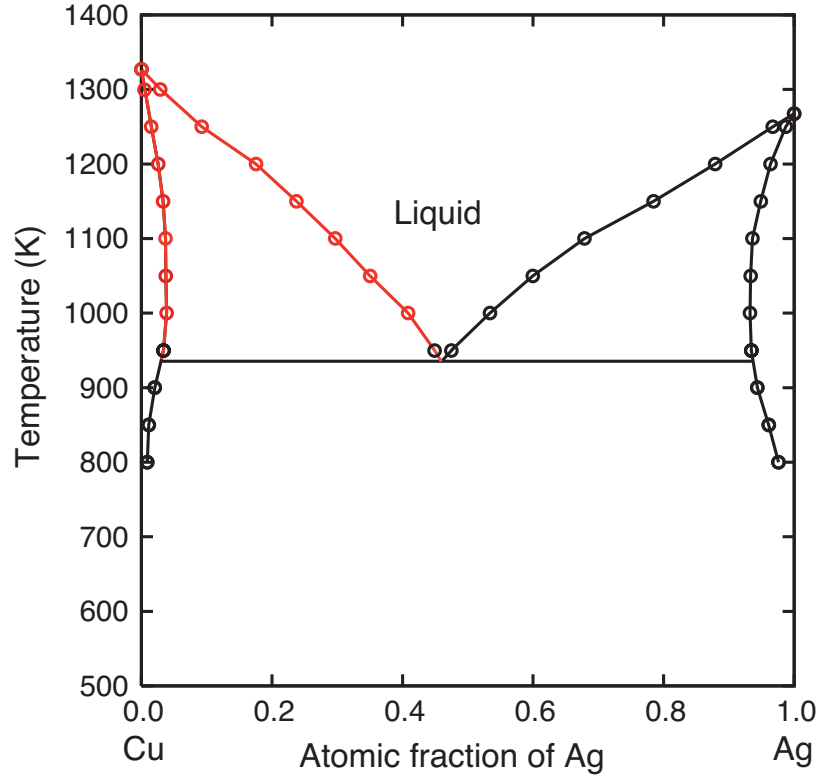


Figure 6.2: The Cu-Ag phase diagram predicted by the embedded-atom potential used in this work. The red lines mark the equilibrium solid and liquid compositions implemented in this work.

The semi-grand canonical MC method [36, 48, 51] was applied to calculate equilibrium thermodynamic properties of the interface. The MC simulations were performed at temperatures from 1327 K (melting point of pure Cu) down to 1000 K. The values of M_{21} corresponding to solid-liquid coexistence at different temperatures were previously computed using the same MC technique [40]. For each T and M_{21} , the initial configuration of the simulation block was equilibrated by 10^5 MC steps per atom, followed by a production run of 10^6 additional MC steps. Snapshot files containing instantaneous atomic positions, stresses and energies were saved every 50 MC steps and used for calculations of excess quantities at the post-processing stage. The stresses were computed from the standard virial expression.

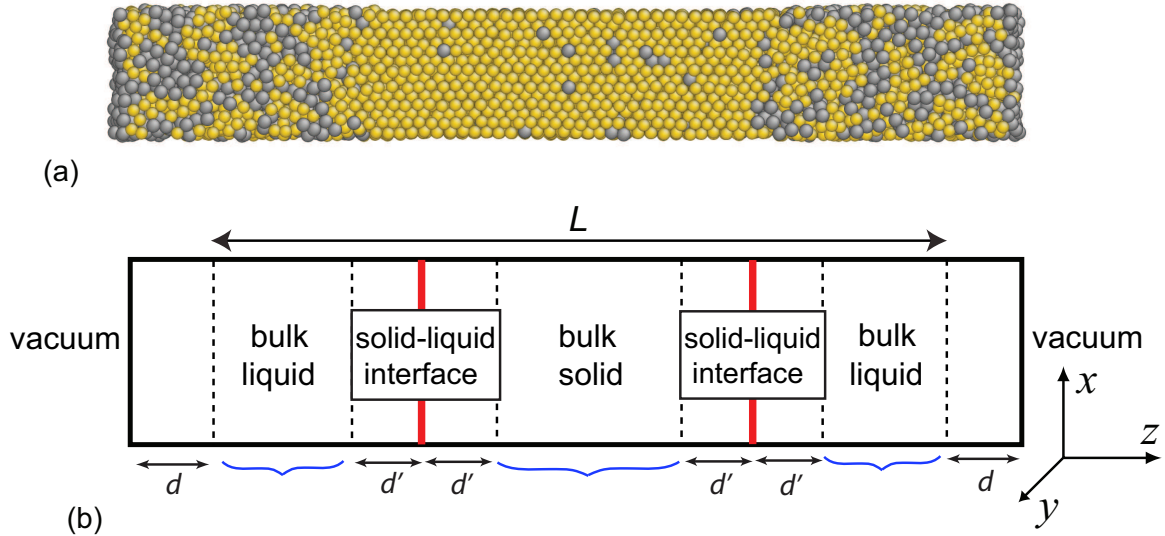


Figure 6.3: (a) Snapshot of the simulation block at 1000 K. The solid phase is sandwiched between two liquid layers, each exposed to vacuum to ensure zero pressure in the z -direction. The yellow and gray colors designate Cu and Ag atoms, respectively. (b) Schematic presentation of different regions involved in the calculations of excess quantities. L is the total thickness of the layer used for interface excess calculations. The solid-liquid interfaces are indicated by vertical red lines. The curly braces mark homogeneous solid and liquid regions. Distances d and d' are discussed in the text.

6.3.2 Interface excess quantities and thermodynamic integration

The excess values of energy, stresses and amounts of components were calculated from the determinants (8.5) introduced in Section 6.2. The quantities appearing in those determinants were first computed for individual snapshots and then averaged over all snapshots before inserting them in the determinants. This calculation requires an appropriate selection of the bounds of the homogeneous and interfacial regions (Fig. 6.3(b)). This selection was made automatically and was guided by the knowledge of approximate positions of interfaces in individual snapshots. It should be mentioned that the interface positions somewhat varied during the simulations as a result of thermal fluctuations. The solid-liquid interface positions were estimated from profiles of the structure factor $S(\mathbf{k})$ using the reciprocal

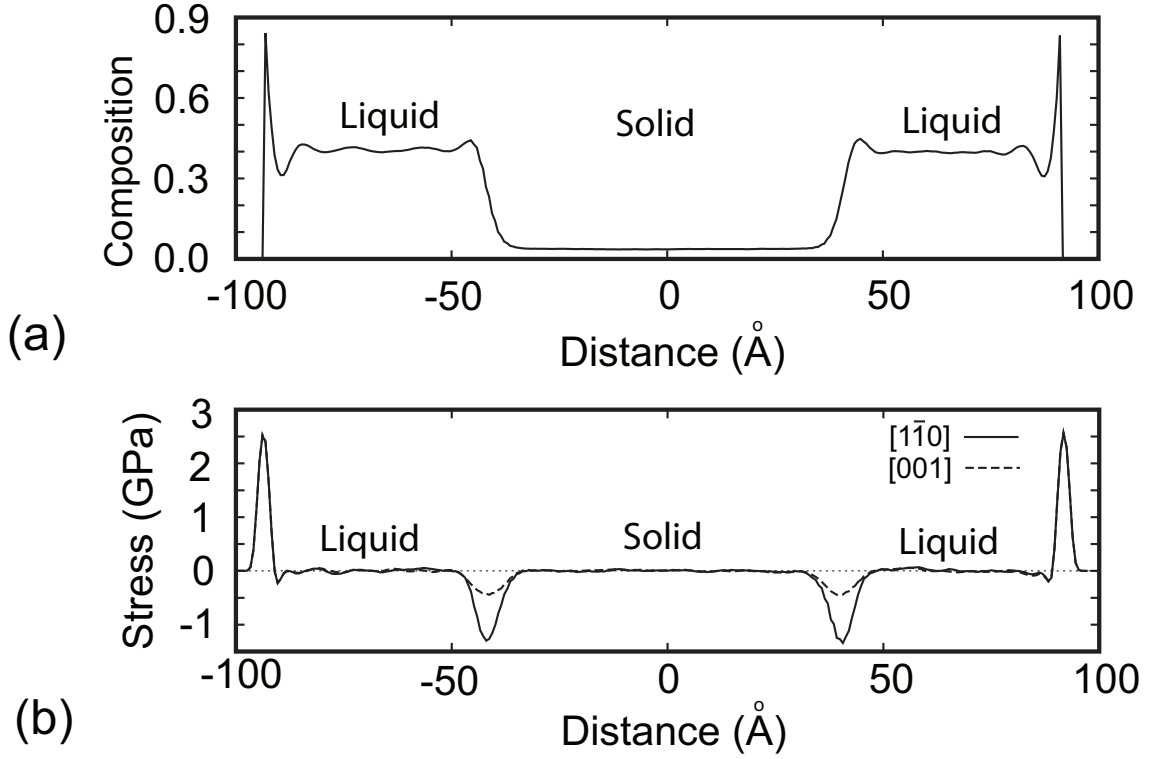


Figure 6.4: Profiles of (a) Ag concentration and (b) lateral components of stress in the $[1\bar{1}0]$ and $[001]$ directions of the solid at 1000 K.

lattice vector $\mathbf{k} = 2\pi[2\sqrt{2}/a, 0, 0]$. The procedure of interface location by this method was described in detail in our previous work [60]. The approximate liquid-vacuum interface positions were identified with the maximum and minimum z -coordinates of all atoms.

Knowing the approximate interface locations, the bulk solid was represented by a solid layer separated by a distance d' from each of the solid-liquid interfaces (Fig. 6.3(b)). The bounds of the bulk liquid layers were placed a distance d from a liquid-vacuum interface and a distance d' from the solid-liquid interface. The solid-liquid interface region itself was represented by the entire simulation block less the two near-surface layers of thickness d . This region is shown in Fig. 6.3(b) as the layer with the thickness L . (All interface excess quantities of this region were divided by two since it contains two solid-liquid interfaces.) Because the estimated interface positions fluctuated from one snapshot to the next, the

bounds of the bulk and interface regions were re-defined on the fly, keeping the values of d and d' constant. These values were adjusted to be large enough to exclude the influence of the interfaces on bulk properties. The latter was verified by increasing these distances until the computed excess quantities reached constant values within statistical errors. Typical values of d and d' were around 19 Å. In order to place error bars of the calculated quantities, the entire set of snapshots was divided into 6 subsets. The error bar was identified with the standard deviation of the subset averages from the global average.

When one of the conserved properties X and Y in Eq. (8.5) was volume, slight changes in the exact positions of the bounding surfaces could sometimes produce small but sudden variations in the interface excess quantities, reflecting the discrete atomic nature of the selected regions. To average over such fluctuations, we found it useful to represent atoms by small cubes with sides λ parallel to the coordinate axes. Accordingly, all physical properties assigned to atoms were uniformly distributed over the volumes of the cubes. This “smearing” of atoms is similar to the finite impulse response filtering method [55]. For reasonable choices of λ , the average values of the excess quantities were not noticeably affected by λ . The results reported below were obtained with $\lambda = 2$ Å.

Although our calculations of the interface excesses did not require a construction of interface profiles, such profiles were still computed as they often give insights into the structure of the interface region. As an illustration, Fig. (6.4) presents profiles of composition and lateral components of stress at 1000 K. They were obtained by dividing the simulation block into 0.7 Å thick slices normal to the z direction and averaging the composition and stress components within each slice. In addition, each profile was averaged over 2,000 snapshots. At this relatively low temperature the random interface displacements were small. The latter was verified by dividing the entire series of snapshots into groups according to the progress of the simulation and computing the profiles for each group. It should also be mentioned that the shape of the profiles depended to some extent on the size λ of the cubes representing the atoms. Larger values of λ tended to give smoother profiles, but at the risk of losing interesting details. The particular profiles shown in Fig. (6.4) were computed with

$\lambda = 3 \text{ \AA}$. The details revealed by their shapes will be discussed later.

The free energy γ of the solid-liquid interface was computed as a function of temperature (and thus the chemical compositions of the phases) by thermodynamic integration based on Eqs. (6.26) and (6.27). These two equations are based on different choices of X and Y and were used to check the invariance of the obtained γ values. After the excess quantities appearing in these equations were computed from MC simulations as functions of T , the integrands were approximated by cubic splines and integrated to recover $\gamma(T)$. The reference temperature for the integration was chosen to be $T_0 = 1300 \text{ K}$. The corresponding reference value γ_0 was chosen so that the plot of $\gamma(T)$ would be smoothly connected to $\gamma = 0.199 \text{ J/m}^2$ for pure copper (1327 K). The latter value was obtained in our previous work for the same interface orientation [60].

6.4 Simulation results

Examples of composition and lateral stress profiles are shown in Fig. 6.4. Observe the large difference between the bulk solid and liquid compositions. The stresses fluctuate around zero in the liquid phase and are non-zero but very small in the solid phase (residual thermal stresses). The large concentration peaks at the ends of the composition profile reflect the strong segregation of Ag to the open surfaces of the liquid. Note that these peaks are followed by oscillations penetrating deep into the liquid. The large positive peaks of the lateral stress are due to the large positive tension of the open surfaces. Both stress components produce identical peaks as expected from the anisotropy of the liquid surface.

The solid-liquid interfaces are characterized by smaller peaks of Ag concentration, whose positive sign is indicative of Ag attraction to these interfaces. The negative sign of the stress peaks suggests that the solid-liquid interface is under compression. The different magnitudes of the peaks for different stress components indicate that the interface stress is significantly anisotropic. It is interesting to note that the positions of the composition and stress peaks at the solid-liquid interfaces do not coincide, with the composition peaks being slightly

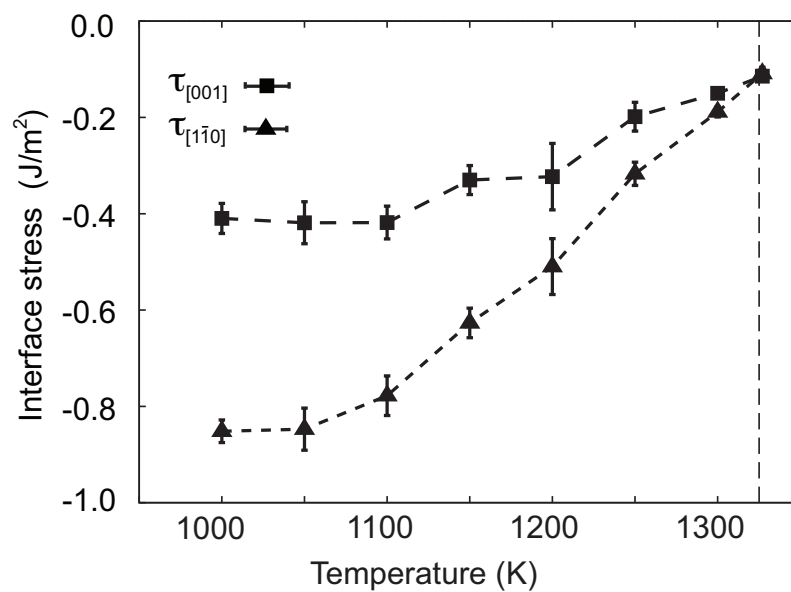


Figure 6.5: Principal components of the solid-liquid interface stress as functions of temperature. The vertical dashed line indicates the melting point of pure Cu.

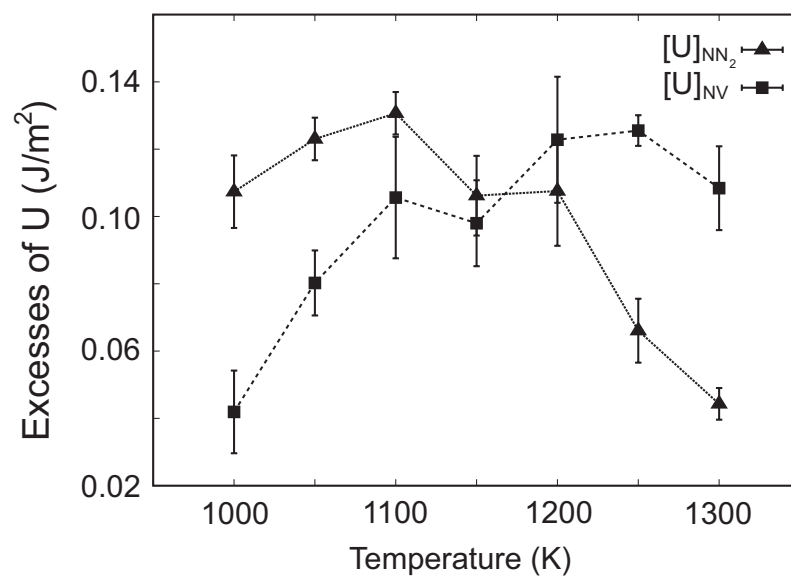


Figure 6.6: Excess values of internal energy U at the solid-liquid interface for two different choices of the conserved properties X and Y . This plot demonstrates that the excess of U depends on the choice of the conserved variables.

shifted towards the liquid phase. In other words, if the interface position is identified with the maximum of stress, then Ag atoms segregate to the interface on the liquid side. At high temperatures, the Ag concentration peaks at the solid-liquid interfaces could not be resolved due to larger thermal fluctuations and more extensive interface movements.

Because the coordinate axes are chosen to be parallel to crystallographic directions with twofold symmetry, the interface stress tensor τ_{ij} is diagonal. Let us denote the principal components of τ_{ij} by $\tau_{[001]}$ and $\tau_{[1\bar{1}0]}$, with the subscripts indicating the principal directions. These stress components were computed from Eq. (6.20) for two different choices of the conserved properties X and Y : $X = N$, $Y = V$ and $X = N$, $Y = N_2$. These choices were found to give identical interface stresses within statistical errors. This is not surprising given that the residual thermal stresses in the solid are very small. Recall that τ_{ij} must be independent of the choice of X and Y if the bulk state of stress is hydrostatic, which includes the stress-free case.

The temperature dependence of the principal components of τ_{ij} is shown in Fig. 6.5. In pure Cu, both components are negative and nearly equal. In the binary system they remain negative and their magnitude drastically increases with decreasing temperature. As T approaches the eutectic temperature, the average magnitude of the interface stress becomes almost by order of magnitude larger than in pure Cu. Furthermore, the interface stress becomes highly anisotropic, with the magnitude of compression in the $[1\bar{1}0]$ direction being more than a factor of two larger than in the $[001]$ direction.

Fig. 6.6 shows the excesses of internal energy U computed with different choices of X and Y . The excess values are clearly different, especially at the ends of the temperature interval. This was to be expected since interface excess of energy is not unique but depends on the choice of the conserved properties. These two different excesses of U were used for both thermodynamic integration and for indirect evaluation of the segregation.

The interface segregation $[N_2]_{NV}$ was calculated by two methods: directly using the determinants and indirectly using Eq. (6.29). Since we have already established that our interface stress is virtually independent of the choices of X and Y , Eq. (6.29) reduces to

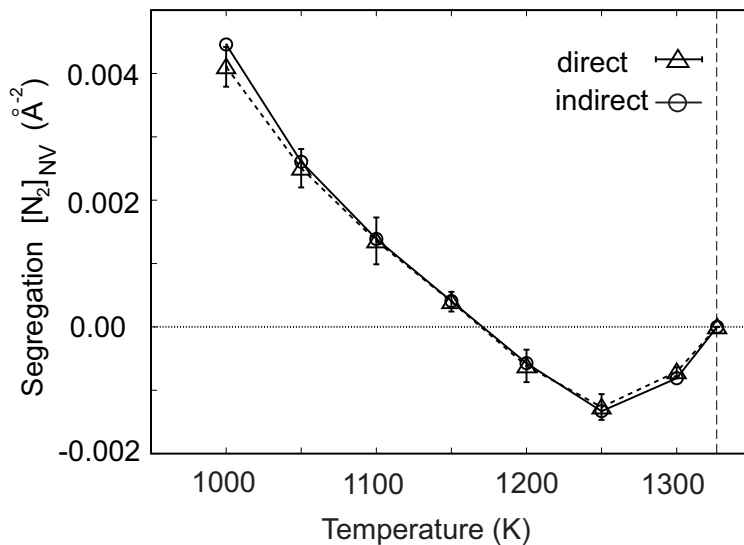


Figure 6.7: Ag segregation $[N_2]_{NV}$ at the solid-liquid interface as a function of temperature. Note the agreement between the direct and indirect calculations (see text for detail). The vertical dashed line indicates the melting point of pure Cu.

$$[N_2]_{NV} = \frac{[U]_{NN_2} - [U]_{NV}}{T \left(\frac{dM_{21}}{dT} \right)_{P,coex.} - M_{21}}. \quad (6.33)$$

To evaluate $(dM_{21}/dT)_{P,coex.}$ for this equation, M_{21} as a function of T was fitted with cubic splines and differentiated. The obtained temperature dependence of the segregation is plotted in Fig. 6.7. The good agreement between the direct and indirect calculations confirms the correctness of our methodology. Note that the segregation is negative at high temperatures but becomes positive below 1175 K. The temperature dependence of the segregation is almost linear when approaching the eutectic point.

Finally, Fig. 6.8 displays the interface free energy obtained by thermodynamic integration as a function of T for different choices of X and Y . As expected, the results are identical within the accuracy of the calculations. γ decreases with decreasing temperature

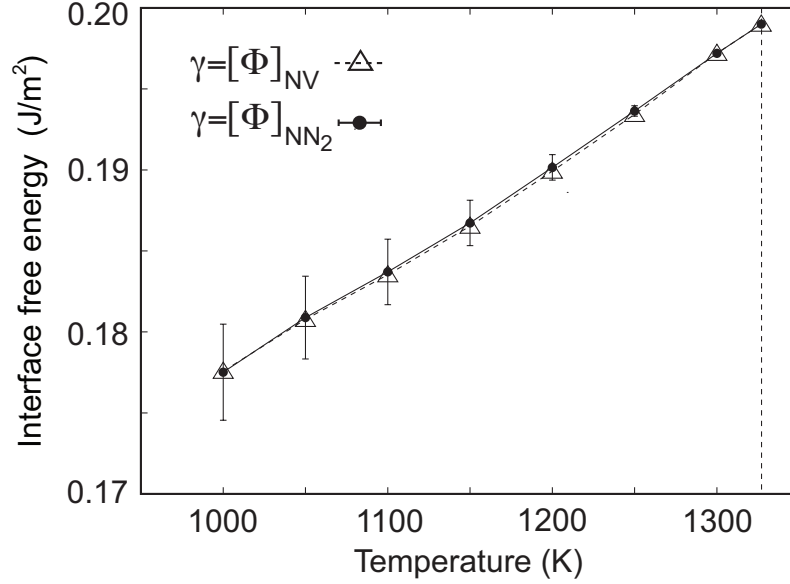


Figure 6.8: Temperature dependence of the solid-liquid interface free energy computed with different choices of the conserved properties X and Y . As expected, the computed values are identical within the accuracy of calculations. The vertical dashed line indicates the melting point of pure Cu.

approximately linearly from 0.199 J/m² for pure copper to 0.178 J/m² in the alloy system at 1000 K. A similar trend was found in recent CFM calculations for a Lennard-Jones system with lens-type solid-liquid phase diagram [71]. The variation of γ is much smaller than the change in the interface stress in the same temperature interval.

6.5 Discussion and conclusions

Starting from the general Gibbsian definition of interface free energy γ as non-mechanical reversible work of interface creation, we have derived expressions for γ in binary solid-liquid systems with a non-hydrostatically stressed solid. Although chemical potentials of one (for an interstitial solution) or both (for a substitutional solution) components are undefined inside of the solid, the familiar expression (6.7) derived by Gibbs for fluid systems still holds with μ_1 and μ_2 taken as chemical potentials in the liquid phase. γ can also be expressed

as an excess of a thermodynamic potential Φ introduced in Section 6.2.1. The excess of Φ , as well as all other interface excess properties, can be calculated from determinants (8.5) without constructing interface profiles or introducing dividing surfaces. This formulation offers significant advantages for atomistic simulations.

We have also derived an adsorption equation expressing variations of γA in terms of variations of seven intensive properties which are uniform throughout the solid-liquid system at equilibrium. The differential coefficients in this equation have the meaning of interface excesses of extensive properties. Two of these excesses must be zero, leaving five independent terms corresponding to the five degrees of freedom of the two-phase coexistence system. The final form of the adsorption equation depends on the arbitrary choice of two conserved properties X and Y whose excesses must be zero. Taking the total number of atoms as one of such conserved properties, the adsorption equation contains only the chemical potential difference $\mu_2 - \mu_1$, which for substitutional solid solutions is identical to the diffusion potential M_{21} [18,23]. A formulation of the adsorption equation in terms of $\mu_2 - \mu_1$ is important because $\mu_2 - \mu_1$ is the control parameter in semi-grand canonical Monte Carlo simulations.

Three terms in the adsorption equation define the interface stress tensor τ_{ij} , representing it as an excess over the bulk stress tensor σ_{ij} . While the interface free energy is independent of the choice of conserved properties, the interface stress does generally depend on X and Y (unless the solid is hydrostatic). The non-uniqueness of interface stress in non-hydrostatic systems is an interesting fact that should be taken into account in the interpretation of simulation results and experimental data. For example, interface stresses create a non-hydrostatic state of bulk stress inside a free-standing thin solid film in equilibrium with its melt. If the film thickness is on the order of a few nanometers, the non-hydrostatic components of the bulk stress can be quite significant, creating some uncertainty in the interface stress extracted from the measured bulk stresses inside and outside the film.

More generally, it should be remembered that all interface excesses are non-unique with the exception of γ . Considering the freedom of choice of the variables used in the

adsorption equation, care should be taken when assigning a physical meaning to excess quantities or comparing them with experiment. For example, solute segregation can be characterized by different excess quantities, such as $[N_2]_{NV}/A$, $[N_2]_{N_1V}/A$, $[N_2]_{SV}/A$, etc. Gibbs [13] used the segregation $\Gamma_{2(1)}$ which in our notations is $[N_2]_{N_1V}/A$. In this work we preferred $[N_2]_{NV}/A$ whose positive sign at low temperatures is consistent with the peak of Ag concentration in the interface region (Fig. (6.4)). However, all other definitions of segregation would be equally legitimate and could give us positive, negative or zero values. As another example, Fig. (6.6) demonstrates that the interface energy is non-unique and strongly depends on the choice of the conserved variables.

Finally, our simulations demonstrate that the interface free energy and interface stress can be very different in magnitude and even sign. The conceptual difference between the two quantities was emphasized by Gibbs [13], who defined γ as reversible work of creation of a unit area of new interface, while τ_{ij} as work of elastically stretching a unit area of an existing interface. For stable interfaces, γ is always positive and usually varies with crystallographic orientation within a few percent [71]. By contrast, we find that both principal components of τ_{ij} for the (110) solid-liquid interface are negative and drastically increase in magnitude with increasing alloying. At the same time, γ decreases by only about 10%. Furthermore, the anisotropy τ_{ij} also drastically increases with alloying, reaching a factor of two near the eutectic point. The difference between the interface free energy and interface stress is an important factor in phase nucleation theory. For example, in the spherical model of a solid particle nucleating from a fluid, assuming that the interface properties are isotropic, the difference between chemical potentials of components inside the phases is proportional to $\gamma - \tau$ [20,63]. For negative and large τ values such as those found in this work, the difference $\gamma - \tau$ is positive and could be significant.

Chapter 7: Effect of non-hydrostatic stresses on solid-fluid equilibrium. I. Bulk thermodynamics

7.1 Introduction

The problem of equilibrium between non-hydrostatically stressed solids and fluids is relevant to many processes encountered in nature and technological applications. For example, crystallization of solid materials may occur in the presence of pressure in the liquid. The pressure gives rise to mechanical stresses in the growing solid, which are generally not hydrostatic. As another example, during deposition of thin solid films by growth from vapor, the films are often subject to non-hydrostatic stresses imposed by the substrate, especially during epitaxial growth. In a more general context, non-hydrostatic stresses can strongly affect phase stability and phase transformations and are very important in high-pressure physics.

Equilibrium between non-hydrostatically stressed solids and fluids was first discussed by Gibbs [13]. He derived equilibrium conditions between the phases and showed that a non-hydrostatic single-component solid¹ can be equilibrated with three separate multicomponent fluids each having a different chemical potential. Gibbs also showed that a multicomponent fluid equilibrated with a single-component solid is supersaturated with respect to the substance of the solid except when the solid is hydrostatic. He pointed out that for variations of stress away from the hydrostatic state at a constant pressure p in the fluid, the change in the equilibrium temperature T is zero to first order. Using isotropic linear elasticity, Sekerka and Cahn [73] recently showed that the change in equilibrium temperature in a single-component system at a fixed pressure in the fluid is quadratic in non-hydrostatic

¹Gibbs[13] allowed the solid to contain several chemical elements but assumed its chemical composition to be unvaried. This fixed chemical composition defines the single component of the solid.

components of the stress in the solid.

In this work we analyze general variations of state of an equilibrium solid-fluid system. We evaluate the changes in T and p caused by stress variations away from an initially hydrostatic state along a hydrostatic path, as well as along non-hydrostatic isobaric and isothermal paths. Our treatment includes analysis of special points where volumes per atom or entropy per atom in the initial hydrostatic state are the same in both phases. We treat the elastic deformations of the solid within a small-strain approximation and anisotropic linear elastically. Using atomistic simulations with a semi-empirical potential, we study non-hydrostatic solid-liquid equilibrium in pure copper with a (110) oriented interface. As most crystalline solids, copper is elastically anisotropic. Using molecular dynamics (MD), we directly compute several equilibrium temperatures at a fixed zero pressure in the liquid and several equilibrium pressures at a constant temperature. The calculations are performed for a set of different states of stress in the solid, including biaxial deformations. The results are compared with our theoretical predictions and are found to be in quantitative agreement. We also study the instability of non-hydrostatic systems predicted by Gibbs and show how a non-hydrostatic system can transform to hydrostatic by growth of hydrostatically stressed solid layers.

The chapter is organized as follows. In Sec. 7.2 we analyze thermodynamic relations for non-hydrostatic solid-fluid equilibrium and derive analytical expressions for the equilibrium temperature and pressure. In Sec. 7.3 we describe our methodology of atomistic simulations. The results of the simulations are presented in Sec. 7.4, followed by a discussion in Sec. 7.5. The results obtained in this work will be used for the analysis of solid-fluid interface thermodynamics [74].

7.2 Thermodynamics of non-hydrostatic solid-fluid equilibrium

7.2.1 Thermodynamic relations

Consider a rectangular block containing a single-component homogeneous solid under a general state of mechanical stress at equilibrium with a fluid of the same component. The phases are separated by a planar interface and the effect of gravity [75, 76] is neglected. Gibbs derived the following equilibrium conditions for this system: 1) temperature T is uniform throughout the system; 2) one of the principal axes of the Cauchy stress tensor σ_{ij} in the solid (call it axis 3) is perpendicular to the solid-fluid interface, with the principal value $\sigma_{33} = -p$, where p is pressure in the fluid; and 3) the phase-change equilibrium condition requires

$$u^s - Ts^s + p\Omega^s = \mu^f. \quad (7.1)$$

Here u^s , s^s and Ω^s are the energy, entropy and volume per atom in the solid and μ^f is the chemical potential in the fluid.

For a general variation of the state of stress and the entropy of the solid, the differential of u^s is given by the fundamental equation

$$du^s = Tds^s + \sum_{i,j=1,2,3} \Omega_0^s \sigma_{ij} de_{ij}, \quad (7.2)$$

where e_{ij} is the small-strain tensor and Ω_0^s is atomic volume in the reference state used to define the strain. As the reference state we choose the stress-free state of the solid at a fixed reference temperature T_0 . The differential of the chemical potential in the fluid is given by

$$d\mu^f = -s^f dT + \Omega^f dp, \quad (7.3)$$

where s^f and Ω^f are entropy and volume per atom in the fluid. Taking a differential of Eq. (7.1) and using Eqs. (7.2) and (7.3) in conjunction with the relation

$$d\Omega^s = \sum_{i,j=1,2,3} \Omega_0^s \delta_{ij} de_{ij} \quad (7.4)$$

(δ_{ij} being the Kronecker symbol) we obtain

$$\Delta s dT - \Delta \Omega dp + \sum_{i,j=1,2} \Omega_0^s (\sigma_{ij} + \delta_{ij} p) de_{ij} = 0 \quad (7.5)$$

where we denoted $\Delta s = s^f - s^s$ and $\Delta \Omega = \Omega^f - \Omega^s$. Note that the summation now extends only to $i, j = 1, 2$ because $\sigma_{3k} + \delta_{3k} p = 0$ for $k = 1, 2, 3$. Gibbs derived Eq. (7.5) for a more general case of finite strains [13]. This equation contains five differentials and defines a four-dimensional (4D) phase coexistence surface in the 5D configuration space of variables. Thus the system has four degrees of freedom (four independent variables).

Eq. (7.5) immediately leads to two important conclusions regarding the behavior of T and p on the phase coexistence surface. If Eq. (7.5) is applied to a variation away from a hydrostatic state, the coefficients $\sigma_{ij} + \delta_{ij} p$ vanish. Then, if Δs in the hydrostatic state is finite and the solid is deformed elastically at a constant pressure in the fluid, the change in temperature is zero to first order: $dT = 0$. Similarly, if $\Delta \Omega$ in the hydrostatic state is finite and temperature is constant, the change in pressure due to elastic strains is zero to the first order: $dp = 0$.

To make further progress in this analysis, additional approximations have to be made. Specifically, we will adopt the approximation of anisotropic linear elasticity, in which the strain and stress tensors are related by

$$e_{ij} = \sum_{k,l=1,2,3} S_{ijkl} \sigma_{kl} + \eta_{ij}. \quad (7.6)$$

Here S_{ijkl} is the tensor of isothermal compliances, which we assume to be constant. η_{ij} is a tensor function of $T - T_0$, where T_0 is the chosen reference temperature. This tensor represents the contribution to strain due to thermal expansion of the stress-free solid. If η_{ij} is approximated by a linear function of $T - T_0$, Eq. (7.6) becomes the Duhamel-Neumann form of Hooke's law [22].

Inserting Eq. (7.6) in Eq. (7.5) and denoting the non-hydrostatic components of the stress by $q_{ij} = \sigma_{ij} + \delta_{ij}p$, we obtain

$$\begin{aligned} (\Delta s + \Omega_0^s q_{ij} \eta'_{ij}) dT - \left(\Delta \Omega + \Omega_0^s \sum_{i,j,k,l=1,2,3} q_{ij} S_{ijkl} \delta_{kl} \right) dp \\ + \Omega_0^s \sum_{i,j,k,l=1,2} S_{ijkl} q_{ij} dq_{kl} = 0 \end{aligned} \quad (7.7)$$

where η'_{ij} is the temperature derivative of η_{ij} representing the thermal expansion tensor. Although the summation in the differential coefficient before dp goes from 1 to 3, some of the terms are zero because $q_{i3} = 0$.

Some of the quantities appearing in the differential coefficients of Eq. (7.7) are related to each other. Using the Maxwell relations derived in Section 7.6, it can be shown that the following differential equations must be satisfied:

$$\frac{\partial s^s}{\partial q_{ij}} = \Omega_0^s \eta'_{ij}, \quad i, j = 1, 2, \quad (7.8)$$

$$\frac{\partial \Omega^s}{\partial q_{ij}} = \Omega_0^s \sum_{k=1,2,3} S_{ijkk}, \quad i, j = 1, 2, \quad (7.9)$$

$$\frac{\partial \Omega^s}{\partial T} = -\frac{\partial s^s}{\partial p}, \quad (7.10)$$

$$\frac{\partial \Omega^f}{\partial T} = -\frac{\partial s^f}{\partial p}. \quad (7.11)$$

These equations will be used at the next step of the calculations.

Suppose the solid-fluid system is initially in an equilibrium state, denoted H , in which the solid is hydrostatic ($q_{ij} = 0$) and the temperature and pressure are T_H and p_H , respectively. Our goal is to integrate Eq. (7.7) from state H to other (generally, non-hydrostatic) equilibrium states in a small vicinity of H . The integration will involve a linearization of the differential coefficients of dT and dp . To this end, we expand s^f , s^s , Ω^f and Ω^s in Taylor series in the variables $T - T_H$, $p - p_H$ and q_{ij} and limit the expansions to linear terms:

$$s^f = \bar{s}^f + \left(\frac{\partial s^f}{\partial T} \right)_H (T - T_H) + \left(\frac{\partial s^f}{\partial p} \right)_H (p - p_H), \quad (7.12)$$

$$s^s = \bar{s}^s + \left(\frac{\partial s^s}{\partial T} \right)_H (T - T_H) + \left(\frac{\partial s^s}{\partial p} \right)_H (p - p_H) + \sum_{i,j=1,2} \left(\frac{\partial s^s}{\partial q_{ij}} \right)_H q_{ij}, \quad (7.13)$$

$$\Omega^f = \bar{\Omega}^f + \left(\frac{\partial \Omega^f}{\partial T} \right)_H (T - T_H) + \left(\frac{\partial \Omega^f}{\partial p} \right)_H (p - p_H), \quad (7.14)$$

$$\begin{aligned} \Omega^s &= \bar{\Omega}^s + \left(\frac{\partial \Omega^s}{\partial T} \right)_H (T - T_H) + \left(\frac{\partial \Omega^s}{\partial p} \right)_H (p - p_H) \\ &+ \sum_{i,j=1,2} \left(\frac{\partial \Omega^s}{\partial q_{ij}} \right)_H q_{ij}. \end{aligned} \quad (7.15)$$

The quantities \bar{s}^f , \bar{s}^s , $\bar{\Omega}^f$ and $\bar{\Omega}^s$ are properties of the initial hydrostatic state and subscript H emphasizes that the derivatives are evaluated at that state. The derivatives $(\partial s^f / \partial T)_H$,

$(\partial s^s/\partial T)_H$, $(\partial \Omega^f/\partial p)_H$, $(\partial \Omega^s/\partial p)_H$, $(\partial \Omega^f/\partial T)_H$ and $(\partial \Omega^s/\partial T)_H$ correspond to variations from state H along hydrostatic paths and are related to the heat capacities, compressibilities and thermal expansions of the phases. By contrast, the derivatives $(\partial s^s/\partial q_{ij})_H$ and $(\partial \Omega^s/\partial q_{ij})_H$ correspond to non-hydrostatic variations of the solid away from state H . No q_{ij} terms appear in the expansions for s^f and Ω^f because the fluid is incapable of non-hydrostatic variations.

Substituting expansions (7.12)-(7.15) in Eq. (7.7) and using relations (7.8)-(7.11) we obtain

$$\begin{aligned} & \left[\Delta \bar{s} + \left(\frac{\partial \Delta s}{\partial T} \right) (T - T_H) - \left(\frac{\partial \Delta \Omega}{\partial T} \right) (p - p_H) \right] dT \\ & - \left[\Delta \bar{\Omega} + \left(\frac{\partial \Delta \Omega}{\partial T} \right)_H (T - T_H) + \left(\frac{\partial \Delta \Omega}{\partial p} \right)_H (p - p_H) \right] dp \\ & + \Omega_0^s \sum_{i,j,k,l=1,2} S_{ijkl} q_{ij} dq_{kl} = 0. \end{aligned} \quad (7.16)$$

We can now integrate Eq. (7.16) from the hydrostatic state H to a new state with T , p , q_{ij} to obtain

$$\begin{aligned} & \Delta \bar{s} (T - T_H) + \frac{1}{2} \left(\frac{\partial \Delta s}{\partial T} \right)_H (T - T_H)^2 - \Delta \bar{\Omega} (p - p_H) \\ & - \frac{1}{2} \left(\frac{\partial \Delta \Omega}{\partial p} \right)_H (p - p_H)^2 - \left(\frac{\partial \Delta \Omega}{\partial T} \right)_H (T - T_H) (p - p_H) \\ & + \frac{\Omega_0^s}{2} \sum_{i,j,k,l=1,2} S_{ijkl} q_{ij} q_{kl} = 0. \end{aligned} \quad (7.17)$$

Mathematically, this equation defines a 4D quadric surface representing two-phase equilibrium states in the 5D configuration space of the variables T , p , q_{11} , q_{12} and q_{22} .

Eq. (7.17) is the central result of our thermodynamic analysis of solid-fluid equilibrium. This equation permits predictions of temperature-pressure-stress relations for equilibrium processes in which the two-phase system deviates from a given hydrostatic state H along hydrostatic or non-hydrostatic paths. This equation is also valid for processes whose path

is confined to a small vicinity of point H but does not necessarily go through this point. Below we will analyze three particular paths on the 4D coexistence surface: hydrostatic, isobaric and isothermal. Yet another path will be discussed separately in Sec. 7.2.2.

Hydrostatic path

The solid-fluid system is initially in the hydrostatic state H . Consider a process in which p and T vary but the solid phase remains hydrostatic, i.e. all q_{ij} remain zero. Since three variables are fixed, the system has only one degree of freedom. Eq. (7.17) becomes

$$\begin{aligned} & \Delta\bar{s}(T - T_H) + \frac{1}{2} \left(\frac{\partial\Delta s}{\partial T} \right)_H (T - T_H)^2 - \Delta\bar{\Omega}(p - p_H) \\ & - \frac{1}{2} \left(\frac{\partial\Delta\Omega}{\partial p} \right)_H (p - p_H)^2 - \left(\frac{\partial\Delta\Omega}{\partial T} \right)_H (T - T_H)(p - p_H) = 0. \end{aligned} \quad (7.18)$$

Suppose $\Delta\bar{s}$ and $\Delta\bar{\Omega}$ are nonzero, i.e. state H is not a special point. Then in a small enough vicinity of this state the second-order terms can be neglected and Eq. (7.18) reduces to

$$\Delta\bar{s}(T - T_H) = \Delta\bar{\Omega}(p - p_H). \quad (7.19)$$

As expected, this is an integrated form of the Clapeyron-Clausius equation for hydrostatic phases. This equation is often written in the form

$$\Delta\bar{h}(T - T_H) = \Delta\bar{\Omega}T_H(p - p_H), \quad (7.20)$$

where $\Delta\bar{h} \equiv \Delta\bar{s}/T_H$ is the latent heat of the hydrostatic solid-fluid transformation. The latter is experimentally more readily accessible than $\Delta\bar{s}$.

A special case arises when $\Delta\bar{s} = 0$ (and thus $\Delta\bar{h} = 0$) but $\Delta\bar{\Omega} \neq 0$. At this point the equilibrium pressure is an extremum as a function of temperature. ${}^3\text{He}$ is an example of a system exhibiting this type of behavior [77, 78]. Keeping the term with $(T - T_H)^2$ and

$(p - p_H)$ and neglecting higher-order terms, Eq. (7.18) gives the parabolic equilibrium curve

$$p - p_H = \frac{1}{2\Delta\bar{\Omega}} \left(\frac{\partial\Delta s}{\partial T} \right)_H (T - T_H)^2. \quad (7.21)$$

For ${}^3\text{He}$ Δs is negative below T_H and positive above T_H , whereas $\Delta\bar{\Omega}$ remains positive. This produces a minimum of the melting pressure at T_H [77, 78].

In another special case $\Delta\bar{\Omega} = 0$ but $\Delta\bar{s} \neq 0$. The equilibrium temperature is an extremum as a function of pressure. Retaining the terms with $(T - T_H)$ and $(p - p_H)^2$ and neglecting all other terms, the phase coexistence equation is again parabolic,

$$T - T_H = \frac{T_H}{2\Delta\bar{h}} \left(\frac{\partial\Delta\Omega}{\partial p} \right)_H (p - p_H)^2. \quad (7.22)$$

For melting, $\Delta\bar{h}$ is usually positive while $\Delta\Omega$ is likely to decrease with pressure due to larger compressibility of the liquid phase. In such cases the melting temperature reaches a maximum at a certain pressure, as observed experimentally and in simulations for several materials [79–82].

Isobaric path

In the second type of variation, the pressure in the fluid is fixed while the solid is subject to a non-hydrostatic stress. The system has three degrees of freedom and Eq. (7.17) reduces to

$$\Delta\bar{s}(T - T_H) + \frac{1}{2} \left(\frac{\partial\Delta s}{\partial T} \right)_H (T - T_H)^2 + \frac{\Omega_0^s}{2} \sum_{i,j=1,2} S_{ijkl} q_{ij} q_{kl} = 0. \quad (7.23)$$

If the $\Delta\bar{s}$ is finite and the second term can be neglected in a given temperature range, we obtain

$$T - T_H = -\frac{\Omega_0^s T_H}{2\Delta\bar{h}} \sum_{i,j=1,2} S_{ijkl} q_{ij} q_{kl}. \quad (7.24)$$

Thus the temperature change is quadratic in non-hydrostatic stresses. The equilibrium surface is a 3D paraboloid in the coordinates T , q_{11} , q_{12} and q_{22} (see Fig. 7.1a,b for a particular case when $q_{12} = 0$ and the surface is a 2D paraboloid). Eq. (7.24) generalizes the Sekerka and Cahn [73] result which was derived for an elastically isotropic solid. The quadratic form on the right hand side of Eq. (7.24) is positive-definite because it can be formally identified with work of elastic straining from a stress-free state to a state with $\sigma_{ij} = q_{ij}$, which is always positive for a stable crystal. Thus, if $\Delta\bar{h}$ is positive (as it usually is for melting), then the equilibrium temperature decreases under non-hydrostatic stresses regardless of their sign.

For some cases it is advantageous to reformulate Eq. (7.24) in terms of strains instead of stresses. An expression for the equilibrium temperature as a function of lateral components of the strain tensor is derived in Section 7.7. The strain formulation will be used in Part II of this work.

Combining Eqs. (7.3) and (7.24) we can evaluate the change in the chemical potential μ^f in the fluid due to deviation from hydrostatic equilibrium along a path defined by solid-fluid coexistence at a constant p :

$$\mu^f(T, p_H) - \mu^f(T_H, p_H) = \frac{\bar{s}^f \Omega_0^s T_H}{2\Delta\bar{h}} \sum_{i,j,k,l=1,2} S_{ijkl} q_{ij} q_{kl}. \quad (7.25)$$

To evaluate the stability of the fluid with respect to crystallization, μ^f should be compared with the chemical potential, μ_*^s , of a hydrostatic solid at the same temperature and the same pressure. The latter can be evaluated by

$$\mu_*^s(T, p_H) = \mu^f(T_H, p_H) - \bar{s}^s (T - T_H). \quad (7.26)$$

Thus,

$$\mu^f(T, p_H) - \mu_*^s(T, p_H) = -\Delta\bar{s} (T - T_H) = \frac{\Omega_0^s}{2} \sum_{i,j=1,2} S_{ijkl} q_{ij} q_{kl}, \quad (7.27)$$

where we used Eq. (7.24). Because this difference is positive, the fluid equilibrated with a non-hydrostatic solid is unstable with respect to crystallization to a hydrostatic solid.

If the initial hydrostatic state is a special point with $\Delta\bar{s} = 0$, then we keep the quadratic term in Eq. (7.23) to obtain

$$(T - T_H)^2 = -\frac{\Omega_0^s}{\left(\frac{\partial\Delta s}{\partial T}\right)_H} \sum_{i,j,k,l=1,2} S_{ijkl} q_{ij} q_{kl}. \quad (7.28)$$

Recall that the quadratic form $\Sigma S_{ijkl} q_{ij} q_{kl}$ is positive-definite. Therefore, if $(\partial\Delta s/\partial T)_H > 0$ as in the case of ^3He melting [78], the only solution of this equation is $T = T_H$ and $q_{ij} = 0$. Thus, any infinitely small non-hydrostatic stress applied at constant p destroys the phase equilibrium. But if $(\partial\Delta s/\partial T)_H < 0$, then Eq. (7.28) has two solutions with opposite signs of $T - T_H$ for each nonzero q_{ij} . Geometrically, the vicinity of this bifurcation point can be represented by two ellipsoidal 3D-cones with touching tips in the 4D configuration space of T , q_{11} , q_{12} and q_{22} (see Fig. 7.1c for a particular case of $q_{12} = 0$ when the cones are 2D surfaces). Indeed, at a fixed value of $|T - T_H|$ Eq. (7.28) defines an ellipsoid in the coordinates q_{ij} . In the full space of T and q_{ij} , there are two such ellipsoids lying in hyperplanes intersecting the temperature axis at $\pm(T - T_H)$. The dimensions of the ellipsoids scale linearly with $|T - T_H|$ and shrink to a point at $|T - T_H| \rightarrow 0$, producing 3D double-cone. If all components of q_{ij} are increased simultaneously in proportion to each other, then $T - T_H$ increases, or respectively decreases, linearly with q_{ij} .

Isothermal path

A third example is an isothermal variation from the hydrostatic state H . Just as in the isobaric case, the system has three degrees of freedom. Eq. (7.17) gives the phase equilibrium

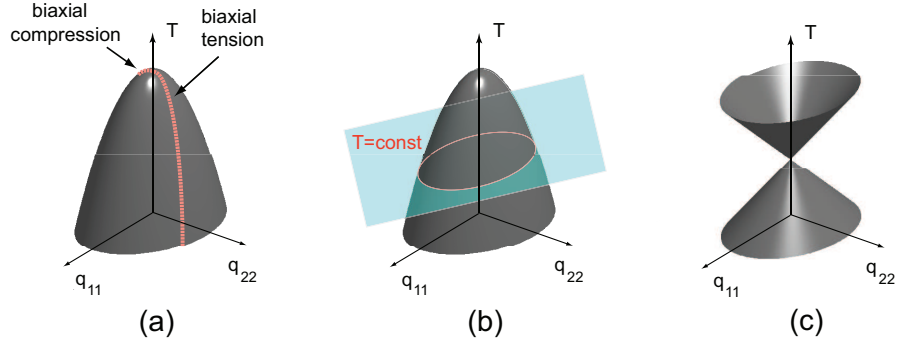


Figure 7.1: Schematic illustration of solid-fluid coexistence surfaces at constant pressure p in the fluid and $q_{12} = 0$ in the solid. The equilibrium temperature T is plotted as a function of two remaining non-hydrostatic components of the stress in the solid. (a) Path of biaxial tension and compression on the coexistence surface. (b) Iso-fluid path obtained by intersection of the paraboloid with an isothermal plane. (c) Phase coexistence surface when the initial hydrostatic state is a special point. If $q_{12} \neq 0$, the coexistence surfaces shown here become 3D and are difficult to visualize, but they remain paraboloids in (a) and (b) and an ellipsoidal double-cone in (c).

condition

$$-\Delta\bar{\Omega}(p - p_H) - \frac{1}{2} \left(\frac{\partial\Delta\Omega}{\partial p} \right)_H (p - p_H)^2 + \frac{\Omega_0^s}{2} \sum_{i,j=1,2} S_{ijkl} q_{ij} q_{kl} = 0. \quad (7.29)$$

If $\Delta\bar{\Omega}$ is finite and the second term is small in a given pressure range, we obtain the equation

$$p - p_H = \frac{\Omega_0^s}{2\Delta\bar{\Omega}} \sum_{i,j,k,l=1,2} S_{ijkl} q_{ij} q_{kl}, \quad (7.30)$$

showing that the pressure change is quadratic in non-hydrostatic stresses. Combining Eqs. (7.3) and (7.30), the change in the chemical potential μ^f in the fluid due to the deviation from the hydrostatic equilibrium along a path defined by solid-fluid coexistence at a constant T is

$$\mu^f(T_H, p) - \mu^f(T_H, p_H) = \frac{\bar{\Omega}^f \Omega_0^s}{2\Delta\bar{\Omega}} \sum_{i,j,k,l=1,2} S_{ijkl} q_{ij} q_{kl}. \quad (7.31)$$

Similarly to the isobaric variation, the change in chemical potential is quadratic in non-hydrostatic stresses. Crystallization of the fluid to a hydrostatic solid is accompanied by a change in the chemical potential

$$\mu^f(T_H, p) - \mu_*^s(T_H, p) = \Delta\bar{\Omega} (p - p_H) = \frac{\Omega_0^s}{2} \sum_{i,j=1,2} S_{ijkl} q_{ij} q_{kl}, \quad (7.32)$$

where we used the chemical potential of a hydrostatic solid

$$\mu_*^s(T_H, p) = \mu^f(T_H, p_H) + \bar{\Omega}^s (p - p_H). \quad (7.33)$$

Since the right-hand side of Eq. (7.32) is positive, the liquid is unstable against crystallization to a hydrostatic solid.

For a special point with $\Delta\bar{\Omega} = 0$, the linear term in Eq. (7.29) drops out and we obtain

$$(p - p_H)^2 = \frac{\Omega_0^s}{\left(\frac{\partial\Delta\Omega}{\partial p}\right)_H} \sum_{i,j,k,l=1,2} S_{ijkl} q_{ij} q_{kl}. \quad (7.34)$$

If $(\partial\Delta\Omega/\partial p)_H < 0$, this equation has only a zero solution, so that any non-hydrostatic stress applied at constant T destroys the phase equilibrium. If $(\partial\Delta\Omega/\partial p)_H > 0$, the hydrostatic state is a bifurcation point generating two different equilibrium pressures $\pm(p - p_H)$ for each set of non-hydrostatic stresses q_{ij} . The geometric model of touching cones is again valid but the configuration space is now p, q_{ij} (in Fig. 7.1c, the T -axis is replaced by p). Increasing all components of q_{ij} in proportion to each other results in a linear shift of the equilibrium pressure up or down.

7.2.2 Deformation of a solid in equilibrium with the same fluid

So far we have only discussed equilibrium processes in which the solid-fluid system deviates away from its initial hydrostatic state along a hydrostatic, isobaric or isothermal paths. We will now consider equilibrium processes in which both T and p remain constant. Because temperature and pressure uniquely define the state of a single-component fluid, it is only the solid that can change its state due to the additional degrees of freedom associated with the non-hydrostatic stresses q_{11} , q_{12} and q_{22} . Due to these degrees of freedom, solids in different non-hydrostatic states can be equilibrated with the same fluid. We will refer to such states as “iso-fluid” states. Accordingly, processes in which the solid changes its state while maintaining equilibrium with the same fluid will be called iso-fluid process.

The equation of iso-fluid processes is obtained from Eq. (7.17) by fixing the values of $T - T_H$ and $p - p_H$. The general form of this equation is

$$\sum_{i,j=1,2} S_{ijkl} q_{ij} q_{kl} = \text{const}, \quad (7.35)$$

describing an ellipsoid in the 3D space of q_{11} , q_{12} and q_{22} . If the constant in this equation is zero, the ellipsoid shrinks to a point and the only solution is $q_{ij} = 0$, which precludes any processes. If the constant is not zero, the ellipsoid has finite dimensions and does not contain a point at which $q_{ij} = 0$. Thus, an iso-fluid path cannot contain a hydrostatic point. The solid must always remain in a non-hydrostatic state.

As a simple illustration, consider processes in which q_{12} remains zero. At a fixed pressure, the equilibrium temperature is a function of the principal non-hydrostatic stresses q_{11} and q_{22} . For a non-special point, this function is given by Eq. (7.24) and its plot is a paraboloid shown in Fig. 7.1b. The plane $T = \text{const}$ intersects the paraboloid along an ellipse on which both p and T are constant and thus the state of the fluid is fixed. This ellipse contains all iso-fluid processes possible in the system (at $q_{12} = 0$). During such processes, the solid undergoes a compression along one principal direction of stress and simultaneous tension along the other direction, so that Eq. (7.35) is satisfied.

Referring to Fig. 7.1b, one can imagine that if the temperature increases, the size of the ellipse decreases until it collapses to a single point at $T \rightarrow T_H$. At this point the isothermal plane touches the paraboloid at the hydrostatic point ($T = T_H, q_{11} = q_{22} = 0$), prohibiting any changes in the state of the solid without changing the state of the fluid. This construction graphically illustrates the impossibility of iso-fluid processes passing through a hydrostatic state. The latter conclusion remains valid for special points, which is evident from examining the double-cone plot in Fig. 7.1c.

Iso-fluid processes can also be represented by ellipsoidal surfaces (ellipses if $e_{12} = \text{const}$) in terms of lateral strains instead of stresses. An expression for the slope $(de_{22}/de_{11})_{T,p,e_{12}}$, which will be used Part II of this work [74], is derived in Section 7.8.

7.3 Methodology of atomistic simulations

In this Section we describe our methodology of atomistic simulations of solid-liquid equilibrium. The simulations included non-hydrostatic variations of two types: (i) at zero pressure in the liquid (isobaric path) and (ii) at constant temperature (isothermal path). As the initial hydrostatic state H we chose the liquid at zero pressure and the stress-free solid in equilibrium with each other. For the material which we study, this state is not a special point, i.e. both $\Delta\bar{\Omega}$ and $\Delta\bar{s}$ are finite. Furthermore, within the range of simulated non-hydrostatic stresses, $\Delta\Omega$ and Δs vary but do not go through zero.

7.3.1 Simulated models

We used copper as a model material. The simulation block composed of 23,040 atoms contained a layer of solid phase sandwiched between two liquid layers. The (110) oriented solid-liquid interfaces were perpendicular to the z direction of the block. The x and y directions were parallel to crystallographic directions $[\bar{1}10]$ and $[001]$, respectively. The boundary conditions in the x and y directions were periodic. Two types of boundary conditions were used in the z direction. For simulations at constant zero pressure in the

liquid, the liquid layers were terminated at open surfaces. The exposure of the liquid layers to vacuum ensured $p = 0$ in the liquid. For isothermal simulations, periodic boundary conditions were applied in the z direction.

To create non-hydrostatic states of stress in the solid, the block was subject to tensile or compressive deformations parallel to the coordinate axes by scaling the respective dimensions of the block. Due to crystallographic symmetry of the solid, the principal axes of stress and strain coincide and are parallel to the coordinate axes. For example, an applied biaxial strain creates a biaxial state of stress.

Four types of deformation were applied to the initially hydrostatic simulation block: (i) biaxial compression parallel to the lateral directions x and y , (ii) biaxial tension in the x and y directions, (iii) compression in x with simultaneous tension in y , and (iv) compression in y with simultaneous tension in x . All strains applied are listed in Tables 7.2 and 7.3 together with the stresses that arise. The stress components range from -2.3 GPa to 3.4 GPa. In some of the cases (iii) and (iv), σ_{11} and σ_{22} were close to each other in magnitude but opposite in sign, so that the trace ($\sigma_{11} + \sigma_{22} + \sigma_{33}$) was small.

Application of strain to the initially stress-free block destroyed the phase equilibrium. To re-equilibrate the phases at a constant zero pressure or at a constant temperature, different MD ensembles were implemented as explained below.

7.3.2 Simulations at constant zero pressure in the liquid

To equilibrate the phases at $p = 0$ in the liquid, a 2 ns long MD run in micro-canonical (NVE) ensemble was performed [62]. The zero pressure in the liquid was maintained by the liquid surfaces. During the equilibration, the temperature changed from the initial T_H to an equilibrium value T as a result of partial melting or crystallization of the phases. For example, if a part of the solid melts, the potential energy of the system increases by the amount of latent heat expended for the melting. To keep the total energy of the system constant, this heat is taken from the kinetic energy of atoms, resulting in a decrease in temperature. This temperature decrease reduces and eventually reverses the thermodynamic

driving force of melting. Similar processes occur during partial crystallization of the liquid. As a result, after equilibration the temperature and the amounts of phases fluctuate around their equilibrium average values by spontaneous melting-crystallization processes. To verify that the system has reached the true equilibrium, we checked that the temperature and energy distributions were Gaussian. We also verified that the average amounts of solid and liquid phases remained constant after the equilibration.

The equilibration stage was followed by a 40 ns production run using again *NVE* ensemble. During this run, snapshots of the system were saved every 0.01 ns. The snapshots contained information about positions and energies of all atoms, as well as the atomic stresses. This data was used at the post-processing stage. The equilibrium temperatures T reported below were computed by averaging over the production stage.

7.3.3 Simulations at constant temperature

Isothermal equilibration was achieved by a 2 ns MD run in the canonical (*NVT*) ensemble using a Noose-Hoover thermostat at T_H and all-periodic boundary conditions. During the run, the liquid pressure p changes from zero to an equilibrium value. The equilibration is reached due to the constant volume of the system and the existence of the volume effect of melting. Indeed, consider a fluctuation in which a small part of the solid melts or crystallizes. Because the atomic volume of solid Cu, Ω^s , is smaller than the atomic volume of liquid Cu, Ω^l , in the simulated temperature and strain range, this fluctuation results in an increase, or respectively decrease, of pressure in the liquid. This change of p counteracts further melting or crystallization and eventually stops them. As a result, p begins to fluctuate around an equilibrium value. As in the isobaric case, the equilibration was followed by a 40 ns *NVT* production run to compute the pressure and stress and to produce snapshots for subsequent post-processing.

7.3.4 Calculation of elastic constants and elastic compliances

To compare the MD results with the equilibrium temperatures and pressures predicted by Eqs. (7.24) and (7.30), we needed to know the elastic compliances of the material at T_H . The elastic constants and compliances were computed by MD simulations in the NVT ensemble at T_H using a Noose-Hoover thermostat. The solid block with periodic boundary conditions in all directions had the same crystallographic orientation and dimensions as the solid layer in the solid-liquid simulations. To compute the components of the elastic constant tensor C_{ijkl} , three different types of elastic deformations were applied to the initially unstressed solid. Each time the block was deformed along one of the principal axes of strain, keeping two other components of strain zero. During subsequent MD simulations at T_H , the stresses produced by the deformation were computed for each of the three directions of the strain. The elastic constants C_{ijkl} were computed from linear fits of stress versus strain. Inverting the elastic constants tensor gives the elastic compliances tensor S_{ijkl} .

7.4 Results

7.4.1 The phase coexistence surface

Due to crystal symmetry and the geometric setup of our system, the principal axes of the stress and strain coincide with the coordinate axes, resulting in $q_{12} = 0$ in the stressed solid. At $p = 0$, the heat of melting equals the difference, $\Delta\bar{u}$, between the energies per atom of the phases. Eq. (7.24) thus reduces to

$$T - T_H = -\frac{\bar{\Omega}^s T_H}{2\Delta\bar{u}} [S_{1111}\sigma_{11}^2 + 2S_{1122}\sigma_{11}\sigma_{22} + S_{2222}\sigma_{22}^2]. \quad (7.36)$$

For isothermal variations at $T = T_H$ and $q_{12} = 0$, Eq. (7.30) becomes

$$p - p_H = \frac{\bar{\Omega}^s T_H}{2\Delta\bar{\Omega}} [S_{1111}q_{11}^2 + 2S_{1122}q_{11}q_{22} + S_{2222}q_{22}^2]. \quad (7.37)$$

Table 7.1: Elastic constants and elastic compliances of Cu at $T_H = 1327$ K with $[\bar{1}10]$, $[001]$ and $[110]$ crystallographic directions aligned with x , y and z axes. Due to crystal symmetry, there are only four distinct elastic constants (compliances), only three of which are independent. The two-index elastic constants in the cubic system at T_H are $c_{11} = 106.6$ GPa, $c_{12} = 86.4$ GPa and $c_{44} = 41.1$ GPa, which are smaller than the 0 K values $c_{11} = 169.9$ GPa, $c_{12} = 122.6$ GPa and $c_{44} = 76.2$ GPa.

Elastic constants	C_{1111}	C_{2222}	C_{3333}	C_{1122}	C_{1133}	C_{2233}
Value (GPa)	137.6	105.7	137.6	86.4	55.5	86.4
Elastic compliances	S_{1111}	S_{2222}	S_{3333}	S_{1122}	S_{1133}	S_{2233}
Value (10^4 GPa $^{-1}$)	157.7	353.8	157.7	-158.4	35.9	-158.4

Table 7.2: Lateral strains and stresses in the solid and the corresponding solid-liquid equilibrium temperatures predicted by Eq. (7.36) (T_{Theor}) and computed directly from MD simulations (T_{MD}) for variations at constant zero pressure in the liquid.

e_{11} (%)	e_{22} (%)	σ_{11} (GPa)	σ_{22} (GPa)	T_{MD} (K)	T_{Theor} (K)
-1.196	biaxial	-2.147	-1.262	1308.9	1308.2
-0.895	biaxial	-1.563	-0.936	1316.5	1316.1
-0.593	biaxial	-1.048	-0.642	1321.9	1321.8
-0.290	biaxial	-0.509	-0.322	1324.9	1325.2
0.000	biaxial	0.004	-0.009	1326.4	1326.4
0.165	biaxial	0.286	0.167	1325.5	1326.0
0.333	biaxial	0.577	0.350	1324.0	1325.0
0.628	biaxial	1.077	0.674	1321.2	1321.5
0.928	biaxial	1.583	1.010	1315.0	1315.8
1.236	biaxial	2.095	1.360	1306.4	1307.3
1.544	biaxial	2.604	1.714	1295.0	1296.1
2.020	biaxial	3.394	2.282	1271.0	1275.6
-3.399	5.559	-1.652	1.480	1267.7	1242.3
2.240	-3.469	0.720	-0.433	1309.6	1315.9
1.798	-2.899	0.448	-0.489	1315.2	1318.5
-0.960	1.4709	-0.414	0.301	1323.0	1322.2

Table 7.1 summarizes the elastic constants and elastic compliances of the solid computed by MD simulations at T_H for the particular crystallographic orientation implemented in this work. The elastic constants recomputed to the cubic coordinate system and expressed via the standard two-index notations c_{ij} are included in the caption to this Table. For the hydrostatic state at temperature T_H , the energies per atom in the solid and liquid phases

Table 7.3: Biaxial lateral strains, stresses in the solid, and the equilibrium pressures in the liquid predicted by Eq. (7.37) (p_{Theor}) and computed directly from MD simulations (p_{MD}) for isothermal variation at T_H .

e (%)	σ_{11}^s (GPa)	σ_{22}^s (GPa)	p_{MD} (GPa)	p_{Theor} (GPa)
-1.155	-2.256	-1.479	0.339	0.348
-0.803	-1.501	-0.970	0.174	0.168
-0.466	-0.838	-0.552	0.068	0.059
0.000	0.000	0.000	0.000	0.000
0.300	0.519	0.296	0.041	0.030
0.631	1.015	0.590	0.152	0.135
0.803	1.269	0.723	0.234	0.225
1.155	1.709	0.920	0.558	0.523
1.266	1.827	0.965	0.686	0.647
1.503	2.058	1.014	1.056	1.005
1.650	2.180	1.015	1.339	1.292
1.740	2.238	0.979	1.619	1.563

were found to be $\bar{u}^s = -3.17$ eV and $\bar{u}^l = -3.04$ eV, respectively, giving the latent heat $\Delta\bar{u} = 0.13$ eV. The atomic volumes of the phases at T_H were $\bar{\Omega}^s = 12.75 \text{ \AA}^3$ and $\bar{\Omega}^l = 13.37 \text{ \AA}^3$, respectively. Using this data, we computed the equilibrium temperatures T at zero pressure in the liquid from Eq. (7.36) and the equilibrium liquid pressures p at constant temperature T_H from Eq. (7.37) for a set of non-hydrostatic stresses q_{ij} . The results are reported in Figs. 7.2-7.4 and in Tables 7.2 and 7.3.

We will now compare these theoretical predictions with results of MD simulations. For isobaric variations, Table 7.2 demonstrates that, for biaxial stresses, the predicted temperatures agree with the MD results within 1 K or better, except for the largest stress when the discrepancy reaches 4.6 K. For some of the mixed tension-compression loads associated with relatively large strains, the discrepancies become larger. Nevertheless, the entire set of MD points shows a very close agreement with the paraboloidal coexistence surface predicted by Eq. (7.36) (Fig. 7.2). In particular, for all stresses tested, the coexistence temperature is reduced in comparison with T_H independently of the signs of the stress components. Furthermore, calculations from Eq. (7.36) demonstrate excellent agreement with

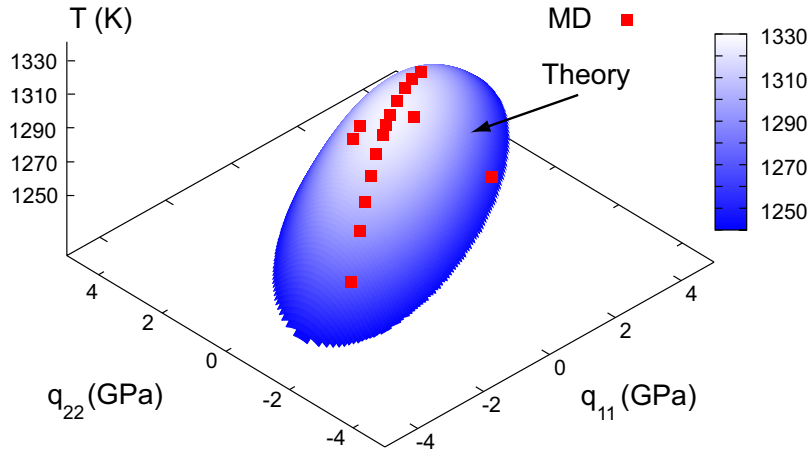


Figure 7.2: Equilibrium temperature T as a function of lateral stresses σ_{11} ($[\bar{1}10]$ direction) and σ_{22} ($[001]$ direction) in the solid computed for copper with the (110) solid-liquid interface. Pressure in the liquid remains zero. The blue surface is the theoretical prediction from Eq. (7.36), the red points are results of direct MD simulations.

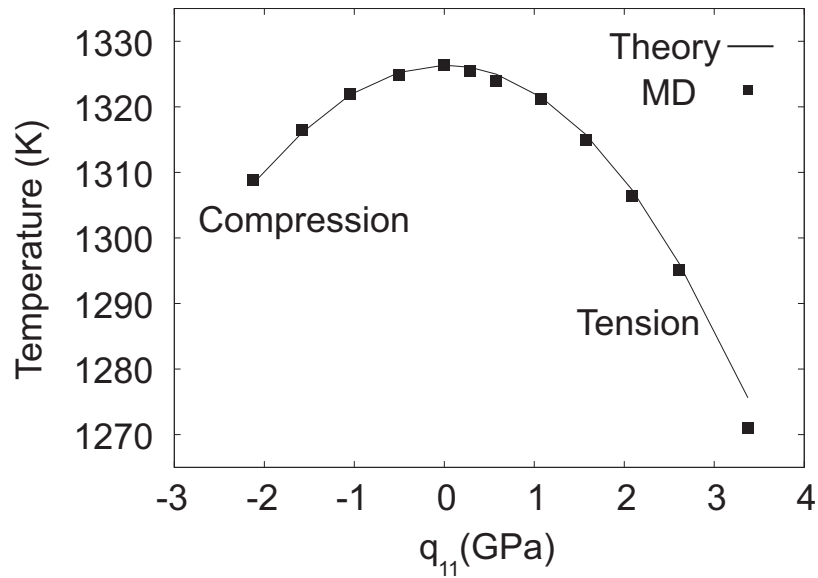


Figure 7.3: Equilibrium temperature as a function of the non-hydrostatic stress component q_{11} in the solid subject to biaxial tension or compression. Pressure in the liquid remains zero. The points are results of direct MD simulations, the line was computed from Eq. (7.36).

MD simulations for the biaxial tension and compression paths as shown in Fig. 7.3.

In addition, the MD results directly confirm that the hydrostatic part of the stress tensor,

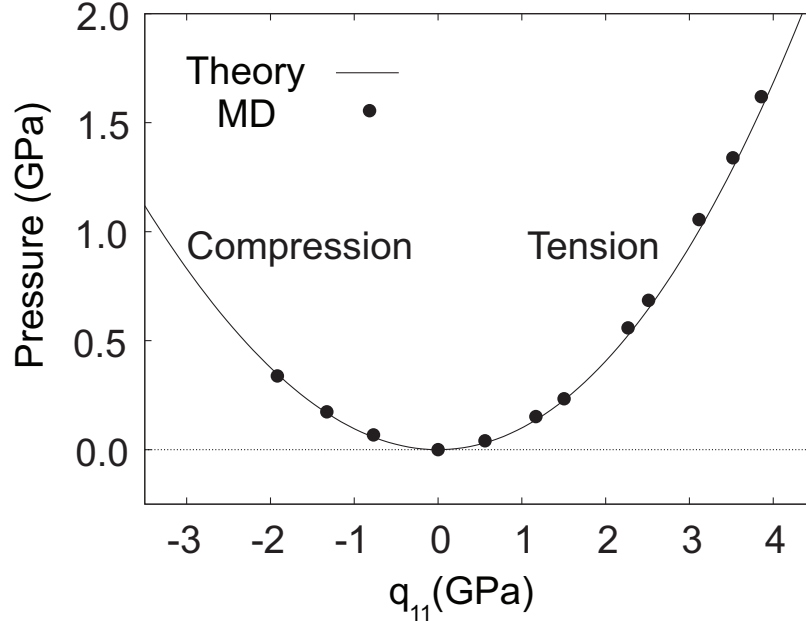


Figure 7.4: Equilibrium pressure in the liquid as a function of the non-hydrostatic stress component q_{11} in the solid subject to biaxial tension or compression at a constant temperature T_H . The points are results of direct MD simulations, the line was computed from Eq. (7.37).

$\bar{p} = -(\sigma_{11} + \sigma_{22} + \sigma_{33})/3$, is not a meaningful physical parameter to characterize the effect of stresses on phase equilibrium. As was discussed by Sekerka and Cahn [73], previous theories attempting to fold the stress effect into the “solid pressure” \bar{p} were erroneous. For example, the last but one line in Table 7.2 refers to a mixed-load case when $\sigma_{11} = 0.448$ GPa, $\sigma_{22} = -0.489$ GPa and $\sigma_{33} = 0$, thus giving a very small “solid pressure” $\bar{p} = -0.014$ GPa. Nonetheless, the reduction in temperature of about 10 K found for this case is close to that for biaxial compression by $e_{11} = -0.895\%$ when $\bar{p} = 0.833$ GPa and for biaxial tension by $e_{11} = 0.928\%$ when $\bar{p} = -0.864$ GPa. This example is a clear demonstration that it is the combination of non-hydrostatic stress components q_{ij} appearing in the right-hand side of Eq. (7.36) that determines the temperature depression $T - T_H$, not \bar{p} alone.

For isothermal variations at $T = T_H$ (Table 7.3), the equilibrium liquid pressure increases as the solid deviates from the hydrostatic state of stress regardless of the sign of

the deviation. Fig. 7.4 shows an excellent agreement between the liquid pressures predicted theoretically from Eq. (7.37) and obtained by MD simulations for biaxial tension and compression.

7.4.2 Instability of non-hydrostatic systems

As discussed in Sec. 7.2, a liquid equilibrated with a non-hydrostatically stressed solid is unstable or metastable and should eventually crystallize into a hydrostatically stressed solid. The liquid is metastable when there is a nucleation barrier that prevents it from immediate crystallization into a hydrostatic solid. If liquid is equilibrated with a solid under sufficiently large non-hydrostatic stresses, the barrier can be reduced to a level when crystallization can be observed on a given time scale.

To verify this prediction, we performed MD simulations of a solid-liquid system in which the solid was stressed by $\sigma_{11} = 2.3$ GPa and $\sigma_{22} = 3.4$ GPa. As above, the *NVE* ensemble was implemented to bring the system to phase equilibrium at $p = 0$, which was reached at $T = 1271$ K (66 K below T_H). The size of the simulation block was then increased to 207,360 atoms by multiplying the x and y dimensions by a factor of three while keeping the same dimension in the z direction. The ensemble was switched to *NVT* to allow heat absorption by a thermostat should crystallization begin.

After 0.12 ns of the *NVT* simulation, the liquid began to crystallize. Fig. 7.5a shows a typical snapshot of the simulation block during the crystallization process. The block contains a region of the initial solid under tension, newly crystallized solid regions, and the remaining liquid. The stress profiles (Fig. 7.5b) reveal that the initial solid has approximately the same stresses as prior to the crystallization. The new solid regions grow under a much smaller stress and are nearly hydrostatic (within uncertainties caused by fluctuations). The stress in the liquid layers is equally small and also nearly hydrostatic as it should. The peaks at the liquid surfaces are due to the surface tension. During the subsequent 0.5 ns time the remaining liquid crystallizes completely.

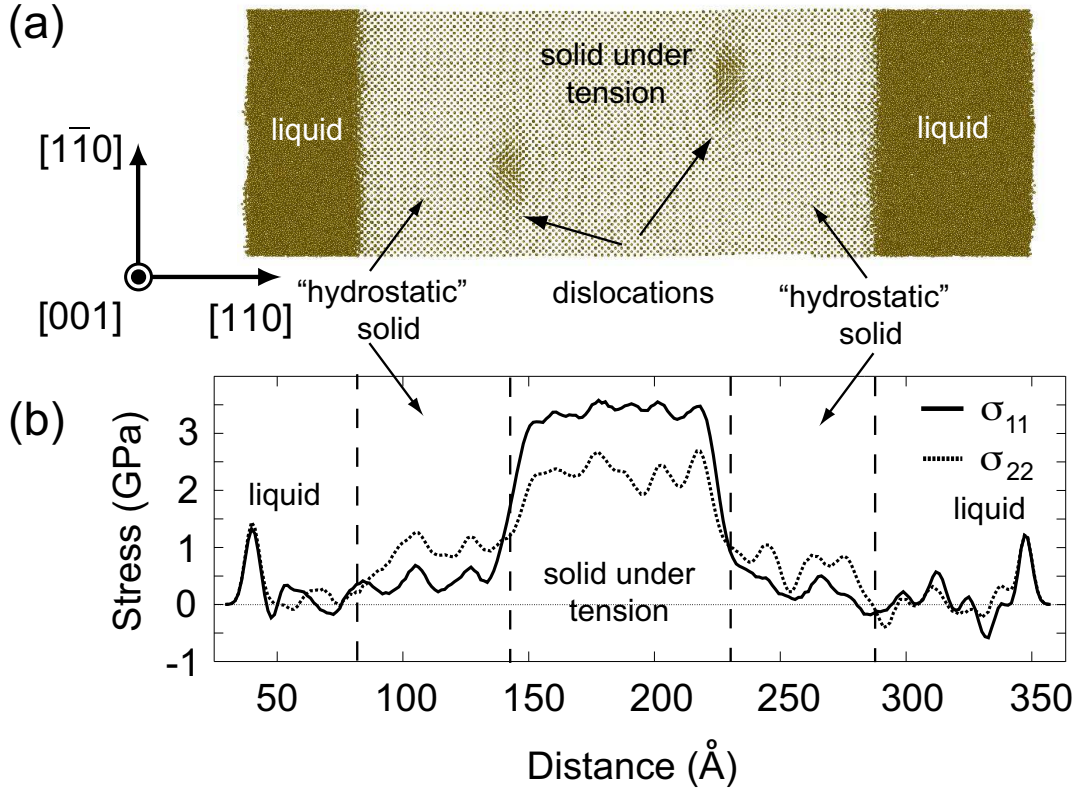


Figure 7.5: (a) Snapshot of the simulation block during crystallization at $T = 1271$ K. (b) Profiles of the lateral components of stress σ_{11} and σ_{22} across the simulation block. Before the crystallization, the stresses in the solid were $\sigma_{11} = 3.4$ GPa and $\sigma_{22} = 2.3$ GPa.

Upon completion of crystallization, the block contains two solid-solid interfaces separating layers of the same material with the same crystallographic orientation but slightly different lattice constants due to different stress states. The lattice misfit between the old and new solid regions is accommodated by $\frac{1}{2}[110]$ edge dislocations [83, 84], which were identified by construction of Burger circuits. These dislocations dissociate into Shockley partials on $\{111\}$ gliding planes, which are not parallel to the interfaces. As a result, the dislocation lines are not straight but have zigzag shapes with $\langle 211 \rangle$ segments dissociated on $\{111\}$ facets. Fig. 7.6a shows the entire simulation block with the solid-solid interfaces, while Fig. 7.6b illustrates separately the zigzag dislocation lines with dissociated segments.

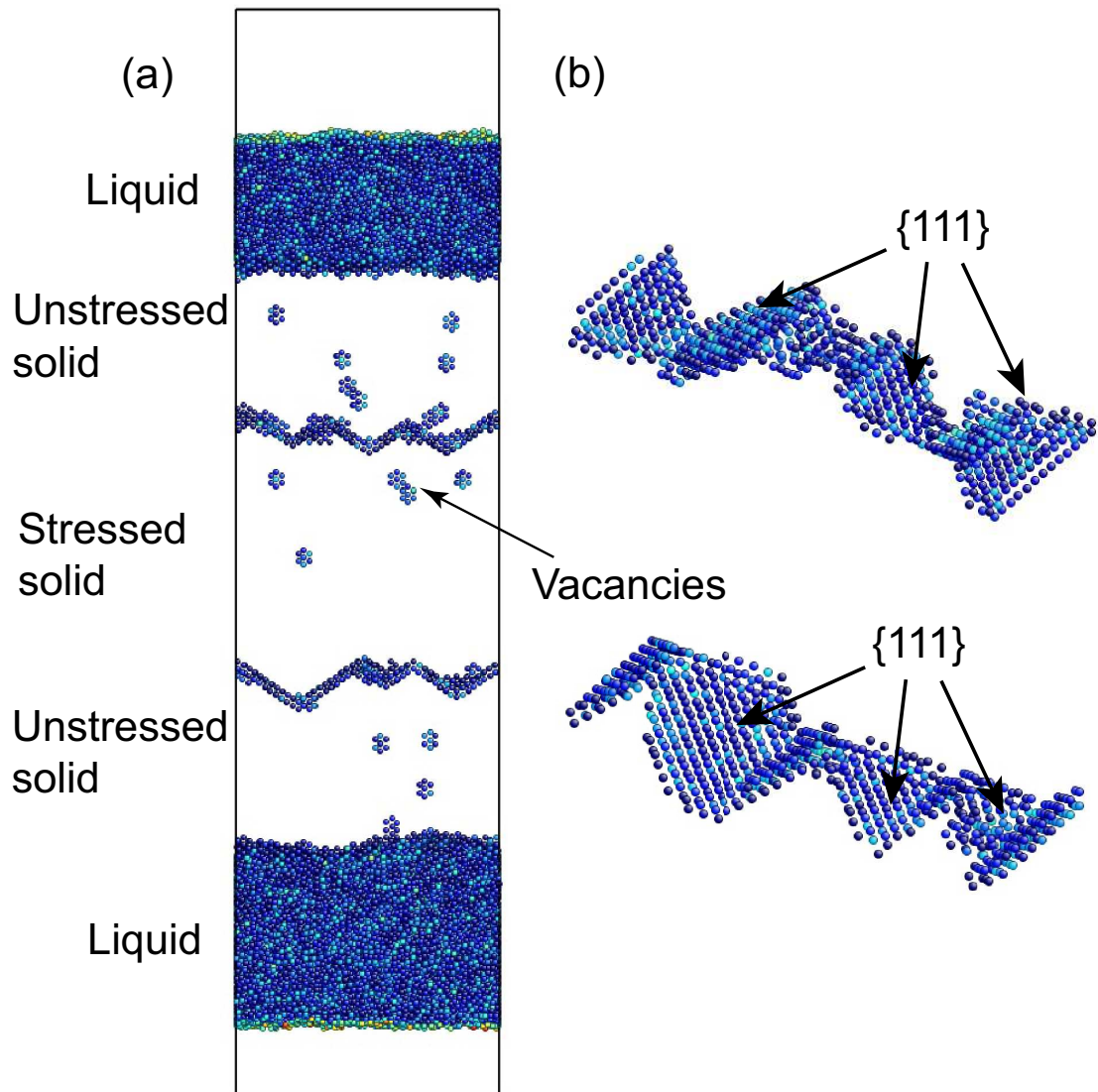


Figure 7.6: (a) Simulation block with edge dislocations visualized using central symmetry analysis. Atoms with large values of the symmetry parameter are invisible. (b) Different views of $\frac{1}{2}[110]$ edge dislocations showing its dissociation into partials.

The solid contains a few vacancies revealed by the centrosymmetry parameter [85].

The delayed start of the crystallization is consistent with the existence of a nucleation barrier. Furthermore, similar simulations in a block containing only 23,040 atoms did not produce a crystallization on time scales accessible by MD, suggesting that the barrier is size-dependent.

7.5 Discussion and conclusions

As pointed out in Sec. 7.1, the problem of solid-fluid equilibrium is relevant to many materials phenomena and applications. It is important to have a clear understanding of the effect of non-hydrostatic stresses on solid-fluid equilibrium. Unfortunately, literature contains a number of misconceptions, such as the “solid pressure” discussed in Section 7.4.1.

For a single-component system, Gibbs [13] derived an equation (406) which is similar to our Eq. (7.5) and to Sekerka and Cahn’s [73] Eq. (14) (they assumed $dp = 0$). On p. 199 Gibbs pointed out that if $p = \text{const}$, equation (406) can be used for predicting how the equilibrium temperature is affected by strain variations in the solid. He then noted that if the initial state of the solid is hydrostatic, the differentials of temperature with respect to strain components vanish. This comment can be understood, although it was not stated by Gibbs explicitly, that non-hydrostatic deformations produce high-order effects on equilibrium temperature.

Sekerka and Cahn [73] employed isotropic linear elasticity to show that this effect is quadratic in non-hydrostatic stresses q_{ij} , which is consistent with Gibbs. Their analysis was focused on isobaric variations from a hydrostatic state and assumed a non-zero latent heat (a non-special point).

In this work we have extended Sekerka and Cahn’s work [73] in several ways. We treat elastic deformations of the solid using anisotropic linear elasticity and a generalized Hooke’s law which includes the thermal expansion effect η , see Eq. (7.6). In the future, this approach could be readily generalized to multicomponent systems, in which η is a function of not only temperature but also chemical composition (compositional strain) [24]. Our main result is expressed by Eq. (7.17) which relates deviations of the equilibrium temperature, pressure and lateral stress components from their hydrostatic values. This equation permits predictions of the non-hydrostaticity effect on the equilibrium temperature and pressure. Furthermore, this effect has been analyzed not only for non-special points considered by Gibbs [13] and Sekerka and Cahn [73] but also special points where the latent heat or volume

effect go through zero. To make our equations and their ramifications more intuitive, we have presented a geometric interpretation of the phase coexistence surface as a quadric or its sections by appropriate planes.

For non-special points, our analysis predicts that if pressure in the liquid is fixed, the change in the equilibrium temperature is quadratic in q_{ij} , which is in agreement with Sekerka and Cahn's result for isotropic solids [73]. If temperature is fixed, the change in the equilibrium pressure is quadratic in q_{ij} . If both temperature and pressure are fixed, which fixes the thermodynamic state of the fluid, the stress state of the solid can still be varied along a so-called "iso-fluid" path without violating the phase coexistence. In short, the same fluid can be equilibrated with many solids, all of which are non-hydrostatic.

In special points, the stress effect can be very different from that in non-special points. Depending on the material properties, non-hydrostatic stresses can either completely destroy the phase coexistence or produce a bifurcation in which the equilibrium temperature or pressure can either increase or decrease. Special points exist in a number of systems. It would be interesting to test our predictions for such systems by experiment or atomistic simulations in the future.

Our analysis for non-special points has been tested against MD simulations of solid-liquid equilibrium in copper. Very encouraging agreement has been observed between our theory and the simulations for both isobaric and isothermal variations from hydrostatic equilibrium.

Another interesting effect studied in this work is the instability of the fluid with respect to crystallization to a hydrostatic solid. This instability was discussed in detail by Gibbs [13] (p. 196-197) who showed that the chemical potential of the solid component in a fluid equilibrated with a non-hydrostatic solid is greater than in a fluid equilibrated with a hydrostatic solid at the same temperature and pressure. Gibbs concluded that the fluid is always supersaturated with respect to the solid component unless the solid is hydrostatic. He predicted that, if a fluid equilibrated with a non-hydrostatic solid contains a fragment of hydrostatic solid composed of the same substance, this fragment will tend to grow. Even

if such fragments are not present in the fluid, Gibbs asserted that layers of hydrostatically stressed solid will grow on the surface of the non-hydrostatically distorted solid.

Formally, this latter prediction has been verified by our MD simulations, in which a nearly stress-free solid layer was found to grow on top of a stressed solid (Figs. 7.5 and 7.6). It should be noted, however, that Gibbs' discussion was for a fluid that contained not only the component of the solid (Gibbs always assumed that a homogeneous solid could be composed of only one component) but also at least one other component insoluble in the solid.² It is only under this condition that the chemical potential of the solid component in the fluid could vary at a fixed temperature and pressure.

By contrast, our analysis as well as simulations were for a truly single-component system. Nevertheless, we have shown that the chemical potential of a single-component fluid equilibrated with a non-hydrostatic solid composed of the same component is always larger than the chemical potential of a hydrostatic solid at the same temperature and pressure. Specifically, the chemical potential differences for isobaric and isothermal deformations are given by Eqs. (7.27) and (7.32), respectively. This result is especially intuitive when $\Delta\bar{h} > 0$, as in our simulations for the melting of copper. In this case Eq. (7.24) predicts that the fluid equilibrated with a non-hydrostatic solid is overcooled relative to the hydrostatic melting point. This overcooled fluid is ready to crystallize to a hydrostatic solid. It is important to recognize that Eqs. (7.27) and (7.32) are valid regardless of the signs of the latent heat or the transformation volume. In particular, since the latent heat of melting of ^3He is negative at temperatures below the minimum of the melting pressure [77, 78], the liquid equilibrated with a non-hydrostatic solid is overheated relative to the hydrostatic state. Nevertheless, this liquid is still unstable against crystallization to a hydrostatic solid. This fact, which was noted by Sekerka and Cahn (their footnote 7) [73], follows immediately from Eq. (7.27).

²The fluid components insoluble in the solid can be composed of chemical elements whose concentrations in the solid are negligibly small. As another case, the liquid can be composed of the same elements as the solid but have a different chemical composition. In the latter case, the difference between the composition of the fluid and the fixed composition of the solid can be formally described in terms of additional components insoluble in the solid. When the chemical compositions of the solid and fluid remain equal, the system can be treated as a single-component one.

Likewise, non-hydrostatic distortions destabilize not only typical materials with $\Delta\bar{\Omega} > 0$ but also Si, Ge and other elements whose density increases upon melting.

Thus, our analysis shows that the Gibbsian prediction of crystallization of hydrostatic layers on surfaces of non-hydrostatically distorted solids remains valid also for single-component systems. Although we arrived at this conclusion in Sec. 7.2 assuming linear elasticity and the small-strain approximation, it actually reflects a general rule. In Section 7.9 we derive this rule from general principles of thermodynamics without any approximations.

Finally, some of our results can be applied to incoherent solid-solid interfaces. If the system is deformed along a path on which the one of the phases remains hydrostatic while the other is not, our equations can be applied by formally treating the hydrostatic phase as a “fluid”.

7.6 Maxwell relations for an elastic solid

In this section we derive Maxwell relations for a single-component solid phase whose elastic properties are described by Eq. (7.6) with a constant compliance tensor S_{ijkl} . Consider a thermodynamic function ϕ per atom of the solid phase, defined by

$$\phi = u^s - Ts^s + p\Omega^s. \quad (7.38)$$

Here, $-p$ is the principal component σ_{33} of the stress tensor whose other principal components are not necessarily equal to $-p$. Differentiating ϕ and using Eqs. (7.2) and (7.4), we obtain

$$d\phi = -s^s dT + \Omega^s dp + \Omega_0^s \sum_{i,j=1,2} q_{ij} de_{ij}. \quad (7.39)$$

After substituting e_{ij} from Eq. (7.6), this equation becomes

$$\begin{aligned}
d\phi &= - \left(s^s - \Omega_0^s \sum_{i,j=1,2} q_{ij} \eta'_{ij} \right) dT + \left(\Omega^s - \Omega_0^s \sum_{i,j,m=1,2,3} q_{ij} S_{ijmm} \right) dp \\
&+ \Omega_0^s \sum_{i,j,k,l=1,2} S_{ijkl} q_{ij} dq_{kl}.
\end{aligned} \tag{7.40}$$

Since Eq. (7.40) is a perfect differential in the variables T , p , q_{11} , q_{12} and q_{22} , the following Maxwell relations must be satisfied

$$- \frac{\partial \left(s^s - \Omega_0^s \sum_{i,j=1,2} q_{ij} \eta'_{ij} \right)}{\partial q_{kl}} = \frac{\partial \left(\Omega_0^s \sum_{i,j=1,2} S_{ijkl} q_{ij} \right)}{\partial T}, \quad k, l = 1, 2, \tag{7.41}$$

$$\frac{\partial \left(\Omega^s - \Omega_0^s \sum_{i,j,m=1,2,3} q_{ij} S_{ijmm} \right)}{\partial q_{kl}} = \frac{\partial \left(\Omega_0^s \sum_{i,j=1,2} S_{ijkl} q_{ij} \right)}{\partial p}, \quad k, l = 1, 2, \tag{7.42}$$

$$- \frac{\partial \left(s^s - \Omega_0^s \sum_{i,j=1,2} q_{ij} \eta'_{ij} \right)}{\partial p} = \frac{\partial \left(\Omega^s - \Omega_0^s \sum_{i,j,m=1,2,3} S_{ijmm} q_{ij} \right)}{\partial T}. \tag{7.43}$$

In Eqs. (7.41) and (7.42), the terms in the right hand side are independent of T and p and the partial derivatives are zero. In Eq. (7.43), the derivatives are computed at fixed q_{ij} . Thus, the terms containing q_{ij} vanish. The final form of these relations is given by Eqs. (7.8)-(7.10) in the main text.

7.7 Non-hydrostatic stress-strain transformation

We will derive an expression for the temperature change at a constant pressure p in terms of strains instead of non-hydrostatic stresses. For convenience of the derivation, we will use the matrix form of Hooke's law obtained by inversion of Eq. (7.6):

$$\hat{\sigma} = \mathbf{C} \cdot (\hat{e} - \hat{\eta}). \quad (7.44)$$

Here $\hat{\sigma}$ and \hat{e} are columns containing six different components of the stress and strain tensors, respectively, \mathbf{C} is a 6×6 symmetrical matrix of elastic constants, and the dot denotes matrix-column multiplication (contraction). The thermal strain is also represented by a column $\hat{\eta}$ whose six components depend on $T - T_0$. The order in which we list the components of the stress and strain tensors is dictated by the goal of our calculation and is different from the standard Voigt notation. Specifically, we first list the lateral components of the stress and strain followed by the components related to the solid-fluid interface:

$$\begin{aligned}
\hat{\sigma} &= \begin{bmatrix} \sigma_{11} \\ \sigma_{22} \\ \sigma_{12} \\ \sigma_{13} \\ \sigma_{23} \\ \sigma_{33} \end{bmatrix} \equiv \begin{bmatrix} \sigma_1 \\ \sigma_2 \\ \sigma_3 \\ \sigma_4 \\ \sigma_5 \\ \sigma_6 \end{bmatrix}, & \hat{e} &= \begin{bmatrix} e_{11} \\ e_{22} \\ 2e_{12} \\ 2e_{13} \\ 2e_{23} \\ e_{33} \end{bmatrix} \equiv \begin{bmatrix} e_1 \\ e_2 \\ e_3 \\ e_4 \\ e_5 \\ e_6 \end{bmatrix}, \\
\hat{\eta} &= \begin{bmatrix} \eta_{11} \\ \eta_{22} \\ 2\eta_{12} \\ 2\eta_{13} \\ 2\eta_{23} \\ \eta_{33} \end{bmatrix} \equiv \begin{bmatrix} \eta_1 \\ \eta_2 \\ \eta_3 \\ \eta_4 \\ \eta_5 \\ \eta_6 \end{bmatrix}.
\end{aligned} \tag{7.45}$$

The matrix of the elastic constants is

$$\begin{aligned}
\mathbf{C} &= \begin{pmatrix} C_{1111} & C_{1122} & C_{1112} & C_{1113} & C_{1123} & C_{1133} \\ C_{2211} & C_{2222} & C_{2212} & C_{2213} & C_{2223} & C_{2233} \\ C_{1211} & C_{1222} & C_{1212} & C_{1213} & C_{1223} & C_{1233} \\ C_{1311} & C_{1322} & C_{1312} & C_{1313} & C_{1323} & C_{1333} \\ C_{2311} & C_{2322} & C_{2312} & C_{2313} & C_{2323} & C_{2333} \\ C_{3311} & C_{3322} & C_{3312} & C_{3313} & C_{3323} & C_{3333} \end{pmatrix} \\
&\equiv \begin{pmatrix} C_{11} & C_{12} & C_{13} & C_{14} & C_{15} & C_{16} \\ C_{21} & C_{22} & C_{23} & C_{24} & C_{25} & C_{26} \\ C_{31} & C_{32} & C_{33} & C_{34} & C_{35} & C_{36} \\ C_{41} & C_{42} & C_{43} & C_{44} & C_{45} & C_{46} \\ C_{51} & C_{52} & C_{53} & C_{54} & C_{55} & C_{56} \\ C_{61} & C_{62} & C_{63} & C_{64} & C_{65} & C_{66} \end{pmatrix}.
\end{aligned} \tag{7.46}$$

When the solid is hydrostatic at a temperature T_H , the stress components σ_1, σ_2 and σ_6 are identical and equal to $-p$, whereas the three shear components are zero. This hydrostatic stress $\hat{\sigma}_H$ and the respective strain \hat{e}_H satisfy Hooke's law

$$\hat{\sigma}_H = \mathbf{C} \cdot (\hat{e}_H - \hat{\eta}_H). \tag{7.47}$$

Here \hat{e}_H has the meaning of strain required for bringing the solid from the stress-free reference state at a temperature T_0 to the hydrostatic state at temperature T_H . $\hat{\eta}_H$ is the stress-free thermal strain measured when the temperature changes from T_0 to T_H .

We choose the coordinate system so that the principal component of stress $\sigma_6 = -p$ and the shear components σ_4 and σ_5 are zero. Furthermore, we choose T_H as the reference temperature T_0 , resulting in $\hat{\eta}_H = 0$. Subtracting Eqs. (7.44) and (7.47) we obtain

$$\begin{bmatrix} q_1 \\ q_2 \\ q_3 \\ 0 \\ 0 \\ 0 \end{bmatrix} = \begin{pmatrix} C_{11} & C_{12} & C_{13} & C_{14} & C_{15} & C_{16} \\ C_{21} & C_{22} & C_{23} & C_{24} & C_{25} & C_{26} \\ C_{31} & C_{32} & C_{33} & C_{34} & C_{35} & C_{36} \\ C_{41} & C_{42} & C_{43} & C_{44} & C_{45} & C_{46} \\ C_{51} & C_{52} & C_{53} & C_{54} & C_{55} & C_{56} \\ C_{61} & C_{62} & C_{63} & C_{64} & C_{65} & C_{66} \end{pmatrix} \cdot \begin{bmatrix} E_1 - \eta_1 \\ E_2 - \eta_2 \\ E_3 - \eta_3 \\ E_4 - \eta_4 \\ E_5 - \eta_5 \\ E_6 - \eta_6 \end{bmatrix}, \quad (7.48)$$

where $\hat{q} \equiv \hat{\sigma} - \hat{\sigma}_H$ and $\hat{E} \equiv \hat{e} - \hat{e}_H$ are the non-hydrostatic stress and strain, respectively. The meaning of \hat{E} is the strain of bringing the solid from the hydrostatic state at temperature T_H to a given non-hydrostatic state at a temperature T and a constant pressure p in the fluid. The non-zero components q_1 , q_2 and q_3 are the lateral components of the non-hydrostatic stress. All components of $\hat{\eta}$ are functions of $T - T_H$.

Our next goal is to express the lateral components of \hat{q} in terms of the lateral components of \hat{E} . To this end, we rewrite Eq. (7.48) in the form

$$\begin{bmatrix} \hat{q}_L \\ \hat{q}_\perp \end{bmatrix} = \begin{pmatrix} \mathbf{C}_1 & \mathbf{C}_2 \\ \mathbf{C}_3 & \mathbf{C}_4 \end{pmatrix} \cdot \begin{bmatrix} \hat{E}_L - \hat{\eta}_L \\ \hat{E}_\perp - \hat{\eta}_\perp \end{bmatrix}, \quad (7.49)$$

where we break \mathbf{C} into 3×3 matrices \mathbf{C}_1 , \mathbf{C}_2 , \mathbf{C}_3 and \mathbf{C}_4 and introduce the notations

$$\hat{q}_L \equiv \begin{bmatrix} q_1 \\ q_2 \\ q_3 \end{bmatrix}, \quad \hat{q}_\perp \equiv \begin{bmatrix} 0 \\ 0 \\ 0 \end{bmatrix},$$

$$\hat{E}_L - \hat{\eta}_L \equiv \begin{bmatrix} E_1 - \eta_1 \\ E_2 - \eta_2 \\ E_3 - \eta_3 \end{bmatrix}, \quad E_\perp - \hat{\eta}_\perp \equiv \begin{bmatrix} E_4 - \eta_4 \\ E_5 - \eta_5 \\ E_6 - \eta_6 \end{bmatrix}. \quad (7.50)$$

Due to the symmetry of matrix \mathbf{C} (Eq. (7.46)), matrices \mathbf{C}_1 and \mathbf{C}_4 are also symmetric, while \mathbf{C}_2 and \mathbf{C}_3 are transpose of each other and generally not symmetric.

Eq. (7.49) can be rewritten as a system of two matrix equations:

$$\hat{q}_L = \mathbf{C}_1 \cdot (\hat{E}_L - \hat{\eta}_L) + \mathbf{C}_2 \cdot (\hat{E}_\perp - \hat{\eta}_\perp), \quad (7.51)$$

$$0 = \mathbf{C}_2^T \cdot (\hat{E}_L - \hat{\eta}_L) + \mathbf{C}_4 \cdot (\hat{E}_\perp - \hat{\eta}_\perp), \quad (7.52)$$

where superscript T denotes transposition. Solving Eq. (7.52) for $\hat{E}_\perp - \hat{\eta}_\perp$ and inserting this in Eq. (7.51), we arrive at the following expression for \hat{q}_L in terms of $\hat{E}_L - \hat{\eta}_L$:

$$\hat{q}_L = \mathbf{A} \cdot (\hat{E}_L - \hat{\eta}_L). \quad (7.53)$$

Here

$$\mathbf{A} \equiv \mathbf{C}_1 - \mathbf{C}_2 \cdot \mathbf{C}_4^{-1} \cdot \mathbf{C}_2^T \quad (7.54)$$

is a symmetric 3×3 matrix. Eq. (7.53) can be inverted to

$$\hat{E}_L - \hat{\eta}_L = \mathbf{A}^{-1} \cdot \hat{q}_L. \quad (7.55)$$

Furthermore, it can be easily shown that

$$\mathbf{A}^{-1} = \mathbf{S}_L, \quad (7.56)$$

where \mathbf{S}_L is the upper-left-corner 3×3 matrix of the 6×6 matrix of compliances \mathbf{S} defined in a matter similar to Eq. (7.48). Matrix \mathbf{S} appears in Hooke's law rewritten in our notations as $\hat{E} - \hat{\eta} = \mathbf{S} \cdot \hat{q}$. Using Eqs. (7.53)-(7.56), the quadratic form of q 's which frequently appears in our equations can now be written as

$$\begin{aligned} \sum_{i,j=1,2} S_{ijkl} q_{ij} q_{kl} &= \hat{q}_L^T \cdot \mathbf{S}_L \cdot \hat{q}_L = q_L^T \cdot (\hat{E}_L - \hat{\eta}_L) \\ &= (\hat{E}_L - \hat{\eta}_L)^T \cdot \mathbf{A} \cdot (\hat{E}_L - \hat{\eta}_L). \end{aligned} \quad (7.57)$$

We can now derive an expression for the equilibrium temperature at a constant pressure. Changing variables in Eq. (7.23) by means of Eq. (7.57) we obtain

$$\begin{aligned} \Delta \bar{s}(T - T_H) &+ \frac{1}{2} \left(\frac{\partial \Delta s}{\partial T} \right)_H (T - T_H)^2 \\ &+ \frac{\Omega_0^s}{2} \sum_{i,j=1,2,3} A_{ij} (E_i E_j - 2E_i \eta_j + \eta_i \eta_j) = 0. \end{aligned} \quad (7.58)$$

If the hydrostatic state H is far enough from special points, Eq. (7.58) reduces to

$$T - T_H = -\frac{\Omega_0^s T_H}{2\Delta\bar{h}} \sum_{i,j=1,2,3} A_{ij} E_i E_j. \quad (7.59)$$

Combining Eqs. (7.59) and (7.3), the respective change in the chemical potential in the fluid is

$$\mu^f(T, p_H) - \mu^f(T_H, p_H) = \frac{\bar{s}^f \Omega_0^s T_H}{2\Delta\bar{h}} \sum_{i,j=1,2,3} A_{ij} E_i E_j. \quad (7.60)$$

Thus, for isobaric variations from the hydrostatic state the changes in T and μ^f are quadratic in lateral components of the strain.

7.8 Iso-fluid equations in terms of strains

Eq. (7.58) can be applied to iso-fluid processes. Indeed, for a fixed temperature this equation defines an ellipsoid in the variables E_1 , E_2 and E_3 :

$$\sum_{i,j=1,2,3} A_{ij} (E_i E_j - 2E_i \eta_j + \eta_i \eta_j) = \text{const.} \quad (7.61)$$

This ellipsoid is centered at point $\hat{\eta}_L$ and represents the phase coexistence surface when the state of strain of the solid varies continuously at constant temperature and pressure, i.e. for a fixed state of the fluid.

Consider a particular iso-fluid path on which the shear strain E_3 remains zero. In this case Eq. (7.61) defines an ellipse (a cross-section of the ellipsoid by the $E_3 = 0$ plane) in the variables E_1 and E_2 . When the system undergoes a variation along this ellipse, the solid strained by an amount dE_1 has to simultaneously contract by an amount dE_2 to maintain the equilibrium with the fluid. To evaluate the derivative $(dE_2/dE_1)_{T,p,E_3}$ along this path, we take a derivative of Eq. (7.61) and take into account that at fixed T and p we have

$d\hat{E} = d\hat{e}$ and $d\hat{\eta}_L = 0$. This gives

$$\left(\frac{dE_2}{dE_1}\right)_{T,p,E_3} = \left(\frac{de_{22}}{de_{11}}\right)_{T,p,e_{12}} = -\frac{A_{11}(E_1 - \eta_1) + A_{12}(E_2 - \eta_2)}{A_{21}(E_1 - \eta_1) + A_{22}(E_2 - \eta_2)}. \quad (7.62)$$

For cubic crystals thermal expansion is isotropic and $\eta_1 = \eta_2$. In particular, for a biaxially deformed cubic solid $E_1 = E_2$ and Eq. (7.62) becomes

$$\left(\frac{de_{22}}{de_{11}}\right)_{T,p,e_{12}} = -\frac{A_{11} + A_{12}}{A_{22} + A_{12}}. \quad (7.63)$$

Since our calculations assume that elastic properties are temperature independent, so is the right hand side of this equation.

Calculations of matrix \mathbf{A} are simplified in the presence of crystal symmetry. For example, if the solid-fluid interface has the point symmetry of the group $2mm$ with the twofold axis along its normal, the full elastic constant matrix reduces to

$$\mathbf{C} = \begin{pmatrix} C_{11} & C_{12} & 0 & 0 & 0 & C_{16} \\ C_{21} & C_{22} & 0 & 0 & 0 & C_{26} \\ 0 & 0 & C_{33} & 0 & 0 & 0 \\ 0 & 0 & 0 & C_{44} & 0 & 0 \\ 0 & 0 & 0 & 0 & C_{55} & 0 \\ C_{61} & C_{62} & 0 & 0 & 0 & C_{66} \end{pmatrix} \quad (7.64)$$

Accordingly, matrix \mathbf{A} computed by Eq. (7.54) is

$$A_{ij} = C_{ij} - \frac{C_{i6}C_{6j}}{C_{66}} \quad i, j = 1, 2, 3. \quad (7.65)$$

Using this equation, the coefficients A_{11} , A_{12} and A_{22} appearing in Eq. (7.63) can be computed from the elastic constants C_{ijkl} as follows: $A_{11} = C_{1111} - C_{1133}^2/C_{3333}$, $A_{22} =$

$C_{2222} - C_{2233}^2/C_{3333}$, $A_{12} = C_{1122} - C_{1133}C_{2233}/C_{3333}$. These expressions in conjunction with Eq. (7.63) will be used in Part II of this work [?].

7.9 Stability of the fluid with respect to crystallization to a hydrostatic solid

In this section we give a general proof that a single-component fluid equilibrated with a non-hydrostatically stressed solid composed of the same component tends to crystallize to a hydrostatic solid at the same temperature T and pressure p . The proof follows the general line of Gibbs' derivation [13], which was for a fluid containing at least one more component and thus capable of changing the chemical potential at fixed T and p .

We will first revisit Gibbs' famous example with three fluids and point to differences between his multi-component case and our single-component case. Consider a cubic block of a homogeneous solid whose faces are normal to principal axes of the stress tensor. The principal stresses σ_{ii} are generally different. Suppose the block is immersed in a fluid of the same component and the whole system is in contact with a thermostat. Suppose the solid could be locally equilibrated with the fluid on each face of the cube. Then, the local equilibrium conditions on the separate faces would be

$$u^s - Ts^s + p_i\Omega^s = \mu^f(T, p_i), \quad i = 1, 2, 3, \quad (7.66)$$

where $p_i = -\sigma_{ii}$ are pressures in the fluids. For the multicomponent fluid considered by Gibbs, these three equations could be satisfied with three different chemical potentials adjusted by varying the chemical compositions of the fluids. Thus the solid could be equilibrated with three different fluids. For a single-component fluid, its pressure is the only parameter that could be varied in attempt to satisfy equations Eqs. (7.66). It is generally impossible to satisfy all three equations for any realistic pressure dependence of μ^f at a fixed temperature. Thus, in a single-component system a non-hydrostatic solid cannot be

equilibrated with three fluids.

We now proceed to our proof. For a hydrostatically stressed solid, its chemical potential μ_*^s is a well-defined quantity that follows the standard relation [13]

$$u_*^s - T s_*^s + p \Omega_*^s = \mu_*^s(T, p), \quad (7.67)$$

where the asterisk is a reminder that the state is hydrostatic. Subtracting this equation from Eq. (7.66) for $p = p_1$,

$$[(u^s - u_*^s) - T (s^s - s_*^s)] + p_1 (\Omega^s - \Omega_*^s) = \mu^f(T, p_1) - \mu_*^s(T, p_1). \quad (7.68)$$

Note that left-hand side of this equation depends on properties of the solid, the only property of the fluid being its pressure p_1 . Therefore, the sign of the left-hand side can be determined from the following thought experiment. Immerse the same solid in a large container filled with some other fluid medium (e.g., inert gas) which is not soluble in the solid, nor is the solid component soluble in that fluid. The fluid has pressure p_1 and the whole system is sealed in a rigid container embedded in a thermostat at temperature T . Initially, the solid is in a hydrostatic state at pressure p_1 and thus in mechanical and thermal equilibrium with the fluid. Consider another state in which the solid has the stresses σ_{ii} . It is again in thermal equilibrium with the fluid at temperature T but obviously not in mechanical equilibrium.

In Eq. (7.68), the term in the square brackets is the change in the Helmholtz free energy per atom of the solid upon its deformation at a fixed temperature T from the initial state to the final. The next term has the meaning of mechanical work done by the solid when displacing the surrounding large mass of the fluid at pressure p_1 . Thus, the left-hand side of Eq. (7.68) equals the change (per atom of the solid) in Helmholtz free energy of an isothermal closed system in a rigid container. Since in the initial state the system is in full

equilibrium while in the final state not, this change must be positive. It follows that

$$\mu^f(T, p_1) > \mu_*^s(T, p_1). \quad (7.69)$$

Return to the solid in contact with the actual fluid composed on the same component. Eq. (7.69) shows that the fluid equilibrated with the solid locally at the face with pressure p_1 will tend to crystallize to a hydrostatic solid at the same temperature and pressure. The same is obviously true for two other pressures p_2 and p_3 .

Chapter 8: Effect of non-hydrostatic stresses on solid-fluid equilibrium. II. Interface thermodynamics.

8.1 Introduction

In many situations, the solid phase is subject to non-hydrostatic mechanical stresses. At present, there is no clear understanding of how such stresses can affect interface properties. The goal of this work is to perform a rigorous analysis of interface thermodynamics in the presence of non-hydrostatic stresses in the solid. As in Part I of this work dedicated to bulk thermodynamics of non-hydrostatic systems [86], we study a simple case of a single-component material as an example. We also perform atomistic simulations in order to verify some of our theoretical results and to evaluate the relative strength of different effects predicted by the analysis.

A relation between γ and τ was first established for a single-component solid surface by Shuttleworth [15]. In this simple case, arbitrary lateral strains can be applied at a constant temperature, performing work against τ and changing γ . By contrast, elastic deformations of a solid-fluid interface cannot be arbitrary but must satisfy the phase coexistence conditions. For example, in a single-component system, elastic stretching at a constant temperature and pressure in the fluid can result in complete melting/evaporation of the solid phase. Such prohibited strains cannot be used in a definition of the interface stress and cannot appear in the Shuttleworth equation.

In this chapter we analyze possible elastic deformations of a solid-fluid interface which are consistent with phase equilibrium. The interface stress tensor is defined through an appropriate term in the adsorption equation. This term represents the work of reversible elastic deformation of the interface without violating the phase coexistence. For a given initial state of a two-phase system, there are multiple paths on the phase coexistence surface,

each corresponding to a different physical process, on which the interface area can change elastically. The work of stretching along different paths is generally different, making τ a non-unique thermodynamic quantity. We analyze different definitions of the interface stress implied by the adsorption equation and compute three of such stresses using atomistic computer simulations.

Most of the thermodynamic quantities appearing in the adsorption equation cannot be directly measured in experiments but are readily accessible by computer simulations. The interface free energy along phase coexistence paths was previously computed for several single-component and binary solid-liquid interfaces using the cleaving technique [54, 68], the capillary fluctuation method [62, 69, 71], various thermodynamic integration schemes [58, 60, 61, 87] and other approaches [88, 89]. For curved interfaces, γ was computed from modeling of homogeneous nucleation events [90–92]. However, previous atomistic studies of solid-liquid interfaces were restricted to systems in which the solid was either unstressed or stressed hydrostatically (or nearly hydrostatically). In this work we apply atomistic simulations to compute γ and different interface stresses $\hat{\tau}$ along strongly non-hydrostatic coexistence paths. Such paths were obtained by equilibration of a biaxially strained solid with its melt at a constant zero pressure p in the melt. When designing and interpreting our simulations, we used results for non-hydrostatic solid-fluid equilibrium between bulk phases presented in Part I of this work [86].

The rest of the chapter is organized as follows. In Sec. 8.2 we analyze interface thermodynamics of non-hydrostatic single-component systems. After introducing our atomistic simulation methodology in Sec. 8.3, we present the simulation results in Sec. 8.4 and draw conclusions in Sec. 8.5.

8.2 Thermodynamics of solid-fluid interfaces

8.2.1 Interface free energy γ and the adsorption equation.

Interface free energy.

Consider a rectangular block containing a single-component solid under a general state of mechanical stress in thermodynamic equilibrium with a fluid of the same component (Fig. 8.1). The solid-fluid interface is planar and perpendicular to the z direction of the block. Thermal equilibrium between the phases requires that temperature T be uniform throughout the system. Due to mechanical equilibrium, the principal component σ_{33}^s of the stress tensor σ_{ij}^s in the solid is perpendicular to the interface and equal to negative pressure p in the fluid. The phase-change equilibrium condition relates properties of the solid to the chemical potential μ^f in the fluid [13],

$$U^s - TS^s + pV^s = \mu^f N^s, \quad (8.1)$$

where U^s , S^s , V^s and N^s are the energy, entropy, volume and number of atoms of an arbitrary homogeneous region of the solid phase. For any homogeneous region of the fluid phase we have

$$U^f - TS^f + pV^f = \mu^f N^f, \quad (8.2)$$

where U^f , S^f , V^f and N^f are the energy, entropy, volume and number of atoms of the fluid region. Examples of homogeneous regions inside the phases are illustrated in Fig. 8.1.

Consider a layer containing the solid-fluid interface (Fig. 8.1). The choice of this layer is arbitrary as long as its boundaries are placed inside of homogeneous parts of the solid and fluid phases. Using Gibbs' definition of the interface free energy¹ in conjunction with Eqs. (8.1) and (8.2), it can be shown that [13]

¹This definition is valid for single-component systems. Multicomponent systems require a separate treatment.[61]

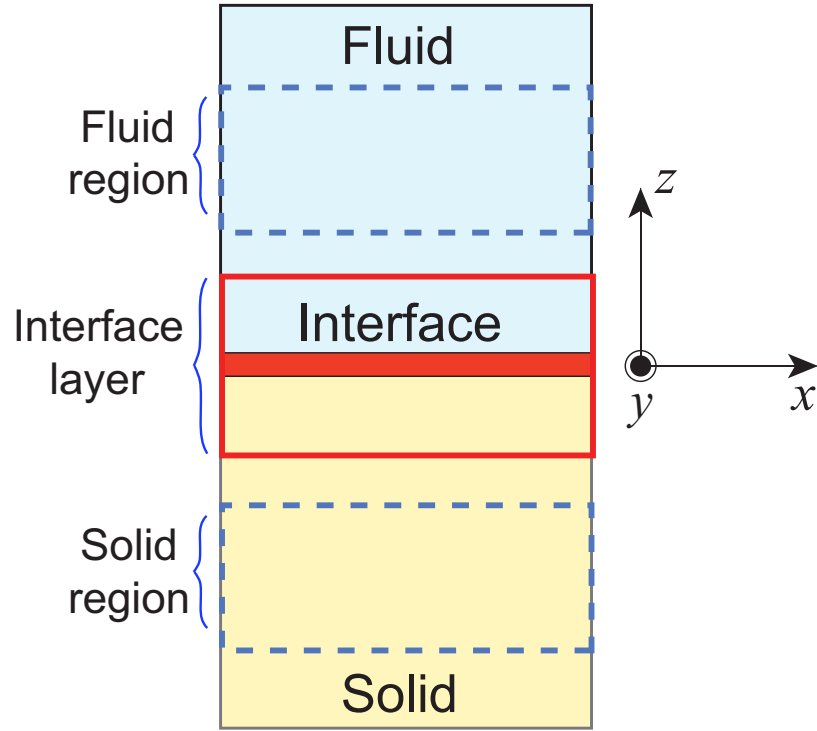


Figure 8.1: Schematic of a solid-fluid system with a plane interface. The interface layer and the homogeneous solid and fluid regions are outlined.

$$\gamma A = U - TS + pV - \mu^f N, \quad (8.3)$$

where U , S , V and N are the total energy, entropy, volume and number of atoms in the layer and A is the physical area of the interface. The extensive quantities U , S , V and N are not physically meaningful interface properties because they depend on the choice of the boundaries of the layer. To eliminate this dependence, we solve the system of three Eqs. (8.1), (8.2) and (8.3) for γA using Cramer's rule of linear algebra. This results in the following expression for γA in terms of interface excesses of extensive properties [61]:

$$\gamma A = [U]_{XY} - T[S]_{XY} + p[V]_{XY} - \mu^f [N]_{XY}. \quad (8.4)$$

Here X and Y are any two out of four extensive properties U , S , V and N . In Eq. (8.4)

and other equations appearing below, $[Z]_{XY}$ denotes the ratio of two determinants [14]:

$$[Z]_{XY} \equiv \frac{\begin{vmatrix} Z & X & Y \\ Z^s & X^s & Y^s \\ Z^f & X^f & Y^f \end{vmatrix}}{\begin{vmatrix} X^s & Y^s \\ X^f & Y^f \end{vmatrix}}. \quad (8.5)$$

The quantities appearing in the first row of the 3×3 determinant are computed for the chosen layer containing the interface, whereas the quantities with superscripts s and f are computed for homogeneous regions in the solid and fluid phases, respectively. When two columns in the 3×3 determinant in Eq. (8.5) are identical, the excess is zero:

$$[X]_{XY} = [Y]_{XY} = 0. \quad (8.6)$$

In other words, excesses of the properties X and Y are identically zero. Due to Eq. (8.6), two terms in the right-hand side of Eq. (8.4) are eliminated by specifying X and Y , leaving only two nonzero terms.

The adsorption equation.

Our next goal is to derive a differential equation for reversible variations of γA in terms of variations of intensive properties. Consider a closed solid-fluid block, as in Fig. 8.1, containing a fixed number of unit cells of the solid in the cross-section parallel to the interface (in other words, a fixed Lagrangian area of the interface). Consider a reversible variation of state of the system in which it can receive/release heat and do mechanical work by changing its shape and dimensions, including changes in the physical area of the interface by elastic deformation. Differentiating Eqs. (8.1), (8.2) and (8.3) one can derive the following Gibbs-Duhem-type equations for the interface layer and the bulk solid and

fluid regions:

$$d(\gamma A) = -SdT + Vdp - Nd\mu^f + \sum_{i,j=1,2} (\sigma_{ij} + \delta_{ij}p)Vd\epsilon_{ij}, \quad (8.7)$$

$$0 = -S^s dT + V^s dp - N^s d\mu^f + \sum_{i,j=1,2} (\sigma_{ij}^s + \delta_{ij}p)V^s d\epsilon_{ij}, \quad (8.8)$$

$$0 = -S^f dT + V^f dp - N^f d\mu^f. \quad (8.9)$$

Here, σ_{ij} is the stress tensor averaged over the layer and ϵ_{ij} is a symmetrical 2×2 lateral strain tensor computed relative to the current state. We are assuming that the distorted shape of the block is triclinic, hence $d\epsilon_{ij}$ is the same in all three equations. Gibbs derived Eq. (8.8) for a more general case of finite deformations [13],

The differentials appearing in the right-hand side of Eq. (8.7) are not independent. They are subject to constraints imposed by thermodynamic equilibrium between the bulk phases and expressed by Eqs. (8.8) and (8.9) [14]. Solving the system of these three equations, we obtain the adsorption equation expressing a variation of the total interface free energy γA in terms of independent intensive variables:

$$\begin{aligned} d(\gamma A) &= -[S]_{XY} dT + [V]_{XY} dp - [N]_{XY} d\mu^f + \\ &+ \sum_{i,j=1,2} [(\sigma_{ij} + \delta_{ij}p)V]_{XY} d\epsilon_{ij}. \end{aligned} \quad (8.10)$$

The excess quantities $[Z]_{XY}$ appearing in Eq. (8.10) are computed by Eq. (8.5), where Z , X and Y are three out of the extensive properties S , V , N and $(\sigma_{ij} + \delta_{ij}p)V$. By specifying X and Y , two terms in Eq. (8.10) are eliminated, leaving four variables that can be varied

independently.²

It is important to note that some choices of the extensive properties X and Y are prohibited by Cramer's rule. For example, if $X = (\sigma_{11} + p)V$ and $Y = (\sigma_{22} + p)V$, then $X^f = Y^f = 0$ and the excess $[Z]_{XY}$ of any property Z is undefined. This restriction on the choice of X and Y originates from the fact that the solid and fluid phases have different numbers of degrees of freedom: two for the fluid and five for the solid³. The Gibbs-Duhem equation for fluid phase, Eq. (8.9), does not contain the lateral strain variables. As a result, only one strain variable can be eliminated from the system of three equations but not two. Thus, the four degrees of freedom of the solid-fluid system can be represented by four intensive variables from the set $(T, p, \mu^f, \epsilon_{11}, \epsilon_{22}, \epsilon_{12})$, with the requirement that at least two of them are strain components.

8.2.2 The interface stress

Definition and multiplicity of interface stresses

In this section we analyze different interface stresses introduced through the adsorption equation. By choosing different extensive variables X and Y in Eq. (8.10), several forms of the adsorption equation can be obtained, each having a different set of independent variables and leading to different definitions of the interface stress. Indeed, the change of γA due to elastic work done by or against interface stress is represented by the last term in Eq. (8.10). From this term we can express $\boldsymbol{\tau}$ as an excess of the tensor $(\sigma_{ij} + \delta_{ij}p)V$ over its bulk values on either side of the interface:

²Out of the four differentials $d\epsilon_{ij}$, only three are independent due to the symmetry of tensor ϵ_{ij} .

³A generally stressed single-component solid has seven degrees of freedom, e.g. T and σ_{ij}^s . Mechanical equilibrium with the fluid requires that σ_{13}^s and σ_{23}^s be identically zero, imposing two constraints.

$$\begin{aligned}
\tau_{ij}^{XY} &= \frac{1}{A} \frac{\partial(\gamma A)}{\partial \epsilon_{ij}} = \frac{1}{A} [(\sigma_{ij} + \delta_{ij} p) V]_{XY} \\
&= \frac{1}{A} \frac{\begin{vmatrix} (\sigma_{ij} + \delta_{ij} p) V & X & Y \\ (\sigma_{ij}^s + \delta_{ij} p) V^s & X^s & Y^s \\ 0 & X^f & Y^f \end{vmatrix}}{\begin{vmatrix} X^s & Y^s \\ X^f & Y^f \end{vmatrix}}, \tag{8.11}
\end{aligned}$$

where $i, j = 1, 2$.⁴ The variables held constant during the variation of ϵ_{ij} depend on the choice of X and Y . The only case when the interface stress is independent of X and Y is when the solid is hydrostatic, in which case $\sigma_{ij}^s + \delta_{ij} p = 0$ and τ_{ij} has a unique value $\tau_{ij} = (\sigma_{ij} + \delta_{ij} p) V/A$.

To further demonstrate that the interface stress is not unique if the solid is non-hydrostatic, we will consider examples of different choices of X and Y . Three examples will be given in this section and one more in Sec. 8.2.2.

First, let $X = V$ and $Y = N$. The adsorption equation becomes

$$d(\gamma A) = -[S]_{NV} dT + \sum_{i,j=1,2} [(\sigma_{ij} + \delta_{ij} p) V]_{NV} d\epsilon_{ij}, \tag{8.12}$$

with four independent variables T , ϵ_{11} , ϵ_{12} and ϵ_{22} . Consider an elastic deformation of the interface at a constant temperature when one of the strain components, ϵ_{ij} , varies while other components are fixed. The interface stress obtained, which we denote $\boldsymbol{\tau}^{NV}$, represents the change in γA at a constant T and is given by

⁴Although ϵ_{ij} is a symmetric tensor, the partial derivative $\partial(\gamma A)/\partial \epsilon_{ij}$ is taken by *formally* treating the four components of ϵ_{ij} as independent variables.

$$\begin{aligned}
\tau_{ij}^{NV} &= \frac{1}{A} \left(\frac{\partial(\gamma A)}{\partial e_{ij}} \right)_T = \frac{1}{A} [(\sigma_{ij} + \delta_{ij}p)V]_{NV} \\
&= \frac{1}{A} \frac{\begin{vmatrix} (\sigma_{ij} + \delta_{ij}p)V & N & V \\ (\sigma_{ij}^s + \delta_{ij}p)V^s & N^s & V^s \\ 0 & N^f & V^f \end{vmatrix}}{\begin{vmatrix} N^s & V^s \\ N^f & V^f \end{vmatrix}}. \tag{8.13}
\end{aligned}$$

This deformation is implemented along the isothermal path discussed in Part I [86], on which p and μ^f vary in order to maintain equilibrium. For variations away from a hydrostatic state of the solid, the changes in p and μ^f were shown to be quadratic in non-hydrostatic components of the stress tensor in the solid.

In the second example, we choose $X = S$ and $Y = N$. This eliminates the differentials dT and $d\mu^f$ in the adsorption equation, which becomes

$$d(\gamma A) = [V]_{NS} dp + \sum_{ij=1,2} [(\sigma_{ij} + \delta_{ij}p)V]_{NS} d\epsilon_{ij}. \tag{8.14}$$

The independent variables are now p , ϵ_{11} , ϵ_{12} and ϵ_{22} , whereas T and μ^f vary to maintain equilibrium. By contrast to the previous case, the interface now has an excess volume $[V]_{NS}$.⁵ The interface stress τ^{NS} is defined through the work of elastic deformation at a constant pressure in the fluid:

⁵If related per unit area, excess volume of an interface is the relative rigid translation of the phases normal to the interface during its formation.

$$\begin{aligned}
\tau_{ij}^{NS} &= \frac{1}{A} \left(\frac{\partial(\gamma A)}{\partial e_{ij}} \right)_p = \frac{1}{A} [(\sigma_{ij} + \delta_{ij}p)V]_{NS} \\
&= \frac{1}{A} \frac{\begin{vmatrix} (\sigma_{ij} + \delta_{ij}p)V & N & S \\ (\sigma_{ij}^s + \delta_{ij}p)V^s & N^s & S^s \\ 0 & N^f & S^f \end{vmatrix}}{\begin{vmatrix} N^s & S^s \\ N^f & S^f \end{vmatrix}}. \tag{8.15}
\end{aligned}$$

The deformation path implied by Eq. (8.15) corresponds to the isobaric case discussed in Part I [86]. For variations away from a hydrostatic state of the solid, the changes in T and μ^f are quadratic in non-hydrostatic stresses in the solid.

The interface stresses τ^{NV} and τ^{NS} are generally different. They could be determined by measuring changes of γA during elastic deformations in two *different* thermodynamic processes: an isothermal and isobaric, respectively. Another possible interface stress is τ^{NS} , corresponding to elastic deformation at a constant chemical potential μ^f in the fluid (T and p vary to maintain equilibrium). We do not discuss this case in details, but this interface stress can also be expressed as an appropriate excess of the non-hydrostatic stress tensor in a manner similar to τ^{NV} and τ^{NS} .

Interface stress on an iso-fluid path

We will now introduce yet another definition of the interface stress. Let X or Y be one of the non-hydrostatic stresses $(\sigma_{ij} + \delta_{ij}p)V$. For example, suppose $Y = (\sigma_{22} + p)V$ while X is one of the extensive variables S , V or N . This choice of Y eliminates $d\epsilon_{22}$ in Eq. (8.10) and reduces it to

$$\begin{aligned}
d(\gamma A) &= -[S]_{X(\sigma_{22}+p)V} dT + [V]_{X(\sigma_{22}+p)V} dp \\
&- [N]_{X(\sigma_{22}+p)V} d\mu^f + [(\sigma_{11} + p)V]_{X(\sigma_{22}+p)V} d\epsilon_{11} \\
&+ [\sigma_{12}V]_{X(\sigma_{22}+p)V} d\epsilon_{12} + [\sigma_{21}V]_{X(\sigma_{22}+p)V} d\epsilon_{21}.
\end{aligned} \tag{8.16}$$

In this equation, one variable out of set (T, p, μ^f) is eliminated by specifying X , leaving four independent variables (recall that $\epsilon_{12} = \epsilon_{21}$). For example, $(T, p, \epsilon_{11}, \epsilon_{12})$ or $(T, \mu^f, \epsilon_{11}, \epsilon_{12})$ are possible sets of independent variables.

Note that if any two variables from the set (T, p, μ^f) are fixed, the third variable is also fixed because a single-component fluid has two degrees of freedom. A relation between these three variables is given by the Gibbs-Duhem equation (8.9). Thus, if any two variables from the set (T, p, μ^f) are held constant, γA can only vary due to the remaining strain terms, which represent the work of elastic deformation of the interface. This elastic work is done by an interface stress which we denote $\hat{\tau}^{(22)}$. The superscript (22) indicates the component of the strain tensor which is eliminated from the adsorption equation and becomes a dependent variable. The components of $\hat{\tau}^{(22)}$ are

$$\tau_{11}^{(22)} = \frac{1}{A} \left(\frac{\partial(\gamma A)}{\partial \epsilon_{11}} \right)_{T,p,\epsilon_{12}} = \frac{1}{A} [(\sigma_{11} + p)V]_{X(\sigma_{22}+p)V}, \tag{8.17}$$

$$\tau_{12}^{(22)} = \tau_{21}^{(22)} = \frac{1}{2A} \left(\frac{\partial(\gamma A)}{\partial \epsilon_{12}} \right)_{T,p,\epsilon_{11}} = \frac{1}{A} [(\sigma_{12} + p)V]_{X(\sigma_{22}+p)V}, \tag{8.18}$$

whereas $\tau_{22}^{(22)}$ is identically zero due to the property of determinants (8.6).

Computing the determinants in Eqs. (8.17) and (8.18) explicitly,

$$\begin{aligned}
\tau_{11}^{(22)} &= \frac{1}{A} \frac{\begin{vmatrix} (\sigma_{11} + p)V & (\sigma_{22} + p)V & X \\ (\sigma_{11}^s + p)V^s & (\sigma_{22}^s + p)V^s & X^s \\ 0 & 0 & X^f \end{vmatrix}}{\begin{vmatrix} (\sigma_{22}^s + p)V^s & X^s \\ 0 & X^f \end{vmatrix}} = \\
&= \frac{V}{A} \left\{ (\sigma_{11} + p) - (\sigma_{11}^s + p) \frac{(\sigma_{22} + p)}{(\sigma_{22}^s + p)} \right\}, \tag{8.19}
\end{aligned}$$

$$\begin{aligned}
\tau_{12}^{(22)} = \tau_{21}^{(22)} &= \frac{1}{A} \frac{\begin{vmatrix} \sigma_{12}V & (\sigma_{22} + p)V & X \\ \sigma_{12}^sV^s & (\sigma_{22}^s + p)V^s & X^s \\ 0 & 0 & X^f \end{vmatrix}}{\begin{vmatrix} \sigma_{22}^sV^s & X^s \\ 0 & X^f \end{vmatrix}} = \\
&= \frac{V}{A} \left\{ \sigma_{12} - \sigma_{12}^s \frac{(\sigma_{22} + p)}{(\sigma_{22}^s + p)} \right\}. \tag{8.20}
\end{aligned}$$

Note that these expressions are independent of X .

Having introduced the interface stress $\boldsymbol{\tau}^{(kl)}$, we will now discuss the physical processes which can be implemented to measure it. The process to determine $\tau_{11}^{(22)}$ is a variation of ϵ_{11} at constant ϵ_{12} , T and p . In this process, μ^f is automatically fixed by the equation of state of the fluid. The remaining strain component ϵ_{22} is varied simultaneously with ϵ_{11} to maintain phase equilibrium. Likewise, $\tau_{12}^{(22)}$ and $\tau_{21}^{(22)}$ are determined in a process in which ϵ_{11} , T , p (and thus μ^f) are fixed while ϵ_{12} and ϵ_{22} vary simultaneously to maintain phase equilibrium. While the state of stress of the solid changes in these processes, the state of the

fluid remains the same. Such processes were introduced in Part I of this work,[86] where they were called iso-fluid processes. Thus, $\tau^{(kl)}$ can be referred to as iso-fluid interface stress.

There is a unique hydrostatic state of the solid, denoted H, in which it is equilibrated with a given fluid. It was shown [86] that no iso-fluid path can go through or originate from the hydrostatic point (T_H, p_H) . Thus, $\hat{\tau}^{(kl)}$ is only defined for non-hydrostatic states of the solid.

Iso-fluid processes have the following geometric interpretation in the configuration space of variables. The iso-fluid constraints eliminate two degrees of freedom, leaving a single-component solid-fluid system with two remaining degrees of freedom. Iso-fluid states can be represented by a surface in the three-dimensional space of strain variables E_{11} , E_{12} and E_{22} . The strain E_{ij} was introduced in Part I [86] and is defined relative to the reference hydrostatic state (T_H, p_H) . In the linear elasticity approximation, the iso-fluid surface is an ellipsoid centered at $E_{11} = E_{12} = E_{22} = 0$ (Appendix C of Part I) [86].

To apply this analysis to atomistic simulations discussed later, let us consider a particular case in which E_{12} remains fixed at zero. Then the iso-fluid path is an ellipse in the coordinates E_{11} and E_{22} , which can be obtained as an intersection of the ellipsoid mentioned above with the plane $E_{12} = 0$. Alternatively, this ellipse can be viewed as an intersection of two other surfaces. Specifically, at $E_{12} = 0$ and a fixed pressure in the fluid, the solid-fluid coexistence surface is an elliptical paraboloid in the coordinates T versus E_{11} and E_{22} (Fig. 8.2a). The equation of this paraboloid was derived in Appendix B of Part I [86]. The iso-fluid ellipse is obtained as an intersection of this paraboloid with a constant-temperature plane (Fig. 8.2b).

For any infinitesimal iso-fluid process on the ellipse, the solid phase is stretched by an amount dE_{11} and simultaneously compressed in the perpendicular direction by an amount dE_{22} in order to maintain equilibrium with the same fluid. Some of the equations involving the iso-fluid interface stress (see below) contain the slope of the iso-fluid curve. Since the reference state (T_H, p_H) is fixed during iso-fluid processes, the slope equals $dE_{22}/dE_{11} =$

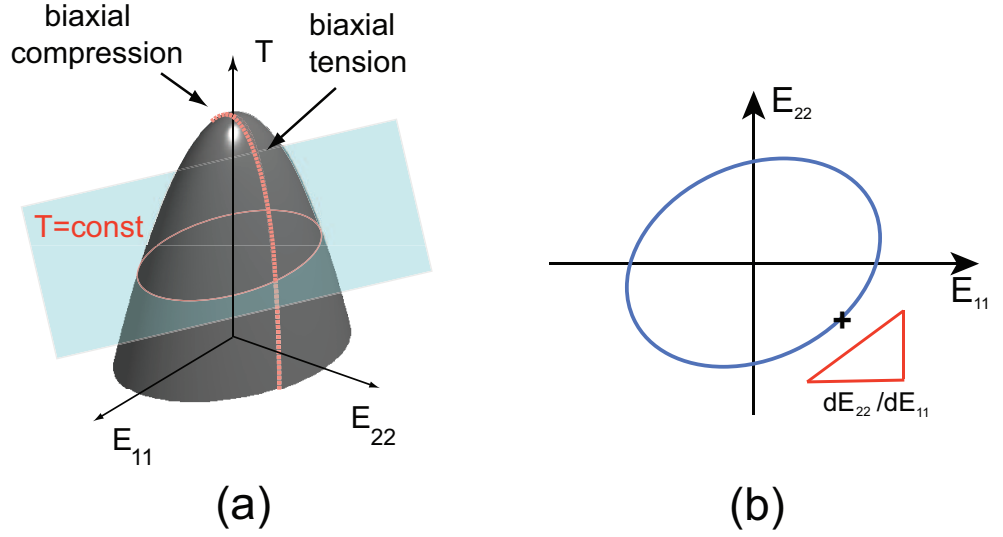


Figure 8.2: Equilibrium temperature T as a function of non-hydrostatic components of strain E_{ij} at a constant pressure p in the fluid and a constant E_{12} . (a) The line of biaxial tension/compression. (b) An iso-fluid path. The triangle shows the slope of the iso-fluid path at a particular point marked by a cross.

$d\epsilon_{22}/d\epsilon_{11}$, where the strain ϵ_{ij} is defined relative to the current state.

Relations between different interface stresses

In this section we analyze relations between different interface stresses. Such relations are readily obtained by equating right-hand sides of the adsorption equation for different choices of X and Y . Some of these relations will be later tested by atomistic simulations. We will limit the discussion to the particular case of $d\epsilon_{12} = 0$.

Since there is no preference of choosing $d\epsilon_{11}$ over $d\epsilon_{22}$ as the independent variable to describe iso-fluid processes, we have two versions of the adsorption equation:

$$d(\gamma A) = \tau_{11}^{(22)} d\epsilon_{11} = \tau_{22}^{(11)} d\epsilon_{22}. \quad (8.21)$$

It follows that the components $\tau_{11}^{(22)}$ and $\tau_{22}^{(11)}$ are proportional to each other,

$$\frac{\tau_{11}^{(22)}}{\tau_{22}^{(11)}} = \left(\frac{\partial \epsilon_{22}}{\partial \epsilon_{11}} \right)_{T,p,\epsilon_{12}}. \quad (8.22)$$

The slope of the iso-fluid curve (Fig. 8.2b) is assumed to be known from bulk thermodynamic properties. On the other hand, using Eq. (8.19) $\tau_{11}^{(22)}/\tau_{22}^{(11)}$ can be expressed as a ratio of non-hydrostatic components of stress in the solid:

$$\frac{\tau_{11}^{(22)}}{\tau_{22}^{(11)}} = \frac{\sigma_{11}^s + p}{\sigma_{22}^s + p}. \quad (8.23)$$

These relations permit useful cross-checks during interface stress calculations, which will be done in Sec. 8.4.

A relation between $\boldsymbol{\tau}^{NV}$ and $\boldsymbol{\tau}^{(22)}$ can be obtained by applying Eq. (8.12) to the particular case of an iso-fluid variation ($dT = 0$):

$$d(\gamma A) = \tau_{11}^{NV} d\epsilon_{11} + \tau_{22}^{NV} d\epsilon_{22}. \quad (8.24)$$

Because $d\epsilon_{11}$ and $d\epsilon_{22}$ must be proportional to each other to keep the system on the iso-fluid path, we can rewrite this equation as

$$d(\gamma A) = \left\{ \tau_{11}^{NV} + \tau_{22}^{NV} \left(\frac{\partial \epsilon_{22}}{\partial \epsilon_{11}} \right)_{T,p,\epsilon_{12}} \right\} d\epsilon_{11}. \quad (8.25)$$

Comparing this equation with Eq. (8.21), we obtain

$$\tau_{11}^{(22)} = \tau_{11}^{NV} + \tau_{22}^{NV} \left(\frac{\partial \epsilon_{22}}{\partial \epsilon_{11}} \right)_{T,p,\epsilon_{12}}. \quad (8.26)$$

This relation suggests another cross-check because $\boldsymbol{\tau}^{NV}$ and $\boldsymbol{\tau}^{(22)}$ can be computed independently.

The derivative $(\partial\epsilon_{22}/\partial\epsilon_{11})_{T,p,\epsilon_{12}}$ appearing in the above equations was computed in Part I [86] in the linear elasticity approximation. It can be expressed through elastic constants of the solid phase and the strain E_{ij} relative to the hydrostatic state:

$$\left(\frac{\partial\epsilon_{22}}{\partial\epsilon_{11}}\right)_{T,p,\epsilon_{12}} = -\frac{A_{11}E_{11} + A_{12}E_{22}}{A_{22}E_{22} + A_{12}E_{11}}. \quad (8.27)$$

Here $A_{11} = C_{1111} - C_{1133}^2/C_{3333}$, $A_{22} = C_{2222} - C_{2233}^2/C_{3333}$ and $A_{12} = C_{1122} - C_{1133}C_{2233}/C_{3333}$, C_{ijkl} being the tensor of elastic constants in the hydrostatic state.

For each of the different interface stresses introduced in this work, there are points on the phase coexistence surface where the particular type of interface stress is undefined. For example, $\tau^{(kl)}$ cannot be defined whenever $\sigma_{kl}^s + \delta_{kl}p = 0$, although τ^{NV} , τ^{NS} and τ^{SV} generally remain well-defined at such points. τ^{NV} is undefined when a non-hydrostatic solid and a fluid have the same volume per atom (atomic density). Likewise, τ^{NS} is undefined when entropy per atom is the same in both phases.

8.2.3 Relation to the Shuttleworth equation

The adsorption equation derived in Sec. 8.2.1 can be rewritten in a form similar to the Shuttleworth equation for open surfaces [15]. Taking the differential of γA in the left-hand side of Eq. (8.10) and using $dA = A \sum_{i,j=1,2} \delta_{ij} d\epsilon_{ij}$ we obtain

$$Ad\gamma = -[S]_{XY} dT + [V]_{XY} dp - [N]_{XY} d\mu^f + \sum_{i,j=1,2} (\tau_{ij}^{XY} - \delta_{ij}\gamma) Ad\epsilon_{ij}. \quad (8.28)$$

As before, two differentials in Eq. (8.28) are eliminated by specifying X and Y and the remaining differentials are independent. Taking a partial derivative of γ with respect to the

elastic strain tensor while holding all the other independent variables fixed, we obtain ⁶

$$\frac{\partial\gamma}{\partial\epsilon_{ij}} = \tau_{ij}^{XY} - \delta_{ij}\gamma. \quad (8.29)$$

In this equation, τ_{ij}^{XY} depends on the choice of X and Y . Accordingly, the derivative $\partial\gamma/\partial\epsilon_{ij}$ is taken along a path on the coexistence surface on which the intensive variables conjugate to the chosen X and Y are allowed to vary while all other variables are fixed. In effect, Eq. (8.29) represents a set of equations for different interface stresses τ_{ij}^{XY} and different partial derivatives $\partial\gamma/\partial\epsilon_{ij}$ taken along corresponding paths.

8.2.4 Thermodynamic integration methods

If γ is known at one point on the phase coexistence surface, the adsorption equation (8.10) can be integrated along a chosen path on this surface to compute γ as a function of intensive variables. However, if temperature varies along the path, the integration requires knowledge of the excess entropy $[S]_{XY}$. The latter is rarely accessible in experiments or simulations. To circumvent this problem, we combine Eqs. (8.4) and (8.10) to derive the interface version of the Gibbs-Helmholtz equation, which is more suitable for thermodynamic integration [26]:

$$d\left(\frac{\gamma A}{T}\right) = -\frac{[\Psi]_{XY}}{T^2}dT + \frac{[V]_{XY}}{T}dp - \frac{[N]_{XY}}{T}d\mu^f + \frac{1}{T} \sum_{i,j=1,2} \tau_{ij}^{XY} d\epsilon_{ij}. \quad (8.30)$$

Here

$$\Psi \equiv U + pV - \mu^f N \quad (8.31)$$

is a thermodynamic potential that does not contain the entropy term. Just as the adsorption equation (8.10), Eq. (8.30) contains four independent variables. It can be integrated starting from a chosen reference point to recover γ along the path.

⁶Although ϵ_{ij} is a symmetric tensor, the partial derivative $\partial\gamma/\partial\epsilon_{ij}$ is taken by *formally* treating the four components of ϵ_{ij} as independent variables.

As an example, consider a path on the coexistence surface obtained by biaxial deformation of the solid at zero pressure p in the fluid. Due to the constraints $dp = 0$, $d\epsilon_{11} = d\epsilon_{22} \equiv d\epsilon$ and $d\epsilon_{12} = 0$, we have only one independent variable. Choosing T as the independent variable, Eq. (8.30) is readily integrated to give

$$\gamma A = \frac{(\gamma A)_0 T}{T_0} - T \int_{T_0}^T \left(\frac{[U]_{NV}}{T'^2} - \frac{(\tau_{11}^{NV} + \tau_{22}^{NV})}{T'} \left(\frac{\partial \epsilon}{\partial T'} \right)_{coex.} \right) dT'. \quad (8.32)$$

Here $(\gamma A)_0$ and T_0 are the reference values of total interface free energy and temperature. The derivative $(\partial \epsilon / \partial T)_{coex.}$ is taken along the coexistence path. An advantage of Eq. (8.32) is that all quantities appearing in the integrand are readily accessible in atomistic calculations.

Consider another integration path on which pressure is fixed at zero. Choosing $X = N$, Eq. (8.30) reduces to

$$d \left(\frac{\gamma A}{T} \right) = - \frac{[U]_{NY}}{T^2} dT + \frac{1}{T} \sum_{i,j=1,2} \tau_{ij}^{NY} d\epsilon_{ij}. \quad (8.33)$$

Taking U for Y and integrating, we obtain

$$\gamma A = \frac{(\gamma A)_0 T}{T_0} + T \int_{T_0}^T \left(\frac{[\sigma_{11} + p]_{NU} + [\sigma_{22} + p]_{NU}}{T'} \left(\frac{\partial \epsilon}{\partial T'} \right)_{coex.} \right) dT'. \quad (8.34)$$

This integration path requires calculation of only two excess quantities, $[\sigma_{11} + p]_{NU}$ and $[\sigma_{22} + p]_{NU}$, instead of three in Eq. (8.32). Calculations of excesses $[Z]_{NU}$ instead of $[Z]_{NV}$ have some computational advantages in atomistic simulations. Both Eqs. (8.32) and (8.34) will be used below to compute the interface free energy along biaxial tension and compression paths at zero pressure in the liquid.

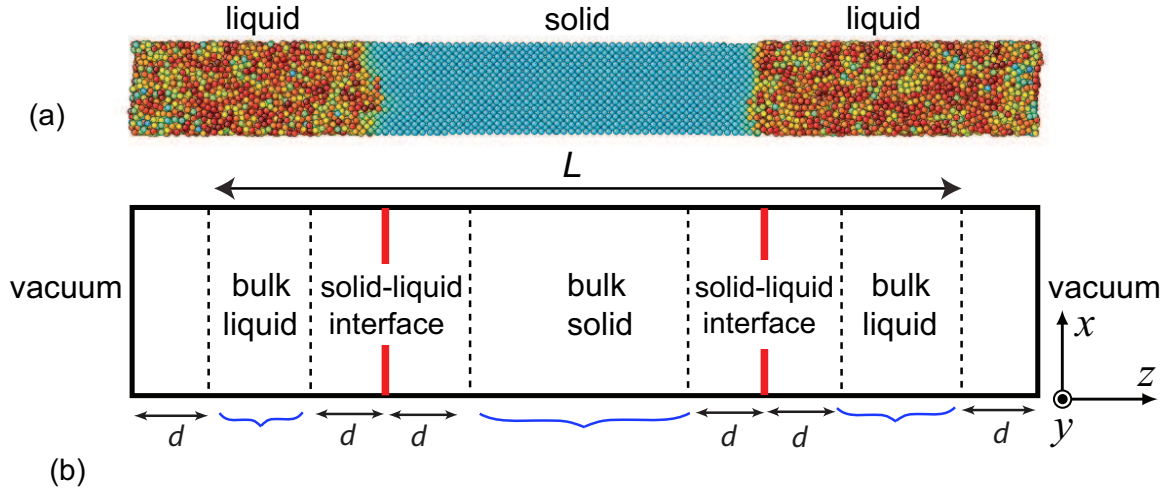


Figure 8.3: (a) Typical snapshot of the simulation block with the solid and liquid phases. (b) Schematic illustration of regions selected for calculations of excess quantities.

8.3 Methodology of atomistic simulations

8.3.1 Simulation block and molecular dynamics methodology

The simulation block with dimensions $x \times y \times z = 32 \times 30 \times 325 \text{ \AA}^3$ contained the total of 23,040 atoms. A 105 \AA thick layer of the solid phase was located in the middle of the block between two 110 \AA thick liquid layers (Fig. 8.3a). The solid and liquid phases were separated by (110) oriented solid-liquid interfaces perpendicular to the z direction. The $[\bar{1}10]$ and $[001]$ crystallographic directions in the solid were parallel to the x and y axes, respectively. The boundary conditions in the x and y directions were periodic, with the free surface condition in the z direction. The termination of the liquid layers at open surfaces ensured constant zero pressure in the liquid phase ($p = 0$).

To create non-hydrostatic stresses in the solid phase, the block was subject to biaxial deformation parallel to the interface. Eleven simulation blocks were prepared with different biaxial tensions and compressions. The lateral stresses created in the solid layer ranged from -2.1 GPa (compression) to 3.4 GPa (tension). The normal stress σ_{33} remained zero due to mechanical equilibrium with the liquid.

After application of the deformation, each simulation block was equilibrated by a 2 ns *NVE* MD run. The obtained equilibrium temperature and lateral stresses in the solid were functions of the applied deformation. In the linear elasticity approximation, T is a paraboloid as a function of the lateral strains E_{11} and E_{22} as shown schematically in Fig. 8.2a [86]. The red dashed line indicates the biaxial deformation path implemented in this work. The equilibration step was followed by a 40 ns production run (also in the *NVE* ensemble) with snapshots generated every 0.01 ns. The snapshots contained coordinates, energies and stresses for all atoms and were used for post-processing.

8.3.2 Calculation of profiles and excess quantities

Profiles of energy, atomic density and stress components as functions of distance in the z direction provide useful information about internal structure of the interface region. To compute such profiles, each snapshot was divided into bins of equal width and the property of interest was averaged within each bin. To obtain smooth profiles, each atom was smeared into a Gaussian along the z axis. Properties related to each atom, such as density, energy and stress, were distributed over its vicinity with the Gaussian distribution.

During an MD run, the position of the interface constantly changes due to thermal fluctuations. The interface implements a random walk along the z axis by spontaneous melting and crystallization processes within thin layers adjacent to the interface.⁷ This interface motion can result in a broadening of the profiles. To avoid the broadening, the interface motion was monitored by computing profiles of the structure factor $|S(\mathbf{k})|$ (\mathbf{k} being a suitable vector of reciprocal lattice), which gave us an approximate interface position in every snapshot [60]. The profiles of other properties computed for individual snapshots were centered relative to the instantaneous position of the interface as identified by $|S(\mathbf{k})|$ and then averaged. After computing the averaged profiles of all properties, they were shifted so that the Gibbsian dividing surface determined from the density profile was at $z = 0$. This shift is dictated by convenience of presentation of profiles and does not constitute any

⁷In the *NVE* ensemble, the walks of the two interfaces are not completely random. They are constrained to keep the average amount of each phase constant.

approximation of our analysis.

All excess quantities, such as the interface stress, excess energy etc., were calculated from Eq. (8.5). Each entry of the determinants was computed for individual snapshots and then averaged. Such entries represented extensive quantities that were computed for selected regions of the simulation block. Properties of individual atoms continued to be represented by Gaussians. The profiles of $|S(\mathbf{k})|$ were used as a guide during the region selection as they indicated approximate positions of the solid-liquid interfaces. The liquid surfaces were identified with the maximum and minimum values of the z coordinate of atoms. An inner region of the solid layer separated by a distance d from both solid-liquid interfaces was taken as the bulk solid region (Fig. (8.3b)). Two liquid regions separated by d from the solid-liquid interfaces and from the liquid surfaces represented by the bulk liquid phase. Finally, the region containing two solid-liquid interfaces and separated by a distance d from the liquid surfaces was selected as the interface layer. In Fig. (8.3b this layer is labeled by L . Since boundaries of the regions were placed relative to the instantaneous positions of the interfaces and surfaces, they slightly varied from one snapshot to the next. Due to properties of determinants in Eq. (8.5), the locations of the boundaries do not affect the excesses as long as these boundaries are within homogeneous phases [14]. A choice of $d = 20$ was found to satisfy this condition. Note that the profiles of properties discussed above were not used for interface excess calculations. They were constructed for illustration purposes only.

8.4 Results

Figs. 8.4a and b display typical profiles of atomic density and energy density across the simulation block when the solid phase is under tension, under compression and nearly hydrostatic. The profiles shown in Fig. 8.4b reveal that the internal energy in the solid decreases with biaxial compression. This is not surprising since quadratic behavior of energy with applied biaxial strain is not expected in this case. It is the free energy that is quadratic in strain and stress, whereas the internal energy is linear. Figs. 8.4c and d show the

corresponding profiles of the stress components σ_{11} and σ_{22} . These two components exhibit different behaviors in the interface region. The σ_{11} component has a peak of compression on the solid side of the Gibbsian dividing surface accompanied by a peak of slight tension on the liquid side. By contrast, σ_{22} shows a single compressive peak. Note also that the magnitudes of the stress components inside the solid are significantly different, which is explained by the anisotropy of elastic constants. The overall thickness of the non-homogeneous interfacial region is about 20 .

The excess energy per unit area, $[U]_{NV}/A$, which is needed for thermodynamic integration by Eq. (8.32), is plotted in Fig. 8.5 as a function of biaxial compression and tension. Within the relatively narrow temperature range implemented in this work, $[U]_{NV}/A$ does not change significantly. It slightly decreases as the solid deviates from the hydrostatic state but increases again under a larger tension. The magnitude of $[U]_{NV}/A$ is nearly an order of magnitude smaller than the interface free energy (see below).

The diagonal components of the interface stress $\hat{\tau}^{NV}$ are shown in Fig. 8.6 as functions of biaxial strain. When the solid is hydrostatic, the interface stress is only slightly anisotropic with the components $\tau_{11}^{NV} = -0.105 \pm 0.004 \text{ J/m}^2$ and $\tau_{22}^{NV} = -0.110 \pm 0.002 \text{ J/m}^2$ [93]. The negative sign indicates that the interface is in a state of compression. As the solid deviates from the hydrostatic state, the anisotropy of $\hat{\tau}^{NV}$ increases significantly. A reversal of the bulk stress from compression to tension changes the sense of the anisotropy. It should be mentioned, however, that the average of τ_{11}^{NV} and τ_{22}^{NV} is much less affected by the applied stresses than the individual components.

Fig. 8.7 shows a plot of the iso-fluid interface stresses $\tau_{11}^{(22)}$ and $\tau_{22}^{(11)}$ as functions of lateral strain. Both stresses were computed from Eq. (8.19) with switches between (11) and (22). Note that these two stresses have different signs which change within the simulated range of lateral strains. As discussed in Sec. 8.2.2, the ratio of these interface stresses equals $(\partial\epsilon_{22}/\partial\epsilon_{11})_{T,p,\epsilon_{12}}$, which has the meaning of the slope of the iso-fluid path in the coordinates E_{11} and E_{22} . In the linear elasticity approximation, the derivative $(\partial\epsilon_{22}/\partial\epsilon_{11})_{T,p,\epsilon_{12}}$ must

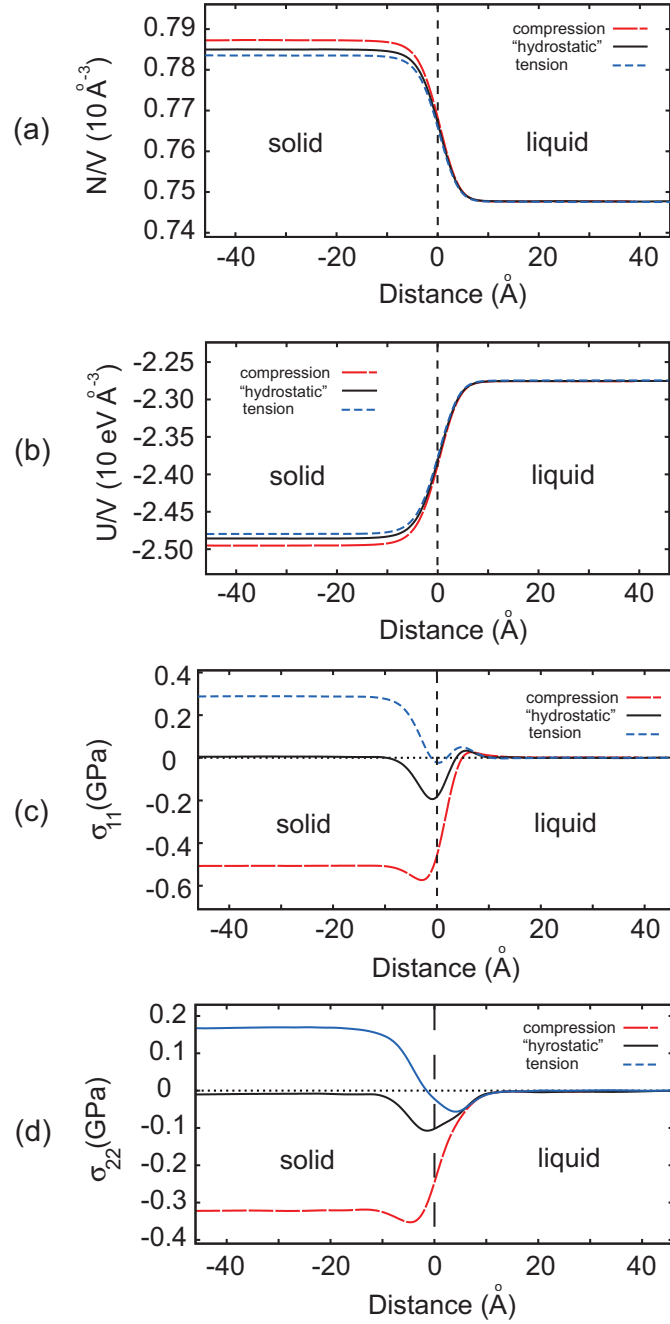


Figure 8.4: Profiles of (a) atomic density, (b) energy density, and stress components (c) σ_{11} and (d) σ_{22} when the solid is under compression ($T = 1325.2$ K), tension ($T = 1325.5$ K) and nearly hydrostatic ($T = 1326.4$ K). The vertical dashed line indicates the position of the Gibbsian dividing surface.

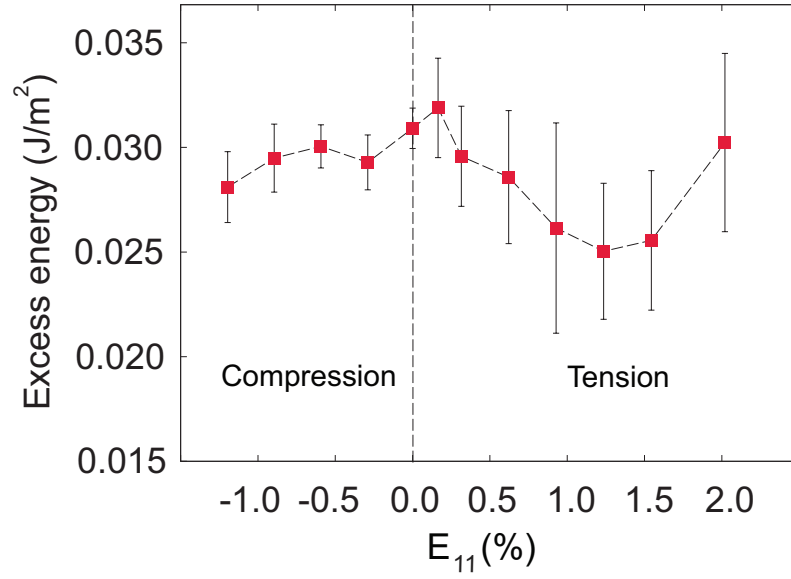


Figure 8.5: Excess energy per unit area, $[U]_{NV}/A$, as a function of biaxial strain. The vertical dashed line indicates the stress-free state of the solid phase.

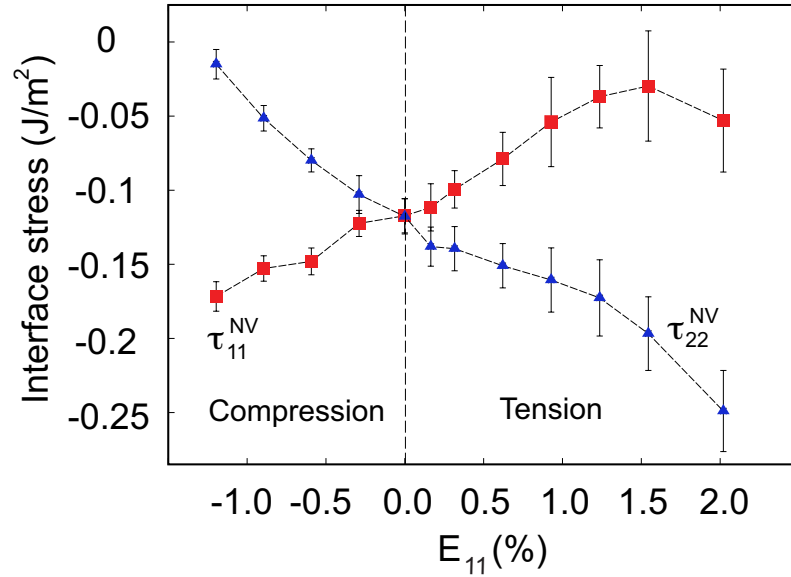


Figure 8.6: Components of the interface stress $\hat{\tau}^{NV}$ as functions of biaxial strain. The vertical dashed line indicates the stress-free state of the solid phase.

be constant along a biaxial deformation path. This constant value was calculated from Eq. (8.27) using the elastic constants of the solid determined in Part I [86] at the temperature

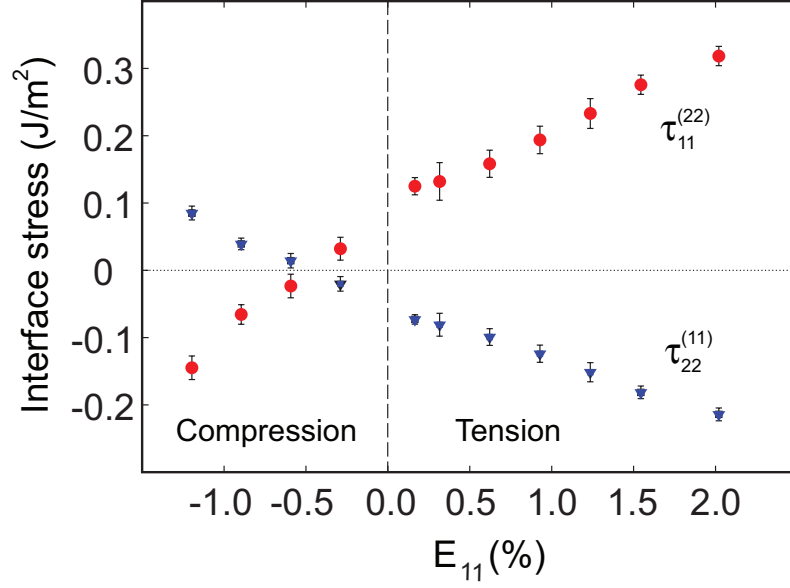


Figure 8.7: Iso-fluid interface stresses as functions of biaxial strain . The vertical dashed line indicates the stress-free state of the solid phase.

T_H . The value obtained, $(\partial\epsilon/\partial\epsilon_{11})_{T,p,\epsilon_{12}} = -1.62$, is shown by the dashed line in Fig. 8.8.

The individual points on this plot are the ratios $\tau_{11}^{(22)}/\tau_{22}^{(11)}$ computed for different states of tension and compression. Although the points display noticeable deviations from the predicted line, the relation (8.22) is approximately followed. There can be several reasons for the discrepancy, including deviations from linear elasticity, the system size effect and other factors. It should be noted that reducing the magnitude of the applied strain does not improve the accuracy of the calculations because the iso-fluid ellipse becomes too small (Fig. 8.2). In the limit of a hydrostatic solid, the ellipsoid shrinks to a point and the ratio $(\partial\epsilon_{22}/\partial\epsilon_{11})_{T,p,\epsilon_{12}}$ becomes undefined.

Finally, Fig. 8.9 reports the temperature dependence of the interface free energy γ obtained by thermodynamic integration of Eqs. (8.32) and (8.34). As the reference state we used the hydrostatic solid-liquid coexistence at $p = 0$. The interface free energy for this state, 0.199 J/m^2 , was computed in our previous work [60]. To find the derivative $(\partial\epsilon/\partial T)_{coex}$ appearing in Eqs. (8.32) and (8.34), the previously obtained[86] biaxial strain

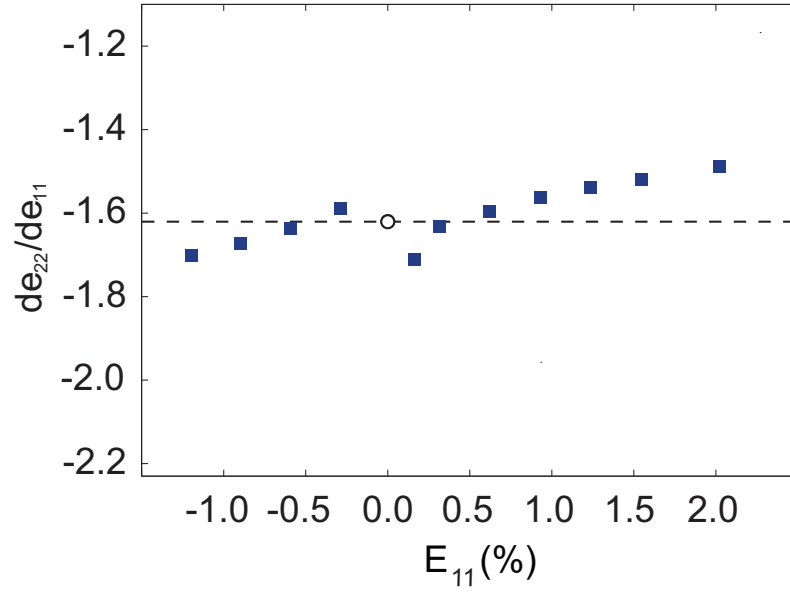


Figure 8.8: The slope of the iso-fluid path as a function of biaxial strain. The value -1.62 computed from Eq. (8.27) is shown by the horizontal dashed line. The open circle is a reminder that the slope is undefined for the hydrostatic state.

ϵ as a function of T was fitted with a cubic spline and differentiated numerically. Fig. 8.9 shows that the interface free energy decreases under biaxial tension but increases under biaxial compression. In the latter case, it reaches a maximum at 1307 K and apparently reverses. In the range of strains studied in this work, the maximum decrease of γ under tension is 9.1% and the maximum increase under compression is 2.3%. Thus, the effect of non-hydrostaticity on γ is much weaker than the effect on the interface stresses. As expected, the values of γ computed by the different integration methods are identical within the accuracy of the calculations.

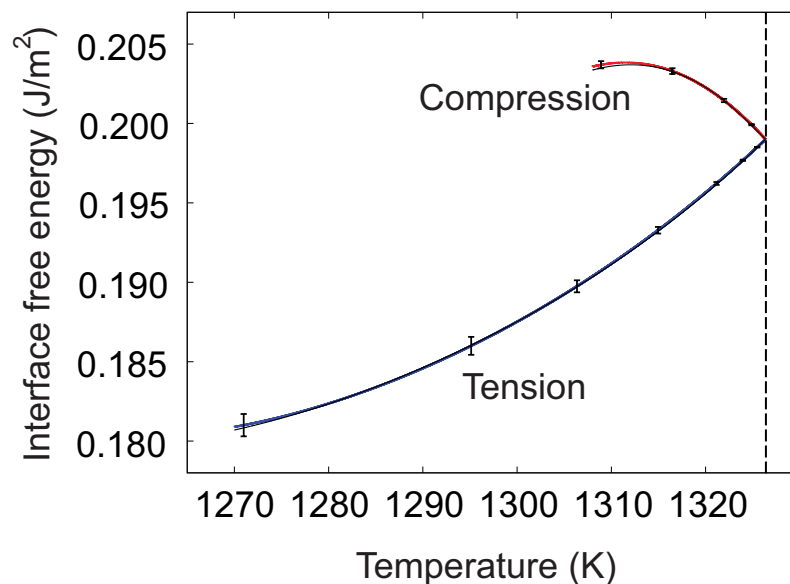


Figure 8.9: Interface free energy γ as a function of equilibrium temperature T for biaxial compression and tension. The red and blue lines were computed from Eq. (8.32), while the black line was computed using Eq. (8.34). The results of the two calculations coincide within the error of integration. The vertical dashed line indicates the stress-free state of the solid phase.

8.5 Summary and conclusions

We have studied thermodynamics solid-fluid interfaces in a single-component system in the presence of non-hydrostatic stresses in the solid phase. While some aspects of this analysis can be found in our previous work dedicated to binary systems [26], the present study was focused on the multiplicity of definitions of the interface stress $\boldsymbol{\tau}$ and its dependence on applied bulk stresses. The interface stress is generally defined as reversible work of elastic deformation of the interface. More specifically, it is defined through the term in the adsorption equation which is responsible for elastic deformations of the interface. We have shown how this term can be expressed as an interface excess quantity similar to excesses of energy, entropy, volume and other properties. The extensive property whose excess per unit area gives the interface stress is the tensor $(\sigma_{ij} + \delta_{ij}p)V$ representing non-hydrostatic stresses in the system (p being pressure in the fluid).

The physical origin of the non-uniqueness of τ is in the fact that the elastic deformations implied by its definition can be implemented under different conditions. Thus, one can talk about an isothermal interface stress τ^{NV} , isobaric τ^{SV} , or an open-system interface stress τ^{SV} (Sec. 8.2.2). As another example, τ can be defined through an iso-fluid process, in which two or more components of strain vary simultaneously while the state of the fluid remains the same. Furthermore, because of the multiplicity of possible iso-fluid deformation paths, there is a multiplicity of iso-fluid interface stresses $\tau^{(kl)}$. It is important to note that the interface stresses not only differ conceptually but can also have different magnitudes or even signs. Thus, care should be exercised when comparing interface stresses obtained by different measurements or simulations. It is only when the solid is hydrostatic that τ has a unique value.

Mathematically, the non-uniqueness of τ arises from the freedom of choice of the independent intensive variables in the adsorption equation. This choice is controlled through the selection of two extensive properties X and Y in the definition of excess quantities by Eq. (8.5). Depending of this choice, different variables are held constant during the deformation, leading to different definitions of τ . By analyzing various choices of variables in the adsorption equation, relationships between different interface stresses can be established as discussed in Sec. 8.2.2. Such relations can be useful for cross-checking results of different experiments or simulations. It should also be pointed out that the formalism presented in this work automatically guarantees that the deformation paths chosen for the definition of τ lie on the phase coexistence surface and are consistent with the Gibbs phase rule. This helps avoid meaningless definitions, such as the derivative $\tau_{ij} = (\partial\gamma A/\partial\varepsilon_{ij})_{p,T}$ which cannot be obtained from Eq. (8.10) and constitutes an impossible variation (a change of a single component of strain at fixed other components, p and T destroys the phase coexistence).

We have applied molecular dynamics simulations to compute several different interface stresses for a (110) solid-liquid interface in copper. The solid phase was subject to biaxial tension and compression producing non-hydrostatic stresses reaching the GPa level. These non-hydrostatic stresses were found to strongly affect the magnitude, anisotropy and even

sign of various interface stresses. As expected from the above analysis, differently defined interface stresses were found to be very different in magnitude, anisotropy and sign. By contrast, the interface free energy is much less sensitive to non-hydrostatic stresses. This observation can be of interest for understanding various interface phenomena, some of which are controlled by the interface free energy while others by interface stress. We hope that this work will motivate further analysis of such phenomena and their dependence on applied stresses.

Chapter 9: Grain boundaries under stress

9.1 Introduction

Thermodynamic properties of GBs are affected by temperature, chemical composition and mechanical stresses. Under hydrostatic conditions effects of temperature [29, 33, 94] and chemical composition [95, 96] have been intensively studied by both experiments and atomistic simulations. In a polycrystalline material subjected to hydrostatic stress the individual grains will generally experience non-hydrostatic stresses due to geometry, anisotropy of the excess GB stress and other factors. The GB stress affects the solubility of nanocrystalline materials which is different from that of the coarse grained materials. The solubility of polycrystalline materials is affected by both segregation at GBs and stresses inside individual grains induced by the excess GB stress [97, 98]. In the absence of sliding at GBs, shear stresses parallel to the boundary plane will be present. The effect of these stresses is not included in the current thermodynamic descriptions of GBs.

In this chapter we GBs in a binary system under stress. Thermodynamic equations introduce a new excess quantity: excess GB shear. The later excess describes a contribution to GB free energy from shear stress parallel to the GB plane. The adsorption equation generates new Maxwell relations [14] that involve derivatives of excess GB properties with respect to shear stress.

In the second part of this work we apply the theory to atomistic simulations. While in experiments measured GB properties are usually averaged over many GBs with different misorientations [97–99], atomistic simulations provide great details about the structure of a particular boundary on the atomic scale and allow for precise calculations of excess GB properties. We studied symmetrical tilt $\Sigma 5(310)[001]$ GB in copper and copper-silver binary alloy. While many of the excess GB properties such as GB stress, segregation, excess volume

and excess shear can be computed directly in atomistic simulations, more sophisticated approaches are necessary to compute γ at finite temperatures. In this work we employ thermodynamic integration to compute GB free energy as a function of temperature and composition. Using the adsorption equation, we evaluate the effects of elastic deformation as well as temperature and chemical composition on γ . We also test Maxwell relations predicted by theory using atomistic simulations.

9.2 Thermodynamics of grain boundaries

9.2.1 Grain boundaries versus phase boundaries

First, we define a GB and emphasise the difference between grain boundaries and phase boundaries. We refer to interfaces that separate two thermodynamically identical grains as GBs. By this definition GB is an interface in a single phase system. Under hydrostatic conditions grains of the same material separated by a planar GB are in equilibrium with each other and represent the same phase. Thus, an interface in such a system satisfies the given definition of a GB. Applied non-hydrostatic stresses usually create driving forces for GB motion. In this case, one grain grows at the expense of the other in absence of curvature, which means that the grains have different thermodynamic states and should be treated as two different phases. Under certain conditions, even when non-hydrostatic stress are present, these phases can be in equilibrium with each other. For example, two grains of the same material one under compression, another under tension (parallel to the GB plane) can be in equilibrium if the elastic energy density is the same in both grains and the stress normal to the GB plane is zero. We call the interface in the later example a phase boundary, since the thermodynamic states of the phases in equilibrium are distinct.

In some cases, due to crystallographic symmetries present in the system, non-hydrostatic stresses preserve equilibrium, while keeping the thermodynamic states of both grains identical, so the bicrystal can still be described as a single phase. These are the type of systems

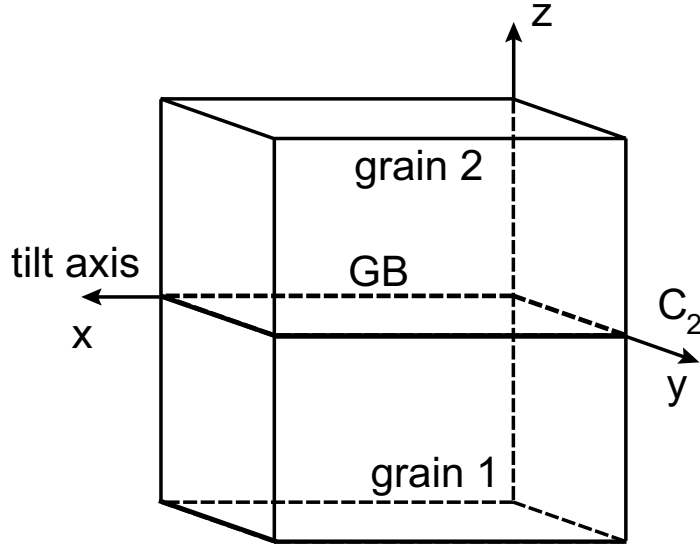


Figure 9.1: Schematics of a bicrystal forming a symmetrical tilt boundary. The grain boundary plane is normal to the z direction.

that will be studied in this work, the general case of phase boundaries was analyzed chapter 2. One example of such a system is symmetrical tilt boundaries. We will focus our discussion on this type of GBs.

Consider a symmetrical tilt boundary schematically shown in Fig. 9.1. The boundary plane is normal to the z direction. The tilt axis is parallel to the x direction. The bicrystal has a twofold symmetry axis parallel to the y direction, which is indicated in Fig. 9.1. There is no twofold symmetry axis parallel to the tilt axis. These symmetries dictate possible equilibrium states under non-hydrostatic stresses. When a symmetrical tilt GB is elastically deformed parallel to the x , y or z axes, the grains remain thermodynamically identical and, therefore, in equilibrium with each other.

Due to the twofold symmetry around the y axis, shear stress σ_{31} , applied parallel to the tilt axis with $\sigma_{32} = 0$, creates identical states stress in the grains and preserves equilibrium. Again, the bicrystal can be treated as a single phase.

When shear is applied normal to the tilt axis (the x_2 direction), symmetrical tilt GBs move by coupled motion, due to the lack of symmetry around the tilt axis [31, 32]. In

this type of GB migration, the normal displacement of the boundary is accompanied by a displacement of grains relative to each other in the direction of the applied shear stress. At the same time, the relative displacement of grains in the direction parallel to the tilt axis is *zero*. This coherent transformation (called coupling) is a process, which means that the grains are not in equilibrium: one grain growth at the expense of the other. Because our goal is a study of GB properties at equilibrium, states with non-zero shear stress σ_{32} will not be considered.

The two different behaviors of the bicrystal with a boundary, when shear is applied parallel to the GB plane in different directions, can be explained treating the grains as two phases and employing Clausius–Clapeyron type equation (2.36) derived in chapter 2.

From the previous discussion we conclude, that symmetrical tilt boundaries can be described as interfaces in a single-phase systems under non-hydrostatic stresses, which include shear parallel to the GB plane in the direction parallel to the tilt axis. In some cases, due to crystallographic symmetries of the bulk, a boundary can be described as symmetrical tilt, with different orientations of the tilt axes and different misorientation angles. This multiplicity of descriptions results in multiplicity of coupling modes and the coupling may occur when shear is applied in any direction. In such system, equilibrium between thermodynamically identical grains under shear is unlikely to occur and such GBs are not a subject of this work.

We finally point out that other systems with GBs under stress (besides the symmetrical tilt) fit into the description of a single phase. In case of pure twist boundaries, elastic deformation parallel to the axis of symmetry will preserve equilibrium. Shear parallel to the GB plane can be applied in two mutually perpendicular directions preserving identical thermodynamic states of the bulk. Shear in other directions will not lead to coupled motion because the gliding planes of the GB dislocations are parallel to the GB plane; however, sliding may occur or due to the elastic anisotropy the generated stresses will be different in the two grains, producing the bulk driving force for boundary motion (by mechanism other than coupling).

9.2.2 Thermodynamic description of the system

We will analyze a system with two crystals of the same phase separated by a coherent GB. The coherency of the boundary should be understood in the same way as discussed in chapter 2 which implies the absence of slip. Atoms in the bulk part and the GB region are allowed to diffuse. Because we consider only equilibrium states, the net diffusive flux must be zero (no creep). The GB may contain disordered regions such as premelted dislocations and remain coherent, as long as the GB migration happens without a slip. This situation is appropriate for low angle GBs, then the premelted GB dislocations are separated by perfectly crystalline parts of the boundary that prohibit slip. There are other premelting scenarios when GBs turn into uniform liquid-like layer near the melting point [100]. Such GBs are incoherent and the grains will slip if shear is applied parallel to the GB plane. Note, that the analysis developed below will remain valid for such GBs, if the shear stresses in the equations are set to zero and remain constant.

The bicrystal and the GB is schematically illustrated in Fig. 9.2 with the GB plane normal to the z direction. To describe elastic variations of a GB with area A we use the small strain \mathbf{e} . The four components e_{11} , e_{12} , e_{21} and e_{22} are variables common to the both grains and the GB region. The local elastic strain normal to the GB plane is not uniform in the system: while it is the same in the homogeneous parts of the grains, it depends on the z coordinate in the GB region. The bicrystal in consideration is under general non-hydrostatic state of stress, described by the Cauchy stress tensor σ_{ij} . Inside the homogeneous parts of the grains 1 and 2, $\sigma_{ij}^1 = \sigma_{ij}^2$. However, inside inhomogeneous GB region the components σ_{11} , σ_{12} , and σ_{22} take values which depend on z and different from the bulk values. These deviation of stress from the bulk values result in excess GB stress.

Here we consider a case of a binary system with solid formed by substitutional mechanism. To describe compositional changes on the substitutional lattice we employ the diffusion potential M_{21} , introduced by Larche and Cahn [18]. The diffusion potential equals the change in the energy of the system when an atom of sort 1 is substituted by an atom of sort 2 at constant total number of substitutional atoms

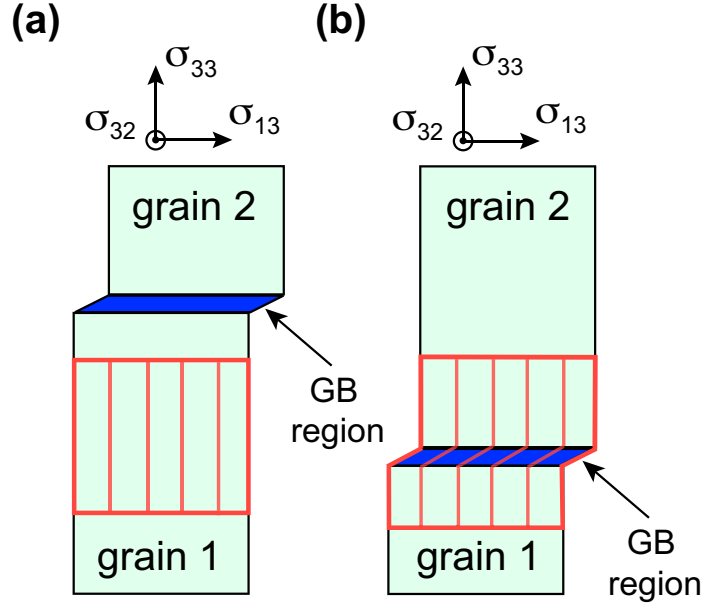


Figure 9.2: Schematic representation of the system with the GB. Grains 1 and 2 are in neutral equilibrium. The figure shows a spontaneous migration of the GB.

$$M_{21} = \left(\frac{\partial U}{\partial N_2} \right) - \left(\frac{\partial U}{\partial N_1} \right), \quad (9.1)$$

where U is the energy of the system, N_1 and N_2 are the numbers of atoms of the first and second components, respectively. In Eq. (9.1) the derivatives are taken at constant entropy and state of strain. To define the diffusion potential M_{21} , component 1 was chosen as the reference one.

The equilibrium between two grains requires that [18] 1) Temperature is uniform throughout the system 2) The diffusion potential M_{21} is uniform in the system 3) Due to mechanical equilibrium, the components of the Cauchy stress tensor σ_{31} , σ_{32} and σ_{33} are continuous across the GB. Here, we consider a case when the system with the GB supports shear σ_{31} only in one direction, so that the other component of the shear stress σ_{32} is always zero.

9.2.3 Excess GB free energy

We start the analysis deriving an expression for GB free energy γ as a reversible work required to create a unit of GB area. Consider the same two grains separated by a coherent GB in equilibrium (Fig. 9.2). Let us select an imaginary region containing N atoms in the homogeneous part of the grain 1 not affected by the GB. The region is indicated in Fig. 9.2a by a solid red line. Because the two grains are thermodynamically identical, the GB can migrate spontaneously without altering the thermodynamic state of the system. This state is defined by values of the intensive parameters $T, M_{21}, \sigma_{31}, \sigma_{33}$ and strains e_{11}, e_{12} and e_{22} . Consider such a migration of the GB at constant $T, M_{21}, \sigma_{31}, \sigma_{33}$ and fixed strains e_{11}, e_{12} and e_{22} , when the GB enters the selected region. The migration may occur due to coupled motion with grains displacing relative to each other in the direction 2 at zero shear stress σ_{32} or due to diffusive motion of GB atoms. In the direction of shear σ_{31} the relative displacement of grains during this migration is identically zero. In the varied state, shown in Fig. 9.2b by a solid red line, the region contains the GB as well as some homogeneous parts of grains 1 and 2. The location of the GB inside the selected region is arbitrary, as long as the boundaries of the region are located inside of the homogeneous parts of grains 1 and 2. The regions in the initial and final state contain the same total number of atoms, however, the average chemical composition is different. Let us compare the energies of the region in the initial state and in the varied state. The energy changed due to the heat supplied to the system, the mechanical work done by stresses σ_{31} and σ_{33} and the chemical work (change of the average composition at constant value of diffusion potential M_{21}). The lateral stresses do not contribute to the energy change, because the transformation happens at a fixed area and shape of the GB. In the varied state the system contains the GB and we denote this contribution to energy of the region as γA , where A is the GB area. Because this process is reversible (the initial and final configurations are equilibrium states), we only need to compare the initial and final states to evaluate the energy change. Thus, we obtain

$$U - U^1 = T(S - S^1) + Ab_1\sigma_{31} + Ab_3\sigma_{33} + M_{21}(N_2 - N_2^1) + \gamma A, \quad (9.2)$$

where U , S , V and N_2 refer to the energy, entropy, volume and number of atoms of the second component in the region containing the GB and the quantities with the superscript 1 refer to the properties of the grain 1 (or simply bulk properties). The components b_1 and b_3 of the displacement vector are illustrated in Fig. 9.23 and have meaning of the excess shear and excess thickness of the GB, respectively. Quantities $U - U^1$, $S - S^1$ and $N_2 - N_2^1$ are the excess energy, entropy and GB segregation.¹ Because the region with the GB and the initial homogeneous region contain the same total number of atoms, Eq. (9.2) can be written in notations introduced by Cahn [14] as

$$\gamma A = [U]_N - T[S]_N - \sigma_{33}[V]_N - \sigma_{31}Ab_1 - M_{21}[N_2]_N. \quad (9.3)$$

The terms $[Z]_N$ are computed as [14]

$$[Z]_N \equiv \frac{\begin{vmatrix} Z & N \\ Z^1 & N^1 \end{vmatrix}}{N^1} = Z - Z^1 \frac{N}{N^1}. \quad (9.4)$$

$[Z]_N$ has a meaning of excess GB property Z when the region with the GB has the same total number of substitutional atoms as the bulk system. In Eq. (9.4) the quantities with and without the superscript are computed inside of the bulk part and the GB region, respectively. In Eq. (9.2) U^1 , S^1 , etc, refer to a bulk region with the same number of atoms N , while in Eq. (9.4) the same bulk properties are computed inside arbitrary bulk region containing arbitrary number of atoms ($N^1 \neq N$). The rule of the excess calculation in Eq. (9.4) ensures, that Eqs. (9.2) and (9.3) are identical.

The term Ab_3 is equal to the volume change $V - V^1 = [V]_N$ of the region due to the GB,

¹ $N_2 - N_2^1$ is different from Gibbsian segregation introduced through the dividing surface.

so we wrote it as $\sigma_{33}[V]_N$. Thus, in Eq. (9.3) $[U]_N$, $[S]_N$, $[V]_N$, and $[N_2]_N$ are the total excesses of energy, entropy, volume and segregation of the GB with area A . These excesses are different from those introduced by Gibbs using a concept of the dividing surface, in which case excess volume is zero by definition [13].

9.2.4 The adsorption equation.

Having derived the expression for GB free energy γ , we are now in a position to derive the adsorption equation. Consider a reversible variation in the state of the system with the GB, when it exchanges heat, elastically deforms and changes its composition. The differentials of energy of the region containing the GB and the bulk region with the same total number of atoms N are given by

$$dU = TdS + M_{21}dN_2 + \sum_{i=1,2} (\bar{\sigma}_{ij}V - \delta_{ij}\sigma_{3i}Ab_i)de_{ij} + \sum_{i=1,3} A\sigma_{3i}du_i, \quad (9.5)$$

and

$$dU^1 = TdS^1 + M_{21}dN_2^1 + \sum_{i=1,2} \sigma_{ij}^1 V^1 de_{ij} + \sum_{i=1,3} A\sigma_{3i}du_i^1, \quad (9.6)$$

where $\bar{\sigma}_{ij}$ are the components of stress averaged over the volume with the GB. The first terms Eqs (9.5) and (9.6) describes heat exchange, second terms describe change in chemical composition at constant total number of atoms and the rest describes elastic deformation. Work of the deformation parallel to the GB plane (e_{11} , e_{12} and e_{22}) was separated from work of stresses σ_{31} and σ_{33} . Because we do not consider rotation, six variables describe possible independent elastic deformations (e_{12} and e_{21} represent one variable). Thus, each solid has eight degrees of freedom.

In Eqs (9.5) and (9.6) the elastic work is computed as traction vector times the displacement integrated over the surface of the two regions. Here, du_i and du_i^1 denote the displacement of the upper face of the region containing the GB and the homogeneous bulk

region, respectively. While the vectors $d\mathbf{u}$ and $d\mathbf{u}^1$ each have three components, du_2 and du_2^1 do not appear in Eqs. (9.5) and (9.6) because σ_{32} is zero. Differentiating Eq. (9.2) and using the differentials of energy from Eqs. (9.5) and (9.6) in conjunction with $db_i = du_i - du_i^1$ we obtain

$$d(\gamma A) = -(S - S^1)dT - Ab_1d\sigma_{31} - Ab_3d\sigma_{33} - (N_2 - N_2^1)dM_{21} + \sum_{i,j=1,2} \tau_{ij}Ade_{ji}, \quad (9.7)$$

with the components of $\boldsymbol{\tau}$ given by

$$\tau_{ij}A = \bar{\sigma}_{ij}V - \sigma_{ij}^1V^1 - \delta_{ij}\sigma_{3i}Ab_i - \delta_{ij} \sum_{k=1,3} Ab_k\sigma_{3k}. \quad (9.8)$$

$\boldsymbol{\tau}$ is a (2×2) symmetrical tensor.

Again, Eq. (9.7) can be written using the determinants notation introduced by Cahn [14] as

$$d(\gamma A) = -[S]_NdT - [V]_Nd\sigma_{33} - Ab_1d\sigma_{31} - [N_2]_NdM_{21} + \sum_{i,j=1,2} \tau_{ij}Ade_{ji}. \quad (9.9)$$

Eq. (9.9) is the adsorption equation. It provides a differential of the total GB free energy γA in terms of differentials of the intensive parameters. The number of degrees of freedom in the adsorption equation is eight and each differential coefficient (excess quantity) correspond to a partial derivative of γA . If applied to a hydrostatic process, Eq. (9.9) corresponds to the adsorption equation with differential $d\mu_1$ eliminated, where μ_1 is the chemical potential of the component 1 [14].

$\boldsymbol{\tau}$ describes the change in GB free energy due to elastic deformation of GB area. We

identify it with the excess GB stress tensor. τ naturally appears in the adsorption equation as an excess of stresses in the region containing the GB relative to the bulk stresses σ_{ij}^1 . Note that the shear stress σ_{31} is involved in the expression for τ .

Eq. (9.9) shows that both stresses σ_{31} and σ_{33} affect γ . The new term $Ab_1d\sigma_{31}$ in the adsorption equation is specific to coherent GBs. While excess GB volume $[V]_N$ was measured both experimentally and in simulations [101, 102], the excess GB shear has not been estimated before. In the atomistic simulation part of this work we calculate b_1 as a function of σ_{31} and analyze the significance of this term in comparison with other terms.

9.2.5 Lagrangian and physical forms of the adsorption equation

Eq. (9.9) expresses a differential of the total GB free energy γA through differentials of intensive parameters. We will refer to this form of the adsorption equation as Lagrangian. We now derive physical form of the adsorption equation which operates with excess quantities per unit of the current physical area. Differentiating the product γA in Eq. (9.9) using $dA = \delta_{ij} A de_{ij}$ and dividing both sides of the equation by the physical area A of the current state, we obtain the differential of the specific GB free energy γ

$$d\gamma = -\frac{[S]_N}{A} dT - \frac{[V]_N}{A} d\sigma_{33} - b_1 d\sigma_{31} - \frac{[N_2]_N}{A} dM_{21} + \sum_{i,j=1,2} (\tau_{ij} - \delta_{ij}\gamma) de_{ji}. \quad (9.10)$$

In Eq. (9.10) the excess quantities are computed per unit of physical area. The differentials of the intensive parameters in the adsorption equation are independent variables. Therefore, the differential coefficients correspond to partial derivatives of γ . From Eq. (9.10) we immediately obtain :

$$\frac{\partial\gamma}{\partial e_{ij}} = \tau_{ij} - \delta_{ij}\gamma \quad (9.11)$$

The partial derivative in Eq. (9.11) is taken at constant T , M_{21} , σ_{31} and σ_{33} . Thus, Eq. (9.11) is the version of the Shuttleworth equation generalized for a GB in open binary system under stress normal to the GB plane.

The two forms of the adsorption equation in Eqs. (9.9) and (9.10) are perfect differentials and generate two sets of Maxwell relations between the partial derivatives of the excess properties. These relations will be discussed in Sec. 9.2.7.

9.2.6 Thermodynamic integration

Here we derive another version of the adsorption equation, which can be useful in applications. GB free energy as a function of intensive properties can be computed by integration of the adsorption equation. However, in applications excess entropy $[S]_N$ is rarely accessible. Combining Eqs. (9.3) and (9.9), we eliminate $[S]_N$ and derive the interface version of the Gibbs-Helmholtz equation

$$d\left(\frac{\gamma A}{T}\right) = -\frac{[\Psi]_N}{T^2}dT - \frac{[V]_N}{T}d\sigma_{33} - \frac{Ab_1}{T}d\sigma_{31} - \frac{[N_2]_N}{T}dM_{21} + \frac{1}{T} \sum_{i,j=1,2} \tau_{ij}de_{ji}, \quad (9.12)$$

where the excess of the thermodynamic potential Ψ is given by

$$[\Psi]_N \equiv [U]_N - [V]_Nd\sigma_{33} - Ab_1\sigma_{31} - [N_2]_NM_{21}. \quad (9.13)$$

Eq. (9.12) does not contain the entropy term and can be integrated from some reference point to recover γ as a function of the intensive variables. Eq. (9.12) is yet another form of the adsorption equation and has the same set of intensive variables. It produces another set of Maxwell relations, which do not involve excess entropy.

9.2.7 Maxwell relations

As we mentioned before, the adsorption equation (9.9) (and its various forms (9.10) and (9.12)) is an exact differential. It generates Maxwell relations between the derivatives of the excess quantities. We will analyze these Maxwell relations in the Lagrangian and physical forms simultaneously. Maxwell relations in the Lagrangian form involve derivatives of the total excesses, while in the physical form the excesses are computed per unit of the current area. Some of the relations in the physical form involve the derivatives of $\tau_{ij} - \delta_{ij}\gamma$ and require knowledge of γ as a function of intensive parameters to evaluate the derivatives. The advantage of the Lagrangian formulation is that the knowledge of γ is not required. In subsequent equations of this section the first relation corresponds to the Lagrangian formulation and second to the physical. We discuss separately the following cross relations 1) mechanical-mechanical 2) mechanical-chemical 3) mechanical-thermal and 4) thermal-chemical. The partial derivatives involved in the equations below will be computed in atomistic simulations to test the Maxwell relations.

Mechanical-mechanical relations

Equations of this section examine effects of lateral strains e_{11} , e_{22} and e_{12} and stresses σ_{31} and σ_{33} on GB stress, GB volume and shear. The partial derivatives in the equations below are taken at constant T and M_{21} :

$$\frac{\partial(\tau_{ij}A)}{\partial e_{kl}} = \frac{\partial(\tau_{kl}A)}{\partial e_{ij}}, \quad \frac{\partial(\tau_{ij} - \delta_{ij}\gamma)}{\partial e_{kl}} = \frac{\partial(\tau_{kl} - \delta_{kl}\gamma)}{\partial e_{ij}}, \quad (9.14)$$

$$\frac{\partial(\tau_{ij}A)}{\partial \sigma_{33}} = -\frac{\partial[V]_N}{\partial e_{ij}}, \quad \frac{\partial(\tau_{ij} - \delta_{ij}\gamma)}{\partial \sigma_{33}} = -\frac{\partial([V]_N/A)}{\partial e_{ij}}, \quad (9.15)$$

$$\frac{\partial(\tau_{ij}A)}{\partial \sigma_{31}} = -\frac{\partial(b_1A)}{\partial e_{ij}}, \quad \frac{\partial(\tau_{ij} - \delta_{ij}\gamma)}{\partial \sigma_{31}} = -\frac{\partial b_1}{\partial e_{ij}}, \quad (9.16)$$

$$\frac{\partial (b_1 A)}{\partial \sigma_{33}} = \frac{\partial [V]_N}{\partial \sigma_{31}}. \quad (9.17)$$

Eqs. (9.14) - (9.16) correspond to variations of state, in which interfacial area changes. As a result, the Lagrangian and physical forms of the relations are different. In Eq. (9.17) the Lagrangian and physical forms are identical, because the partial derivatives are taken at fixed crosssection.

Mechanical-chemical relations

The following equations examine effects of mechanical deformation on GB segregation. All the relations in this section correspond to isothermal processes. The adsorption equation allow to examine how GB segregation is affected by lateral strains e_{ij} and stresses σ_{31} and σ_{33}

$$\frac{\partial (\tau_{ij} A)}{\partial M_{21}} = -\frac{\partial [N_2]_N}{\partial e_{ij}}, \quad \frac{\partial (\tau_{ij} - \delta_{ij} \gamma)}{\partial M_{21}} = -\frac{\partial ([N_2]_N / A)}{\partial e_{ij}}. \quad (9.18)$$

Variations in Eq. (9.18) involve change in GB area, which results in different physical and Lagrangian forms of the relation. Elastic deformation (the derivative on the right hand side) happens at constant value of the diffusion potential M_{21} , so the system is open and the average composition changes.

The following two relations examine effect of the stresses σ_{31} and σ_{33} on segregation

$$\frac{\partial (b_1 A)}{\partial M_{21}} = \frac{\partial [N_2]_N}{\partial \sigma_{31}}, \quad (9.19)$$

$$\frac{\partial [V]_N}{\partial M_{21}} = \frac{\partial [N_2]_N}{\partial \sigma_{33}}. \quad (9.20)$$

In Eqs. (9.19) and (9.20) variations happen at a fixed crosssection (therefore, constant

A), so the Lagrangian and physical forms are identical. Eq. (9.19) show that if excess shear of the GB only exists under shear stress, then the effect of σ_{31} on segregation is at most quadratic (linear term is zero). On the other hand, segregation should depend linearly on σ_{33} , since excess volume is generally not zero even for a stress free state and depends on M_{21} .

Mechanical-thermal relations

Temperature changes affect GB properties. Relevant Maxwell relations involve partial derivatives of the excess entropy $[S]_N$. Evaluation of such derivatives can be difficult or impossible in applications. To analyze effects of temperature on GB properties, we employ interface version of the Gibbs-Helmholtz equation (9.12). The derivatives in these Maxwell relations involve the potential Ψ instead of S . The first set of relations involves change in GB stress $\boldsymbol{\tau}$ with temperature:

$$\frac{\partial (\tau_{ij}A/T)}{\partial T} = -\frac{\partial ([\Psi]_N/T^2)}{\partial e_{ij}}, \quad \frac{\partial \{(\tau_{ij} - \delta_{ij}\gamma)/T\}}{\partial T} = -\frac{\partial ([\Psi]_N/A)}{\partial e_{ij}}. \quad (9.21)$$

Again, in Eq. (9.21) the GB area change and Lagrangian and physical forms of the adsorption equation are different. The following two relations relate changes in GB volume and shear at fixed crosssection to changes in the potential Ψ with stresses σ_{33} and σ_{31} , respectively

$$\frac{\partial ([V]_N/T)}{\partial T} = \frac{\partial ([\Psi]_N/T^2)}{\partial \sigma_{33}}, \quad (9.22)$$

$$\frac{\partial (b_1A/T)}{\partial T} = \frac{\partial ([\Psi]_N/T^2)}{\partial \sigma_{31}}. \quad (9.23)$$

The first derivative in Eq. (9.22) represents the thermal expansion of a GB in the

direction normal to the GB plane at fixed crosssection.

Chemical-thermal relations

Finally, we examine the effect of temperature on GB segregation. We will again use Gibbs-Helmholtz type equation to avoid calculation of $[S]_N$

$$\frac{\partial ([N_2]_N/T)}{\partial T} = \frac{\partial ([\Psi]_N/T^2)}{\partial M_{21}}. \quad (9.24)$$

In Eq. (9.24) variations happen at a fixed lateral dimensions and constant σ_{31} and σ_{33} .

9.3 Methodology of atomistic simulations

The theory developed in the previous section provides expressions for excess quantities and gives relations between them. In this section we apply the developed thermodynamic treatment to study of a symmetrical tilt GB by atomistic simulations. We examine effects of elastic deformation, temperature and chemical composition on interfacial properties and test the derived Maxwell relations.

9.3.1 Description of the studied GB

In this work we studied a symmetrical tilt $\Sigma 5$ (310) GB in Cu and binary CuAg system. The GB was created by joining two crystals of different orientation along a plane normal to the z axis. The structure of the boundary is illustrated in Fig. 9.3. The crystals were rotated relative to each other by angle 36.87° around the (001) tilt axis which was parallel to the x direction. The (001) planes of both grains are parallel to the plane of the figure. (001) and (310) crystallographic directions of the bicrystal are parallel to the x and y directions, respectively. The twofold rotation symmetry axis is parallel to the x direction.

Due to the symmetries of the system with the GB elastic deformation can be applied parallel to the coordinate axis x , y , and z preserving equilibrium between the two grains.

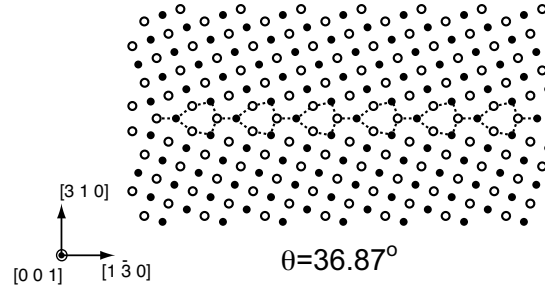


Figure 9.3: Structure of the symmetrical tilt $\Sigma 5(310)$ GB. The figure shows projections of the perfect atomic positions on the (001) plane. The tilt axis is normal to the plane of the figure.

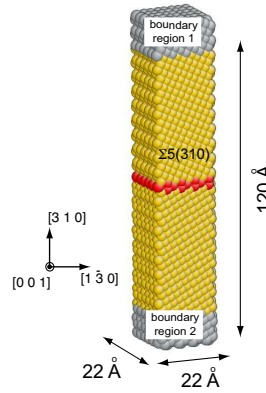


Figure 9.4: Simulation block with the GB. The position of the GB is indicated by red coloration. Atoms colored in grey belong to boundary regions 1 and 2. Boundary conditions in the GB plane are periodic.

The system also supports shear stress σ_{31} parallel to the tilt axis. Due to the lack of the twofold symmetry around the tilt axis, the GB moves by coupled motion [31,32] when shear σ_{32} is applied in the y direction. The coupling factor for this boundary is $\beta = -1.0$. It is defined as a ratio of the parallel and normal GB displacements during the GB migration. While the migration of the GB during the simulations may occur by coupled motion, the corresponding component of the shear stress σ_{32} . Thus, such a migration is not a continuous process and does not modify the equilibrium state.

9.3.2 Simulation block

The simulation block with the GB had dimensions $22 \times 23 \times 145$ and contained 5256 atoms (Fig. 9.4 [85]). The atoms in the GB region are shown in red in Fig 9.4 to indicate the position of the boundary. Periodic boundary conditions were applied in the x and y directions. In the z directions the boundary conditions were not periodic. The grains and the GB were sandwiched between two layers of “boundary” atoms. These layers are indicated in Fig. 9.4 as boundary regions 1 and 2. The thickness of each region is twice the cutoff radius of atomic interaction. Different restrictions, imposed on motion of atoms in the boundary regions during simulation, allow to implement a desired state of stress. In different types of simulations described below positions of atoms in the region 2 were fixed (unless otherwise stated), so that the simulation block could not rigidly displace in the z directions.

9.3.3 Single component copper system and copper-silver binary alloy

The GB properties were studied in both single component and binary systems. We used pure copper (Cu) and copper-silver (CuAg) alloy as model materials in these two cases. In this work we studied GB between grains that are Cu rich solid solutions with atomic concentration of silver less than 1 %.

9.3.4 0K calculations. Single component Cu system.

We start the study of GB properties by investigating the effects of mechanical deformation. To exclude effects of segregation and temperature the simulations were performed in a single component copper system at 0 K (Isothermal calculation still requires calculation of excess entropy $[S]_N$ to evaluate γ). To compute the excess GB properties as functions of e_{11} , e_{22} , σ_{31} and σ_{33} and test Maxwell relations (9.14) - (9.17), we performed several simulations in which the system was elastically deformed. These deformations include tension/compression parallel to the x , y and z directions, as well as shear parallel to the tilt axis (the x direction). Below we describe implementations of these deformations in each case.

Deformation parallel to the GB plane: uniaxial and biaxial

The simulation block with the GB was elastically deformed parallel to the GB plane at constant zero components of stress σ_{31} , σ_{32} and σ_{33} . Three different lateral deformations were applied: two uniaxial and biaxial. In the case of biaxial deformation the bicrystal was strained along the x and y directions by the same amount. The strains were applied parallel to (001) and (310) crystallographic directions, which are the principal axes of strain of the system. As a result, no shear stresses were generated in the deformed state.

In each type of deformation, the simulation block was elastically strained by small discrete amounts and statically relaxed after each subsequent deformation. During the relaxation the lateral dimensions of the system were kept fixed, while atoms allowed to move until the total energy was minimized. Atoms in the boundary region 1 were allowed to move only in the z direction. Because there were no periodic boundary conditions in the z direction the component of stress σ_{33} was identically zero after the relaxation. In the deformed blocks the lateral strain ranged from -1.6% (compression) to 1.6% (tension).

Deformation normal to the GB plain

Tension and compression were applied to the system normal to the GB plane at fixed lateral dimensions. The deformation was realized by scaling of the z coordinates of all atoms by small discrete amounts. After each scaling the system was statically relaxed. During the relaxation atoms in the boundary regions 1 and 2 were fixed. Although there were no periodic boundary conditions in the z direction, the two fixed boundary regions prohibit the system relaxation in the z direction resulting in the finite normal stress σ_{33} . Due to the mirror symmetry relative to the boundary plane the shear components of stress σ_{31} and σ_{32} remained zero. In the obtained relaxed structures σ_{33} ranged from -2.4 GPa (compression) to 2.7 GPa (tension).

Shear deformation parallel to the tilt axis

Shear was applied parallel to the tilt axis at fixed lateral dimensions (e_{11} , e_{12} and e_{22}) and zero σ_{33} . The elastic deformation was implemented by rigid displacement of the boundary region 1 in the x direction (parallel to the tilt axis) by a small distance, keeping the positions of atoms in the region 2 were fixed. After each incremental displacement the system was statically relaxed. During the relaxation lateral dimensions of the system were kept fixed, while atoms in the region 1 were allowed to move only in the z direction. As a result, after the relaxation the normal component of stress σ_{33} was zero, but σ_{31} had a finite value. Increasing the amount of the total rigid displacement of the atoms in the region 1 and relaxing the system after each incremental displacement, we obtained several states of the system with σ_{31} ranging from 0 GPa to 1.49 GPa.

Maxwell relations

To test Maxwell relations discussed in Sec. 9.2.7 at 0 K temperature, we computed the derivatives of the excess quantities with respect to the intensive parameters: e_{11} , e_{22} , σ_{31} and σ_{33} . Discrete data points obtained from atomistic simulations were fitted with polynomial of the second order and the derivative was then evaluated for the stress free state of the bulk grains.

9.3.5 Single component Cu system at finite temperatures

To study GB properties at finite temperature we employed Molecular Dynamics (MD) simulations in NVT ensemble. The simulations were performed in the temperature range from 0 K to 900 K with 100 K interval. At each simulated temperature the simulation block was preexpanded by the thermal expansion factor computed previously in Ref. [39] Due to the expansion procedure the bulk stresses were nearly zero. The components of stress σ_{11} and σ_{22} remained non zero in the GB region due to the excess GB stress. During the MD simulations no restrictions were applied on the motion of atoms in the boundary regions 1 and 2. This type of boundary conditions is equivalent to open surfaces in the z direction

and guarantees that the stresses σ_{31} and σ_{33} are identically zero. At each temperature the system was first equilibrated during 2 ns. The equilibration stage was followed by a production stage during which snapshots of the system were generated. The snapshots contain positions of atoms as well as the energies and stresses on atoms. This data was used later for post processing.

9.3.6 Binary CuAg System

To model binary CuAg system at finite temperatures we used Monte Carlo (MC) simulations in semi-grand canonical ensemble [36, 48, 51]. We performed MC simulations of the binary system at constant temperature $T = 800K$ and sampled the composition range from 0 to 0.58% of Ag in the bulk part of the grains. Simulation blocks with different composition at the same temperature were obtained by changing the value of the diffusion potential M_{21} . In each simulation with a given value of M_{21} , the system was preexpanded according to expansion of the bulk solid at given temperature and composition (value of M_{21}). The expansion coefficient was computed separately by performing simulation of the single crystal with all periodic boundary conditions in semi-grand canonical NPT ensemble with a given value of M_{21} and zero pressure. The expansion procedure was implemented to minimize bulk stresses. During the simulation of the system with the GB the x and y dimensions were fixed. The boundary conditions in the z direction were identical to the boundary conditions in the MD simulations of pure copper, which ensured zero σ_{31} and σ_{33} stresses. In each simulation the system was first equilibrated during 5×10^4 MC steps. The equilibration stage was followed by a production stage, during which snapshots of the system were generated. The snapshots contained information about energies, stresses and atomic sorts of individual atoms. This data was used later for post processing.

9.3.7 Test of Maxwell relations in case of binary system at finite temperature

To test Maxwell relations in the binary system that involve change in segregation we performed four types of simulations: 1) biaxial tension/compression $e = e_{11} = e_{22}$ parallel to the GB plane at constant T , M_{21} , σ_{31} and σ_{33} 2) tension/compression normal to the GB plane at constant T , M_{21} and e , 3) variation of M_{21} at constant T , σ_{31} , σ_{33} and e and 4) variation of T at constant M_{21} , σ_{31} , σ_{33} and e . The elastic deformations were implemented using methodology similar to 0 K calculations described earlier. In each out of the four variations, several separate MC simulations were performed at different values of the relevant intensive parameter (e , σ_{33} , M_{21} and T). The discrete data points obtained from these individual simulations were fitted with polynomial of second order to evaluate the derivatives. The reference state of the system at which the derivatives were evaluated was chosen at $T = 800K$ and $M_{21} = 0.4 eV$ with stress free bulk grains. This value of the diffusion potential corresponds to $c_{Ag} = 0.036\%$ in the bulk. The selected state is shown in Fig. 9.15a. In each MC simulation, the system was first equilibrated during 5×10^4 MC steps. After the equilibration stage, the data was collected to compute relevant properties of the system.

9.4 Results

In this section we report calculated GB properties as functions of the intensive parameters. In each of the calculations performed the general expressions for GB free energy (9.3) and the adsorption equation (9.9) take particular forms. Below we report the results of the calculations and provide particular expressions for GB free energy and the adsorption equation in each case. The results obtained at 0 K are followed by data calculated at finite temperatures.

9.4.1 0K calculations

As we noted before, at 0 K there is no need to compute the excess GB entropy $[S]_N$. As a result, thermodynamic equations take simple form and all the excess properties including γ can be computed directly. This, in turn, allows to test the thermodynamic integration scheme by comparing values of γ calculated directly and obtained by integration of the adsorption equation.

Deformation parallel to the GB plane

GB free energy as a function of strain was computed for two uniaxial (independent variation of e_{11} and e_{22}) and biaxial deformations. At constant zero σ_{31} and σ_{33} stresses, Eq. (9.3) becomes

$$\gamma = [U]_N/A. \quad (9.25)$$

The integrated form of Eq. (9.9) for the three types of deformation is given by

$$\gamma A = \frac{\gamma_0 A_0}{A} + \frac{1}{A} \int \tau_{11} A' de_{11}, \quad (9.26)$$

$$\gamma A = \frac{\gamma_0 A_0}{A} + \frac{1}{A} \int \tau_{22} A' de_{22}, \quad (9.27)$$

$$\gamma A = \frac{\gamma_0 A_0}{A} + \frac{1}{A} \int (\tau_{11} + \tau_{22}) A' de. \quad (9.28)$$

γ_0 and A_0 are the GB free energy and area of the reference state. The reference state was chosen as the stress free state of the bulk with $\gamma_0 = 0.905 \text{ J/m}^2$. The components of the GB stress at this state are $\tau_{11} = 1.305 \text{ J/m}^2$ GB $\tau_{22} = 1.774 \text{ J/m}^2$. The components of GB stress are decreasing functions of corresponding components of strain, which means that GB region is softer than the bulk. The plots of individual components of the GB stress in

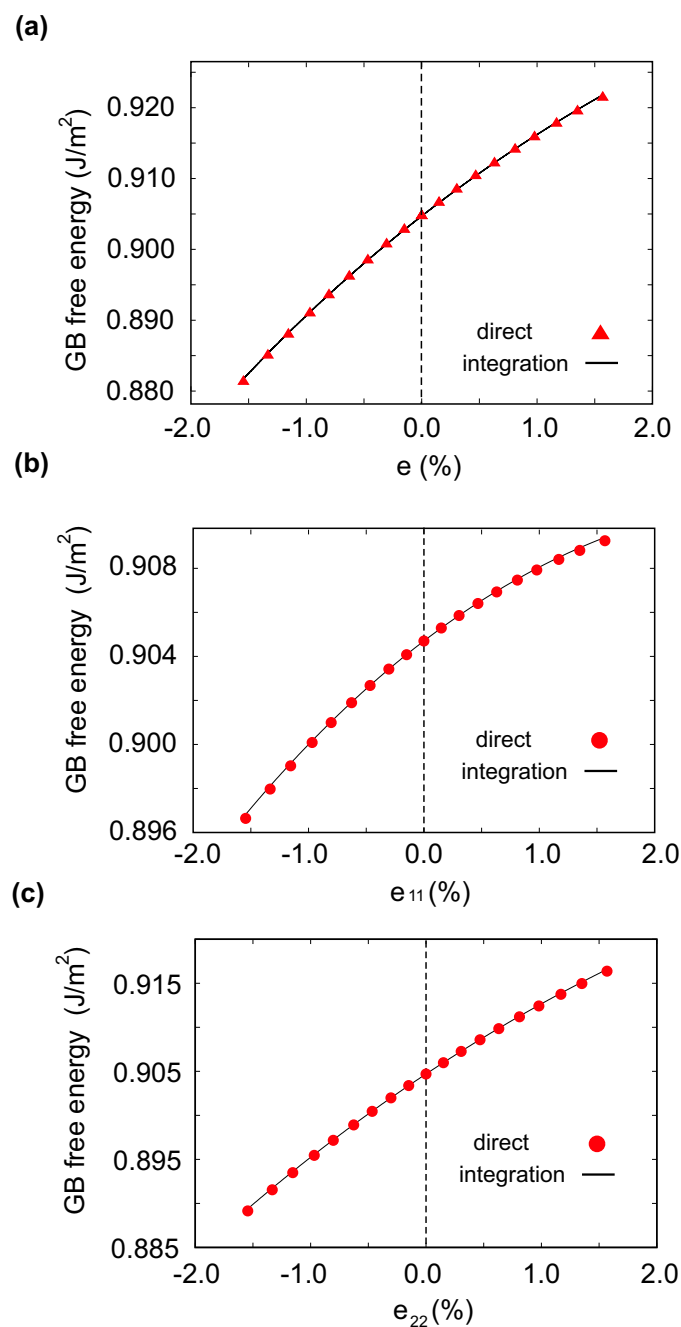


Figure 9.5: Single component Cu system, 0 K. γ as a function of lateral strain at constant zero σ_{31} and σ_{33} a) the simulation block was elastically deformed by the same amount along x and y directions (biaxially $e = e_{11} = e_{22}$) b) uniaxial strain e_{11} was applied along the x direction c) uniaxial strain e_{22} was applied along the y direction

the uniaxial and biaxial deformations can be found in supplemental material.

GB free energy was computed directly using Eq. (9.25) and by thermodynamic integration using Eqs. (9.26), (9.27) and (9.28). Figures. 9.5 (a), (b) and (c) show γ as a function of strain computed for these three cases. The discrete points on the plots correspond to the direct calculations, while the continuous line corresponds to values of γ computed by thermodynamic integration. Because the GB is under tension and both components of τ are large then γ , GB free energy increases with tension and decreases with compression. γ changes differently in the two uniaxial deformations due to anisotropy of τ . It is apparent from the plots that $\partial^2\gamma/\partial e^2$ is negative.

Deformation normal to the GB plane

When the component of stress σ_{33} is not zero, γ is not just excess of energy. In addition to $[U]_N$ there is a term that represents the mechanical work of the normal stress. Eqs. (9.3) and (9.9) in this case become

$$\gamma = [U]_N/A - \sigma_{33}[V]_N/A, \quad (9.29)$$

and

$$\gamma = \gamma_0 - \frac{1}{A} \int [V]_N d\sigma_{33}, \quad (9.30)$$

respectively. Excess GB volume per unit area as a function of σ_{33} is illustrated in Fig. 9.6. It increases with tension and decreases with compression. The dependence of $[V]_N/A$ on σ_{33} is not linear in the stress range studied here with significant difference between tension and compression. The stress free state value of $[V]_N/A$ was 0.316 . It increased by 3.5 % with maximum normal tension applied and decreased by 1% with maximum compression.

Fig. 9.7 shows GB free energy computed as a function of the normal component of stress σ_{33} computed directly from Eq. (9.29) (discrete points) and by thermodynamic integration (9.30) (solid line). γ nearly linearly decreases with tension and increases with compression.

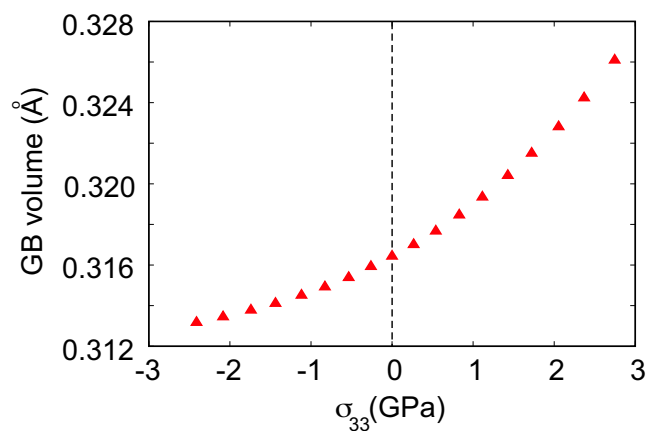


Figure 9.6: Single component Cu system, 0 K. Excess GB volume per unit area $[V]_N/A$ as a function of σ_{33} computed at fixed lateral dimensions.

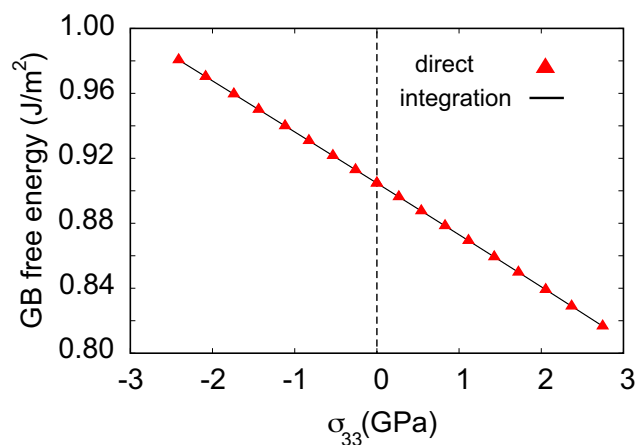


Figure 9.7: Single component Cu system, 0 K. γ as a function of normal stress σ_{33} at fixed lateral dimensions. The discrete points on the plot correspond to direct calculation of γ using Eq. (9.29), while the continuous line was obtained from thermodynamic integration using Eq. (9.30).

This behavior was expected, since the excess GB volume is positive and does not change significantly with σ_{33} .

Shear deformation parallel to the tilt axis

Under a finite shear stress σ_{31} atoms displace in the direction parallel to the tilt axis. Fig. 9.8a demonstrates the displacements of atoms relative to the stress free state in the x direction as a function of z coordinate, when the system is subject to shear stress $\sigma_{31} = 1.5$ GPa. The displacement vectors were computed for each atom and then averaged over the atoms in the same atomic plane parallel to the GB plane (the same coordinate z). The displacement of atoms in the direction x is proportional to the z coordinate. The slope of the displacement is the same inside bulk parts of grains 1 and 2. The figure demonstrates that there is an excess of shear (displacement) at the GB. This excess shear contributes to the total elastic deformation of the bicrystal [103]. If the atomic displacements are computed not relative to the stress free state, but relative to displacement of the bulk atoms, one recovers the deformation profile schematically shown in Fig. 9.2.

The expression for γ includes work of the shear stress and Eqs. (9.3) becomes

$$\gamma = [U]_N / A - \sigma_{31} b_1. \quad (9.31)$$

The integrated form of the adsorption equation (9.9) in this case is given by

$$\gamma = \gamma_0 - \int b_1 d\sigma_{31}. \quad (9.32)$$

Excess GB shear b_1 was computed by subtracting the total shear displacement in the x direction of the region with GB and the total displacement of the bulk region containing the same number of atoms N . b_1 is plotted in Fig. 9.8b as a function of shear stress σ_{31} . It linearly increases with the shear stress. Fig. 9.9 shows GB free energy γ computed directly using Eq. (9.31) (discrete points) and by thermodynamic integration (solid line) (9.32). γ decreases with increasing shear stress. The excess shear is zero in the stress free state of the bulk. As a result, the effect of σ_{31} on γ is higher than the first order. The maximum GB free energy decrease of 0.88% was achieved at $\sigma_{31} = 1.5$ GPa.

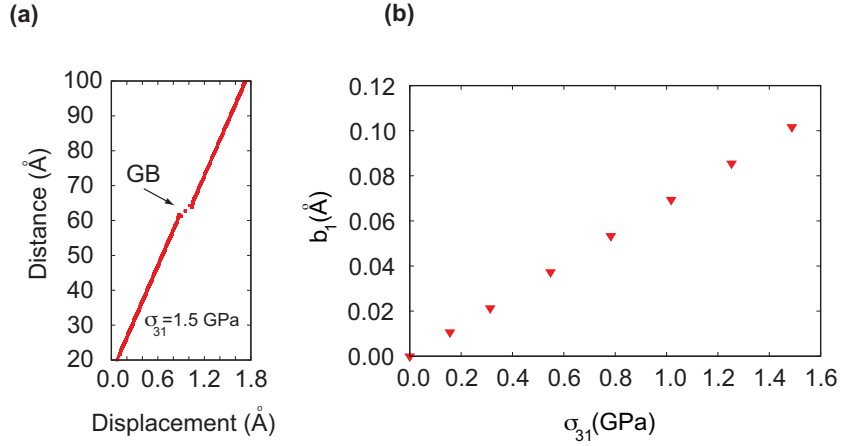


Figure 9.8: (a) Displacement of atoms in the direction of shear parallel to the GB plane with shear stress $\sigma_{31} = 1.5$ GPa computed relative to the stress free state. In the bulk grains the displacement is proportional to the z coordinate. There is an excess displacement in the GB region. (b) Excess GB shear as function of shear stress σ_{31} .

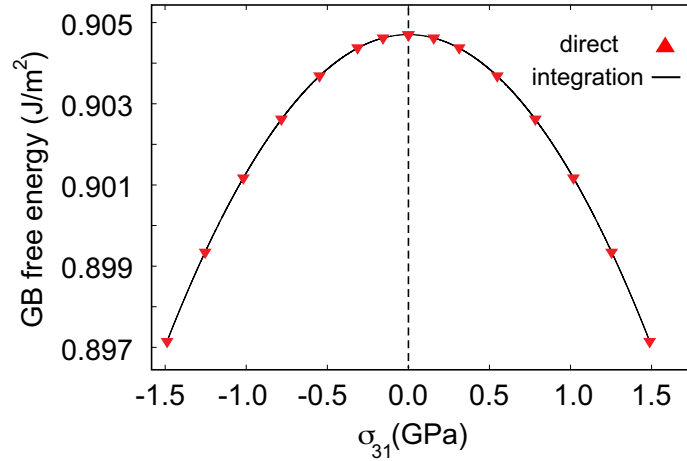


Figure 9.9: Single component Cu system, 0 K. γ shear as a function of shear stress σ_{31} parallel to the tilt axes. The discrete points on the plot correspond to direct calculations from Eq. (9.31), while the continuous line was obtained from thermodynamic integration using Eq. (9.32).

Maxwell relations at 0 K

We conclude the results of 0 K calculations reporting the values of the derivatives involved in Maxwell relations. The adsorption equation for this GB generates six Maxwell relations.

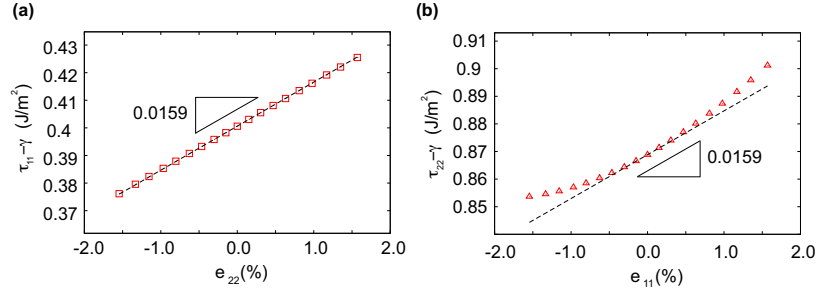


Figure 9.10: Single component Cu system at 0 K. Test of Maxwell relation (9.14) in the physical form.

The physical and Lagrangian formulations of the adsorption equation gives the total of twelve Maxwell relations. We demonstrate the tests of two relations in details, by looking at the dependence of excess properties on the relevant intensive variables.

First, we examine the relation given in Eq. (9.14) in the physical form. Each derivative corresponds to a separate uniaxial deformation described in Sec. 9.3.4. To evaluate the derivatives, we need to calculate both τ and γ as functions of e_{11} and e_{22} for these two separate uniaxial deformations. τ and γ were computed using Eqs. (9.8) and (9.25), respectively for each deformed state. The terms $\tau_{11} - \gamma$ and $\tau_{22} - \gamma$ are plotted as functions of strains e_{22} and e_{11} in Fig. 9.10a and b, respectively. The discrete points on the plot correspond to separate simulations with different strains. The continuous line shows the slope at zero stress in the bulk. The computed slopes were 0.0159 and 0.0159. The values are identical within the accuracy of our calculation as predicted by Eq. (9.14).

In the second example, we examine the relation in Eq. (9.15), this time in the Lagrangian form. To evaluate the first derivative, we computed τ_{11} as a function of σ_{33} for the elastic deformation described in Sec. 9.3.4. To evaluate the second derivative, excess GB volume was computed as a function of e_{11} (Sec. 9.3.4). The two excess quantities at different values of the relevant intensive parameters are shown in Fig. 9.11a and b. The plotted value of the excess GB volume was divided by the GB area of the unstrained state. The derivatives were evaluated at a state of zero stress in the bulk and were found to be -0.113×10^{-10}

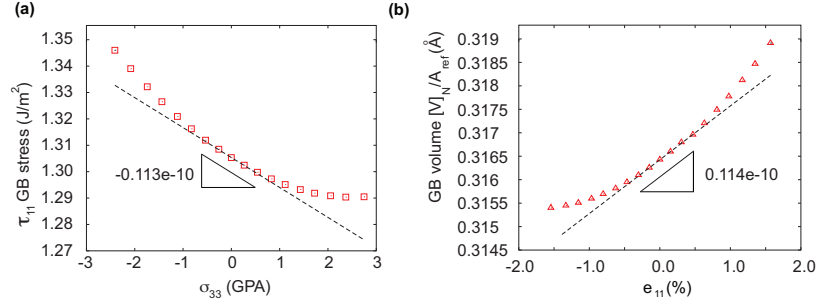


Figure 9.11: Single component Cu system at 0 K. Test of Maxwell relation (9.15) in the Lagrangian form.

Table 9.1: Derivatives involved in the Lagrangian form of Maxwell relations Eqs. (9.14) - (9.17) computed at 0 K. The expressions in the first row represent the denominator of the partial derivative, while the first column contains the numerators. The derivatives were evaluated at a stress free state of the bulk. The table is symmetrical (within accuracy of our calculations) in accord with predictions of the Maxwell relations.

	$\partial\tau_{11}^L$	$\partial\tau_{22}^L$	∂b_1	$\partial[V]_N$
∂e_{11}	-	0.0376	0.0	0.114e-10
∂e_{22}	0.0376	-	0.0	0.3749e-10
$\partial\sigma_{31}$	0.0	0.0	-	0.0
$\partial\sigma_{33}$	-0.113e-10	-0.3771e-10	0.0	-

and 0.114×10^{-10} . The computed values are in excellent agreement with Eq. (9.15).

The calculations of the partial derivatives in all other Maxwell relations are summarized in Table 9.1 (Lagrangian) and Table 9.2 (physical). Notice, that it was possible to compute the derivatives in physical form which involve GB area change, only because γ as function of e_{11} , e_{22} , σ_{31} and σ_{33} was known. Plots illustrating the dependence of the GB properties on the intensive variables are included as supplemental material.

9.4.2 Single component Cu system at finite temperature

In a single component system at finite temperature the expression for GB free energy (2.47) contains the entropy contribution and is given by

Table 9.2: Derivatives involved in the physical form of Maxwell relations Eqs. (9.14) - (9.17) computed at 0 K. The expressions in the first row represent the denominator of the partial derivative, while the first column contains the numerators. The derivatives were evaluated at a stress free state of the bulk. The table is symmetrical (within accuracy of our calculations) in accord with predictions of the Maxwell relations.

	$\partial(\tau_{11} - \gamma)$	$\partial(\tau_{22} - \gamma)$	$\partial(b_1)$	$\partial([V]_N/A)$
∂e_{11}	-	0.0159	0.0	0.203e-10
∂e_{22}	0.0159	-	0.0	-0.06086e-10
$\partial \sigma_{31}$	0.0	0.0	-	0.0
$\partial \sigma_{33}$	0.203e-10	-0.06086e-10	0.0	-

$$\gamma A = [U]_N - T[S]_N, \quad (9.33)$$

where the stresses σ_{31} and σ_{33} were assumed to be zero. The excess entropy $[S]_N$ in Eq. (9.33) cannot be computed directly in MD simulations. As a result, γ as a function of temperature was computed by thermodynamic integration using the interface version of the Gibbs-Helmholtz equation. Along the integration path the stresses σ_{31} and σ_{33} were zero and constant, while the lateral strain varied biaxially due to the thermal expansion. In this case Eq. (9.12) in the integrated form becomes

$$\gamma A = \frac{(\gamma_0 A_0) T}{T_0} - T \int_{T_0}^T \left(\frac{[U]_N}{T'^2} - \frac{(\tau_{11}^N + \tau_{22}^N) A'}{T'} \left(\frac{de}{dT'} \right)_{coex} \right) dT'. \quad (9.34)$$

Here $e = e_{11} = e_{22}$ is the biaxial strain and the derivative de/dT represents the thermal expansion. Quantities γ_0 , A_0 and T_0 are the GB free energy, area and temperature of a reference state. Excess quantities involved in Eq. (9.34) were computed at each simulated temperature. The excess energy $[U]_N/A$ and the two components τ_{11} and τ_{22} of the excess GB stress are shown in Figs. 9.12 and 9.13 respectively. The discrete points on the plots were computed in isothermal MD simulations. The points are connected by a solid line to guide an eye. $[U]_N/A$ increases with temperature. Excess GB stress τ is anisotropic with

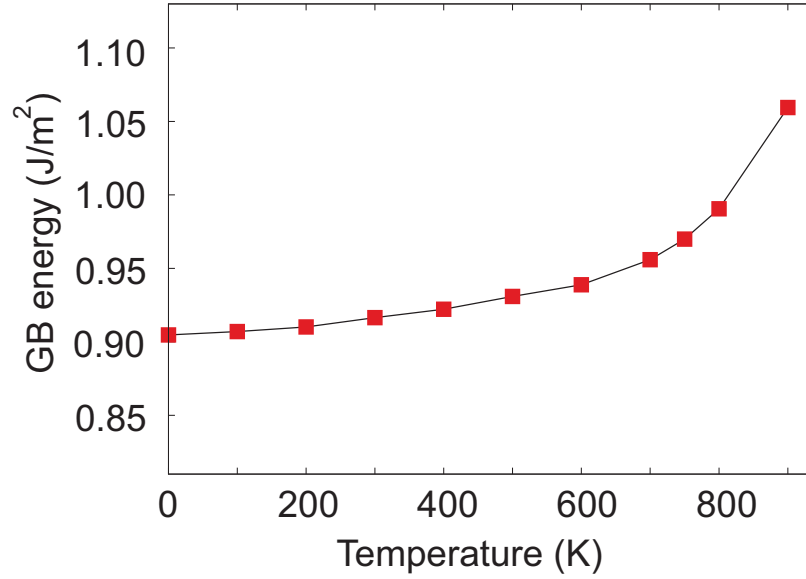


Figure 9.12: Single component Cu system. Excess GB energy per unit area $[U]_N/A$ as a function of temperature. The discrete points were obtained from MD simulations. The continuous line was plotted to guide an eye.

both components decreasing with temperature.

The solid line in Fig. 9.14 shows GB free energy γ computed using Eq. (9.34) as a function of temperature. From the reference temperature $T_0 = 300$ K, γ was calculated by thermodynamic integration in the ranges of increasing and decreasing temperatures. Two solid circles on the plot indicate values of γ computed at 0 K and at 300 K. The reference value γ_0 was computed from harmonic calculations [48], while the 0 K value was computed directly using Eq. (9.25). In the decreasing temperature range the value calculated by integration approaches the 0 K value of γ . In the temperature range studied, γ decreases from $0.905 J/m^2$ at 0 K to $0.66 J/m^2$ at 900 K. This trend is consistent with previous studies [29, 94].

9.4.3 Binary CuAg system at finite temperature

Fig. 9.15a, b and c shows snapshots of the simulation block with 0.036%, 0.24% and 0.58% of Ag in the bulk at 800 K. Cu atoms are shown in yellow and silver atoms are shown in

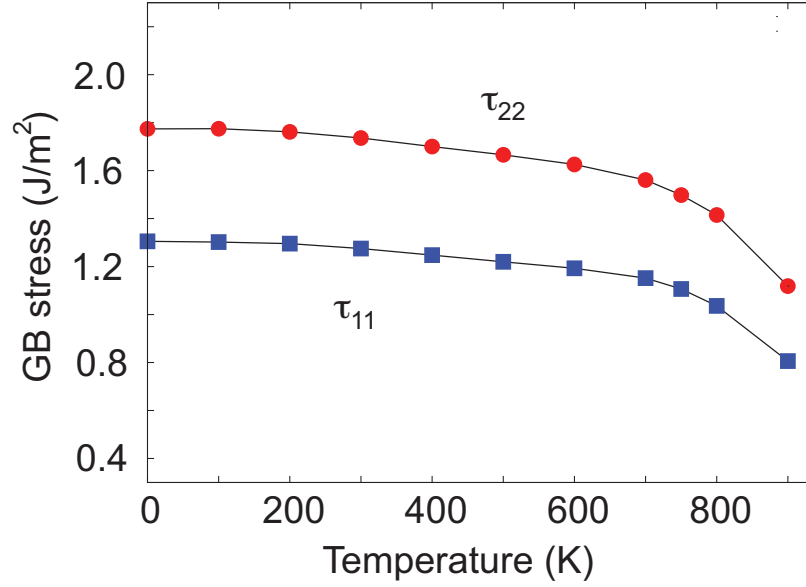


Figure 9.13: Single component Cu system. Components τ_{11} and τ_{22} of excess GB stress as functions of temperature. The discrete points were obtained from MD simulations. The continuous line was plotted to guide an eye.

dark blue. As it is apparent from the pictures, silver atoms strongly segregate to the GB. At highest Ag concentrations studied in this work the boundary becomes visibly disordered. To quantify the effect of chemical composition on the GB thickness, we computed excess GB volume per unit area (thickness). Fig. 9.16 demonstrates $[V]_N/A$ as a function of bulk composition. The discrete points on the plot correspond to individual MC simulations at a given value of the diffusion potential M_{21} . The excess GB volume increases with c_{Ag} in the entire range of sampled compositions, the slope becomes increasingly large when the boundary begins to disorder. At highest silver concentration the GB thickness becomes almost four times greater than that of pure Cu.

The expression for GB free energy (9.3) for this isotherm is given by

$$\gamma A = [U]_N - T[S]_N - [N_2]_N M_{21}. \quad (9.35)$$

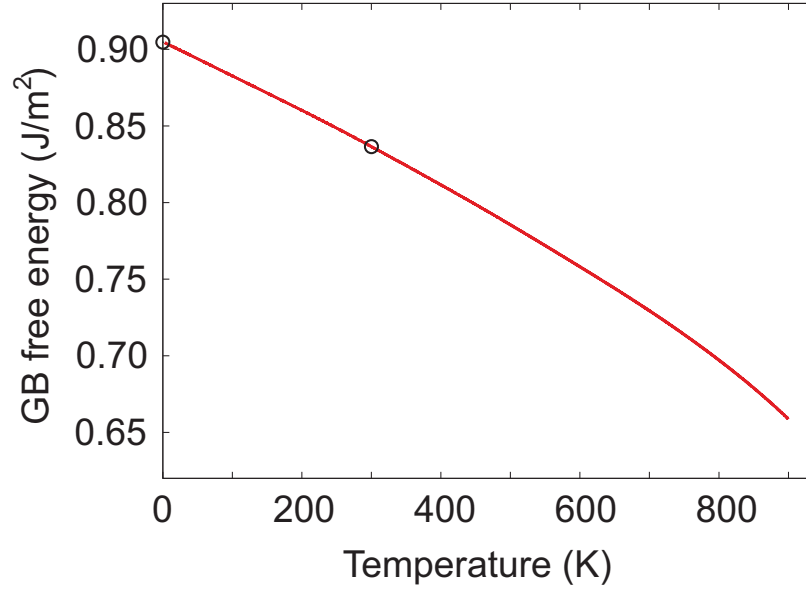


Figure 9.14: Single component Cu system. GB free energy γ as a function of temperature computed by thermodynamic integration (9.34). The reference value of γ at $T = 300$ K indicated by a solid circle was computed from harmonic approximation. The value of γ at $T = 0$ K is indicated by a solid circle.

It again requires knowledge of $[S]_N$ which cannot be computed directly in the MC simulations, and contains the segregation term. Isotherm of γ as a function of c_{Ag} was computed by integration of the adsorption equation from the state with $c_{Ag} = 0$ (pure copper). The reference value of GB free energy was taken from the previous MD calculations. On the integration path the components of stress σ_{31} and σ_{33} were zero and constant, while the value of the diffusion potential M_{21} varied with composition. The lateral dimensions of the system also varied with M_{21} due to the compositional change. For this isotherm, Eq. (9.9) in the integrated form becomes

$$\gamma A = \gamma_0 A_0 - \int_0^{c_{Ag}} \left\{ [N_2]_N \left(\frac{dM_{21}}{dc'_{Ag}} \right) + (\tau_{11} + \tau_{22}) A' \left(\frac{de}{dc'_{Ag}} \right) \right\} dc'_{Ag}. \quad (9.36)$$

The derivative de/dc' reflects the change of the stress free lattice constant with composition.

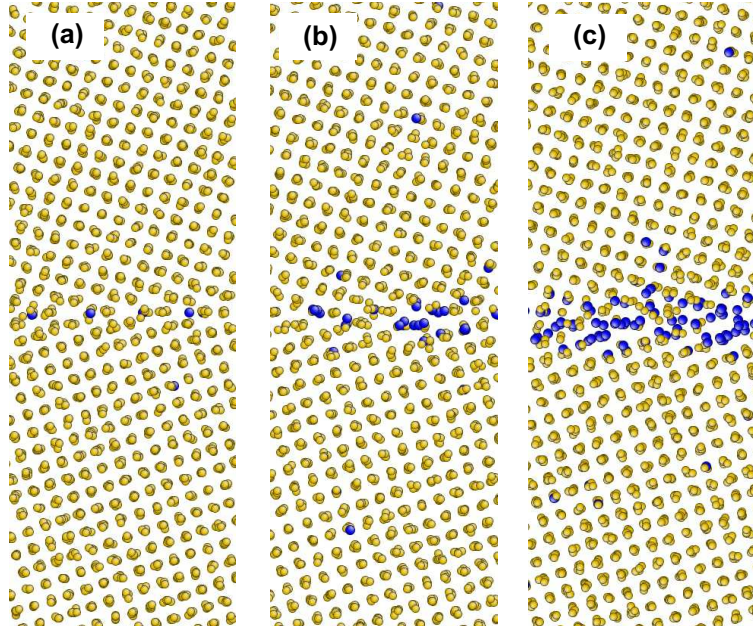


Figure 9.15: Binary CuAg system. Snapshots of the simulation block with the bulk concentration of silver c_{Ag} (a) 0.036%, (b) 0.24%, and (c) 0.58% at $T = 800$ K.

Excess GB properties involved in Eq. (9.36) were computed as functions of composition. GB segregation is demonstrated in Fig. 9.18, it increases with c_{Ag} . In the composition range when boundary preserves its ordered structure the shape of the segregation curve is consistent with Langmuir–McLean model. At high Ag concentration the slope of segregation increases. Fig. 9.17 shows components of $\boldsymbol{\tau}$ as functions of c_{Ag} . Both τ_{11} and τ_{22} decrease with concentration and $\boldsymbol{\tau}$ becomes almost isotropic at higher concentrations of silver.

Finally, Fig. 9.19 shows GB free energy γ computed by thermodynamic integration (9.36) as a function of bulk composition. γ decreases with alloying. All the mentioned GB properties are affected by increasing GB disorder at high c_{Ag} . As more segregation sites appear in the GB region, segregation of Ag becomes higher, leading, in turn, to a large

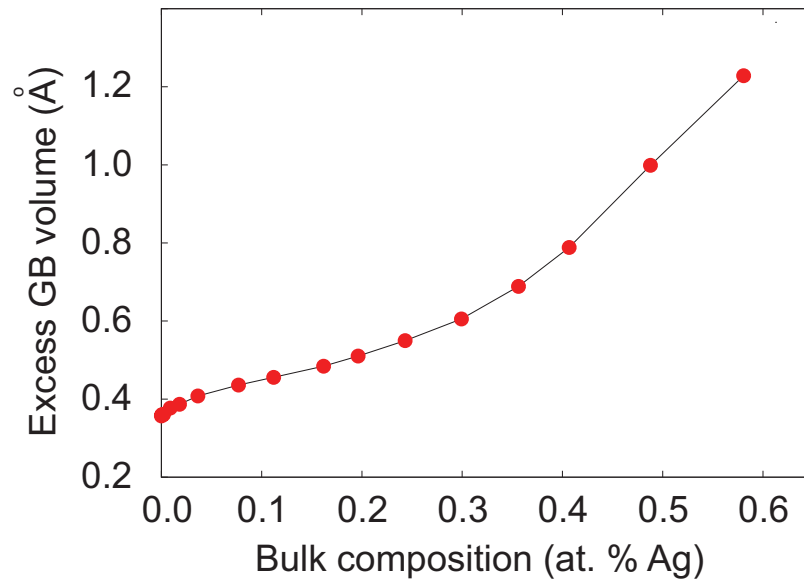


Figure 9.16: Binary CuAg system. Excess GB volume per area $[V]_N/A$ as a function of silver concentration c_{Ag} in the bulk at $T = 800\text{ K}$.

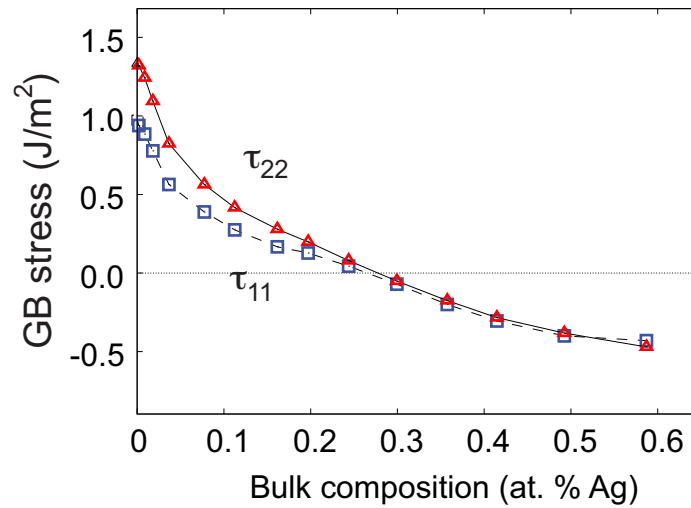


Figure 9.17: Binary CuAg system. Components τ_{11} and τ_{22} of GB stress as a function of silver concentration c_{Ag} in the bulk at $T = 800\text{ K}$.

decrease in γ . GB free energy decreases from $\gamma = 0.7\text{ J/m}^2$ of pure Cu, to $\gamma = 0.54\text{ J/m}^2$ at $c_{Ag} = 0.58\%$.

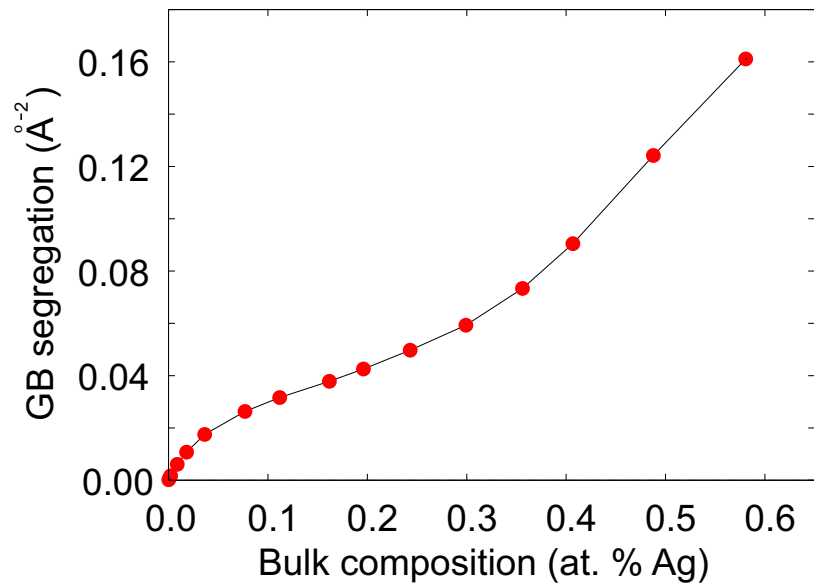


Figure 9.18: Binary CuAg system. GB segregation $[N_2]_N/A$ as a function of silver concentration c_{Ag} in the bulk at $T = 800$ K.

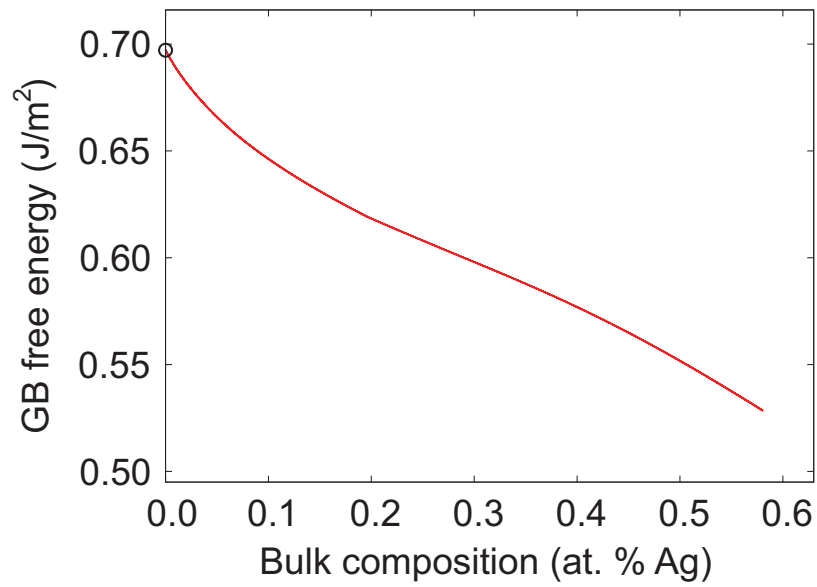


Figure 9.19: Binary CuAg system. GB free energy γ as a function of silver concentration c_{Ag} in the bulk at $T = 800$ K.

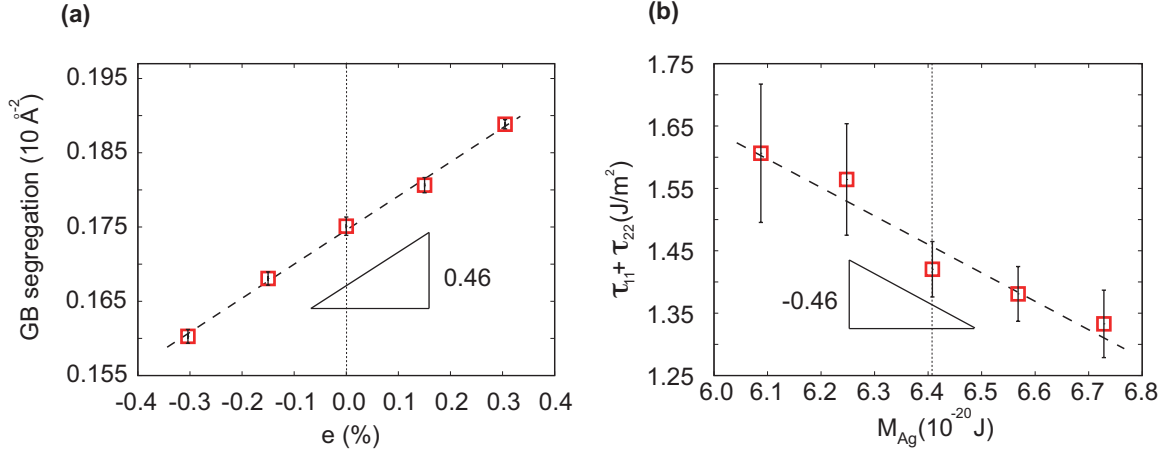


Figure 9.20: Test of the Lagrangian form of Maxwell relation in Eq. (9.18) in binary CuAg system. The discrete points on the figures correspond to MC simulations data, while the dashed lines are linear fits. (a) GB segregation $[N_2]_N$ as a function of biaxial strain parallel to the boundary. (b) Sum of the principal components τ_{11} and τ_{22} of the GB stress as a function of the diffusion potential $M_{21} \equiv M_{Ag}$. The derivative was evaluated for a stress free state in the bulk at $T = 800 \text{ K}$ and $c_{Ag} = 0.036\%$. On the plots this state is indicated by vertical dashed lines. The computed derivatives $\frac{\partial [N_2]_N / A_{ref}}{\partial e} = 0.46 \pm 0.01$ and $\frac{\partial (\tau_{11} + \tau_{22}) / A_{ref}}{\partial M_{Ag}} = -0.46 \pm 0.08$ confirms the correctness of the relation within accuracy of our calculations.

9.4.4 Effects of mechanical deformation and temperature on segregation

Using MC simulations we examined how elastic deformation (parallel and normal to the GB plane) and temperature affect GB segregation. To test the theory we used only the Lagrangian form of Maxwell relations, so the calculation of γ as a function of the intensive variables was unnecessary.

First, we examine the effect of the elastic deformation parallel to the GB plane on GB segregation. In the MC simulations the boundary was deformed biaxially, which means that the strains e_{11} and e_{22} were not varied independently. In this case Eq. (9.18) becomes

$$\frac{\partial ((\tau_{11} + \tau_{22}) A)}{\partial M_{21}} = -\frac{\partial [N_2]_N}{\partial e}. \quad (9.37)$$

Fig. 9.20a illustrates the total GB segregation per unit area of the unstrained state as a function of strain computed at constant M_{21} and constant zero σ_{31} and σ_{33} . The total amount of segregation increases linearly within this range of strain. Fig. 9.20,b illustrates $\tau_{11} + \tau_{22}$ as a function of the diffusion potential. The sum of the components of GB stress decreases with M_{21} (with increasing c_{Ag}). The slopes of the functions at the reference state with area A_{ref} are indicated by the triangles. The computed slopes of the segregation and stress curves were $\frac{\partial [N_2]_N / A_{ref}}{\partial e} = 0.46 \pm 0.01$ $^{-2}$ and $\frac{\partial (\tau_{11} + \tau_{22}) / A_{ref}}{\partial M_{Ag}} = -0.46 \pm 0.08$ $^{-2}$, which agrees with the prediction in Eq. (9.37).

Secondly, we examine the effect of σ_{33} stress on segregation and test the relevant Maxwell relation (9.20). According to Eq. (9.37) the change in segregation is related to change in $[V]_N$ with M_{21} . Fig. 9.21a shows the segregation $[N_2]_N/A$ as a function of normal component of stress σ_{33} at fixed lateral dimensions, constant value of M_{21} and constant zero σ_{31} . Segregation increases with increasing σ_{33} (tension).

Excess GB volume $[V]_N/A$ linearly increases with M_{21} (c_{Ag})(Fig. 9.21a). The slopes of the segregation and the excess volume were $\frac{\partial [N_2]_N / A_{ref}}{\partial \sigma_{33}} = 0.030 \pm 0.0006$ $^{-2}\text{GPa}^{-1}$ and $\frac{\partial [V]_N / A_{ref}}{\partial M_{Ag}} = 0.027 \pm 0.004$ $^{-2}\text{GPa}^{-1}$, and are indicated on the plots by triangles. Within the error of our calculation, these slopes agree with the prediction in Eq. (9.20).

Finally, we tested Eq. (9.24) which involves segregation change with temperature. Fig. 9.22a and b shows $([N_2]_N/T)$ and $([\Psi]_N/T^2)$ as a functions of T and M_{21} respectively. The later variation happens at constant zero σ_{31} and σ_{33} , temperature and fixed area. According to Eq. (9.13), the potential Ψ becomes $[U]_N - [N_2]_N M_{21}$. Within the accuracy of our calculation the values of slopes $\frac{\partial ([N_2]_N / T) / A_{ref}}{\partial T} = -(2.7 \pm 0.1) \times 10^{-8}$ $^{-2}\text{K}^{-2}$ and $\frac{\partial ([\Psi]_N / T^2) / A_{ref}}{\partial M_{Ag}} = -(3.0 \pm 0.9) \times 10^{-8}$ $^{-2}\text{K}^{-2}$ agree with Eq. (9.24).

Effect of shear stress σ_{31} on segregation is expected to have second or higher order effect

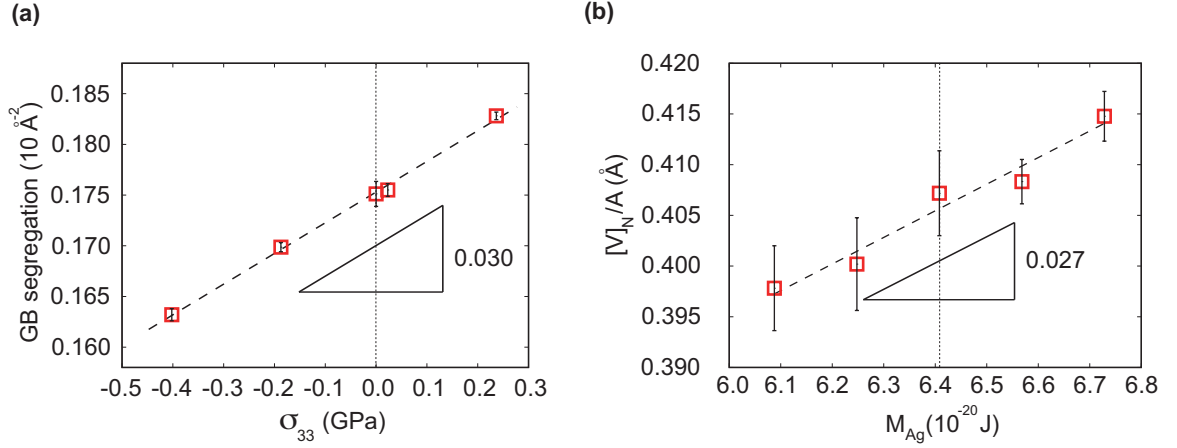


Figure 9.21: Test of the Maxwell relation in Eq. (9.20) in binary CuAg system. The discrete points on the figures correspond to MC simulations data, while the dashed lines are linear fits. (a) GB segregation $[N_2]_N$ as a function of stress σ_{33} normal to the plane of the GB. (b) Excess GB volume per area (GB thickness) as a function of the diffusion potential $M_{21} \equiv M_{Ag}$. The derivative was evaluated for a stress free state in the bulk at $T = 800K$ and $c_{Ag} = 0.036\%$. On the plots this state is indicated by vertical dashed lines. The computed derivatives $\frac{\partial [N_2]_N / A_{ref}}{\partial \sigma_{33}} = 0.030 \pm 0.0006 \text{ }^{-2}\text{GPa}^{-1}$ and $\frac{\partial [V]_N / A_{ref}}{\partial M_{Ag}} = 0.027 \pm 0.004 \text{ }^{-2}\text{GPa}^{-1}$ confirms the correctness of the relation within accuracy of our calculations.

for this GB and was not studied here.

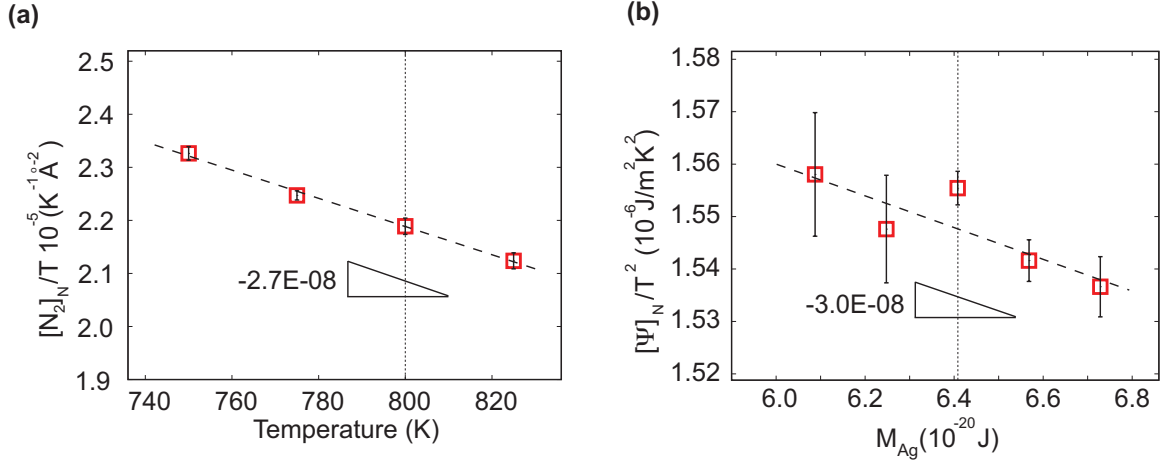


Figure 9.22: Test of the Lagrangian form of Maxwell relation in Eq. (9.24) in binary CuAg system. The discrete points on the figures correspond to MC simulations data, while the dashed lines are linear fits. (a) GB segregation $[N_2]_N$ divided by temperature as a function of temperature. (b) Potential $[\Psi]_N / T^2 = [U - N_2 M_{21}]_N / T^2$ as a function of the diffusion potential $M_{21} \equiv M_{Ag}$. The derivative was evaluated for a stress free state in the bulk at $T = 800 \text{ K}$ and $c_{Ag} = 0.036\%$. On the plots this state is indicated by vertical dashed lines. The computed derivatives $\frac{\partial ([N_2]_N / T) / A_{ref}}{\partial T} = -(2.7 \pm 0.1) \times 10^{-8} \text{ }^{-2}\text{K}^{-2}$ and $\frac{\partial ([\Psi]_N / T^2) / A_{ref}}{\partial M_{Ag}} = -(3.0 \pm 0.9) \times 10^{-8} \text{ }^{-2}\text{K}^{-2}$ confirms the correctness of the relation within accuracy of our calculations.

9.5 Discussion and conclusions

In this work we presented a thermodynamic treatment of GBs in a binary system under stress. The stresses include shear stress parallel to the plain of the boundary. The distinction was made between GBs and phase boundaries. GB in this work was defined as an interface in a single phase system. We discussed the cases when such a description is appropriate and focused on the case of the symmetrical tilt boundaries. These boundaries and twist boundaries with shear stresses applied in certain directions form a special class of systems that can be treated as a single phase system. Other boundaries under non-hydrostatic conditions should be treated as heterophase interfaces.

The developed thermodynamic treatment was applied to atomistic simulation of symmetrical tilt $\Sigma 5(310)$ GB. We first tested the theory at 0 K calculations for the GB in

a single component copper system. We systematically computed excess GB properties as functions of strains and stresses. γ was computed directly and by thermodynamic integration of the adsorption equation for all possible independent mechanical deformations. The values obtained directly and by integration are in excellent agreement, which confirms correctness of our equations. We tested Maxwell relations in both Lagrangian and physical forms.

Elastic deformation of up to 1.7% was applied to the solid with GB normal and parallel to the plane of the boundary. The strains of this magnitude generate stresses on the order of GPa. Effects of stresses normal and parallel to the GB plane on γ have the same order of magnitude. Normal stress σ_{33} had largest effect on value of γ . The effect of shear stress σ_{31} is quadratic, however at large stresses it affects γ as much as interface stress τ or σ_{33} . It is also interesting to notice how differently excess volume and excess shear are affected by stresses. For the boundary studied in this work, excess shear linearly increased with σ_{31} , from zero to $b_1 = 0.11$ at $\sigma_{31} = 1.5$ GPa. Excess volume is less sensitive to σ_{33} and remains about 0.3 at stresses as high as 3 GPa. $[V]_N$ dependence on σ_{33} is also not linear. Extending linear trend of excess shear, we estimate it to be 0.2 at 3 GPa, which approaches the value of the excess volume. Thus, in this work we showed that the effect of shear stress on γ is significant and cannot be neglected. We finally notice that there are GB that have non-zero excess shear even at the stress free state. An example of such boundary is the symmetrical tilt $\Sigma 13(3\bar{4}1)[111]$ in Al which was studied in atomistic simulations [104]. The (111) planes of this bicrystal are discontinuous across the GB region due to the relative displacement of 0.2 parallel to the tilt axis. This displacement represents the excess shear at zero stress σ_{31} . In this case we expect shear stresses to produce linear effect on GB free energy.

At finite temperatures in a single component Cu system γ was computed by thermodynamic integration of the interface version of the Gibbs-Helmholtz equation. γ showed a significant reduction with temperature. We then continued thermodynamic integration along an isothermal path at 800 K adding Ag to the system. γ reduces further with c_{Ag} .

The total decrease in free energy compare to the 0 K value was 40 %. Considering heterogeneous nucleation classical nucleation theory usually assumes that γ is constant. Strong dependence of γ on temperature and composition may have an important effect on the barrier of heterogeneous nucleation [105] and contact angle. We also notice, that other GB properties were affected by temperature and composition even stronger than γ . Excess volume $[V]_N$ increased 4 times and interface stress changed sign with c_{Ag} .

We also checked Maxwell relations for the binary system at finite temperature and examined mechanical and thermal effects on the GB segregation. These derivatives (Lagrangian form) computed in simulations are in agreement with predictions of Maxwell relations within accuracy of our calculations. Both lateral and normal deformations at constant M_{21} produce change in the bulk composition and GB segregation. While, the effects of these to elastic deformations have different effect on GB segregation, they cannot be compared in a rigorous manner, because the state of stress of the bicrystal is different. We could compare GB segregation of the two GBs under different state of stress which have the same bulk concentration c_{Ag} . In this case the slope of segregation versus composition would be large for deformation normal to the GB plane.

9.6 Work of lateral deformation

The elastic work can be evaluated as traction vector times displacement integrated over the surface of the selected region. We focus on the contribution to lateral work from the GB region. The region is schematically illustrated in Fig. 9.23. The normal illustrated in the figure can be computed from the components of the vector \mathbf{b} and dimensions L_3 of the reference bulk system as

$$\mathbf{n} = \left(\frac{L_3 + b_3}{\sqrt{b_1^2 + (L_3 + b_3)^2}}, -\frac{b_1}{\sqrt{b_1^2 + (L_3 + b_3)^2}} \right). \quad (9.38)$$

Now we compute the traction vector \mathbf{t} on this face

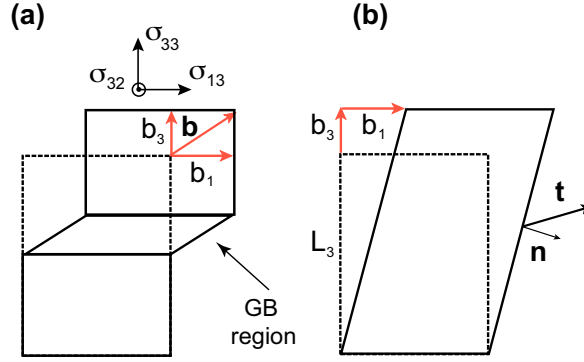


Figure 9.23: Excess shear and excess volume of GB. (a) The dashed line indicates initial homogeneous bulk region. As the GB enters this region at constant σ_{31} and σ_{33} excess shear and excess volume are produced. These excesses are indicated by red arrows. (b) \mathbf{n} is the normal vector direction of which depends on vector \mathbf{b} . \mathbf{t} is the traction vector.

$$\begin{aligned}
 \mathbf{t} &= \boldsymbol{\sigma} \cdot \mathbf{n} = \\
 &= \left(\begin{aligned} &\frac{L_3 + b_3}{\sqrt{b_1^2 + (L_3 + b_3)^2}} \sigma_{11} - \frac{b_1}{\sqrt{b_1^2 + (L_3 + b_3)^2}} \sigma_{31}, \\ &\frac{L_3 + b_3}{\sqrt{b_1^2 + (L_3 + b_3)^2}} \sigma_{31} - \frac{b_1}{\sqrt{b_1^2 + (L_3 + b_3)^2}} \sigma_{33} \end{aligned} \right), \quad (9.39)
 \end{aligned}$$

where the dot denotes the tensor product. Therefore, the work δW of the lateral displacement $(\delta x_1, 0)$ of the face with area $L_2 \sqrt{b_1^2 + (L_3 + b_3)^2}$ becomes

$$\delta W = \int \mathbf{t} \cdot \delta \mathbf{x} = (\bar{\sigma}_{11} V - A b_1 \sigma_{31}) de_{11} \quad (9.40)$$

A is a GB area, L_2 is the dimension of the system in the x_2 direction, and $A b_3$ represents the excess volume of the GB, $\bar{\sigma}_{11}$ should be understood as the average over the volume (σ_{11} depends on z).

Chapter 10: Liquid nucleation at superheated grain boundaries

10.1 Introduction

Solids are difficult to superheat above the melting point T_m due to the relative easiness of heterogeneous nucleation of the liquid phase on the surface, at grain boundaries (GBs) and at other defects. Diffuse-interface modeling [106–109] and molecular dynamics (MD) simulations [100] reveal two different modes of GB melting, depending on the relation between the GB free energy γ_{GB} and the solid-liquid interface free energy γ_{SL} at T_m . If $\gamma_{GB} > 2\gamma_{SL}$, the GB cannot be superheated and its thickness diverges when temperature T approaches T_m . If $\gamma_{GB} < 2\gamma_{SL}$, the GB thickness remains finite at T_m and the boundary can be superheated. Both modes of GB melting can be reproduced within a sharp interface model representing the premelted GB by a thin liquid layer with interactions between the two solid-liquid interfaces described by a disjoining potential (DP). A repulsive DP leads to continuous GB melting while a DP with a minimum reproduces the superheating. Both types of DPs were found in MD simulations of different GBs [100].

The previous DP-based models assumed uniform thickness of the stable or metastable GB, precluding direct comparison with the classical nucleation theory (CNT) [110]. Here we propose a more general model enabling calculations of the size and shape of the critical nucleus, as well as the nucleation barrier, as functions of the superheating $T - T_m$. The same quantities are computed in the heterogeneous CNT using a purely geometric treatment of the interfaces. The proposed model adopts the sharp-interface approach with a DP but makes the critical step of performing a variational calculation of the nucleus shape and size. This step was inspired by Cahn's 1957 paper on nucleation on dislocations [111]. Furthermore, a known limitation of CNT is that it predicts a finite nucleation barrier at

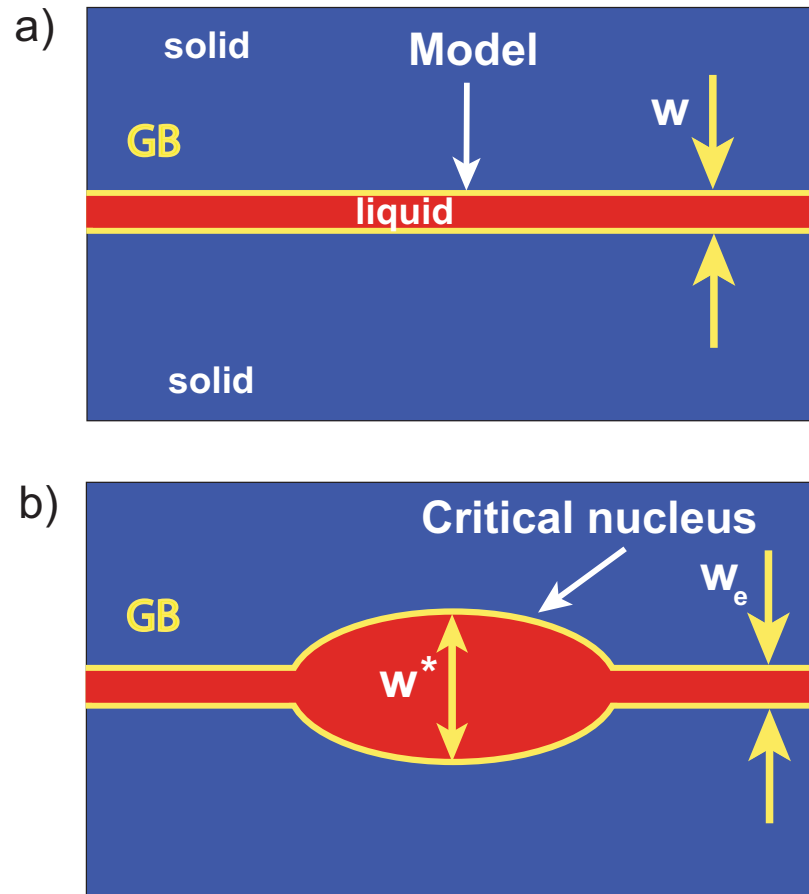


Figure 10.1: Schematics presentation of the GB model with a disjoining potential. (a) Equilibrium GB; (b) Liquid nucleation on the boundary.

arbitrarily high temperatures [110, 112]. The proposed model removes this limitation by incorporating a DP which accounts for the atomistic nature of the GB in a rather general way. This leads to prediction of a critical point of superheating at which the nucleation barrier vanishes.

10.2 GB premelting

The GB is modeled by a liquid layer of a width W separated from the grains by two solid-liquid interfaces (Fig. 10.1a)). The interfaces interact by a DP $\Psi(W)$ with a minimum at

a thickness W_0 . For definitiveness, we will adopt the Morse potential

$$\Psi(W) = (2\gamma_{SL} - \gamma_{GB}) \left[e^{-2a(W-W_0)} - 2e^{-a(W-W_0)} \right], \quad (10.1)$$

which has a minimum of depth $\Psi(W_0) = (\gamma_{GB} - 2\gamma_{SL}) < 0$. Here γ_{GB} and γ_{SL} refer to T_m and are assumed to be constant; a^{-1} defines the range of the potential. The free energy per unit area of a uniform GB is

$$\gamma(W) = \Delta G_V W + 2\gamma_{SL} + \Psi(W), \quad (10.2)$$

where ΔG_V is the difference between Gibbs free energies per unit volume of the solid and liquid phases. In this model we neglect the volume effect of melting, so that ΔG_V is proportional to the chemical potential difference between the phases. At temperatures close to T_m , $\Delta G_V \approx H_m(T_m - T)/T_m$, where H_m is the latent heat of melting per unit volume. At T_m , $\Delta G_V = 0$ and $\gamma(W)$ reaches the minimum value γ_{GB} at $W = W_0$.

Introducing the dimensionless variables $w = W/W_0$, $\Gamma = \gamma/\gamma_{GB}$, $g = -\Delta G_V W_0/\gamma_{GB}$, $\beta = (2\gamma_{SL} - \gamma_{GB})/\gamma_{GB}$, $\alpha = aW_0$ and $\varphi = \Psi/\gamma_{GB}$, Eq. (10.2) becomes

$$\Gamma(w) = -gw + (1 + \beta) + \varphi(w). \quad (10.3)$$

In these variables, length is measured in units of W_0 and free energy per unit area in units of γ_{GB} . The equilibrium GB thickness w_e is found by minimizing $\Gamma(w)$ at a fixed temperature. The condition $\Gamma'(w_e) = 0$ gives the equation

$$-g + \varphi'(w_e) = 0. \quad (10.4)$$

Several general statements can be made about solutions of Eq. (10.4) without specifying the exact analytical form of $\varphi(w)$. For example, suppose $\varphi(w)$ is a continuous function together with its first and second derivatives that has a single minimum and a single inflection

point (zero of $\varphi''(w)$) and approaches zero at $w \rightarrow \infty$. Under these conditions, the plot of $\varphi'(w)$ must have the shape shown schematically in Fig. 10.2a. Solutions of Eq. (10.3) correspond to intersections of this plot with the horizontal line $g = \text{const}$. When the GB is not superheated ($g \leq 0$), there is only one intersection and thus a single solution. This solution gives the equilibrium width w_e of a stable GB and corresponds to the minimum of $\Gamma(w)$ shown in Fig. 10.2b. When $g = 0$ (bulk melting point), $\Gamma(w)$ coincides with the DP (up to a shift by the constant $1 + \beta$) and the minimum occurs at $w_e = 1$. In the superheating region ($g > 0$), Eq. (10.4) has either two solutions or none (Fig. 10.2a). If the superheating is relatively small, there are two solutions: one for the minimum of $\Gamma(w)$ and the other for the maximum which appears at large w . The maximum represents an unstable state of the GB. As superheating increases, the GB widths corresponding to the minimum and maximum shift towards each other until they merge at a critical value $g = g_c$. At $g > g_c$, Eq. (10.4) has no solutions and Γ is a monotonically decreasing function of w . Thus, the boundary is absolutely unstable and the entire system transforms to liquid. This analysis shows that, for *any* DP satisfying the shape conditions formulated above, the model predicts a single critical point. The superheated GB exhibits two branches of $w_e(g)$, stable and unstable, which merge at the critical point. The Morse potential employed in this study satisfies the above conditions, as does for example the Lennard-Jones potential and many other commonly used potential forms.

For the particular case of a DP given by the Morse function, Eq. (10.4) can be solved analytically. Denoting $\chi = e^{-\alpha(w-1)}$, $\Gamma(w)$ is written as

$$\Gamma(w) = -gw + 1 + \beta + \beta(\chi^2 - 2\chi) \quad (10.5)$$

and Eq. (10.4) becomes

$$-g - 2\alpha\beta(\chi_e^2 - \chi_e) = 0 \quad (10.6)$$

where $\chi_e = e^{-\alpha(w_e-1)}$. Solving this quadratic equation we obtain

$$\chi_e = \frac{1}{2} \left(1 \pm \sqrt{1 - \frac{2g}{\alpha\beta}} \right), \quad (10.7)$$

and thus the equilibrium GB width

$$w_e = 1 - \frac{\beta}{2g_c} \ln \frac{1}{2} \left(1 \pm \sqrt{1 - \frac{g}{g^c}} \right), \quad (10.8)$$

where g^c is the critical superheating parameter given by

$$g_c = \frac{\alpha\beta}{2}. \quad (10.9)$$

The positive sign gives the stable or metastable GB thickness (minimum of Γ), whereas the negative sign corresponds to unstable equilibrium (maximum of Γ) existing only at $g > 0$ (superheating). The two solutions merge at $g = g_c$ when a critical temperature $T_c > T_m$ is reached. This temperature sets the upper bound of possible superheating of the GB. Above T_c , Γ is a monotonically decreasing function of w and the GB is absolutely unstable against melting. The GB thickness at the critical point is

$$w_e^c = 1 + (\beta/2g_c) \ln 2, \quad (10.10)$$

i.e., $W_e^c = W_0 + a^{-1} \ln 2$. Physically a^{-1} is comparable with W_0 , thus the critical GB thickness is not expected to be much greater than W_0 . Inserting (10.8) in (10.3), one obtains an analytical expression for the equilibrium GB free energy as a function of g and thus temperature.

At the bulk melting temperature T_m , the difference in free energies of the liquid and solid phases $\Delta G_V = 0$. In the narrow temperature range around T_m , this difference can be approximated by the linear function

$$\Delta G_V \approx -\Delta S_V (T - T_m), \quad (10.11)$$

where ΔS_V is the entropy difference (per unit volume) between the liquid and solid phases at T_m . This difference can be expressed by

$$H_m = T_m \Delta S_V, \quad (10.12)$$

where H_m is the latent heat of melting per unit volume. Thus $\Delta G_V \approx H_m (T_m - T) / T_m$, which leads to the superheating parameter

$$g \approx \frac{W_0 H_m (T - T_m)}{\gamma_{GB} T_m}. \quad (10.13)$$

Using this expression, the equilibrium GB width w_e can be expressed as a function of temperature,

$$w_e = 1 - \frac{\beta}{2g_c} \ln \frac{1}{2} \left(1 + \sqrt{1 - \frac{\Delta T}{\Delta T_c}} \right), \quad (10.14)$$

where $\Delta T = T - T_m$ and $\Delta T_c = T_c - T_m$ is the critical superheating. Combining Eqs. (10.9) and (10.13), the critical temperature equals

$$T_c = T_m + \frac{a T_m (2\gamma_{SL} - \gamma_{GB})}{2H_m}, \quad (10.15)$$

Inserting w_e from Eq. (10.8) into Eq. (10.3), we obtain the GB free energy $\gamma(w_e)$ as a function of temperature,

$$\gamma(w_e) = \frac{g}{g_c} \left(g^c - \frac{\beta}{2} \ln \chi_e \right) + 1 + \beta (\chi_e - 1)^2, \quad (10.16)$$

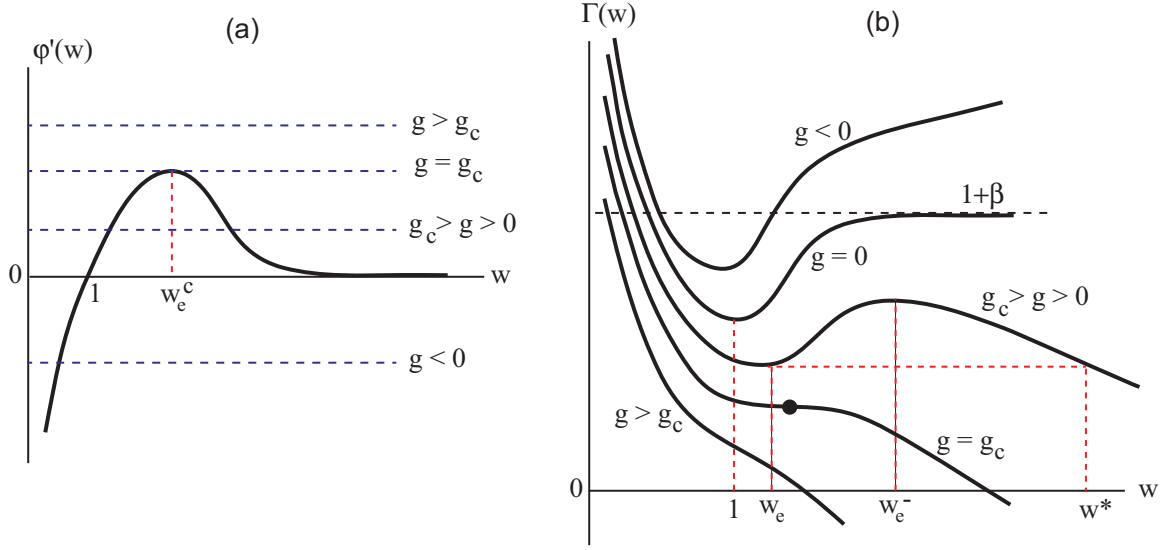


Figure 10.2: Schematic representation of the functions $\varphi'(w)$ and $\Gamma(w)$ involved in the calculation of equilibrium states of a plane grain boundary. (a) Typical shape of $\varphi'(w)$ for a disjoining potential with a single minimum and a single inflection point. Solutions of Eq. (10.27) correspond to intersections of the plot with horizontal lines $g = \text{const}$ for different values of the superheating parameter g . The equation has one solution when $g \leq 0$ (no superheating), two solutions when $0 < g < g_c$ and no solutions when $g > g_c$. (b) The GB free energy Γ as a function of boundary width w for selected values of g . When $g = 0$, this plot gives the disjoining potential $\varphi(w)$ (shifted by $1 + \beta$) with a minimum at $w = 1$. For a superheated boundary, $\Gamma(w)$ has a minimum at w_e and a maximum at w_e^- . The plot also shows the construction to determine the critical thickness w^* of 2D nucleus. The three widths w_e , w_e^- and w^* converge to a common value w_e^c at the critical point shown by a filled circle.

where

$$\chi_e = \frac{1}{2} \left(1 + \sqrt{1 - \frac{g}{g_c}} \right). \quad (10.17)$$

Suppose instead of the Morse function, the DP is some other function satisfying the shape conditions stated above. The ansatz for the GB free energy adopted in the model is

$$\gamma(W) = \Delta G_V W + 2\gamma_{SL} + \Psi(W), \quad (10.18)$$

where the minimum value of $\Psi(W)$ is always $\Psi(W_0) = (\gamma_{GB} - 2\gamma_{SL})$. The range of the DP

can be estimated as the distance, l , from its minimum to the inflection point. Referring to Fig. 10.2b, the maximum of the free energy appears due to the addition to $\Psi(W)$ of the linear term $\Delta G_V W$ with a negative coefficient ΔG_V . At the critical temperature, the linear term is large enough to suppress the maximum. The value of ΔG_V required for this can be roughly estimated by equating $\Delta G_V l$ to the depth of the minimum. This gives the critical value

$$\Delta G_V^c \approx \Psi(W_0)/l = (\gamma_{GB} - 2\gamma_{SL})/l.$$

Using the approximation $\Delta G_V^c \approx H_m (T_m - T_c) / T_m$ (see above), we obtain the estimate of T_c :

$$T_c \approx T_m + \frac{T_m (2\gamma_{SL} - \gamma_{GB})}{l H_m}. \quad (10.19)$$

This is obviously a crude estimate since the range of the DP is defined up to a numerical factor. For the particular case of the Morse potential, the distance between the minimum and the inflection point equals $l = \ln 2/a$.

10.3 Nucleation

In the previous Section we identified an unstable state of the superheated *plane* GB which exists between its metastable state and the bulk liquid (see the curve for $g_c > g > 0$ Fig. 10.2b). However, melting of an infinitely large GB cannot occur by transition through this unstable state because the associated free energy barrier is infinitely large. Instead, the transition occurs by the formation and growth of a local nucleus (Fig. 10.1b) which, after reaching the shape and size with the largest free energy, continues to grow with reduction in free energy until the entire systems turns into liquid. Since the formation of the nucleus is a *local* event, the nucleation barrier is *finite*. Finding the shape, size and free energy of the critical nucleus is a variational problem which will be solved in this Section. The 2D and 3D cases will be discussed separately because their mathematical solutions are different.

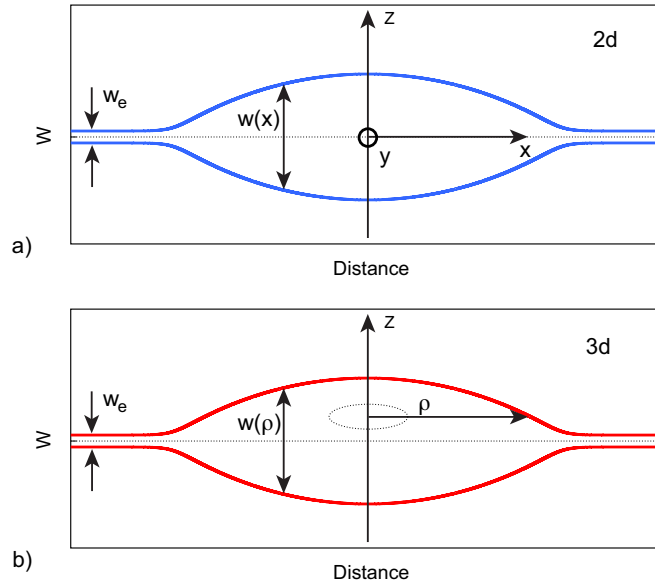


Figure 10.3: Shapes of a critical nucleus in the 2D and 3D cases. (a) 2D case: w is a function of x . The nucleus extends infinitely in the direction y normal to the figure. (b) 3D case: w is a function of the radial distance ρ . The shape of the nucleus in cylindrical coordinates ρ and z is obtained by rotation of $w(\rho)$ around the z axis. w_e indicates the equilibrium thickness of the premelted GB.

10.3.1 2D

Consider two-dimensional nucleation on a superheated GB. This case can arise when a 3D system is subject to a periodic boundary condition in the y direction with a short period L (Fig. 10.3a). Under this condition, the width and all other properties of the GB can be considered independent of the y coordinate, which reduces the problem to two dimensions. Because all boundary properties are uniform and isotropic, the function $w(x)$ describing the nucleus shape must be symmetric, $w(-x) = w(x)$ for all x . For the same reason, the upper and lower boundaries of the nucleus are described by functions $w(x)/2$ and $-w(x)/2$, respectively. Because we neglect the orientation dependence of the solid-liquid interface free energy, faceting is excluded and we can assume that $w(x)$ is a smooth function. This

function is obtained from the zero variational derivative of the excess free energy

$$G = \gamma_{GB} W_0 L \int_0^\infty \left\{ -g(w - w_e) + (1 + \beta) \left[\sqrt{(w')^2 / 4 + 1} - 1 \right] + \varphi(w) - \varphi(w_e) \right\} dx, \quad (10.20)$$

(L being the GB dimension normal to x) with similar boundary conditions. The first term in the integrand represents the decrease in free energy due to the liquid phase being more stable than the solid phase ($g > 0$). The second term is the penalty for the increase in interface area relative to the plane interface. The last term represents the contribution from the DP.

For the critical nucleus, the function $w(x)$ maximizes the functional (10.20) subject to the boundary conditions

$$w' = 0 \text{ at } x = 0, \quad (10.21)$$

$$w' = 0 \text{ at } w \rightarrow w_e. \quad (10.22)$$

Because the integrand F of Eq. (10.20) does not depend on x explicitly, we can use the form of the Euler-Lagrange equation known as the Beltrami identity [113]:

$$F - w' \frac{\partial F}{\partial w'} = C, \quad (10.23)$$

where C is an integration constant. Evaluating Eq. (10.23) with the integrand from Eq. (10.20), we obtain

$$\frac{(w')^2 / 4}{\sqrt{(w')^2 / 4 + 1}} (1 + \beta) + g(w - w_e) - (1 + \beta) (\sqrt{(w')^2 / 4 + 1} - 1) - [\varphi(w) - \varphi(w_e)] = C. \quad (10.24)$$

Due to the boundary condition (10.22), $C = 0$ and Eq. (10.24) gives the following differential

equation for $w(x)$:

$$w' = 2\sqrt{q^2 - 1}, \quad (10.25)$$

where q is a function of w given by

$$q = \frac{-(\beta + 1)}{-(\beta + 1) - g(w - w_e) + \varphi(w) - \varphi(w_e)}. \quad (10.26)$$

The width of the critical nucleus is defined as $w^* = w(0)$. Using Eq. (10.24) and the boundary condition (10.21), we obtain the equation for w^* :

$$-g(w^* - w_e) + \varphi(w^*) - \varphi(w_e) = 0 \quad (10.27)$$

Knowing the DP, this equation can be solved numerically for any given superheating g . For the particular case of the Morse function, there is only one solution different from $w^* = w_e$ as long as $0 < g < g_c$. In fact, the solution continues to be unique for more general forms of the DP formulated above. Indeed, Eq. (10.27) can be written in the form

$$\Gamma(w^*) = \Gamma(w_e), \quad (10.28)$$

where function $\Gamma(w)$ is defined by Eq. (10.3). A geometric interpretation of this equation is shown in Fig. 10.2b, where w^* is obtained from the intersection of the tangent to the plot of $\Gamma(w)$ at $w = w_e$ with the right-hand-side branch of the plot. As long as the DP has the shape shown in this figure, the intersection is unique. This construction also shows that $w_e \leq w_e^- \leq w^*$, where w_e^- is the position of the maximum. Thus, the critical width of a local nucleus is always larger than the critical width of a plane GB. As g approaches g_c , the three widths w_e , w_e^- and w^* converge to a common value w_e^c representing the unstable width of a plane GB.

The barrier of nucleation, G^* , is defined as the amount of free energy required to form

the critical nucleus on the initial uniform superheated GB. It can be obtained by integration of Eq. (10.20) with $w(x)$ computed from Eq. (10.25), which gives

$$G^* = \gamma_{SL}W_0L \int_0^\infty \frac{(w')^2}{\sqrt{1 + (w')^2/4}} dx = 2\gamma_{SL}W_0L \int_{w_e}^{w^*} \frac{\sqrt{q^2 - 1}}{q} dw. \quad (10.29)$$

Taking w_e from Eq. (10.4) and w^* from Eq. (10.27), the nucleation barrier can be computed numerically as a function of superheating g .

10.3.2 3D

In the 3D case we assume that the shape of the critical nucleus has cylindrical symmetry (Fig. 10.2b). This shape is defined by the width w as a function of radius ρ measured in units of W_0 . Similar to the 2D case, the upper and lower parts of the nucleus are described by the functions $w(\rho)/2$ and $-w(\rho)/2$, respectively. The free energy change due to the nucleation on a uniform GB of width w_e is

$$G = \gamma_{GB}W_0^2 \int_0^\infty \left\{ -g_V(w - w_e) + (1 + \beta)(\sqrt{(w')^2/4 + 1} - 1) + \varphi(w) - \varphi(w_e) \right\} 2\pi\rho d\rho. \quad (10.30)$$

The boundary conditions are analogous to the 2D case:

$$w' = 0 \text{ at } \rho = 0, \quad (10.31)$$

$$w' = 0 \text{ at } w \rightarrow w_e. \quad (10.32)$$

The critical nucleus shape is found from the condition $\delta G = 0$.

Because the integrand F of the functional (10.30) depends explicitly on ρ , the Beltrami identity cannot be applied and the calculation requires the use of the full Euler-Lagrange equation [113]:

$$\frac{\partial F}{\partial w} - \frac{d}{d\rho} \left(\frac{\partial F}{\partial w'} \right) = 0 \quad (10.33)$$

Inserting F from Eq. (10.30) into Eq. (10.33), we obtain the non-linear second order differential equation

$$-g\rho + \varphi'(w)\rho - \frac{(1+\beta) \left[w' + (w')^3/4 + \rho w'' \right]}{4 \left(1 + (w')^2/4 \right)^{3/2}} = 0. \quad (10.34)$$

This equation was solved numerically with the boundary conditions (10.31) and (10.32) for a given values of g . The critical nucleus width w^* was obtained as $w(0)$. Knowing the critical nucleus shape $w(\rho)$, the nucleation barrier G^* was computed from Eq. (10.30).

It can be shown analytically that this model reduces to CNT when the superheating is small and thus $w^* \gg 1$. In this limit the model recovers the CNT results

$$W^* = 2 \frac{\gamma_{GB} - 2\gamma_{SL}}{\Delta G_V}, \quad (10.35)$$

$$G^* = \frac{16\pi\gamma_{SL}^3}{3\Delta G_V^2} \left(1 - \frac{3}{2} \cos \frac{\theta}{2} + \frac{1}{2} \cos^3 \frac{\theta}{2} \right) \quad (10.36)$$

in the 3D model and

$$W^* = \frac{\gamma_{GB} - 2\gamma_{SL}}{\Delta G_V}, \quad (10.37)$$

$$G^* = -\frac{L\gamma_{SL}^2}{\Delta G_V} (\theta - \sin \theta) \quad (10.38)$$

in 2D. Here, θ is the contact angle satisfying the Young relation $2\gamma_{SL} \cos(\theta/2) = \gamma_{GB}$. For homogeneous nucleation, the diameter of the spherical droplet W^* and the barrier G^* are obtained from (10.35) and (10.36) with $\gamma_{GB} = 0$ and $\theta = \pi$.

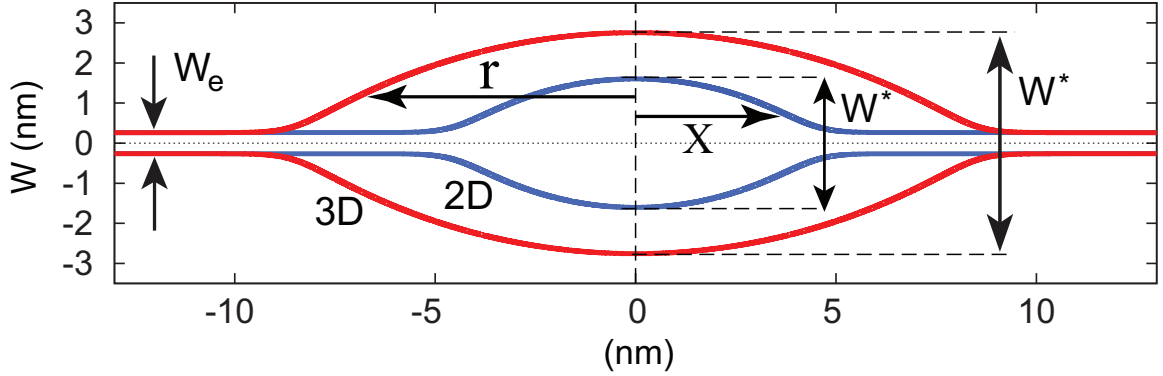


Figure 10.4: Shapes of the critical nuclei computed from the model at $T = 1349$ K for the 2D (blue) and 3D (red) geometries. The finite thickness away from the nuclei represents the premelted boundary and equals 0.5 nm at T_m .

10.4 MD simulations of nucleation

We tested our model by atomistic simulations of the $(540)[001]$ symmetrical tilt GB in Cu with the misorientation angle 77° and the reciprocal density of coincidence sites $\Sigma = 41$. The GB was created in a simulation block with dimensions $20 \times 20 \times 20 \text{ nm}^3$ (543296 atoms). The block had periodic boundary conditions parallel to the GB and terminated at open surfaces in the normal direction. The atoms in thin layers near the surfaces were constrained to move only in the normal direction, imposing zero normal stress. The atomic interactions were modeled with an embedded-atom potential [39] giving $T_m = 1327$ K and $H_m = 9.72$ eV/nm³. The GB structure consists of an array of closely spaced $(1/2)[110]$ dislocations aligned parallel to the tilt axis $[001]$ (Fig. 4d in [31]).

The MD simulations were performed in the canonical and microcanonical ensembles for times up to 50 ns. The temperature was increased by steps starting from 0 K. The block was pre-expanded according to the thermal expansion factor and annealed to achieve point-defect equilibrium at each temperature. At temperatures approaching 1410 K, spontaneous melting was observed by nucleation and growth of a liquid droplet on the GB. Since it was impossible to superheat the GB above 1410 K, it was concluded that this temperature was approximately equal to the critical point T_c .

After a droplet of the liquid phase nucleates and begins to grow on the boundary. Eventually the entire simulation block turns into homogeneous liquid. It should be noted that in the canonical ensemble, the critical nucleus is in a state of *unstable* equilibrium with the solid phase. Thus, if the size of the droplet is less than critical, it will shrink. If it exceeds the critical size, the droplet will grow indefinitely. In order to study properties of the critical nucleus, we had to abandon the canonical ensemble and apply the adiabatic trapping procedure described below.

As soon as a nucleus began to grow in a canonical simulation, we switched the ensemble to microcanonical. The system becomes adiabatic, which cuts the heat supply from the thermostat needed for continuing growth of the droplet. If the droplet stops growing and begins to shrink, the crystallization releases latent heat and the temperature begins to increase. Note that the critical nucleus size decreases with increasing temperature. Thus, when the temperature reaches a high enough value, the droplet size becomes supercritical and it begins to grow. But the growth requires heat supply, which will be drawn from surrounding regions until the temperature of the system drops and the droplet size becomes sub-critical. As a result, the droplet size and temperature fluctuate and eventually settle on certain values, at which the droplet size is exactly critical at the final value of the temperature. Because the amounts of the liquid and solid phases generally change in this process while the volume is fixed, the equilibration produces some lateral stresses in the system (the stress normal to the boundary plane remains zero due to the boundary conditions). These stresses were eliminated by slightly adjusting the system dimensions and re-equilibrating it. This obtained droplet represented the critical nucleus at the temperature T stabilized by the adiabatic trap. To model different sizes of critical nuclei, some amount of heat was added or removed from a system containing a critical nucleus. This was achieved by switching to NVT ensemble, making a picosecond long run at a slightly higher or lower temperature, and then switching back to the NVE ensemble and equilibrating. A similar methodology was applied to study homogeneous nucleation. The simulation block of the same size but

with all-periodic boundary conditions was superheated and small nucleus of liquid was introduced at its center. This method stabilizing critical nuclei by adiabatic trapping is novel and can be applied to other materials and phase nucleation phenomena in the future.

To visualize the nuclei, each atom was assigned to either the solid or the liquid according to its energy relative to a chosen discrimination level. This method was used to compute the GB and nucleus thicknesses W_e and W^* . Alternatively, the centrosymmetry method was applied to produce images revealing the nucleus shape and the surrounding vacancies (Fig. 10.5). To model a heterogeneous 2D nucleation, the block dimension parallel to the tilt axis was reduced by half, resulting in nucleation of droplets whose thickness was uniform in that direction. A similar procedure was used to create nearly spherical droplets representing homogeneous nuclei in the lattice. (The residual stresses were removed by a short isothermo-isobaric run with a switch back to the microcanonical ensemble.)

10.4.1 Results and Discussion

The MD results are summarized in Fig. 10.6. Homogeneous melting is characterized by a large nucleus size and can be treated within the CNT. Fitting the CNT equation $W^* = -2\gamma_{SL}/\Delta G_V$ to the MD points gives $\gamma_{SL} = 0.201 \text{ J/m}^2$, a number which is in good agreement with the experimental value 0.177 J/m^2 [53] and recent direct calculations for the (110) solid-liquid Cu interface, 0.199 J/m^2 [60]. Using this γ_{SL} , the proposed model and CNT were fitted to the MD data for heterogeneous nucleation in 3D and 2D by optimizing the value of γ_{GB} . The numbers obtained (in J/m^2) are 0.332 (3D model), 0.341 (2D model), 0.331 (3D CNT) and 0.333 (2D CNT). They are remarkably consistent and are reasonably below the 0 K value of 0.595 J/m^2 in agreement with the established temperature trend [94]. The contact angle computed within CNT is $\theta = 67.8^\circ$. Fig. 10.4 illustrates typical shapes of critical nuclei predicted by the model, which are consistent with typical shapes observed in the MD simulations (Fig. 10.5). The DP parameters obtained from the fit are $W_0 = 0.5 \text{ nm}$ and $1/a = 0.36 \text{ nm}$.

Despite the close agreement of the computed γ_{GB} values, the CNT and the proposed

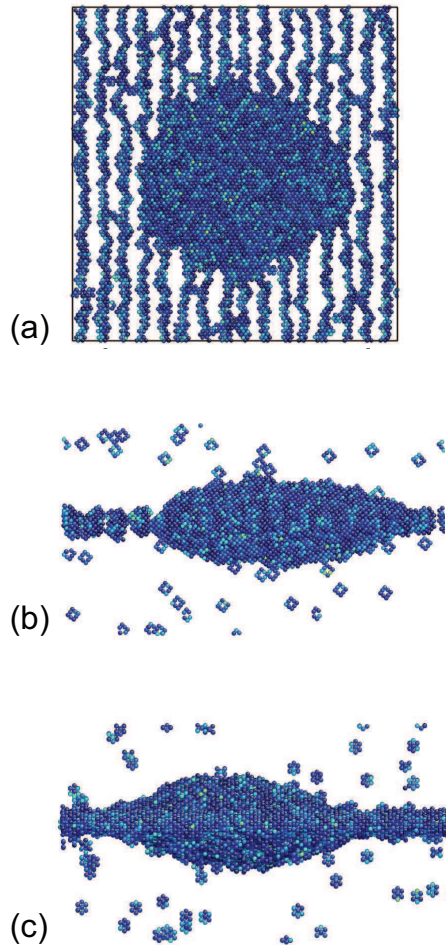


Figure 10.5: Premelted grain boundary (GB) with a three-dimensional critical nucleus at 1357 K stabilized by adiabatic trapping and visualized by centrosymmetry coloring. Atoms with fcc coordination are not shown for clarity. (a) Top view; the dislocation lines are vertical. (b) Dislocation lines are normal to the page. (c) Dislocation lines are horizontal. Although not apparent due to fluctuations, the average shape of the nucleus does not possess a twofold symmetry around the GB normal due to the lack of such symmetry in the GB structure and anisotropy of γ_{SL} . The dots in the grains mark vacancies. See supplementary materials for animations.

model show qualitatively different behaviors near T_c . While the model barrier vanishes at T_c , the CNT barrier continues to decrease with temperature and remains finite and as high as 3.6 eV at T_c (Fig. 10.7). The probability of overcoming this barrier is small, contradicting the MD observations. Overall the model demonstrates a reassuring agreement with the MD

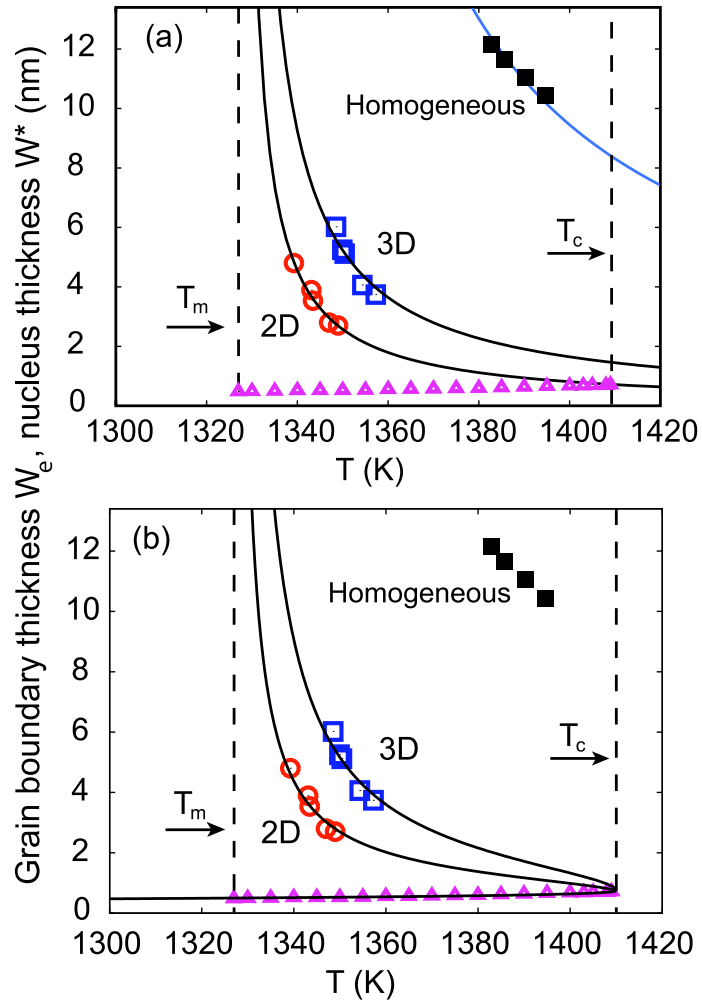


Figure 10.6: The grain boundary (GB) thickness W_e (Δ) and the nucleus thickness W^* (\square, \circ) as functions of temperature. The points are results of molecular dynamics (MD) simulations. The GB thickness increases from 0.5 nm at T_m to 0.75 nm at T_c . In (a) the lines are fits of the classical nucleation theory (CNT) to the MD data; in (b) the lines are fits of the proposed model. Note the qualitative difference at high temperatures.

results.

The proposed model is more general than the heterogeneous CNT [110]. While the latter is not expected to be valid when the nucleus and the barrier are small, our model continues to give physically reasonable results due to the incorporation of the atomic-scale information via the DP. The particular Morse form (10.1) of the DP was used as an example. The results remain qualitatively similar for other smooth functions with a single minimum

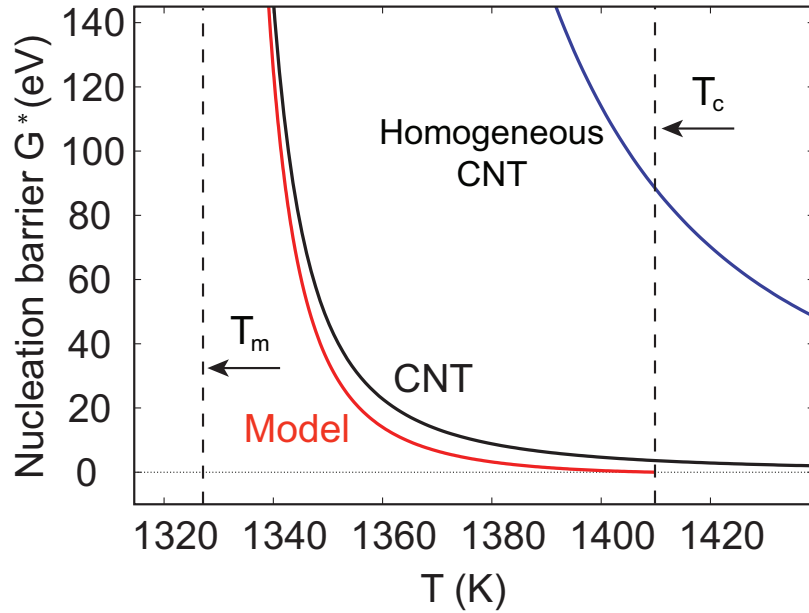


Figure 10.7: Nucleation barriers computed from the proposed model and classical nucleation theory (CNT). The model predicts a critical temperature of superheating at which the barrier vanishes and the boundary becomes unstable against melting. Note that CNT gives a finite barrier at all temperatures and is not capable of predicting a critical temperature.

and a single inflection point. All such functions predict a single critical temperature of superheating, which is obtained from the condition $g = g_c$:

$$T_c = T_m + T_m (2\gamma_{SL} - \gamma_{GB}) / 2H_m l, \quad (10.39)$$

where l is a characteristic lengthscale of the DP (on the order of a nanometer). In the future, the model could be applied for the analysis of the triple line effect. It could also incorporate the effect of applied mechanical stresses.

Chapter 11: Summary

11.1 Thermodynamics of phase boundaries

We developed a thermodynamic treatment of coherent solid-solid interfaces in a multicomponent system under a general non-hydrostatic state of stress. The theory generalizes Gibb'sian treatment of interfaces which focused mainly on fluid interfaces and did not consider elastic deformation of an interface or shear stresses parallel to the interface.

In this work the expression for γ was derived by considering a process in which an interface was created reversibly between two solid phases. The total interface free energy γA was then expressed through excess of an appropriate thermodynamic potential which included the shear stresses σ_{31} and σ_{32} and corresponding excesses of interface shear. In our analysis we did not use the concept of the dividing surface [13], which allowed to track the shape change of the system with interface in a straightforward manner and avoid defining individual chemical potentials of the substitutional atoms. When one of the extensive parameters X or Y is equal to V and shear stresses σ_{31} and σ_{32} are zero, the excess quantities are identical to those introduced by Gibbs.

We also derived the adsorption equation which describes change in γ due to thermal, chemical and mechanical variations of state. In the adsorption equation the diffusion potentials for substitutional components appear instead of the chemical potentials. The expression for γA and the adsorption equation introduces a new excess quantity: excess of shear at a coherent interface. The adsorption equation derived in this work describes processes which include deformation of the interface area and contains the work term of this elastic deformation parallel to the interface plane. The later work is done by interface stress $\boldsymbol{\tau}$. The adsorption equation rigorously defines $\boldsymbol{\tau}$ and gives a recipe how to compute it as an excess quantity. We also showed that $\boldsymbol{\tau}$ is not unique for non-hydrostatic systems.

One of the major challenges in thermodynamics of solid-solid interfaces is a necessity to define chemical potentials of substitutional atoms. Chemical potentials are defined as work required to add an atom to the system. Gibbs showed that for a non-hydrostatically stressed solid chemical potentials are not uniquely defined. Analyzing equilibrium of non-hydrostatic solids Larche and Cahn [18] avoided definition of chemical potentials of substitutional atoms. In this work we only considered variations in chemical composition of substitutional atoms at constant N , so it was unnecessary to define individual chemical potentials of substitutional atoms.

We introduced thermodynamic potentials ϕ_m of a homogeneous solid under stress. When two phases, separated by a coherent interface, are in equilibrium, these potentials have the same value in the phases. The ϕ_m potentials allow to conveniently write thermodynamic equations in a form identical to that of hydrostatic systems. Moreover, when a phase is hydrostatic, ϕ_m become real chemical potentials. It is important to notice, that in this work, the potentials ϕ_m were defined for a homogeneous solid containing constant number of atoms. Based on this definition alone, ϕ_m cannot be identified with chemical potentials of a substitutional atoms. On the other hand, there is no ambiguity in their definition.

Analysis of interface phenomena requires understanding of the bulk phase equilibrium. In this work we derived a Gibbs-Duhem type equation for solid under general state of stress. Solving a system of two Gibbs-Duhem equations for two solid phases in coherent equilibrium, we obtained the equation which describes the equilibrium surface of the two-phase coexistence in configuration space. This equation is analog of the Clausius–Clapeyron relation[34] generalized for non-hydrostatic multicomponent solid system. It includes the effect of non-hydrostatic stresses, temperature and chemical composition on the phase equilibrium conditions. If one equilibrium state is known, other nearby states can be predicted using this equation. The phase equilibrium conditions (i)-(v) are embedded in (2.36). Therefore, testing the relations predicted by this equation one tests the correctness of the equilibrium conditions. Employing the approximation of linear elasticity (and perhaps ideal solution

model), the derived differential equations of phase equilibrium can be integrated along a co-existence path to predict the equilibrium states of the phases as functions of non-hydrostatic stresses, temperature and composition. Thus, the phase transformation conditions under non-hydrostatic conditions can be predicted by theory and tested by extensive atomistic simulations.

The derived Clausius–Clapeyron type relation can be used to predict the effect of large non-hydrostatic stress conditions on the phase transformation temperatures during mechanical processing of high-strength alloys, in materials exposed to extreme environments, and in high-pressure zones of the Earth crust. The equation can be useful not only in metallurgical applications in the context of thermo-mechanical treatment of alloys, but also in high pressure physics, geophysics and planetary sciences.

11.2 Summary of atomistic simulation

Proposed thermodynamic theory offers new thermodynamic integration methods to compute interface free energy γ and gives recipe how to compute other excess properties. Significant efforts in the materials science community are devoted to development of methods, both computational and experimental, for accurate determination of the interface free energy [67–69]. The proposed new methodology for interface free energy calculations is based on integration of the Gibbs-Helmholts type equation. This approach was employed in atomistic simulations of a number of systems both in our work [26, 60, 74] and by other groups [58, 87] and proved to be accurate and more computationally efficient than existing methods. The important advantage of the method is its generality. It is not specific to any particular types of interfaces and can be applied to general multicomponent systems with solid or fluid surfaces, grain boundaries, solid-fluid and solid-solid phase boundaries. This thermodynamic integration method can be used to study coherent and semi-coherent solid-solid phase boundaries at finite temperature, which are not well understood. The proposed thermodynamic integration method will allow to compute γ of such interfaces for the first time as a function of temperature, chemical composition and mechanical stresses.

Application of the thermodynamic integration method allowed us to clarify the behavior of key surface properties with temperature [60], resolving some of the long-standing controversies in surface science. It was argued that due to high mobility of surface atoms, surface stress and surface energy converge near the melting point to surface tension of liquid. Using atomistic simulations we investigated effect of surface premelting on γ and τ . We computed the two properties as functions of temperature employing the thermodynamic integration method and found that despite extensive premelting γ and τ do not converge at the melting point and both values were different from surface tension of liquid. The difference was due to solid-liquid interface below the premelted layer. Calculation of γ using our thermodynamic integration method allowed to estimate interface free energy of the solid-liquid interface γ_{sl} for this particular orientation. From the study of premelting we estimated negative value of τ_{sl} . Our theory provides an expression for calculation of interface stress tensor of solid-liquid interface for a general case of non-hydrostatic system. τ_{sl} was computed for solid-liquid interface with the same crystallographic orientation and was also found to be negative. The close agreement between the estimated and directly computed values confirms the correctness of our interpretation of the premelting data.

Interface stress had been computed previously for solid-liquid interfaces in several systems using expression for hydrostatic systems. However, in atomistic simulations small non-hydrostatic stresses are unavoidable. These stresses affect accuracy of calculations and, thus, the full non-hydrostatic approach is desirable. The calculations in various systems showed that τ can be both positive and negative. It was suggested that the sign of interface stress correlates with density differences between solid and liquid phases. Using our expression for interface stress, we computed individual components of τ in a single component solid-liquid system for different crystallographic orientations of the interface [93]. Both positive and negative values were obtained for different orientations with the same thermodynamic states of bulk phases, which means that the sign of τ cannot be predicted base on the densities of the bulk phases.

We continued to study solid-liquid interfaces by exploring effects of varying composition.

Previously, γ in a binary system was computed in a single study that used CFM [71]. Using our thermodynamic integration method, interface free energy was computed in CuAg system [26]. γ was found to decrease with alloying in agreement with the previous study of a generic binary alloy [71]. Our calculation also demonstrated strong effect of alloying on magnitude and anisotropy of interface stress. Some of the interface excess properties were computed by different methods and demonstrated accurate agreement with each other, confirming the correctness of our analysis.

In a single component system we analyzed effects of strong non-hydrostatic stresses on phase equilibrium and interface properties [86]. Using our generalized Clausius–Clapeyron type relation (for solid-fluid system it was first derived by Gibbs) and employing approximation of linear elasticity we derived expressions for equilibrium temperature and pressure in the fluid as functions of non-hydrostatic stresses. We also considered particular variations of state: hydrostatic, non-hydrostatic at constant temperature, non-hydrostatic at constant pressure in the liquid. The change in equilibrium temperature or pressure with non-hydrostatic stress was found to be quadratic in general case. In special cases when volume per atom or entropy per atom are the same in both phases, non-hydrostatic effects were found to be linear.

Atomistic simulations were employed to model thermodynamic equilibrium between liquid and solid under non-hydrostatic stress. If the stresses are large enough Asaro-Tiller-Grinfeld (ATG) instability may occur [114], in which interface undergoes a morphological change destroying non-hydrostatic equilibrium state. In atomistic simulations we were able to avoid this instability by choosing relatively small cross-section of the interface. Using micro-canonical ensemble, we were able to model a stable solid-liquid coexistence state and measure equilibrium temperature, pressure in the liquid and stresses in the solid. Elastic compliances of the solid and non-hydrostatic stresses were used as input data in our equations to predict equilibrium temperature at constant pressure and equilibrium pressure at constant temperature. The predicted values were in excellent agreement with temperature and pressure computed directly from atomistic simulations of phase coexistence.

This study demonstrated that equilibrium states of solid-liquid coexistence can be predicted if one equilibrium state and properties of individual phases are known. Gibbs analyzed non-hydrostatic solid-fluid equilibrium in a single component system and did not consider compositional variations in the solid. Our generalized Clausius–Clapeyron type equation was derived for a multicomponent system. Using linear elasticity in conjunction with approximation of ideal solution model, we can derive equations to predict non-hydrostatic solid-fluid equilibrium states in a multicomponent system. This analysis would employ open system elastic constants introduced by Larche and Cahn. Prediction of coherent solid-solid equilibrium states can be addressed in the same manner.

Excess interface properties were computed for non-hydrostatic compression and tension at constant zero pressure in the liquid [74]. Our analysis reveals that when the solid is non-hydrostatic, the interface stress is not unique as other excess properties. We showed the existence of several specific types of interface stresses, formulate them as interface excess quantities, and established relationships between them. Using molecular dynamics simulations we computed several different interface stresses. The simulations showed that biaxial tension and compression of the solid produce a strong effect on the magnitude, sign, and anisotropy of the interface stresses. The free energy of the interface was computed by thermodynamic integration along biaxial tension and compression paths. The effect of non-hydrostatic stresses on the interface free energy was much weaker than the effect on interface stresses.

The theory of coherent interfaces was applied to study a symmetrical tilt grain boundary in Cu and CuAg binary system. Grain boundary is an interfaces in a single phase system and represents one of the simplest examples of coherent interfaces. In the study excess properties of the interface were computed as functions of normal and shear stresses, lateral strains, temperature and composition. The new excess quantity introduced in this work, excess shear, was measured for this boundary as a function shear stress. Thermodynamic relations were tested by computing γ directly from definition and by integration of the adsorption equation. Excellent agreement was found between values computed by these two

approaches. The theory was also tested by checking the predictions of Maxwell relations. The derivatives involved in the relations were computed in a single component as well as in the binary system. Excellent agreement between predictions of the theory and results of calculations confirm the correctness of the theory. Temperature and chemical composition were found to significantly reduce γ . It is necessary to take this reduction into account to accurately predict barriers of heterogeneous nucleation on grain boundaries and contact angles between solid and liquid phase.

Understanding the thermodynamic properties of interfaces is crucial to study of heterogeneous phase transformations. At high temperatures some grain boundaries and surfaces turn into liquid like layers while some become more disordered but remain crystalline. Whether or not an interface will premelt can be determined comparing interface free energies of GBs and surfaces to free energies of solid-liquid interface and liquid surface. This premelting behaviour will determine the mechanism of melting of a material with surfaces and interfaces. If premelting is present, the material will melt approaching the melting point. Otherwise material can be superheated and will melt by nucleation of liquid phase.

Grain boundaries with relatively low energies can be superheated above the melting temperature. We developed a thermodynamic model of heterogeneous nucleation of a liquid phase on grain boundaries, which captures the effect of grain boundary premelting and interface-interface interactions on the nucleation properties through incorporation of the so called disjoining potential (DP) [105]. The concept of the DP was successfully used in the past [115] to explain wetting of liquid films on solid substrates and shapes of liquid droplets. Application of DP to grain boundary premelting is a relatively new and rapidly developing concept [100,116]. The nucleation model with a DP allowed to compute the shape of the critical nucleus and predict important effects of interface-interface interactions on the nucleation barrier, which is a significant improvement over the classical nucleation theory.

The proposed model was tested against atomistic simulations of liquid nucleation at a grain boundary in copper. A novel simulation approach was proposed, which allowed to

study equilibrium states that are unstable under usual conditions. This approach, which we call adiabatic trapping, was used to model critical nuclei for homogeneous (in the bulk solid) and heterogeneous (at grain boundaries) nucleation of the liquid phase. Equilibrium shapes of the liquid nuclei were obtained for the first time, which enabled direct comparison of the theory with results of atomistic simulations. The simulation results demonstrated a reassuring agreement with the proposed thermodynamic model.

The proposed method of adiabatic trapping is novel and can be applied to study nucleation in a wide variety of systems. It can be employed in study of homogeneous nucleation to investigate thermodynamic properties of coexisting phases and test equilibrium conditions. The method can also be applied to study equilibrium shapes of liquid droplets on various defects such as dislocations, triple lines, grain boundary dislocations and steps of vicinal surfaces. Such studies will demonstrate if these defects are indeed preferable sites for nucleation and may allow to estimate excess free energy of these defects at high temperature.

Bibliography

Bibliography

- [1] J. Luo, H. Cheng, K. M. Asl, C. J. Kiely, and M. P. Harmer, *Science* **333**, 1730 (2011).
- [2] A. P. Sutton and R. W. Balluffi, *Interfaces in Crystalline Materials*, Clarendon Press, Oxford, 1995.
- [3] M. Asta et al., *Acta Mater.* **57**, 941 (2009).
- [4] D. Herlach, P. Galenko, and D. Holland-Moritz, *Metastable Solids from Undercooled Melts*, Elsevier, Boston, MA, 2007.
- [5] G. Ghosh, *Mater Sci Eng A* **189**, 277 (1994).
- [6] T. Volkman, W. Loeser, and D. N. Herlach, *Metall Mater Trans A* **28**, 453.
- [7] D. M. Herlach, *J Phys Condens Matter* **13**, 7737 (2001).
- [8] P. W. Voorhees, *Annual Review of Materials Science* **22**, 197 (1992).
- [9] P. S. Ho and T. Kwok, *Rep. Prog. Phys.* **52**, 301 (1989).
- [10] F. Mugele and J. Baret, *J. Phys.: Condens. Matter* **17**, 705 (2005).
- [11] J. H. Song, R. Evans, Y.-Y. Lin, B.-N. Hsu, and R. B. Fair, *Microfluid Nanofluid* **7**, 75 (2009).
- [12] T. Krupenkin and J. A. Taylor, *Nat. Commun.* **2**, 448 (2011).
- [13] J. W. Gibbs, *The Scientific Papers of J. Willard Gibbs*, volume 1, Longmans-Green, London, 1906.
- [14] J. W. Cahn, Thermodynamics of solid and fluid surfaces, in *Interface Segregation*, edited by W. C. Johnson and J. M. Blackely, chapter 1, page 3, American Society of Metals, Metals Park, OH, 1979.
- [15] R. Shuttleworth, *Proc. Phys. Soc. A* **63**, 444 (1949).
- [16] R. C. Cammarata, *Prog. Surf. Sci.* **46**, 1 (1994).
- [17] H. Ibach, *Surface Science Reports* **29**, 195 (1997).
- [18] F. C. Larche and J. W. Cahn, *Acta Metall.* **26**, 1579 (1978).

- [19] P. Voorhees and W. C. Johnson, The thermodynamics of elastically stressed crystals, volume 59 of *Solid State Physics*, pages 1 – 201, Academic Press, 2004.
- [20] R. C. Cammarata, *Philos. Mag.* **88**, 927 (2008).
- [21] R. C. Cammarata, Generalized thermodynamics of surfaces with applications to small solid systems, in *Solid State Physics*, edited by H. Ehrenreich and F. Spaepen, volume 61, pages 1–75, Elsevier Academic Press, 2009.
- [22] L. E. Malvern, editor, *Introduction To The Mechanics Of A Continuous Medium*, Prentice-Hall, Upper Saddle River, 1969.
- [23] F. Larche and J. W. Cahn, *Acta Metall.* **21** (1973).
- [24] F. C. Larchè and J. W. Cahn, *Acta Metall.* **33**, 331 (1985).
- [25] P. Y. Robin, *Am. Miner* **59**, 1286 (1974).
- [26] T. Frolov and Y. Mishin, *The Journal of Chemical Physics* **131**, 054702 (2009).
- [27] H. Brooks, *Metal interfaces*, page 20, Metals Park, OH, 1963, American Society for Metals.
- [28] J. Cahn and F. C. Larche, *Acta Metallurgica* **30**, 51 (1982).
- [29] J. Q. Broughton and G. H. Gilmer, *Phys. Rev. Lett.* **56**, 2692 (1986).
- [30] P. L. Williams and Y. Mishin, Thermodynamics of grain boundary premelting in alloys. II. Atomistic simulation, *Acta Mater.*, submitted as Part II of this work, 2009.
- [31] J. W. Cahn, Y. Mishin, and A. Suzuki, *Acta Mater.* **54**, 4953 (2006).
- [32] T. Gorkaya, D. A. Molodov, and G. Gottstein, *Acta Materialia* **57**, 5396 (2009).
- [33] D. L. Olmsted et al., *Phys. Rev. Lett.* **106**, 046101 (2011).
- [34] E. A. Guggenheim, *Thermodynamics. An Advanced Treatment for Chemists and Physicists*, North Holland: Elsevier, 1993.
- [35] J. Stadler, R. Mikulla, and H. R. Trebin, *Int. J. Mod. Phys. C* **8**, 1131 (1997).
- [36] D. Frenkel and B. Smit, *Understanding molecular simulation: from algorithms to applications*, Academic, San Diego, second edition, 2002.
- [37] D. Frenkel and B. Smit, *Understanding Molecular Simulation*, Academic Press, San Diego, 2002.
- [38] P. Gumbsch and M. S. Daw, *Phys. Rev. B* **44**, 3934 (1991).
- [39] Y. Mishin, M. J. Mehl, D. A. Papaconstantopoulos, A. F. Voter, and J. D. Kress, *Phys. Rev. B* **63**, 224106 (2001).
- [40] P. L. Williams, Y. Mishin, and J. C. Hamilton, *Modelling Simul. Mater. Sci. Eng.* **14**, 817 (2006).

- [41] T. B. Massalski, editor, *Binary Alloy Phase Diagrams*, ASM, Materials Park, OH, 1986.
- [42] D. Kramer and J. Weissmuller, *Surf. Sci.* **601**, 3042 (2007).
- [43] J. W. M. Frenken, P. M. J. Maree, and J. F. van der Veen, *Phys. Rev. B* **34**, 7506 (1986).
- [44] C. Gurney, *Proc. Phys. Soc.* **62**, 639 (1949).
- [45] G. L. J. Bailey and H. Watkins, *Proc. Phys. Soc.* **63**, 350 (1949).
- [46] C. Herring, The use of classical macroscopic concepts in surface-energy problems, in *Structure and Properties of Solid Surfaces*, edited by R. Gomer and C. S. Smith, chapter 1, pages 5–81, The Univ. of Chicago Press, Chicago, Illinois, 1953.
- [47] J. S. Vermaak and D. K. Wilsdorf, *J. Phys. Chem.* **72**, 4150 (1968).
- [48] S. M. Foiles, *Phys. Rev. B* **49**, 14930 (1994).
- [49] J. Q. Broughton and G. H. Gilmer, *Acta Metall.* **31**, 845 (1983).
- [50] C. A. Becker, J. J. Hoyt, D. Buta, and M. Asta, *Phys. Rev. E* **75**, 061610 (2007).
- [51] S. M. Foiles, *Phys. Rev. B* **32**, 7685 (1985).
- [52] S. M. Foiles, Calculation of the surface segregation of alloys using the embedded atomic method, in *Surface Segregation Phenomena*, edited by P. Dowben and A. Miller, CRC Press, 1990, p. 79.
- [53] L. E. Murr, *Interfacial Phenomena in Metals and Alloys*, Addison-Wesley, Reading, MA, 1975.
- [54] J. Q. Broughton and G. H. Gilmer, *J. Chem. Phys.* **84**, 5759 (1986).
- [55] R. L. Davidchack and B. B. Laird, *J. Chem. Phys.* **108**, 9452 (1998).
- [56] Y. Mishin, M. Asta, and J. Li, *Acta Materialia* **58**, 1117 (2010).
- [57] C. A. Becker, D. L. Olmsted, M. Asta, J. J. Hoyt, and S. M. Foiles, *Phys. Rev. Lett.* **98**, 125701 (2007).
- [58] B. B. Laird, R. L. Davidchack, Y. Yang, and M. Asta, *J. Chem. Phys.* **131**, 114110 (2009).
- [59] H. Ramalingam, M. Asta, A. van de Walle, and J. J. Hoyt, *Interface Sci.* **10**, 149 (2002).
- [60] T. Frolov and Y. Mishin, *Phys. Rev. B* **79**, 045430 (2009).
- [61] T. Frolov and Y. Mishin, *Phys. Rev. B* **79**, 174110 (2009).
- [62] J. Morris and X. Song, *J. Chem. Phys.* **116**, 9352 (2002).

- [63] J. W. Cahn, *Acta Metall.* **28**, 1333 (1980).
- [64] C. A. Becker, M. Asta, J. J. Hoyt, and S. M. Foiles, *J. Chem. Phys.* **124**, 164708 (2006).
- [65] R. Sibug-Aga and B. B. Laird, *J. Chem. Phys.* **116**, 3410 (2002).
- [66] R. Sibug-Aga and B. B. Laird, *Phys. Rev. B* **66**, 144106 (2002).
- [67] J. Q. Broughton and G. H. Gilmer, *J. Chem. Phys.* **79**, 5095 (1983).
- [68] R. L. Davidchack and B. B. Laird, *Phys. Rev. Lett.* **85**, 4751 (2000).
- [69] J. J. Hoyt, M. Asta, and A. Karma, *Phys. Rev. Lett.* **86**, 5530 (2001).
- [70] M. Amini and B. B. Laird, *Phys. Rev. B* **78**, 144112 (2008).
- [71] C. A. Becker, D. L. Olmsted, M. Asta, J. J. Hoyt, and S. M. Foiles, *Phys. Rev. B* **79**, 054109 (2009).
- [72] M. Asta, J. J. Hoyt, and A. Karma, *Phys. Rev. B* **66**, R100101 (2002).
- [73] R. Sekerka and J. Cahn, *Acta Mater.* **52**, 1663 (2004).
- [74] T. Frolov and Y. Mishin, *Phys. Rev. B* **82**, 174114 (2010).
- [75] D. O. Edwards and W. F. Saam, *J. Low Temp. Phys.* **82**, 119 (1991).
- [76] R. H. Torii and S. Balibar, *J. Low Temp. Phys.* **89**, 391 (1992).
- [77] J. L. Baum, D. F. Brewer, J. G. Daunt, and D. O. Edwards, *Phys. Rev. Lett.* **3** (1959).
- [78] Y. Huang and G. Chen, *Phys. Rev. B* **72**, 184513 (2005).
- [79] E. R. Hernandez, A. Rodriguez-Prieto, A. Bergara, and D. Alfe, *Phys. Rev. Lett.* **104**, 185701 (2010).
- [80] V. V. Kechin, *J. Phys.: Condens. Matter* **7**, 531 (1995).
- [81] M. I. Eremets and I. A. Trojan, *JETP Lett.* **89**, 174 (2009).
- [82] A. Lazicki, Y. Fei, and R. J. Hemley, *Solid State Commun.* **150**, 625 (2010).
- [83] F. C. Frank and J. H. van der Merwe, *Proc. Royal Soc. Lond. Series A* **198**, 205 (1949).
- [84] L. Dong, J. Schnitker, R. W. Smith, and D. J. Srolovitz, *J. Appl. Phys.* **83**, 217 (1998).
- [85] J. Li, *Modelling Simul. Mater. Sci. Eng.* **11**, 173 (2003).
- [86] T. Frolov and Y. Mishin, *Phys. Rev. B* **82**, 174113 (2010).
- [87] B. B. Laird and R. L. Davidchack, *J. Chem. Phys.* **132**, 204101 (2010).

- [88] S. Angioletti-Ubert, M. Asta, M. W. Finnis, and P. D. Lee, *Phys. Rev. B* **78**, 134203 (2008).
- [89] S. Angioletti-Uberti, M. Ceriotti, P. D. Lee, and M. W. Finnis, *Phys. Rev. B* **81**, 125416 (2010).
- [90] X. M. Bai and M. Li, *J. Chem. Phys.* **123**, 151102 (2005).
- [91] X. M. Bai and M. Li, *J. Chem. Phys.* **124**, 124707 (2006).
- [92] V. G. Baidakov, A. O. Tipeev, K. S. Bobrov, and G. V. Ionov, *J. Chem. Phys.* **132**, 234505 (2010).
- [93] T. Frolov and Y. Mishin, *Modelling and Simulation in Materials Science and Engineering* **18**, 074003 (2010).
- [94] S. M. Foiles, *Scri. Mater.* **62**, 231 (2010).
- [95] D. N. Seidman, *Annual Review of Materials Research* **32**, 235 (2002).
- [96] M. Tschopp, M. Horstemeyer, F. Gao, X. Sun, and M. Khaleel, *Scripta Materialia* **64**, 908 (2011).
- [97] C. Lemier and J. Weissmuller, *Acta Mater.* **55**, 1241 (2007).
- [98] J. Weissmüller and C. Lemier, *Phys. Rev. Lett.* **82**, 213 (1999).
- [99] J. Weissmüller, H.-L. Duan, and D. Farkas, *Acta Materialia* **58**, 1 (2010).
- [100] S. J. Fensin et al., *Phys. Rev. B* **81**, 031601 (2010).
- [101] L. Shvindlerman and G. Gottstein, *Scri. Mater.* **54**, 1041 (2006).
- [102] A. Lipnitskii, A. Ivanov, and Y. Kolobov, *The Physics of Metals and Metallography* **101**, 303 (2006), 10.1134/S0031918X0603015X.
- [103] J. Weissmüller, J. Markmann, M. Grewer, and R. Birringer, *Acta Materialia* **In Press, Corrected Proof**, (2011).
- [104] A. Suzuki and Y. Mishin, *Interface Science* **11**, 425 (2003).
- [105] T. Frolov and Y. Mishin, *Phys. Rev. Lett.* **106**, 155702 (2011).
- [106] A. Lobkovsky and J. W. Warren, *Physica D* **164**, 202 (2002).
- [107] M. Tang, W. C. Carter, and R. M. Cannon, *Phys. Rev. B* **73**, 024102 (2006).
- [108] J. Mellenthin, A. Karma, and M. Plapp, *Phys. Rev. B* **78**, 184110 (2008).
- [109] Y. Mishin, W. J. Boettinger, J. A. Warren, and G. B. McFadden, *Thermodynamics of grain boundary premelting in alloys. I. Phase field modeling*, *Acta Mater.* (2008), submitted as Part I of this work., 2008.

- [110] D. A. Porter and K. E. Easterling, *Phase transformations in metals and alloys*, Taylor and Francis, second edition, 2004.
- [111] J. W. Cahn, *Acta Metall.* **5**, 169 (1957).
- [112] J. W. Cahn and J. E. Hilliard, *J. Chem. Phys.* **31**, 688 (1959).
- [113] I. M. Gelfand and S. V. Fomin, *Calculus of Variations*, Dover, Mineola, New York, 1991.
- [114] R. J. Asaro and W. A. Tiller, *Metall. Trans.* **3**, 1789 (1972).
- [115] P. G. de Gennes, *Rev. Mod. Phys.* **57**, 827 (1985).
- [116] H. Song, S. J. Fensin, M. Asta, and J. J. Hoyt, *Scripta Mater.* **63**, 128 (2010).

Curriculum Vitae

Timofey Frolov was born in 1983 in Russia. He earned a B.S. degree in applied physics and math from South Ural State University, Russia in 2004. He enrolled in PhD program in physics at George Mason University, Fairfax, Virginia in 2007 and worked under supervision of Dr. Yuri Mishin.